UNIVERSITY OF READING

Department of Meteorology

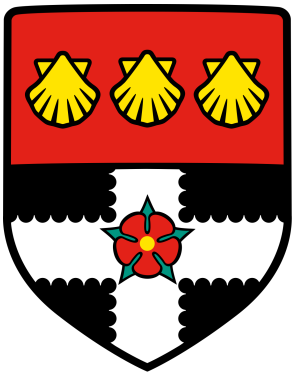

The nature and importance of interactions between convective activity in Western and Eastern Equatorial Africa

Godwin Ayesiga

A thesis submitted for the degree of Doctor of Philosophy

September 2021

Declaration

I confirm that the content herein is my own work and the use of any other material from other sources has been properly and fully acknowledged.

Godwin Ayesiga

Dedication

To My Family

ANNET, RYAN, RINAH & RANITA

Abstract

In Equatorial Africa, millions of people rely on rain-fed agriculture as their only source of livelihood and are vulnerable to varying precipitation patterns, especially extreme precipitation. This thesis investigates, using observations, reanalysis, a state-of-the-art Africa-wide convection permitting climate model (CP4A) and its corresponding global simulation (G25), the precipitation relationship between Western Equatorial Africa (WEA) and Eastern Equatorial Africa (EEA) and the associated physical processes. CP4A and G25 are evaluated against observations and ERA-Interim, with a focus on precipitation and Kelvin wave activity.

Lead/lag correlation and spatio-temporal correlation patterns over various sub-regions reveal a synoptic-scale relationship in precipitation between WEA and EEA in which precipitation over EEA lags precipitation over WEA by 1–2 days. Composites on anomalous precipitation events and an equatorial wave dataset show an apparent connection between eastward/northeastward propagating anomalous precipitation and Kelvin wave low-level convergence, suggesting an influence of Convectively Coupled Kelvin Waves (CCKWs).

Observations/reanalysis and simulations show that the two important processes through which CCKWs modulate the eastward propagation of convection and precipitation across Equatorial Africa are: 1) low-level westerly anomalies that lead to increased low-level convergence, and 2) westerly moisture flux anomalies that amplify the lower-to-mid-tropospheric specific humidity. CP4A and G25 generally simulate the key horizontal structure of CCKWs, with anomalous low-level westerlies in phase with positive precipitation anomalies. On days with an observed high-amplitude Kelvin wave, an extreme precipitation episode is up to twice as likely to occur compared to climatology, and precipitation intensity increases by up to 4 mm day^{-1}, although extreme precipitation patterns associated with intense Kelvin waves vary somewhat from case study to case study.

These results reveal the important processes that need to be satisfactorily represented in models, and they suggest that monitoring the propagation characteristics of CCKWs may be important in synoptic-timescale forecasting over Equatorial Africa.

Acknowledgements

First, I would like to appreciate my supervisors, Dr. Christopher E. Holloway and Dr. Charles JR. Williams, for their tireless support, enthusiasm and availability from the time of developing a research proposal. I would like to thank them for accepting me to take off time from my PhD to undertake a 4 months attachment at the National Oceanic Atmospheric Administration (NOAA) in Washington DC. Thank you very much Chris and Charlie!

I am grateful to Prof. Emily Black, Prof. Andrew Turner and Prof. Richard Washington for their feedback during monitoring committee meetings and the viva examination. I would also like to thank Prof. Steve Woolnough, Dr. Gui-Ying Yang, Dr. Claudia Stephan, Dr. Samantha Ferrett and Dr. Linda Hirons for all the discussions. The feedback you gave me kept me progressing in the desired direction. I would also like to thank the University of Reading for awarding me a fees-only International Research Studentship, the Government of Uganda through the Uganda National Meteorological Authority for supporting me with living expenses and Department of Meteorology for not only supporting this project but also paying tuition for my 4^{th} year.

Thank you to my friends and colleagues Mark, Josh, Bethan, Jake, Kaja, Lais, Tony, Katy, Dan, Steve and Abass for making my time in Reading such an enjoyable experience.

Finally, special appreciation to Annet, my wife for taking care of our lovely children Ryan, Rinah and Ranita while I was away. Thank you my family for allowing me to stay away for several years to pursue a PhD. Thank you for the continued love.

Contents

List of Acronyms

Acronym	Definition
AEWs	African Easterly Waves
AGCMs	Atmospheric General Circulation Models
AR	Assessment Report
CBT	Cloud Brightness Temperature
CCKWs	Convectively Coupled Kelvin Waves
CMIP5	Coupled Model Intercomparison Project Phase 5
DJF	December, January, February
EEA	Eastern Equatorial Africa
ENDGame	Even Newer Dynamics for General Atmospheric Modelling of the Environment
ENSO	El Niño Southern Oscillation
EOF	Empirical Orthogonal Function
EOT	Empirical Orthogonal Teleconnecation
ERA-I	ERA-Interim
EUMETSAT	European Organization for the Exploitation of Meteorological Satellites
GPCC	Global Precipitation Climatology Centre
GPCP 1DD	Global Precipitation Climatology Project 1 Degree Daily
GPCP	Global Precipitation Climatology Project
HadAM	Hadley Centre Atmospheric Model
IOD	Indian Ocean Dipole
IPCC	Intergovernmental Panel on Climate Change
IR	InfraRed
ITCZ	InterTropical Convergence Zone
JAS	July, August, September
JJA	June, July, August
KWs	Kelvin Waves
MAM	March, April, May
MCSs	Mesoscale Convective Systems
MetUM	Met Office Unified Model
MJO	Madden-Julian Oscillation
NCAR	National Centre for Atmospheric Research
NCEP	National Centers for Environmental Prediction
NOAA	National Oceanic Atmospheric Administration
NWP	Numerical Weather Prediction
OLR	Outgoing Longwave Radiation
SON	September, October, November
SST	Sea Surface Temperature
TEJ	Tropical Easterly Jet
TRMM	Tropical Rainfall Measuring Mission
WEA	Western Equatorial Africa

Chapter 1

Introduction

1.1 Motivation and Background

Rainfall plays a vital role in the global water cycle and is important in sustaining key sectors such as agriculture. Over Equatorial Africa (15^{o}S - 15^{o}N, 0 - 51^{o}E), irrigation is relatively underdeveloped, and nearly 95% of agricultural land depends on precipitation (Wani et al., 2009).The communities in this region are part of the 600 million people in Sub-Saharan Africa that not only survive on rain-fed agriculture but are also vulnerable to impacts of extreme precipitation events such as landslides, floods and droughts (e.g., Graham et al., 2015; Salerno et al., 2019). The agricultural sector in several Equatorial African countries contributes between 20%-60% of the Gross Domestic Product (OECD/FAO, 2016) and is the dominant source of employment (e.g., Tomšík et al., 2015). Therefore, precipitation is an important meteorological variable because livelihoods of millions of smallholder farmers and livestock keepers are threatened when floods associated with extreme precipitation events destroy crops. (e.g., Liu, 2020).

Since the agricultural system over Equatorial Africa is rainfall dependent, it thrives on weather and climate information on a combination of timescales, including including sub-daily, daily, synoptic (2-10 days), seasonal and intra-seasonal, annual and interannual, and finally decadal and beyond (Tall et al., 2013). For example, occurrence of an unexpected dry spell after the farming community has already planted is associated with devastating socio-economic impacts and food insecurity due to crop loss and reduced productivity (Parker and Diop-Kane, 2017). However, reliably forecasting the spatial and temporal distribution of precipitation over this region remains one of the most challenging endeavours facing today's operational meteorology. This is because the processes that control precipitation variability occur on a wide range of spatial and temporal scales, many of which are not well understood (e.g., Corfidi, 2017).

In recent decades, the seasonal timescale has been given greater attention both in terms of research and forecasting. For example, before the start of a rainy season, climate scientists, researchers and users of climate

information convene in the Regional Climate Outlook Forums (RCOFs), such as the Greater Horn of Africa Climate Outlook Forum (GHACOF) (e.g., see Graham et al., 2015), to discuss the seasonal forecast. Despite their high socio-economic importance, far less work has been published on Equatorial Africa's convective activity and precipitation variability on synoptic timescales. For example, knowledge on the drivers of synoptic-timescale precipitation variability over Equatorial Africa and how well these drivers are represented in climate models would be valuable. This thesis aims at contributing to the knowledge on synoptic-timescale convective activity and precipitation variability over this region.

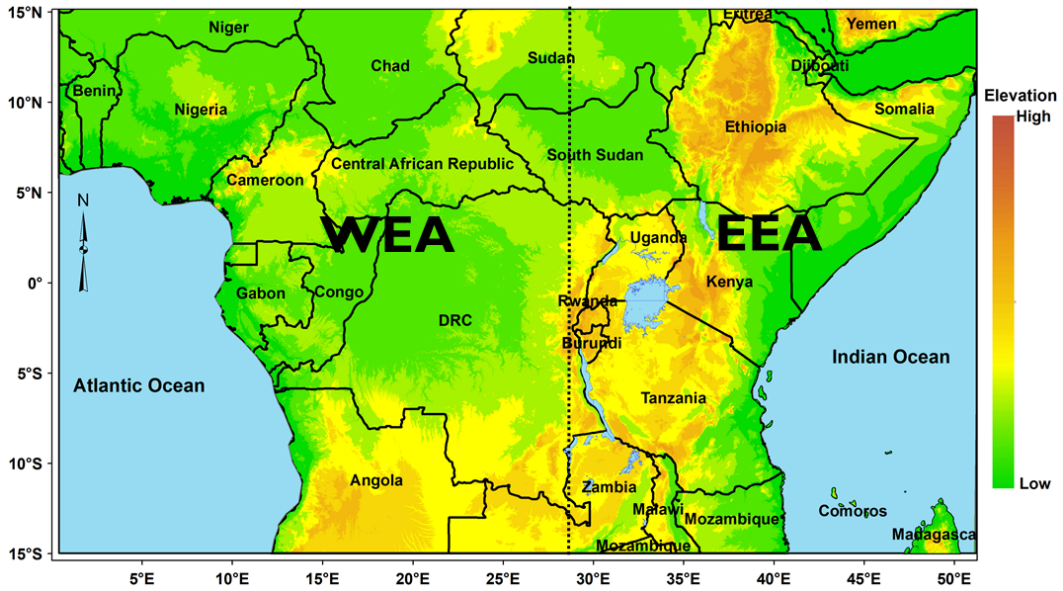

Figure 1.1: Schematic of topography in Equatorial Africa (study domain), with the black dashed line at about 29°E as the longitude separating Western Equatorial Africa (WEA) from Eastern Equatorial Africa (EEA).

Equatorial Africa (defined in this thesis as the region between 15°S - 15°N, 0 - 51°E, with the dotted line at 29°E dividing Western Equatorial Africa (WEA) to the west and Eastern Equatorial Africa (EEA) to the east as shown in Figure 1.1) is a large area that constitutes nearly half of the equatorial landmass and spans different seasons and precipitation patterns (e.g., Nicholson and Dezfuli, 2013a; Nicholson, 2017). Previous publications such as Hills (1979; their Figure 1) and Sandjon et al. (2014) used a similar definition of Equatorial Africa as used in this thesis. The 29°E meridian was chosen to divide Equatorial Africa into WEA and EEA for consistency with previous publications (e.g., see Sandjon et al. (2014; their Figure 1), and an operational weather forecasting model over Lake Victoria in EEA (e.g., see Woodhams et al. (2018; their Figure 1). The general precipitation climatology of this region varies remarkably within short distances (Nicholson, 2017). This is due to a complicated interplay of several factors like large-scale tropical disturbances such as equatorial waves and physical features such as the rugged orography (e.g., Figure 1.1), land-cover properties and inland water bodies (e.g., Beltrando, 1990). But overall, much of Equatorial Africa experiences two rainfall seasons (boreal spring and boreal autumn) with the seasonal cycle attributed to the migration of the tropical rain-belt (e.g., Hills, 1979). The boreal spring rains occur in March-May with a peak in April while the boreal autumn rainfall occurs in September-November (SON) with a peak in October (Dunning et al., 2016). March-May rains

are known as "long rains" in much of EEA (e.g., Nieuwolt, 1978), "Belg" in Ethiopia (e.g., Gissila et al., 2004), "Gu" in Somalia and "Masika" in Tanzania (e.g., Nicholson, 2017) and the boreal autumn rains are also known as the "short rains" in much of EEA (e.g., Nieuwolt, 1978), "Der" is Somalia and "vuli" in Tanzania (e.g., Nicholson, 2017), and the boreal summer (June-September) rains are locally known as "Kiremt" in Ethiopia (e.g., Gissila et al., 2004). While much of Equatorial Africa receives two rainy seasons per year, some areas in WEA that are within approximately $\pm 5^{o}$ about the equator exhibit a unimodal seasonal cycle (e.g., Dunning et al., 2016). In the Congo Basin (part of WEA), about 60% of the annual rainfall occurs in the two rainy seasons. Studies have shown that Ethiopia experiences three rainy seasons per year: the boreal spring rains in February/March-May, the boreal summer rains in June/July-September and boreal autumn rains in October-November (e.g., Gissila et al., 2004). Boreal summer is the main rainfall season (e.g., Belay et al., 2021) and it contributes between 50%–80% of annual rainfall over the country (e.g., Philip et al., 2018). Within each season, precipitation over Equatorial Africa varies considerably in space and time (e.g., Nicholson, 2017) in association with various drivers. This complexity makes forecasting on various timescales a challenge facing the scientific community.

Seasonal precipitation variability over Equatorial Africa is controlled by large-scale features such as the El Niño Southern Oscillation (ENSO) (e.g., Ropelewski and Halpert, 1987; Black, 2005; Moore et al., 2017), the Indian Ocean Dipole (IOD) (e.g., Black, 2005; Wenhaji Ndomeni et al., 2018) and north-south migration of the Intertropical Convergence Zone (ITCZ), the tropical belt that separates trade winds from the southeast and northeast (e.g., Glover et al., 1954; Nicholson, 2018). El Niño-related precipitation over some areas in Equatorial Africa tends to be enhanced but these rains are unevenly distributed across space and time (e.g., Ropelewski and Halpert, 1987). Looking at Equatorial Africa as a whole, there are sub-regional differences in response of precipitation to the ENSO and IOD signal. These large-scale drivers are further discussed below. On the other hand, the ITCZ influences seasonal precipitation by providing favourable conditions for a number of processes, including: i) the development of both localised and deep convection (e.g., Dias and Pauluis, 2011); ii) Mesoscale Convective Systems (MCSs, e.g., Jackson et al., 2009); and iii) coupling between large-scale convection-organising disturbances such as Kelvin waves and the convection (e.g., Dias and Pauluis, 2011). The localised thunderstorms were once thought to be the primary drivers of precipitation over Equatorial Africa (see Nicholson, 2018).

On shorter timescales, recent studies have demonstrated that convection and precipitation in Equatorial Africa is influenced by organised systems such as MCSs (e.g., Jackson et al., 2009) and other major convection organising phenomena such as the Madden-Julian Oscillation (MJO; Madden and Julian, 1971, 1972) and Convectively Coupled Kelvin Waves (CCKWs) (Pohl and Camberlin, 2006a,b; Sinclaire et al., 2015 Mekonnen and Thorncroft, 2016). These results have changed the narrative from one that advanced the idea that Equatorial Africa's precipitation is purely governed by localised convective features to one in which large-scale tropical disturbances play a key role in organising convection and precipitation (Nicholson, 2018). Synoptic scale tropical disturbances include but are not limited to the MJO (e.g., Madden and Julian, 1971, 1972), Kelvin

waves (Gill, 1980), Equatorial Rossby waves (Wheeler and Kiladis, 1999), African Easterly Waves (AEWs) (Reed et al., 1977), Eastward and Westward Inertio-Gravity waves (EIG and WIG), and Eastward and Westward moving Mixed Rossby-gravity waves (EMRG and WMRG) (Wheeler and Kiladis, 1999; Yang et al., 2003). AEWs are westward propagating waves and are present in tropical north Africa during boreal summer. In the next chapter, these tropical disturbances are further discussed.

An inspection of available literature (e.g., Nicholson, 2018; their Figure 8) and results in Figure 2.1 suggest that WEA is wetter in comparison to EEA, and WEA and EEA have been generally treated as two climatologically different regions (e.g., Dezfuli et al., 2015). WEA mainly consists of the Congo Basin, a region that is covered by the second largest tropical rainforest on earth (Tchatchou et al., 2015). Eltahir (1996) discusses the Walker-like large-scale circulation with an ascending branch over the Congo Basin's rainforest (see illustration in their Figure 14). The high precipitation amounts over much of WEA are associated with a large-scale circulation that transports moisture from the Atlantic Ocean into the interior of the continent (e.g., Eltahir, 1996). Pokam et al. (2014) confirmed the Walker-like cell discussed in Eltahir (1996). On the other hand, the drier EEA might be explained by several factors including: the negative vertically integrated moisture flux convergence throughout the year that only becomes weakly positive during boreal spring and boreal autumn (e.g., Yang et al., 2015), the Turkana low-level jet that transport moisture away from the region (e.g., Nicholson, 2016) and large-scale subsidence during early boreal spring (e.g., Vellinga and Milton, 2018). As such, WEA and EEA have several meteorological similarities and differences. One main similarity, as noted above, is that precipitation in both seasons is generally controlled by the ITCZ. Table 1.1 gives a brief summary of some of the physical differences between WEA and EEA.

	WEA (15^{o}S-15^{o}N, 0-29^{o}E)	**EEA (15^{o}S-15^{o}N, 29-51^{o}E)**
Mean topography	Lower than 700m	Higher than 1500m
Major vegetation cover	Tropical rainforest	Semiarid/arid and small forests
Mean annual rainfall	Greater than 1600mm	Generally less than 700mm
Borders	Rift Valley-Atlantic Ocean	Indian Ocean (east)-Rift Valley (west)

Adapted and modified from Sandjon et al. (2012).

Table 1.1: A comparison between WEA and EEA

By studying the two regions concurrently, this study explores the connection between the two regions with an aim of improving the understanding of some of the major aspects of Equatorial Africa's meteorology that are important in operational forecasting and numerical weather and climate prediction. While precipitation connections between regions have been explored in previous studies (e.g., Behrend, 1987), very few publications have attempted to investigate the convective activity and precipitation linkage between WEA and EEA. Yet it was found that convection in WEA influences the meteorology of the neighbouring regions (e.g., Matari, 2002). In one example, Mekonnen and Thorncroft (2016) examined Cloud Brightness Temperature (CBT) for boreal summer (July-September) and found a synoptic scale convective activity connection between the Congo Basin and East Africa. They showed a coherent eastward propagating signal in CBT that had a periodicity of

about 4 days. It remains unclear as to whether the convective activity relationship between the Congo Basin and East Africa is present in observed and simulated precipitation, and also whether this relationship is present in seasons other than boreal summer.

As described above, precipitation over Equatorial Africa sustains several sectors of economies of countries in this region; this implies that the ability to accurately forecast precipitation occurrences on short-to-medium range would yield tremendous benefits to the region. Short-to-medium range forecasts are particularly important in rainy seasons in which forecast models have little or no skill. Over EEA, the predictability of the boreal spring (MAM) rains remains generally a challenge because of its weak connection with the large scale features such as variability in the sea surface temperatures (SSTs) (Vellinga and Milton, 2018). However, the boreal autumn rains have been found to be strongly linked to large-scale drivers such as SSTs (Ogallo, 1988; Nicholson, 2002; Black et al., 2003; Wenhaji Ndomeni et al., 2018) making it relatively predictable. For March-April rains, Vellinga and Milton (2018) attributed 30-60% of the variance in annual precipitation variability over East Africa to a combined effect of the warm SSTs in western Indian Ocean, strong MJO activity in February and March and an easterly phase of the Quasi-Biennial Oscillation (QBO) during the preceding autumn, with each of these associated with increased precipitation. Black et al. (2003) found that extreme precipitation over East Africa in September-November is associated with large-scale positive SST anomalies in the western Indian Ocean. Black et al. (2003) suggested that the positive phase of the IOD (also known as Indian Ocean Zonal Mode (IOZM)) enhances precipitation over East Africa through sustaining anomalous easterly winds over the northern-central Indian Ocean and suppressing moisture transport away from East Africa. Consistent with Black et al. (2003), Wenhaji Ndomeni et al. (2018) reported that the positive phase of the IOD is associated with enhanced rainfall over East Africa. They suggested that the main mechanism of influence is via increased moisture convergence over East Africa caused by anomalous low-level easterly flow over warm Indian Ocean SSTs.

Over WEA, there are several factors that govern the evolution of seasonal precipitation (e.g., Nicholson and Grist, 2003; Balas et al., 2007). For example, warmer tropical Atlantic SSTs indirectly enhances precipitation over WEA through location of the ITCZ that in turn favours development of MCSs and other precipitation organising disturbances (Balas et al., 2007). Precipitation across timescales over WEA remains unpredictable because the influence of large-scale drivers such as SSTs over the Pacific, Indian and Atlantic Oceans varies from season to season and from sub-region to sub-region (Balas et al., 2007; Farnsworth et al., 2011). For instance, Balas et al. (2007) reported that the impact of SSTs on seasonal precipitation over WEA depends on the ocean basin and the season because the same SST anomalies in a particular ocean may cause enhanced precipitation over WEA in one season but suppress it in another season.

On intraseasonal timescales, the MJO (e,g., Madden and Julian, 1971, 1972) is a major tropical disturbance confined in the tropical belt and modulates intraseasonal precipitation variability over Equatorial Africa (e.g., Mutai and Ward, 2000; Sandjon et al., 2012; Berhane et al., 2015; Hogan et al., 2015) and other tropical regions. Observations have shown that the MJO generally originates over the Indian Ocean and its envelope of organised

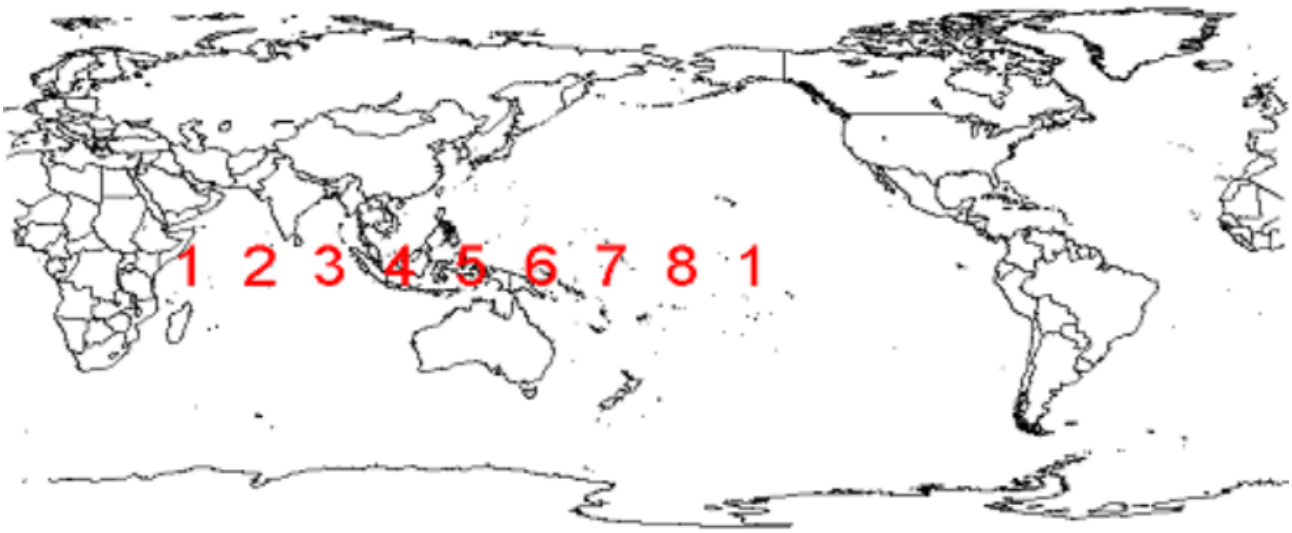

Figure 1.2: An approximate location of the centres of enhanced convection (phases) of the MJO. Phase 1 involves the signals for both the initiation of an MJO event in the western Indian Ocean basin and its decay in the central Pacific Ocean. The speed of propagation varies but between phases 2 and 8, it takes 4-10 days per phase. Figure taken from Donald et al. (2004)

.

convection propagates eastward at a speed of approximately 5 m s^{-1} on a spatial scale of about 10000 km (e.g., Weickmann et al., 1985). The MJO occasionally circumnavigates the global tropics and organises convection on regional scales with the strongest influence on convection and precipitation observed during boreal spring and boreal winter (Madden and Julian, 1994). As the MJO propagates eastward, it causes variations in several atmospheric fields such as lower and upper level wind speed and direction, cloudiness, and convective rainfall (e.g., Sandjon et al., 2012). The MJO has been described as alternating centres of enhanced and suppressed convection with the two centres linked by an overturning zonal circulation (e.g., Madden and Julian, 1972). The lower branch of the overturning circulation is constituted by anomalous westerly flow to the west of the centre of enhanced convection and anomalous easterly winds to its east while at upper levels, these winds reverse direction of flow (e.g., Madden and Julian, 1972; their Figure 16). The interaction between the large-scale circulation associated with the MJO and the centre of enhanced convection forms a coupled structure that propagates eastward (e.g., Zhang, 2005). The influence of the MJO on Equatorial Africa's precipitation is normally discussed in reference to its eight phases (centre of enhanced tropical convection; Figure 1.2) as was determined using an index described in Wheeler and Hendon (2004).

The MJO is of interest to this thesis because of its relationship with synoptic timescale disturbances such as Kelvin waves, its direct impact on precipitation on timescales of one day to weeks thus overlapping with synoptic timescales (Pohl and Camberlin, 2006b; Barlow et al., 2005) and its association with widespread convection over Equatorial Africa (e.g., Laing et al., 2011). Furthermore, Sobel and Kim (2012) suggested that the MJO tends to transition into an eastward propagating dry Kelvin wave after decoupling with convection and Haertel et al. (2015) suggested that as the MJO matures, a Kelvin waves emerges from its eastern edge, transitions into a dry Kelvin wave and propagates eastward. The influence of the MJO on precipitation over

Equatorial Africa will be further discussed in Chapter 2.

One of the most important tropical disturbances that modulates synoptic-timescale convection and precipitation variability over Equatorial Africa is the CCKW (Schlueter, 2020). Atmospheric Kelvin waves (Kelvin waves hereafter) are large-scale tropical disturbances that propagate eastward along a physical boundary such as the equator. In the tropical belt, the change in the polarity of the Coriolis parameter at the equator renders Kelvin waves to be equatorially trapped. Kelvin waves that interact with and are linked to deep, moist convection are commonly known as CCKWs. The interaction of the CCKWs with convection at local and regional scales over Equatorial Africa is an issue whose solution could lead to an improved understanding of Kelvin waves and an improvement in synoptic temporal forecasts over this region. Previous studies such as Mounier et al. (2007) and Laing et al. (2011) showed that the passage of a CCKW over Equatorial Africa is associated with increased size and duration of MCSs. In essence, Kelvin waves play an important role in modulating synoptic-scale precipitation variability (e.g., Nguyen and Duvel, 2008; Laing et al., 2011; Jackson et al., 2019). This suggests that CCKWs might influence extreme precipitation over Equatorial Africa, however, this aspect has not been adequately investigated. This thesis contributes knowledge on this aspect.

The impact of Kelvin waves on deep, moist convection is confined within a latitudinal belt of $\sim \pm 10^{o}$ about the equator (Kiladis et al., 2009). Over Equatorial Africa, Kelvin waves are characterised by periodicity of 2-6 days and wave length of 2000-3000 km (e.g., Mekonnen et al., 2008). The influence of Kelvin waves on convection varies in both time and space (e.g., Roundy and Frank, 2004). These waves can be tracked for several days and thus might constitute an important source of short-to-medium range predictability of convection and precipitation over Equatorial Africa (e.g., Wheeler and Weickmann, 2001). Information on synoptic-timescale precipitation variability helps communities to take advantage of both wet and dry spells to manage agricultural productivity, particularly over Equatorial Africa (e.g., Sinclaire et al., 2015). However, global Numerical Weather Prediction (NWP) models over this region have low skill even for short lead time of a few days to a week (e.g., Vogel et al., 2020). Furthermore, Vogel et al. (2020) reported that these models are not skillful in capturing extreme precipitation episodes. One reason for the low skill might be the poor understanding and representation of the processes that control synoptic-timescale precipitation variability.

Sinclaire et al. (2015) and Mekonnen et al. (2008) suggested that CCKWs play a role in the eastward propagation of convective activity, thereby modulating localised precipitation episodes along their path across tropical Africa. For example, an intense Kelvin wave that propagated through tropical Africa during the period 6-12 August 1987 was associated with an increase in precipitation (e.g., Mekonnen et al., 2008). Similar case studies, but over Equatorial Africa during boreal spring and autumn rains, have not been explored in the existing literature. In addition, the processes through which CCKWs modulate eastward propagation of convective activity and precipitation across Equatorial Africa remain unclear. An inquiry into whether the eastward propagation of convective activity is present in observed precipitation as well as the associated processes will add knowledge on the meteorology of Equatorial Africa. Also, an investigation in relation to how well CCKWs

modulate the eastward propagation of convection and precipitation would likely be useful in improving NWP and climate models.

Most operational weather forecasting at National Meteorological Centres (NMCs) in Equatorial African countries depend on global model guidance. However, global models tend to produce too light and too frequent precipitation (e.g., Stephens et al., 2010), implying that these models are not skillful in capturing extreme precipitation episodes (e.g., Vogel et al., 2020). Due to coarse grid spacing, global models must implement a convection scheme to represent sub-grid scale processes. This, coupled with other limitations linked to parameterisations of other sub-grid scale processes may cause them to struggle to realistically simulate tropical modes such as MJO (e.g., Lin et al., 2006) and CCKWs (e.g., Yang et al., 2009). Due to problems in global models, the scientific community is looking in the direction of Convection Permitting Models (CPMs) to reduce the gap in knowledge about the climate. Unlike models that parameterise convection, CPMs are configured with fine grid spacing ($\sim$1-5 km) so that they are able to physically represent individual clouds and mesoscale convective circulations without using convective parameterisations. CPMs have a realistic representation of clouds and precipitation compared to their counterpart models with the same grid spacing but with a convection parametrisation scheme switched on (Stein et al., 2015). While CPMs are currently being used for numerical weather prediction (e.g., Woodhams et al., 2018) and climate studies (e.g., Kendon et al., 2019), the important processes that control precipitation variability across Equatorial Africa need rigorous evaluation so that findings inform model development (James et al., 2018). This thesis evaluates both a convection permitting simulation and a coarse global simulation with respect to the eastward propagation of convection and precipitation.

Mekonnen and Thorncroft (2016) pointed out that forecasters in EEA and the African Centre for Meteorological Applications and Development (ACMAD) pay attention to the convective activity in the Congo Basin (part of WEA) in their forecasting discussions. This interest might be based on early studies such as Hills (1979) that suggested that the low-level westerly flow (the Congo airmass) is one of the sources of moisture and convective instability that accounts for precipitation over Sudan, Ethiopia, Uganda and western Kenya. Van der Ent et al. (2010) reported that EEA is a source of moisture for convective instability over WEA. The results in Hills (1979) and Van der Ent et al. (2010) suggest an intra-equatorial Africa interaction that warrants attention. To date, studies focusing on the west-east propagation convection and precipitation across Equatorial Africa are scarce. It would be expected that an improved understanding of the propagation of convection and precipitation from west to east across Equatorial Africa might provide a source of synoptic-timescale precipitation predictability downstream. As discussed above, recent work in Mekonnen and Thorncroft (2016) showed a synoptic-timescale convective activity linkage between the Congo Basin and East Africa in boreal summer's CBT (e.g., see §2.1.3). Considering the importance of the west-east propagation of convection and precipitation to forecasters in EEA and ACMAD, the study by Mekonnen and Thorncroft (2016) merits an extension by examining: (i) actual observed daily precipitation instead of CBT; (ii) repeating (i) for a number of different datasets; (iii) undertaking this for the whole year (rather than boreal summer only); (iv) using a higher spatial resolution; (v) and using both observations and state-of-the-art regional climate model to explore the physical

mechanisms that are responsible for the eastward propagation of convection and precipitation.

Against the above background, this thesis investigates, using observations, reanalysis, an Africa-wide state-of-the-art high resolution climate simulation from a convection permitting model, and a coarse global simulation, the precipitation relationship between EEA and WEA and the associated physical processes. Further, the linkage between high-amplitude Kelvin waves and precipitation over Equatorial Africa is investigated. The high resolution climate simulation examined in this thesis was run as part of the Future Climate for Africa (FCFA) Improving Model Processes for African Climate (IMPALA) project. FCFA aims at revitalising climate science over Africa and ensuring that the new climate science causes an impact in the development of the continent. The IMPALA project seeks to understand the impact of high resolution and explicit representation of convection on the present and future climate of Africa (Senior et al., 2020). The results in this thesis highlight the deficiencies in the models in terms of representation of the coupling between Kelvin waves and the precipitation. It is therefore expected that the results in this thesis will have both direct and indirect societal benefits.

1.2 Thesis outline

This section provides a broad structure of the thesis; Section 2.7 reveals the details of each chapter.

Chapter 2 is an expansion of the current introduction and provides a general overview of the past research work concerning precipitation variability over Equatorial Africa.

In Chapter 3, the datasets and the methods used in this thesis are described. For instance, the method used to identify Kelvin wave activity (equatorial wave data in both reanalysis and simulations is illustrated in Section 3.3.1.

In Chapter 4, focus is placed on the observed synoptic-scale precipitation connection between WEA and EEA. Work in this chapter has been published in the International Journal of Climatology (Ayesiga et al., 2021). The material on methods for this chapter can be seen in Chapter 3.

Chapter 5 investigates the presence of the eastward propagating of precipitation signal in a multi-year state-of-the-art Africa-wide convection permitting simulation (CP4A) (§3.2.4.2) alongside its global driving model (G25) (§3.2.4.1). This chapter goes further to explore the processes through which CCKWs modulate the eastward propagation of precipitation across Equatorial Africa by examining both simulations, observed precipitation estimates and reanalysis. Also, both simulations are evaluated against observations and reanalysis. Work in this chapter has been published in the Journal of Atmospheric Sciences (Ayesiga et al., 2022, © **American Meteorological Society. Used with permission**). The material on methods for this chapter is provided in Chapter 3.

Chapter 6 explores the role of high-amplitude Kelvin waves in modulating extreme precipitation over Equatorial Africa. The case studies of eastward propagating extreme precipitation are presented and discussed.

This chapter is currently being written up into a paper and is expected to be submitted soon.

Finally, in Chapter 7, the key findings have been summarised, and the scientific advances are highlighted.

Chapter 2

Scientific Background

In this chapter, a general introduction on precipitation over Equatorial Africa is provided in Section 2.1. An overview of precipitation variability in WEA is given in Section 2.1.1 and Section 2.1.2 looks at precipitation variability over EEA. Since part of this thesis focuses on the precipitation and convection relationship between WEA and EEA, Section 2.1.3 presents a more detailed examination of published work that is relevant to this subject. In Section 2.2, a general overview of the atmospheric circulation. In Section 2.3, an overview of equatorial waves over Equatorial Africa is presented. Then, Section 2.4 provides a brief review of the eastward propagation of the convective signal across Equatorial Africa. A separate examination of literature on Kelvin wave activity and its association with precipitation over Equatorial Africa is given in Section 2.5. Section 2.6 presents a brief overview of CCKWs and extreme precipitation. Finally, Section 2.7 presents the objectives of this thesis and demonstrates how the objectives are achieved.

2.1 Introduction

Rainfall variability at various timescales has a direct influence on rain-fed agricultural productivity because it determines the amount of available soil moisture (e.g., Black et al., 2016) as well as the frequency of replenishing surface and underground water for production (Taylor et al., 2019). Unexpected changes in the frequency, spatial distribution and intensity of rainfall threatens millions of lives in Equatorial Africa that depend on it for not only a decent livelihood but also their very survival (e.g., Ray et al., 2015; FAO, 2016). For example, the occurrence of prolonged dry spells can lead to crop failure (e.g., Usman and Reason, 2004) while excessive rains are likely to cause destructive flooding and landslides; therefore, to minimize loss of life and livelihoods, it is important to develop robust forecasting systems for various timescales (Ongoma et al., 2018).

In Equatorial Africa, however, the reliability of short-term forecasts depends on experts' ability to extrapolate the prevailing conditions, as well as interpretation of forecast maps from global forecast centres (Graham

et al., 2015). While forecast model guidance from convection permitting models has become an additional tool to support forecasting over EEA (e.g., Woodhams et al., 2018), a similar tool for WEA is less common. Even with the evolution of convection permitting models, the challenge of unrealistic representation of the spatial and temporal interaction of key drivers of convection and precipitation variability remains.

One broad question that remains open concerns the drivers of precipitation variability over Equatorial Africa. Satisfactorily addressing this issue is important because a thorough understanding of these variations and their drivers across spatial and temporal scales is a positive step toward improving the precipitation forecasts. Some studies have investigated the potential drivers of precipitation variability over this region. For example, it has been reported that synoptic-scale precipitation variability over Equatorial Africa is largely modulated by large-scale features such as equatorial waves (e.g., Schlueter, 2020). This precipitation variability manifests as episodes of enhanced or suppressed daily rainfall. This suggests that representation of large-scale features and their interaction with convection and precipitation in climate models and weather forecasting models is important for forecasting systems.

One major step in improving short-to-medium-range forecasting is enhancing knowledge on the role of synoptic scale disturbances such as equatorial waves in modulating convection and precipitation over Equatorial Africa. These disturbances influence convection and precipitation by significantly perturbing the basic state of atmospheric fields such as pressure, temperature and wind. The resulting latent heat released by the deep convection associated with the perturbed fields can cause the generation of new equatorial waves (e.g., Lindzen, 2003). As a wave propagates, it interacts with convection through, for example, enhancing low-level moisture flux (e.g., Mekonnen et al., 2008; Sinclaire et al., 2015) and influencing convection and precipitation downstream, and this may cause a reduction in its speed of propagation.

The major wave-like tropical disturbances that influence precipitation variability over Equatorial Africa include the MJO (e.g., Pohl and Camberlin, 2006b; Hogan et al., 2015), Kelvin waves (e.g., Wheeler and Kiladis, 1999), Equatorial Rossby Waves and mixed Rossby-gravity waves (e.g., Roundy and Frank, 2004). These are further briefly discussed in Sections 2.2 and 2.5. These tropical disturbances occur on different spatial scales and frequency. However, multiscale interactions between, for example, Kelvin waves and the MJO have been found to be major sources of synoptic-timescale convection and precipitation variability over Equatorial Africa (e.g., Laing et al., 2011). Incidentally, there are few publications that have studied synoptic-timescale convection and precipitation over Equatorial Africa as a whole (e.g., Kamsu-Tamo et al., 2014; Mekonnen and Thorncroft, 2016). There might be several reasons for this but one such reason is the lack of long-term high resolution observations over most of Equatorial Africa (e.g., Washington et al., 2013). The availability of recent high-resolution and long-term simulations over large domains provides an opportunity to study the meteorology of Equatorial Africa in detail and in a physically consistent manner.

This work focuses on all of Equatorial Africa, rather than focusing exclusively on WEA or EEA. To provide context to this work, below a brief review of precipitation variability in both regions is presented.

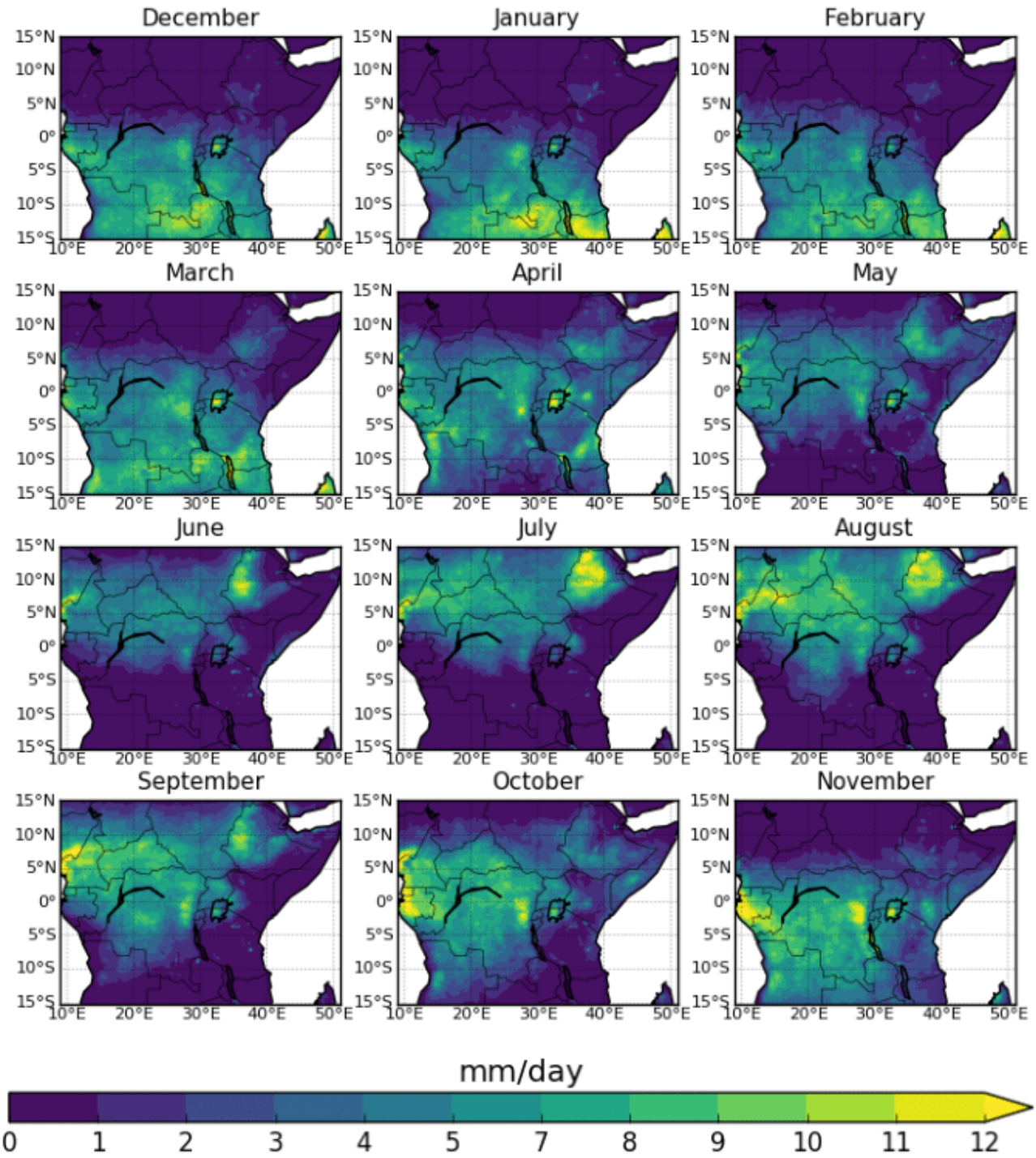

Figure 2.1: Monthly mean precipitation (mm day^{-1}) based on 16 years (1998 - 2013) of TRMM daily estimates.

2.1.1 Precipitation variability in WEA

Across Equatorial Africa, WEA is the least studied region (Washington et al., 2013; Alsdorf et al., 2016) yet convection in this region influences convective activity and precipitation in neighbouring regions (Matari, 2002). Since large-scale convection in WEA is important for the entire global tropics, comprehensive understanding of convective activity in this region is likely to provide information on convection and precipitation variability of other regions like EEA.

The precipitation regime in much of WEA is generally a bimodal annual rainfall cycle with the maxima in April and October as shown in Figure 2.1 based on TRMM. However, in the regions within approximately $\pm 5^{o}$ about the equator a unimodal rainfall cycle prevails (Dunning et al., 2016). WEA is one of the most convective regions in the global tropics (e.g., Hartman, 2021), and so precipitation in this region is dominated by MCSs (Nicholson and Grist, 2003). In Jackson et al. (2009), TRMM satellite estimates were used to investigate MCS activity over western equatorial Africa. They found three sub-regions of maximum MCS activity, two over elevated orography and the other over Lake Victoria. These authors concluded that the interaction between large-scale circulation and upslope winds favours development of intense convection and precipitation over the region. The maximum MCS activity found in Jackson et al. (2009) may be associated with the peak rainfall over Lake Victoria in Figure 2.1. The results in Jackson et al. (2009) are in agreement with those in Nguyen and Duvel (2008) who also found initiation of MCSs over the East African highlands on the western branch of the East African rift valley. What this suggests is that any disturbance that modifies MCSs over WEA indirectly impacts the precipitation variability over this part of the continent.

Over WEA, most studies have focused on precipitation climatology, interannual variability (Nicholson and Grist, 2003; Todd and Washington, 2004; Balas et al., 2007) and MCSs (Zipser et al., 2006; Jackson et al., 2009) and only a few have looked at drivers of synoptic-timescale variability (Nguyen and Duvel, 2008; Laing et al., 2011). For example, Nicholson and Grist (2003) analysed precipitation records from 1400-stations and National Centers for Environmental Prediction-National Center for Atmospheric Research (NCEP-NCAR) reanalysis to explore the annual cycle in precipitation and the associated general circulation features over West Africa and Central Africa. They found that in the Northern Hemisphere east of 10^{o}E, upper level divergence associated with the Tropical Easterly Jet (TEJ) influences the development of the seasonal rains by providing a favourable environment for convective activity and in turn, the precipitation indirectly influences the jet through modulation of the surface temperature gradient.

Balas et al. (2007) examined monthly precipitation rain gauge data and SSTs obtained from the Comprehensive Ocean Atmospheric Dataset (COADS) to investigate the relationship between SSTs in various Ocean basins (tropical Atlantic, Pacific and Indian) and interannual precipitation variability over western equatorial Africa (defined in their study as 5^{o}S-10^{o}N,7^{o}E-30^{o}E). They found that interannual precipitation variability is associated with several drivers such as a general warming or cooling over the ocean basins, particularly the Atlantic, the Pacific Ocean El Niño and the SST contrast between the Atlantic and Indian Oceans. They noted that the Atlantic Ocean, for example, influences seasonal precipitation through modulation of the location of the ITCZ. As noted earlier, the ITCZ provides a favourable environment for the development of deep convective systems. They also suggested that the SST contrast between the Indian and Atlantic Oceans leads to an east-west shift of convective activity. Todd and Washington (2004) investigated the connection between interannual precipitation variability over Central Equatorial Africa (12^{o}S-7^{o}N,15^{o}E-32^{o}E) and large-scale circulation over North Atlantic Ocean during boreal spring and boreal winter. They found that anomalous precipitation over Central Equatorial Africa is associated with anomalous westerly mid-tropospheric zonal winds over the Atlantic

Ocean.

The key sources of moisture for precipitation in WEA are the Indian Ocean (e.g., McCollum et al., 2000), moisture recycling from Congo Basin (e.g., Pokam et al., 2014), and moisture transported from the Atlantic Ocean (e.g., Pokam et al., 2012). Dyer et al. (2017) investigated these moisture sources and found that in both boreal spring and autumn, the southwestern Indian Ocean accounts for about 21% and 25%, respectively, for the recycling ratio for moisture over the region. It is possible that the Turkana Low-Level Jet (TLLJ) (e.g., §2.2) helps in the eastward transport of moisture. While the Indian Ocean has been identified as a source of moisture for the Congo Basin, it has also been suggested that near the surface (1000-825hPa), the East African highlands tend to block moisture from the Indian Ocean from penetrating deep into the interior of Equatorial Africa (McCollum et al., 2000).

2.1.2 Precipitation variability in EEA

The weather and climate patterns over EEA are highly variable and are associated with several physical mechanisms. As discussed in Chapter 1, EEA is climatologically drier than WEA. For instance, the mean seasonal rainfall for March through to June is less than 200 mm over much of EEA (e.g., Berhane et al., 2015; their Figure 1). Why is EEA generally drier than other equatorial regions remains an open question. Recently, Yang et al. (2015) examined the monthly precipitation amounts from Global Precipitation Climatology Centre (GPCC), Global Precipitation Climatology Project (GPCP), SSTs from the National Oceanic and Atmospheric Administration (NOAA) National Climate Data Center (NCDC) and ERA-Interim Atmospheric fields from the European Centre for Medium-Range Weather Forecasts (ECMWF) over East Africa (10^{o}S-12^{o}N, 30-52^{o}E, note that their definition is similar to EEA used in this thesis). They found weak positive vertically integrated moisture flux convergence during the rainy seasons and negative during most of the year. They concluded that the low climatological precipitation over EEA is explained by the low moist static energy air that originates from the Indian Ocean. Vellinga and Milton (2018) found that precipitation in early boreal spring is suppressed by large-scale subsidence of dry air, a result that might explain why East Africa is generally drier than other equatorial regions.

Several other publications that studied precipitation variability over EEA focused on seasonal timescales (Ogallo, 1988; Mutai et al., 1998; Philippon et al., 2002; Camberlin and Philippon, 2002; Gitau et al., 2015) and interannual variability (e.g., Beltrando and Cadet, 1990; Gong et al., 2016). Results from studies conducted on a seasonal timescale show agreement in that seasonal precipitation over EEA has a high potential for predictability especially for the boreal autumn (e.g., Ogallo, 1988; Mutai et al., 1998; Washington et al., 2013; Gitau et al., 2015; Wenhaji Ndomeni et al., 2018). Like in WEA, synoptic-timescale variability remains largely insufficiently researched over EEA.

Intraseasonal timescale precipitation variability over EEA has also been looked at by some studies (e.g., Mutai and Ward, 2000; Sandjon et al., 2014;Pohl and Camberlin, 2006b; Chan et al., 2008; Hogan et al.,

2015). For example, Hogan et al. (2015) analysed TRMM, ERA-I and a global model simulation from the UK Met Office and demonstrated that when the MJO is in phases 2-4, precipitation over East Africa's highlands is enhanced while that over the coast is suppressed. Results in Hogan et al. (2015) lend support to results in Pohl and Camberlin (2006b). The role of the MJO in impacting precipitation over Equatorial Africa is further discussed in Section 2.4

Both large-scale and local forcing have been found to drive precipitation variability over EEA. For instance, Ogwang et al. (2014) used the International Centre for Theoretical Physics (ICTP) Regional Climate Model (RCM) and demonstrated that local variations in precipitation over EEA during September-December are partly accounted for by EEA's complex topography. An earlier study by Slingo et al. (2005) assessed the sensitivity of EEA's precipitation to topography using a global model. In agreement with Ogwang et al. (2014), they found that the retention of East Africa's topographic effects in the model lead to enhancement of precipitation over East Africa. In addition, Nicholson (2017) reported that the East African highlands on the western branch of the rift valley tend to cut off moisture transport associated with the low-level westerly flow and this causes suppressed precipitation over EEA. Findings in Jackson et al. (2009), Nguyen and Duvel (2008), Slingo et al. (2005) and Ogwang et al. (2014) are suggestive of an important role of topography across Equatorial Africa. In terms of sources of convective instability over EEA, the key sources of moisture for precipitation over EEA is the Congo airmass (e.g., Basalirwa, 1995; Finney et al., 2020) and the Indian Ocean (e.g., Black, 2005; Wenhaji Ndomeni et al., 2018). In general, precipitation over EEA is accounted for by coupling between convection and anomalous zonal wind, more especially the low-level anomalous westerly flow (e.g., Nicholson, 2017; Finney et al., 2020).

2.1.3 Convection and Precipitation relationship between WEA and EEA

Convection and precipitation relationships between different regions are valuable in that they can provide useful information for improving statistical and dynamical weather and climate models. The precipitation and convective activity connection between WEA and EEA has been alluded to in previous publications. For example, moisture advection from WEA contributes to convective activity variability over EEA (e.g., Basalirwa, 1995; Levin et al., 2009; Williams and Funk, 2011) and in return, EEA is also known for being a source of moisture for the MCSs in WEA (e.g., Dezfuli, 2017; Van der Ent et al., 2010). Understanding the synoptic-timescale precipitation relationship between WEA and EEA may be a source of precipitation predictability for precipitation downstream. However, not much literature is available in terms of the interaction between WEA and EEA. As noted above, this could be due to the scarcity of high spatial and temporal resolution observations over much of Equatorial Africa (Nicholson and Dezfuli, 2013).

Nonetheless, recent studies such as Mekonnen and Thorncroft (2016) found a synoptic-scale convective activity relationship between Congo Basin and East Africa. These authors analysed 22-years of Kelvin wave filtered and unfiltered cloud brightness temperature and reanalysis (ERA-Interim) to explore the convective ac-

tivity connection between Congo Basin and East Africa during boreal summer. To retain the synoptic timescale (2-10 days) variability in cloud brightness temperature and wind field, these researchers applied a band-pass filter as described in Duchon (1979), and the Kelvin wave signal was isolated using zonal wavenumber-frequency filtering based on Wheeler and Kiladis (1999). Using regression composite analysis, Mekonnen and Thorncroft (2016) found a dipole pattern of synoptic-scale convective activity between the Congo Basin and Eastern Africa. They suggested that CCKWs modulate a coherent eastward/northeastward propagating convective signal that oscillates between enhanced and suppressed phases with a periodicity of 3–4 days. They also found that low-level westerly and southwesterly anomalous winds are linked to enhanced convection over East Africa, while northeasterly wind anomalies are linked to suppressed convection. In relation to drivers of the convective activity connection between Congo Basin and East Africa, Mekonnen and Thorncroft (2016) concluded that Kelvin waves play a significant role in the eastward propagation of convective activity.

Note that results in Mekonnen and Thorncroft (2016) are based on cloud brightness temperature during boreal summer. This suggests that there should also be a relationship between WEA and EEA based on observed *precipitation* for boreal spring and autumn. However, the intra-equatorial Africa precipitation relationship has not been comprehensively explored. In addition, the physical processes through which CCKWs modulate the eastward propagation of convection and precipitation across Equatorial Africa have not been studied in detail. Furthermore, the literature on the representation of both aspects in climate model output is still scarce. This study aims at advancing knowledge on these aspects. The findings from this study will benefit the wider forecasting community because, as mentioned above, the interactions between WEA and EEA are considered important in synoptic weather discussions over Equatorial Africa (Mekonnen and Thorncroft, 2016).

Consistent with Mekonnen and Thorncroft (2016), the variations in precipitation amounts on a synoptic timescale over tropical Africa is predominantly influenced by CCKWs (e.g., Kamsu-Tamo et al., 2014; Schlueter, 2020). Although Kamsu-Tamo et al. (2014) did not focus on the relationship between WEA and EEA, they investigated synoptic timescale and intraseasonal convection and precipitation variability across Equatorial Africa. They analysed the boreal spring TRMM satellite estimates, GPCP, Outgoing Longwave Radiation (OLR) from NOAA and daily ERA-Interim reanalysis atmospheric fields using regression and space-time spectral analysis of OLR. They found an eastward propagating signal in atmospheric fields consistent with CCKWs dynamics. They concluded that CCKWs and the MJO are the dominant modes of synoptic scale precipitation variability, particularly over the Guinean coast.

CCKW activity over Equatorial Africa has been detected in both observations (e.g., Nguyen and Duvel, 2008; Laing et al., 2011; Wheeler and Nguyen, 2015; Mekonnen and Thorncroft, 2016) and regional climate model simulations (e.g., Tulich et al., 2011; Jackson et al., 2019). These convection-organizing waves are most active during MAM (Roundy and Frank, 2004). They originate from various regions in the tropics such as the eastern Pacific (e.g., Mekonnen et al., 2008; Liebmann et al., 2009), and their speed of propagation depends on the extent to which they are coupled to convection (Mounier et al., 2007; Laing et al., 2011). Section 2.5 below

gives further discussion on CCKWs.

Pohl and Camberlin (2006b) used composite analysis on daily rain-gauge records over the period 1971-1995, GPCP rainfall data, daily OLR obtained from NOAA as a proxy for deep convection and various atmospheric fields from NCEP reanalysis and detected a Kelvin wave signal that causes upper tropospheric cooling during boreal spring, thereby enhancing the convective potential over EEA. Nguyen and Duvel (2008) performed a spectral analysis of daily OLR time series and examined daily precipitation dataset from the Climate Prediction Center (CPC) Merged Analysis of Precipitation (CMAP), ECMWF's ERA-40 reanalysis and satellite infrared brightness temperature from Cloud Archive User Service (CLAUS). They revealed Kelvin wave structure in the horizontal wind field that resemble theoretical Kelvin waves. Their results indicated that CCKWs modulate MCSs into larger and organised convective features. In addition, they also found that the eastward propagating convective signal associated with Kelvin waves tends to weaken while propagating over highlands on the western branch of the East African rift valley. The weakening of the Kelvin wave signal over the East African highlands was also highlighted in Mounier et al. (2007).

Laing et al. (2011) examined daily OLR from NOAA, cloud brightness temperature from the European geostationary meteorological satellite (meteosat-7) and atmospheric fields from NCEP Global Final Analysis (FNL) for both boreal spring and boreal autumn. They undertook zonal wavenumber-frequency filtering of OLR to isolate CCKWs. Their findings suggest that CCKWs provide a favourable environment for westward propagating convective features to become larger in association with the low-level wind shear that is related to southwesterly monsoonal winds and mid-troposheric easterly jets. Wheeler and Nguyen (2015) examined 22 years of Kelvin wave filtered cloud brightness temperature from CLAUS. They found that the passage of a CCKW over Equatorial Africa is preceded by low-level easterly wind anomalies, while the trailing end of the wave is dominated by anomalous low-level westerlies that are in phase with positive low-level geopotential height anomalies.

Results in studies described above highlight the importance of Kelvin waves to Equatorial Africa's synoptic-timescale precipitation variability. This means that understanding the physical processes through which CCKWs modulate precipitation over Equatorial Africa may be helpful in improving weather and climate models. However, this aspect has not been given sufficient attention.

Further scrutiny of the literature suggests that a greater number of the studies that have paid attention to the dynamics of CCKWs over Africa focused on tropical North Africa (e.g., Mounier et al., 2007; Mekonnen et al., 2008; Ventrice and Thorncroft, 2013; Yang et al., 2018; Schlueter et al., 2019) and only a handful (e.g., Nguyen and Duvel, 2008; Laing et al., 2011; Sinclaire et al., 2015; Mekonnen and Thorncroft, 2016) have looked at Equatorial Africa, defined here as approximately $\pm 15^{o}$ about the equator. Also, the representation of Kelvin wave activity and the associated eastward propagating convection and precipitation signal in climate models has not been sufficiently investigated.

2.2 Atmospheric circulation over Equatorial Africa

Atmospheric circulation is important in understanding synoptic-timescale precipitation variability. This is because it drives several processes such as low-level convergence and also transports moisture which is necessary for moist convection (e.g., Longandjo and Rouault, 2020). Synoptic-timescale precipitation variability can be influenced by large-scale circulation, local circulation systems or an interaction of both (Longandjo and Rouault, 2020). The large-scale circulation over Equatorial Africa is dominated by the interaction between the southeast and northeast trade winds, a feature that is identified as the ITCZ. The regional circulation patterns over WEA are generally complicated. Pokam et al. (2014) noted that the heating contrast between the eastern Atlantic Ocean and the landmass over WEA generates a Walker-like cell with the low-level westerlies as the lower branch. This westerly flow is important for transporting moisture into EEA (e.g., Basalirwa, 1995; Finney et al., 2020).

Hastenrath (2000) proposed that during boreal autumn, a zonal-vertical circulation cell develops along the Indian Ocean equator with its ascending branch over Indonesia, descending branch over East Africa and low-level winds blowing away from East Africa. This zonal-vertical circulation suggested in Hastenrath (2000) suppresses precipitation over the East African coastal areas. It is plausible that the existence of various circulation systems and their interactions account for the heterogeneity of precipitation across Equatorial Africa highlighted in Nicholson and Dezfuli (2013). Other regional circulation features include the Congo Air Boundary (CAB), a region of convergence for the moisture laden low-level westerlies/southwesterlies and easterlies from the Indian Ocean. This feature is present in central WEA during boreal summer (e.g., Mekonnen and Thorncroft, 2016; their Figure 2) and further south with an extension into EEA during boreal spring (e.g., Howard and Washington, 2019; their Figure 13). The low-level convergence within the CAB might be associated with precipitation over some areas in Equatorial Africa.

Another regional circulation feature that is worth noting in as far as precipitation climatology over Equatorial Africa is concerned is the Turkana Low-Level Jet (TLLJ) (Kinuthia and Asnani, 1982; Indeje et al., 2001; Nicholson, 2016; Munday et al., 2021). The TLLJ is a nocturnal low-level jet located between the Ethiopian Highlands and East African Highlands (e.g., see Nicholson, 2016; their Figure 1) and exists all year round, with wind speeds occasionally in excess of 50 m s^{-1}. Using ERA-Interim dataset, Nicholson (2016) found that the high wind speeds in the TLLJ are linked to drier conditions particularly during nocturnal hours (0000UTC, 0600UTC) and may partly explain the low mean annual precipitation over southern Somalia, southeastern Ethiopia and northeastern Kenya. In agreement with Nicholson (2016), results in Munday et al. (2021) showed that at interannual timescales, stronger TLLJ leads to suppressed precipitation over East Africa due to low-level divergence and moisture transport away from the region associated with the jet. Munday et al. (2021) further showed that the annual cycle of convective instability over a larger area in WEA is connected to the easterly moisture transport by the TLLJ. On daily timescales, Vizy and Cook (2019) found a significant negative cor-

relation between the daily TLLJ strength and precipitation over eastern South Sudan, and East African and Ethiopian Highlands. Clearly, the TLLJ is an important circulation feature for precipitation climatology over Equatorial Africa.

Over EEA, Lake Victoria generates its own mesoscale circulation system that modulates precipitation over the lake and the surrounding areas. It is also documented that Lake Victoria's surface temperatures influence circulation and precipitation over several areas in EEA (Sun et al., 2015). The MCSs found within the Lake Victoria Basin as found in Jackson et al. (2009) might be partly associated with the lake's mesoscale circulation. Over the coast of east Africa, mesoscale sea-breeze circulations interact with the large-scale circulation to produce convective activity and precipitation that is remarkably different from that in the interior of Equatorial Africa (Camberlin and Planchon, 1997).

2.3 Atmospheric equatorial waves over Equatorial Africa

Atmospheric equatorial waves (equatorial waves hereafter) are large-scale disturbances that drive precipitation variability through modulation of convection in the tropics. Convectively Coupled Equatorial Waves (CCEWs) have in past studies been defined as large coherent structures that are formed when dry equatorial waves couple with water vapour and convection (e.g., Stechmann et al., 2013). Equatorial Africa is part of the tropical belt that harbours a wide spectrum of equatorial waves. These include Equatorial Rossby Waves (ERWs), Kelvin waves (KWs) (e.g., Nguyen and Duvel, 2008; Mekonnen et al., 2008; Laing et al., 2011; Zebaze et al., 2017; Mekonnen and Thorncroft, 2016), and mixed Rossby-gravity Waves (Roundy and Frank, 2004). The basic structures of these modes of precipitation variability can be obtained as solutions to shallow-water equations on an equatorial β-plane linearised about a state of rest (Matsuno, 1966); however, this theory alone may not explain the structure of equatorial waves observed in the real atmosphere (Roundy and Frank, 2004).

Kelvin waves are eastward propagating modes of tropical convection and precipitation variability and they are associated with variance in tropical convection that is symmetric about the equator (e.g., Kiladis and Wheeler, 1995). Kelvin waves are also referred to as the $n = -1$ waves (see Chapter 3). These waves are briefly introduced here for purposes of completeness. A further discussion about them is given in Section 2.5.

ERWs, also referred to as the n=1 equatorial Rossby waves, are westward propagating tropical disturbances (e.g., Kiladis and Wheeler, 1995). ERWs have a symmetric circulation about the equator and propagate with a speed of about 5 m s^{-1}. They show a maximum zonal wind perturbation along the equator and the meridional wind maximum perturbation is located at about 10^{o}-15^{o} off the equator (e.g., Kiladis and Wheeler, 1995) (see Figure 2.2). On the global scale, in comparison to the MJO and Kelvin waves, ERWs explain a lower variance of tropical convection but strongly modulate convection in a few off-equatorial regions such as over the Philippines (e.g., Wheeler and Kiladis, 1999). During boreal spring and boreal autumn, ERWs account for

less than 3% of the total variance in convection over Equatorial Africa (Roundy and Frank, 2004).

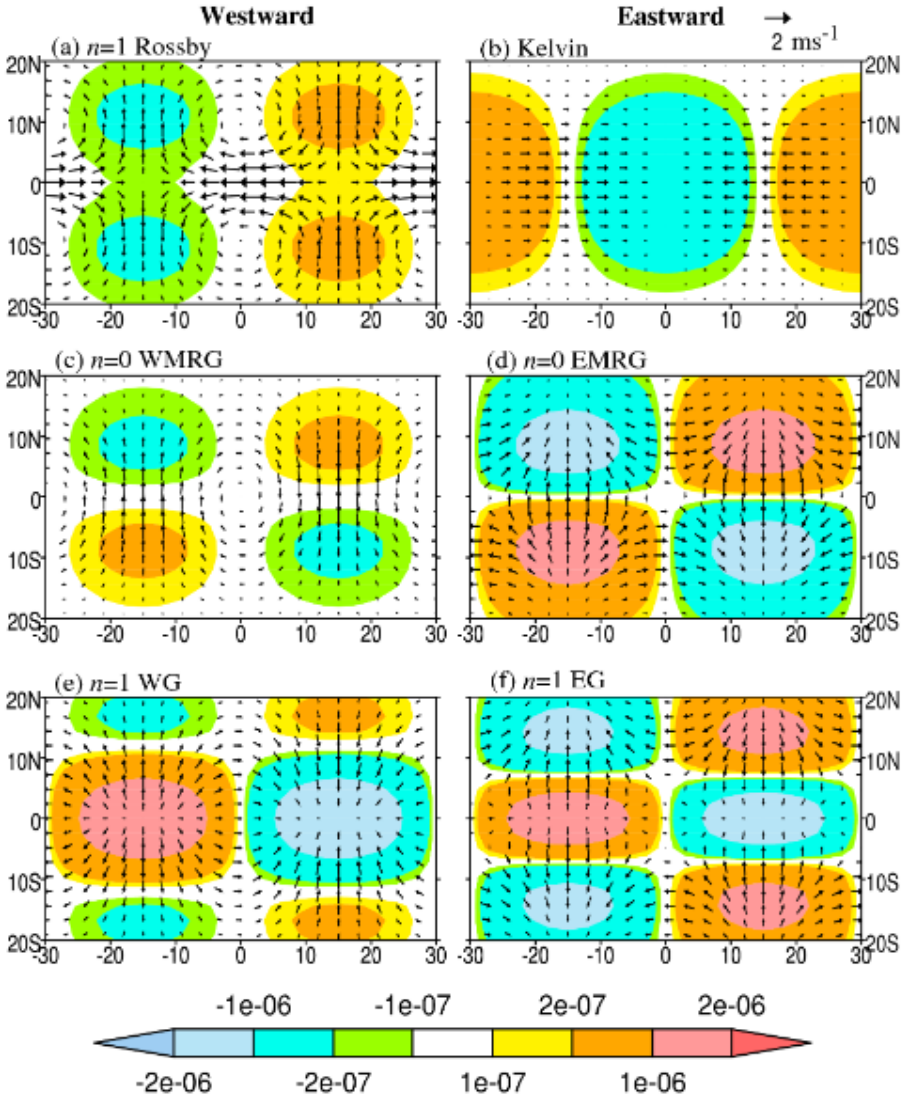

Figure 2.2: The theoretical horizontal structures of some of the equatorial waves. (a) the n=1 westward-propagating Rossby waves, (b) Kelvin wave, (c) n=0 west-ward propagating mixed Rossby-gravity (WMRG) wave, n=0 eastward-propagating mixed Rossby-gravity (EMRG), n=1 westward-propagating Gravity wave (WG) and eastward-propagating Gravity (EG). The vectors indicate horizontal wind and divergence is shown in colors. The maximum zonal wind in the Kelvin wave has been taken to be 1 m s^{-1}, and the maximum meridional wind in the n=0 MRG waves to be 1 m s^{-1} and in the n=1 waves 0.86 m s^{-1}. The trapping scale was considered to be 6° and the zonal wavenumber k=6. The unit for divergence is s^{-1}. Adapted and modified from Yang et al. (2007a)

Mixed Rossby-gravity (MRG) waves are planetary-to-synoptic-scale westward (WMRG) and eastward (EMRG) propagating equatorial waves. These waves have a periodicity of 4-5 days and influence off-equatorial convection. MRG waves propagate with a speed of between 15-20 m s^{-1}, have a zonal wavelength of between 7000-9000 km and are associated with antisymmetric fluctuations in tropical convection (Hendon and Liebmann, 1991) (see Figure 2.2). Convectively coupled MRG waves exhibit the strongest activity over central and eastern Pacific during boreal summer (e.g., Wheeler and Kiladis, 1999). Over Equatorial Africa, MRG waves explain less than 3% of the total variance in convection (Roundy and Frank, 2004).

Other high frequency equatorial waves include the n=0 Eastward Inertio-gravity waves. Whether ERWs, MRG (WMRG and EMRG) waves or Eastward Inertio-gravity waves play a role in modulating precipitation

over Equatorial Africa is a topic for future research.

2.4 The eastward propagating convective signal over Equatorial Africa

Studies over Equatorial Africa have found an eastward propagating convective signal in OLR (e.g., Mpeta and Jury, 2001; Mekonnen et al., 2008; Chan et al., 2008; Kamsu-Tamo et al., 2014; Mekonnen and Thorncroft, 2016). This is perhaps not completely surprising because earlier studies such as Nakazawa (1988) identified eastward moving super cloud clusters composed of individual westward moving mesoscale convective systems over the western Pacific Ocean. Figure 2.3, adapted from (Mekonnen et al., 2008), shows a convective signal that propagates eastward together with a Kelvin wave filtered cloud brightness temperature between 7-11 August 1987. This figure motivates questions like: is such an eastward propagating feature present in observed, or simulated, precipitation?

Another important eastward propagating tropical disturbance that has a lower frequency and larger spatial scale than Kelvin waves is the MJO (e.g., Wheeler and Kiladis, 1999). In fact, some early studies such as Wang (1988) likened the MJO to CCKWs described in Chapter 1. Other studies such as Roundy (2008) and Guo et al. (2014) suggest that the MJO amplifies Kelvin wave activity. This may imply that the MJO indirectly modulates synoptic-timescale precipitation variability. Consistent with Roundy (2008), Guo et al. (2014) showed that the Kelvin wave amplitude over Atlantic Ocean is enhanced when the MJO is in phases 1, 2 and 8 and suppressed when the MJO is in phases 4, 5 and 6. The similarities (e.g., direction of propagation) and the aforementioned evidence suggesting the connection between the Kelvin waves and the MJO is the reason the MJO is discussed in this thesis.

The literature discussed in Chapter 1 demonstrated that the MJO is an eastward propagating tropical disturbance that enhances and suppresses convection along its trajectory. Pohl and Camberlin (2006b), Berhane and Zaitchik (2014), Berhane et al. (2015), Hogan et al. (2015) and Kilavi et al. (2018) are some of the examples of the publications that found an MJO-related eastward propagating convective signal over Equatorial Africa. For instance, Berhane et al. (2015) showed the MJO directly enhances precipitation as it propagates across Equatorial Africa. During boreal spring, convectively active MJO phase is associated with daily precipitation enhancement of up to between 20-50% from the mean daily rates. Berhane et al. (2015) found that the MJO impacts on convective activity and precipitation over Equatorial Africa through modulation of the low-level anomalous westerly flow that transports moisture from Atlantic Ocean into convective regions over the continent.

Both Berhane and Zaitchik (2014) and Pohl and Camberlin 2006b showed that the MJO influences precipitation over East Africa at both daily and pentad timescales in boreal spring by modulating wet and dry spells. However, the impact of MJO on precipitation over East Africa varies from season to season and sub-region to sub-region depending on the location of the centre of its active convection phase. For instance, Berhane

and Zaitchik (2014) found that when the MJO enhanced convective activity is located over the Indian Ocean (70-80°E), East Africa experiences enhanced precipitation. They also reported that the location of the MJO's active convection at about 120°E is associated with suppressed precipitation over the East Africa's coast, and when located at about 10°W, it is linked to enhanced precipitation at the coast of East Africa. The MJO influences precipitation over East Africa via various processes including but not limited to modulation of moisture transport into the region by the low-level Somali jet, Walker circulation cell (e.g., Berhane and Zaitchik, 2014) and anomalous low-level westerly flow (e.g., Pohl and Camberlin 2006b; Berhane et al., 2015).

It was earlier noted that seasonal precipitation over Equatorial Africa is enhanced in association with El Niño and positive IOD phase. Zaitchik et al. (2015) suggested that the El Niño and positive IOD phase enhance precipitation over East Africa through modification of the MJO, and in turn, the MJO can amplify or suppress Kelvin wave activity depending on its phase. Chapter 4 will only briefly assess whether or not the MJO plays an indirect role in the synoptic-timescale convection and precipitation variability over Equatorial Africa.

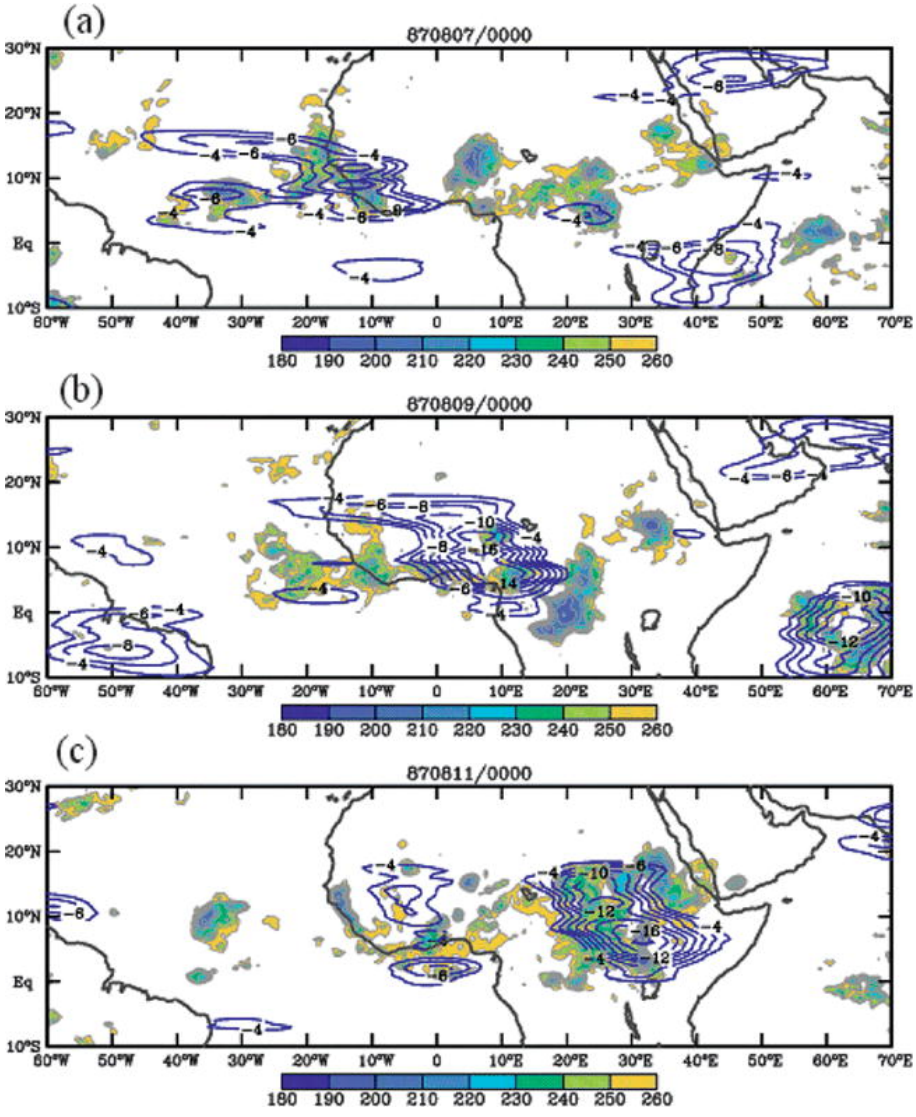

Figure 2.3: Synoptic maps of Kelvin-filtered cloud brightness temperature (contoured every 2 K; only the enhanced phase is shown for clarity) and unfiltered TB (shaded; $<$ 260 K) every 2 days between 7 and 11 Aug 1987. Reproduced from Mekonnen et al. (2008)

2.5 Kelvin Wave activity over Equatorial Africa

Knowledge of Kelvin wave activity is important because CCKWs increase the size, intensity and life cycle of MCSs over Equatorial Africa (Nguyen and Duvel, 2008; Laing et al., 2011). They also play a role in synoptic-scale convective variability between Congo Basin and East Africa (Mekonnen and Thorncroft, 2016). Over the Atlantic Ocean, Kelvin waves influence the intensity and location of convection (Wang and Fu, 2007). And globally, they account for the same amount of convective variance as the MJO (Wheeler and Kiladis, 1999). The influence of Kelvin waves on synoptic-timescale precipitation over West Africa is comparable to the influence of African Easterly Waves (AEWs) on precipitation over West Africa (Mounier et al., 2007). Thus, understanding the role of Kelvin waves in modulating precipitation over Equatorial Africa adds value to the operational synoptic-scale forecasting and the wider scientific community.

Theoretically, Kelvin waves are equatorially trapped eastward propagating tropical disturbances that cause fluctuations in the zonal wind and geopotential height (e.g., Yang et al., 2003). Meridionally, the influence of Kelvin waves is confined within approximately $\pm 10^{o}$ about the Equator (e.g., Kiladis et al., 2009). Kelvin waves circumnavigate the entire global tropical belt, but their impact on convection and precipitation varies in both space and time. For example, over Equatorial Africa Kelvin wave activity is common in March-May (e.g., Roundy and Frank, 2004; Zebaze et al., 2017). Kelvin wave activity is strongest over the Indian Ocean, central and eastern Pacific ocean and over Africa (e.g., Mekonnen et al., 2008). Africa being one of the regions where the Kelvin wave activity is strongest is a good reason for this study to explore the Kelvin wave-precipitation connection across Equatorial Africa.

Kelvin waves influence convection and precipitation by significantly perturbing the basic state of atmospheric fields such as pressure, temperature and wind. The resulting latent heat released by the deep convection associated with the perturbed fields can cause the generation of new equatorial waves (Lindzen, 2003). As a wave propagates, it interacts with convection through, for example, enhancing low-level moisture flux (e.g., Mekonnen et al., 2008; Sinclaire et al., 2015) thereby enhancing precipitation downstream, and this causes the waves to propagate at a slower speed in comparison to the dry Kelvin waves for a given equivalent depth.

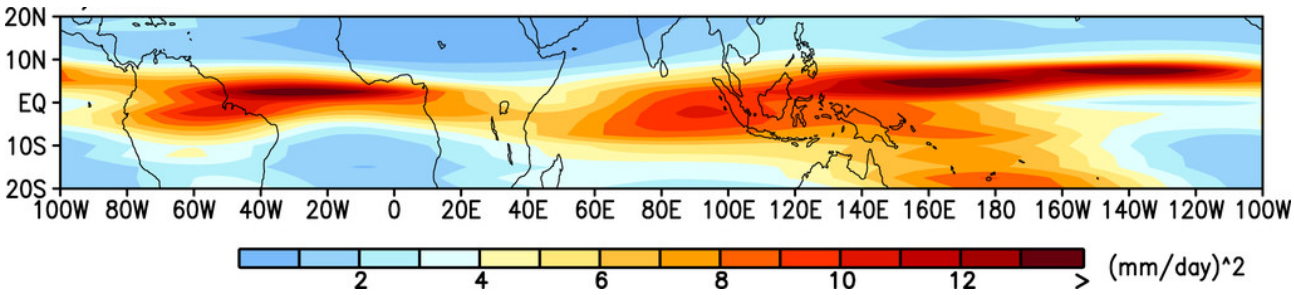

Figure 2.4: The distribution of December-April mean variance of Kelvin wave-filtered TRMM precipitation (mm^2 day^{-2}) for the period 1998-2012. Taken from Guo et al. (2014)

CCKWs are generally slower than the dry Kelvin waves that propagate at a speed of between 30 m s^{-1} - 60 m s^{-1}. CCKWs have been found to propagate through Equatorial Africa at a speed of between 15 m s^{-1} - 22

m s^{-1} with the horizontal scale of approximately 3000-6600 km (Mekonnen et al., 2008; Laing et al., 2011). As discussed above, Figure 2.4 shows that Kelvin waves have been observed over the Indian Ocean (e.g., Roundy and Frank, 2004), Pacific Ocean (e.g., Straub and Kiladis, 2003b) and over Africa (e.g., Mekonnen et al., 2008). For example, the 1997 Tropical Eastern Pacific Processes Study (TEPPS) showed aspects of the horizontal and vertical structures of Kelvin Waves (e.g., Straub and Kiladis, 2003b). In the conceptual structure of Kelvin wave at low-levels, convection dominates the areas between low-level convergence and the high-pressure anomaly to its west as shown in Figure 2.5. The observed vertical structure of CCKWs has been found to have a westward tilt with height in the zonal wind and specific humidity (e.g., Straub and Kiladis, 2003b; Kiladis et al., 2009) as shown in a schematic in Figure 2.6. Since Kelvin waves modulate precipitation over the global tropics, it is important that they are satisfactorily simulated in both global and regional climate models.

Huang et al. (2013) investigated the representation of equatorial waves in Coupled Model Intercomparision Project phase 3 (CMIP3) models and found that only 20% of the models evaluated were able to simulate a realistic seasonal cycle of Kelvin wave activity. Results in Straub et al. (2010) showed that 75% of the 20 CMIP3 model simulations failed to reasonably represent CCKWs and that most models exhibited deficiencies in capturing the lower tropospheric humidity signal. Yang et al. (2009) evaluated the representation of equatorial waves in the Hadley Centre Atmospheric Model, version 3 (HadAM3) and the New Hadley Centre Atmospheric Model, version 1 (HadGAM1) against ERA-15 and satellite data and concluded that both models had inadequacies in capturing the coupling between these waves, particularly CCKWs, and convection. The findings from investigations related to the representation of equatorial waves in CMIP3 models (e.g., Straub et al., 2010; Huang et al., 2013) and phase 5 (CMIP5) simulations (e.g., Wang and Li, 2017) suggest that in general, global models struggle to produce horizontal and vertical structure that resembles observed CCKWs.

Weber et al. (2021) examined two global simulations run under Model for Prediction Across Scales (MPAS), developed at the National Center for Atmospheric Research (NCAR). One of the simulations has a 3 km grid spacing with convection explicitly represented while the other has a 15 km grid spacing and employs a parameterized convection scheme. The two simulations were examined to assess their fidelity in capturing the CCKW event that was observed over the Indian Ocean during the November 2011 Dynamics of the Madden–Julian Oscillation (DYNAMO) field campaign. Their results showed that the 3 km simulation capture both the structure of the CCKW and realistic amounts of precipitation when compared to the observed while the 15 km model simulated the structure of the CCKW reasonably well but underestimated the precipitation associated with the wave. They reported that the weak precipitation signal in the 15 km simulation is linked to the model's unrealistic linear relationship between the moisture and the precipitation. Lin et al. (2006) examined 8 years of daily precipitation data from 14 GCMs that are part of the Intergovernmental Panel on Climate Change (IPCC) Fourth Assessment Report (AR4). They found that about 50% of the models had a signal of Kelvin waves but the variance of the waves was too weak and the phase speeds were too fast compared to the observed. Frierson et al. (2011) investigated the sensitivity of CCKWs to a convection parameterisation scheme under various convection triggers. They found that regardless of the convection scheme, strong convective triggers caused

slower and intense Kelvin wave activity. These results suggest that the both resolution and model physics are important for realistic simulation CCKWs. This literature suggests that the coarse resolution and parameterised convection in Atmospheric General Circulation Models (AGCMs) limits their ability to capture the interaction between equatorial waves and precipitation. Comparison of model output from coarse-resolution models that have parameterised convection with observations and convection permitting model output could potentially lead to improvements in the coarse-resolution models.

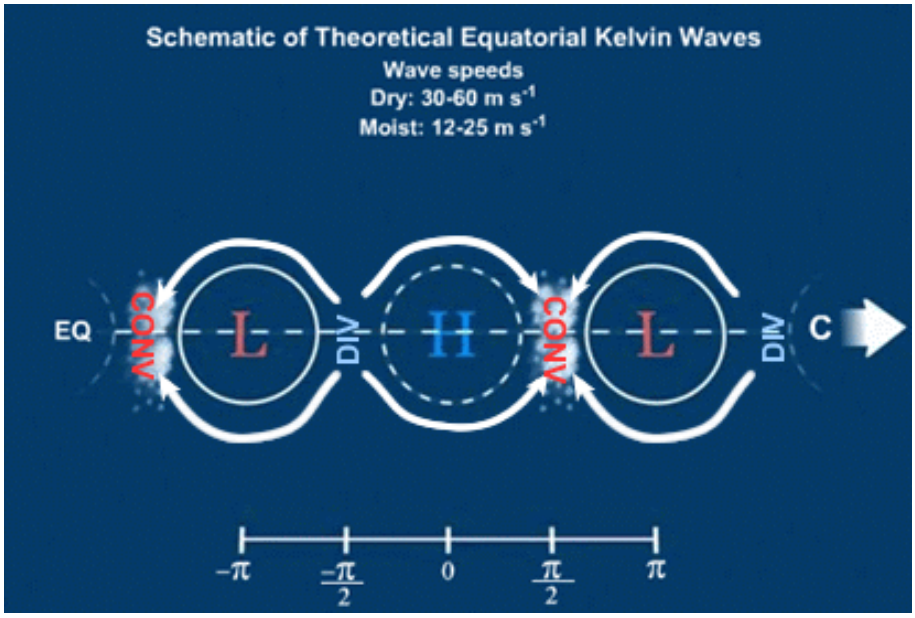

Figure 2.5: Conceptual horizontal structure of a low-level theoretical Kelvin wave. H is high pressure, L is low pressure, Div is mass divergence, Cov is mass convergence, π is half the wavelength and c with an arrow shows direction of propagation. Reproduced from The COMET Program.

Regional climate model runs have been used to improve our understanding of wave-convection coupling (e.g., Tulich and Mapes, 2008; Tulich et al., 2011). For instance, Tulich et al. (2011) evaluated the performance of a regional climate model in simulating Kelvin waves and easterly waves. Although their simulation captured the propagation speed and the 3-dimensional structure of the Kelvin waves similar to the observed, the Kelvin waves were generally underactive. They reported that the biases in the activity of Kelvin waves were partly explained by too strong coupling between the Kelvin waves and anomalous rotational circulation. In Tulich and Mapes (2008), a two-dimensional cloud resolving model forced by uniform cooling simulated multiscale convective wave disturbances with structures similar to the observed tropical waves. These waves triggered new convective features through perturbation of the low-level fields. Despite being computationally expensive, results in Tulich and Mapes (2008) suggest that convection permitting models can help us to understand wave-convection coupling. In this thesis, a regional convection permitting simulation and its driving global simulation (in which convection is parameterised) are analysed. While Jackson et al. (2019) investigated the response of precipitation to CCKWs in both CP4A and the global simulation analysed here, they used continent-wide observed and modelled OLR as a proxy for convection, and focused on April only.

As described above, much of the knowledge on Kelvin wave activity over Equatorial Africa is based on

filtering of OLR and cloud brightness temperature in a zonal wavenumber-frequency Kelvin wave band. However, cloud brightness temperature does not always guarantee precipitation on the earth's surface (e.g., Arkin, 1979). And ground-based precipitation measurements tend to be weakly related to cloud brightness temperatures (e.g., So and Shin, 2018). Also, deep convection tends to lead OLR because of its sensitivity to cirrus clouds left behind by convective activity (e.g., Roundy and Frank, 2004). Furthermore, using OLR to identify Kelvin waves has two other potential limitations. Firstly, filtering OLR in the zonal wavenumber-frequency domain to partition "wave modes" can be susceptible to errors associated with changes in the frequency of the wave due to Doppler shifting by the background flow or effects of shear. Secondly, over regions that are not convectively active, there can be failure to identify equatorial waves because of absence of the OLR signal from which the waves are identified. Also, Kelvin waves identified in OLR cannot easily be used to independently explore the true strength of the relationship between the Kelvin waves and the precipitation. Due to these issues, this thesis uses zonal wind and geopotential height (e.g., Yang et al., 2003) to quantify Kelvin wave activity in both reanalyses and model simulations. The full description of this method is given in Chapter 3. Unlike several studies described here, work in this thesis uses precipitation both as an important measurement in its own right and as a measure of convection.

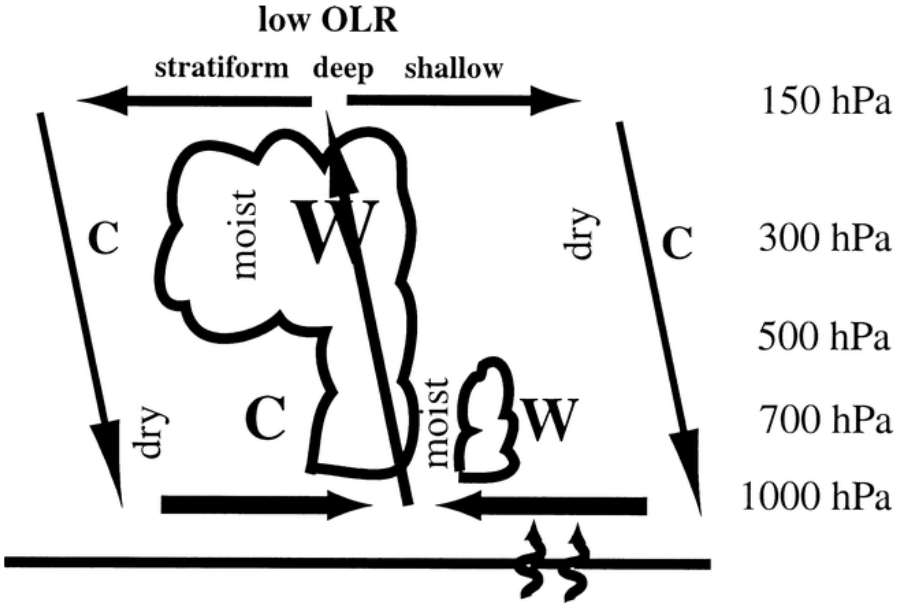

Figure 2.6: Schematic diagram of a CCKW structure. The letters W and C represent warm and cold respectively. The magnitudes of the anomalies are represented by the width and size of the arrows and the text. Surface fluxes are shown by the upward arrows crossing the lower boundary. Reproduced from Straub and Kiladis (2003b).

2.6 CCKWs and extreme precipitation

Investigating the drivers and spatio-temporal variations of intense and flood-causing precipitation episodes over Equatorial Africa is important for agriculture and action-based flood forecasting. Extreme precipitation episodes usually associated with deep convection are poorly captured in both global and regional weather prediction models partly because of insufficient in situ observations for data assimilation (e.g., Woodhams

et al., 2018) and incomplete understanding of what drives these extreme precipitation episodes.

The intensity of these extreme precipitation episodes over East Africa, for example, are expected to increase under global warming (e.g., Shongwe et al., 2011), although some observational studies found a significant decrease in heavy precipitation days over East Africa (e.g., Omondi et al., 2014) and western central Africa (e.g., Aguilar et al., 2009). Thorough understanding of the processes and mechanisms that influence extreme precipitation episodes in the current climate is one way of boosting confidence in the projected changes in extreme precipitation events. Since extreme precipitation episodes are of a major concern, previous studies have investigated their spatial and temporal distribution over Africa as a whole (e.g., Crétat et al., 2014; Harrison et al., 2019) or part of it (e.g., Camberlin et al., 2020). For example, Camberlin et al. (2020) examined daily TRMM estimates over West Africa (4-8^{o}N, 7^{o}W-3^{o}E) for the period 1998-2014 and found that, in the interior of their domain of study, extreme precipitation episodes are influenced by both mid-tropospheric Easterly waves and CCKWs.

Crétat et al. (2014) examined modelled precipitation from a RCM with a convection scheme as well as Atmosphere-only Global Circulation Models (AGCMs) and coupled Atmosphere-Ocean general circulation models (AOGCMs) of the Climate Model Intercomparison Phase 5 (CMIP5). They found that RCMs captured the spatial and temporal patterns of extreme precipitation episodes. Their general conclusion was that RCMs performed better at capturing extreme precipitation episodes over Africa.

Ferrett et al. (2020) investigated the connection between extreme precipitation and equatorial waves over Southeast Asia and found a robust connection between equatorial waves and heavy precipitation. For example, they reported the likelihood of occurrence of a heavy precipitation episode increases up to threefold when a Kelvin wave propagates over this region. Subudhi and Landu (2019) probed the role of Equatorial waves in modulating extreme precipitation over India and showed that the presence of equatorial waves increased the probability of occurrence of an extreme rainfall event by up to 150%. Although these studies were not conducted over Africa, they provide a clue of the role of CCKWs in influencing extreme precipitation. The impact of CCKWs on extreme precipitation episodes over Equatorial Africa has not been adequately explored. Chapter 6 of this thesis devotes special attention to the linkage between high-amplitude Kelvin waves and extreme precipitation. Although linking an individual extreme rainfall episode to a single Kelvin wave event is not straightforward, one can quantify the probability of a Kelvin wave influencing an extreme precipitation episode (e.g., Ferrett et al., 2020; Baranowski et al., 2020). CCKWs over Equatorial Africa can provide a source of predictability of extreme precipitation episodes (e.g., Respati and Lubis, 2021), and so it is important to develop an understanding of how CCKWs influence the occurrence of extreme precipitation episodes over Equatorial Africa.

2.7 The objectives of the thesis

As discussed above, there is a considerable amount of research that has explored the climatology and interannual variability of precipitation in both WEA and EEA. However, synoptic-timescale convection and precipitation variability across Equatorial Africa remains relatively under-explored, and the drivers of convection and precipitation variability at this timescale are still inadequately understood. Up to now it has been unclear whether the synoptic-scale convective activity connection between Congo Basin and East Africa found in cloud brightness temperature (e.g., Mekonnen and Thorncroft, 2016) is present in observed and simulated precipitation. In addition, how well the drivers of the aforementioned synoptic-scale connection are represented in climate models is not fully explored.

While OLR has been used as a proxy to convection in a multitude of studies, as indicated in Section 2.5, OLR exhibits weaknesses in providing an estimate for ground-based precipitation measurement. It would thus be appropriate to investigate synoptic-timescale convection and precipitation variability using precipitation records as a proxy to convection. Since models are currently being used for climate projections (e.g., Kendon et al., 2019), it is important that results based on observations are compared with model-based results to improve the representation of various processes in climate models. Hence the objectives of this thesis are:

1) To assess the precipitation linkage between WEA and EEA based on small sub-regions characterized by similar daily precipitation characteristics.

2) To identify the possible mechanisms driving variability associated with the precipitation connection between WEA and EEA.

3) To assess how well a state-of-the-art convection permitting model reproduces observational results in (1) and (2), and to use this model output as a "virtual laboratory" to further explore the physical mechanisms.

4) To evaluate the role of high-amplitude Kelvin waves in influencing extreme precipitation episodes over Equatorial Africa.

To address the above thesis objectives, Chapter 3 describes that datasets examined and the methods used. The precipitation datasets and reanalysis are described in Sections 3.2.1, 3.2.2, 3.2.3 and the methodology used to generate the equatorial wave dataset is explained in Section 3.3.1. The procedure for generating a simulated equatorial wave dataset is described in Section 3.3.2. Since Equatorial Africa is a large area characterised by different precipitation pattern with respect to daily timescale, the Empirical Orthogonal Teleconnection (EOT) technique that is described in Section 3.3.3 is used to objectively identify small sub-regions characterised by similar daily precipitation characteristics. Past studies discussed above demonstrate that Kelvin wave activity over Equatorial Africa has mostly been isolated by filtering cloud brightness temperature or OLR in a wavenumber-frequency Kelvin wave domain. This thesis uses zonal wind and geopotential height to identify Kelvin waves as explained in Chapter 3 (§3.3.1).

To address the first two thesis objectives, Chapter 4 examines daily TRMM estimates (§3.2.1) and ERA-Interim (§3.2.3) atmospheric fields with an aim of investigating whether the eastward propagation of convective activity is present in observed precipitation. To achieve this aim, Equatorial Africa is first sub-divided into small sub-regions of similar daily precipitation variability (§4.3). Sections 4.4 and 4.5 explore the connection between WEA and EEA. Further, two indices are developed as described in sections 4.6 and 4.2.2 and used in composite analysis in Section 4.2.2 to reveal the association between CCKWs and the eastward propagating precipitation signal. Section 4.8 discusses the results of this chapter. As mentioned in Section 1.2, this chapter is based on a published paper.

The third thesis objective is addressed in Chapter 5. In this chapter, the first multi-year state-of-the-art Africa-wide convection permitting climate simulation (CP4A) and a coarse global simulation are examined to investigate whether the eastward propagating signal seen in observations (Chapter 4) is present in the model simulations (§5.3 and 5.5). Also, this chapter evaluates both the CP4A and the global simulation against observations (TRMM) and reanalysis (ERA-I). Simulated equatorial wave datasets are produced as described in Section 3.3.2 and a Kelvin wave index constructed for use in composite analysis. Section 5.4 looks at the seasonal cycle of Kelvin activity over Equatorial Africa, and the processes through which CCKWs influence the west-to-east propagation of precipitation are discussed in Sections 5.7.1,5.7.2, and 5.7.3. The energy conversions in the models are also explored (5.7.4). Section 5.8 discusses the results of this chapter. As noted in Section 1.2, this chapter is based on a paper under review.

To explore the role of high-amplitude Kelvin waves on extreme precipitation over Equatorial Africa and address the fourth thesis objective, Section 6.3 of Chapter 6 discusses the statistical linkage between high-amplitude Kelvin waves and extreme precipitation. Further, Section 6.4 discusses specific case studies based on TRMM and ERA-I. To further learn about the influence of high-amplitude Kelvin waves on extreme precipitation, case studies based on simulated precipitation and Kelvin waves are discussed in Section 6.5. Finally, Section 6.6 gives the discussion of results in this chapter. This chapter is based on a paper in preparation.

Finally, in Chapter 7, the purpose of the chapter is stated in Section 7.1, and the key findings presented in Section 7.2. In Section 7.3, the known limitations to this work, and possible lines of future research are presented. Finally, the implications of this work and the scientific advances made by this thesis are presented in Section 7.4.

Chapter 3

Data and Methods

3.1 Purpose of this Chapter

This chapter is intended to describe the datasets (such as observations, reanalysis, and a simulation from a state-of-the-art convection permitting model together with its global driving model) and methods (e.g., the Empirical Orthogonal Teleconnection) used here.The description of the observations and reanalysis is presented in Sections 3.2.1, 3.2.2, and 3.2.3 respectively. The simulations examined are described in Section 3.2.4. In Section 3.3.2, the procedure used to generate the simulated equatorial wave dataset is described. Finally, Section 3.3 describes the methods used in this thesis.

3.2 Datasets

3.2.1 Tropical Rainfall Measuring Mission (TRMM)

Satellite precipitation estimates provide an alternative source of data for regions where observations are scarce and unreliable, for example, over Equatorial Africa. Examining this dataset contributes toward addressing all four thesis objectives stated in Chapter 2 (§2.7).

The Tropical Rainfall Measuring Mission (TRMM) daily precipitation dataset is a global data set with latitudinal coverage spanning 50^{o}S–50^{o}N and is produced at a resolution of $0.25^{o} \times 0.25^{o}$, as described in Huffman et al. (2007). The 3B42 version 7 of the daily TRMM estimates is computed by accumulating eight 3-hourly TRMM 3B42 records obtained by merging precipitation estimates from multiple satellites (Huffman et al., 2007), and for regions where the Global Precipitation Climatology Centre (GPCC) global precipitation analysis dataset (Schneider et al., 2008) is available, GPCC is used for bias correction of the final TRMM product. Gebremicael et al. (2019) found a percentage bias and correlation coefficient between the TRMM

precipitation product and rain gauge data of within ±25% and greater than 0.5, respectively, for various time scales. Dinku et al. (2007) found that TRMM 3B42 performed well compared to other satellite precipitation products over EEA. This dataset is available for a period 1998-2015. In Chapter 4, we use the above described version for the period 1998–2013 while Chapters 5 and 6 use the same version but for a 9 year period (1998-2006).

3.2.2 Global precipitation climatology project (GPCP-1DD)

The Global Precipitation Climatology Project (GPCP-1DD) is a $1^o \times 1^o$ global daily precipitation product produced by merging various satellite estimates and rain gauge observations (e.g., Huffman et al., 2001). The microwave estimates are generated from the Special Sensor Microwave Imager (SSM/I) on board the Defence Meteorological Satellite Program, and the Infrared (IR) data uses the Geostationary Operational Environmental (GOES) Precipitation Index (GPI) which relates cloud top temperature to precipitation rate (Huffman et al., 2001). Precipitation estimates are then computed using the Threshold-Matched Precipitation Index (TMPI) that is applied on the SSM/I data to isolate raining pixels in the IR data (Huffman et al., 2001). Rain gauge observations are indirectly used when the GPCP-1DD accumulations are scaled to match the GPCP monthly product. This dataset is available for a period 1996-present. This thesis uses the 1DD daily estimates for the period 1997–2012 to assess the robustness in the location of sub-regions identified in Chapter 4.

3.2.3 Reanalysis (ERA-Interim; ERA-I)

A reanalysis dataset is produced using a global forecast model, input observations, and a data assimilation scheme Fujiwara et al. (2017). ERA-Interim (ERA-I) is a reanalysis dataset from the European Centre for Medium-Range Weather Forecasts (ECMWF). ERA-I is a global reanalysis produced with ECMWF's Integrated Forecast System (IFS) (e.g., Dee et al., 2011) and spans 1 January 1979 - 31 August 2019. This dataset was output at a spatial resolution of $\sim 0.7^o$x 0.7^o, 6-hourly temporal resolution and 37 vertical levels. While ERA-I will contain biases and uncertainties related to its model components (particularly the convection parametrisation) as well observational uncertainty. We however, rely on it as an estimate of observational "truth" with respect to equatorial waves and their environment, because these large-scale fields should be relatively well constrained. Since large-scale winds are influenced by observed wind fields (e.g., during data assimilation), it is expected that they will be better resolved than erratic fields such as precipitation (e.g., James et al., 2018). ERA-I is one of the reanalysis datasets that have been widely used to diagnose large circulation features over Equatorial Africa (e.g., see Mekonnen and Thorncroft, 2016; Zebaze et al., 2017; Nicholson 2018; Jackson et al., 2019). It is therefore expected that the dynamical and thermodynamical fields from ERA-I would be appropriate for this thesis. Although ERA-I is available for a period 1 January 1979-31 August 2019, Chapter 4 uses the daily averaged fields for the period 1998–2013 while Chapters 5 and 6 uses a 9 year period (1998-2006). This thesis uses ERA-I rather than a recently released ERA5 because at the time this research

commenced, ERA5 was not yet available. However, when ERA5 was released, it was used alongside ERA-I in Chapter 6 but results based on ERA5 where similar to those in ERA-I, and therefore not shown.

3.2.4 Model simulations

To address the second, third, and fourth thesis objectives, this thesis examines two climate model simulations: 1) A multi-year state-of-the-art Africa-wide convection permitting climate simulation (CP4A), and 2) the N512L85-resolution global model climate simulation. Both simulations are based on the UK Met Office Unified model (UM) thus, the two simulations are consistent with each other. The UM is a model that can be used for a wide range of applications, from being a numerical weather prediction model to being a fully coupled atmosphere-Ocean global climate model, and runs in both regional and global setup. It solves the compressible non-hydrostatic equations of motion with semi-lagrangian advection and semi-implicit time stepping (Davies et al., 2005). This model uses a convection scheme based on Gregory and Rowntree (1990) with a number of extensions to include down-drafts and convective momentum transport.

3.2.4.1 The Global Model

The global model simulation examined in this thesis is from the latest prototype version of the Global Atmosphere/Land (GA 7.0/GL7.0) configuration of the UM (e.g.,Walters et al.,2019). This model is based on the Even Newer Dynamics for General Atmospheric Modelling of the Environment (ENDGame) (Wood et al., 2014). The ENDGame dynamical core employs a semi-implicit semi-Lagrangian formulation to solve the non-hydrostatic, fully compressible deep atmosphere equations of motion as described in Wood et al. (2014). For consistency with Jackson et al. (2019), we refer to this simulation as “G25”. The major atmospheric prognostics from this model are the 3-D wind field, virtual dry potential temperature, Exner pressure, and dry density. The Arakawa C-grid staggering (Arakawa, 1977) is implemented in G25 to horizontally discretise these fields onto a regular longitude/latitude grid. The vertical discretisation applies the Charney-Phillips staggering (Charney and Phillips, 1953) using terrain-following hybrid height coordinates.

G25 is a simulation from a free-running standard parameterised convection Global Circulation Model (GCM), the latest configuration of the UM. This model uses a deep convection scheme that differs from the original Gregory and Rowntree (1990) in using a Convective Available Potential Energy (CAPE) closure based on Fritsch and Chappell (1980) and a shallow convection scheme based on Grant (2001). The shallow convection scheme has larger entrainment rates than the deep convection scheme consistent with the shallow convection in a cloud-resolving model (Walters et al., 2019). The role of the convection scheme is to handle sub-grid scale convection and precipitation events and hand them to model dynamics while the microphysics scheme handles the formation and evolution of convection and precipitation associated with grid scale processes. This is achieved through taking the average values within the grid box and working out the vertical mass transport. The input fields for the microphysics scheme are temperature, moisture, cloud and precipitation for the end of

the previous time step. G25 implements the microphysics scheme based on Wilson and Ballard (1999) with extensive modifications. The reader is referred to Walters et al. (2019) for details on the extensive modification on the microphysics scheme.

To provide the model with realistic vertical structure in the thermodynamic and wind profiles, G25 implements an atmospheric boundary layer scheme based on Lock et al. (2000) but with modifications described in Lock (2001) and Brown et al. (2008). The shortwave and the longwave radiation are handled by the radiative transfer scheme based on Edwards and Slingo (1996). Radiation scheme provides prognostic atmospheric temperature increments, and prognostic surface fluxes. Strong soil moisture gradients increase the likelihood of initiation of convection (e.g., Taylor et al., 2011). To account for convection that is forced by surface properties, soil processes in G25 are parameterised using a four-layer scheme for the heat and water fluxes with hydraulic relationships as described in Van Genuchten (1980) and the heterogeneity of soil moisture within a grid box is handled by a large-scale hydrology approach based on topography-based rainfall–runoff model (TOPMODEL) discussed in Kirkby and Beven (1979). Several other parameterisation schemes are implemented in G25 as shown in Table 3.1.

The model is forced with Sea Surface Temperatures (SSTs) obtained from the Reynolds dataset of the daily high-resolution blended analyses for SST, and the Global sea-Ice and Sea Surface Temperature (GISST) climatology was used for the Lake Victoria SSTs (Stratton et al., 2018). G25 was run using a 10 minute timestep with 85 vertical levels (50 levels below 18 km and 35 levels above this) up to 85 km. The model has approximately 26 km and 39 km grid spacing in latitudinal and longitudinal direction respectively. This simulation is available for a period 1988-2010, however, this thesis uses the fields for 1998-2006 in Chapters 5 and 6. The 9 year period of this simulation is used in this thesis because it matches that of the convection permitting simulation described below.

3.2.4.2 The Convection Permitting Simulation: CP4A

CP4A is a free-running decade long (1997-2006) simulation from a convection permitting UM run over an Africa-wide domain (Stratton et al., 2018). The model is a regional model configuration from the UK Met Office Unified model (UM). It is based on the UKV regional model, that is, the variable horizontal resolution model with a 1.5km uniform horizontal grid spacing over the UK. CP4A is an Africa-wide simulation that spans 45.525^{o}S-39.505^{o}N, 24.5^{o}W-56.48^{o}E. This simulation has a spatial resolution of approximately 4.5 km at the equator, 80 vertical levels up to 38.5 km. The higher vertical resolution (with the lowest 5 km having 32 levels, and 56 levels below 16 km) in CP4A helps the model to explicitly represent convection and the horizontal grid space gives it the capability to resolve inland water bodies and topographic features.

Most importantly, the CP4A was run without a convection scheme and therefore, convective updrafts and downdrafts in the model are formed based on the model dynamics. Because of the 4.5 km grid spacing, CP4A is expected to partially explicitly represent deep , but shallow convection, weak convective plumes and

small-scale clouds would not be resolved (Stratton et al., 2018). What this means is that the model is likely to under-perform in regions where shallow convection is the dominant process for formation of precipitation.

CP4A is driven by one-way nesting in G25 (described above) with G25 supplying the 3-hourly lateral boundary conditions. The lateral boundary conditions were updated at a 3-hour frequency. The fields from G25 that were used to compile the lateral boundary conditions for the CP4A are; the 3-hourly and 3-dimensional winds, potential temperature, water vapour, cloud liquid water, cloud ice water, density and Exner pressure. The atmospheric fields from G25 for 1 January 1997 were used as the initial conditions.

The SSTs used to force CP4A are the same as those used in G25; however, over Lake Victoria, the monthly nighttime climatological lake temperature from the Lake Surface Water Temperature and Ice Cover (ARC-Lake) was used in CP4A. The climatological data with a resolution of 50 km from an offline Joint UK Land Environment Simulator (JULES) land surface simulation was used to initialise the soil moisture. It is worth noting that while the CP4A has stochastic perturbations in the subcloud layer of cumulus-capped boundary layer that help the model to trigger resolved convection (e.g., Lock et al., 2000), G25 does not have such perturbations. Besides the difference in grid spacing and representation of convection, there are other differences in the model physics between CP4A and G25. For example, while CP4A implements a large-scale cloud scheme based on Smith (1990), G25 implements a prognostic cloud scheme as described in Wilson et al. (2008). Table 3.1 gives more differences between the two simulations examined in this thesis. The reader is referred to Stratton et al. (2018) and Walters et al. (2019) for detailed description of the parameterisation schemes used in CP4A and G25 respectively. Because precipitation in Equatorial Africa is produced by convective systems (e.g., Jackson et al., 2009), CP4A provides a virtual laboratory to better understand convection-dynamics interactions, thereby aiding model developers in efforts to improve the representation of the coupling between convection and the large-scale environment and circulation in models.

Another RCM was run over a similar domain as CP4A but with $\sim$25 km grid spacing and parameterised convection (P25; Stratton et al.,2018). Partly inspired by a proposition in Frierson (2007) that the representation of equatorial waves in climate models is constrained partly by the convection scheme, the present thesis will explore how the horizontal and vertical structure of CCKWs in a convection permitting model compares with that in a convection parameterised model. G25 is chosen instead of P25 because it has data over the entire tropics, allowing for reliable identification of equatorial waves.

3.3 Methods

3.3.1 The equatorial wave dataset: Identifying equatorial waves in reanalysis and simulations

The equatorial wave dataset is the wind field associated with a particular equatorial wave (discussed in Section 2.3). This dataset is produced using the zonal and meridional wind, and geopotential height field in ERA-I (for Kelvin waves, only the low-level (850 hPa) and upper level (200 hPa) zonal wind and the geopo-

Quantity	CP4-Africa (4.5 km)	Global
Convective parameterization	No	Yes
Radiation scheme	Edwards-Slingo	Edwards-Slingo
Period of full radiation calculation (min)	15	60
Substepped corrections due to cloud (min)	5	None
Aerosols and ozone	Climatology	Interactive U.K. Chemistry and Aerosols model (UKCA)
Large-scale cloud scheme	Smith scheme	PC2
Cloud microphysics	Wilson and Ballard	Wilson and Ballard
Subgrid turbulent production of mixed-phase cloud	No	Yes
Source of cloud droplet No. concentration	Aerosol climatology	Interactive UKCA aerosols
Microphysics time step (s)	100(75)	120
Includes graupel?	Yes	No
Lightning diagnosis	Yes	No
Boundary layer scheme	Blended scheme	No blending
Stochastic perturbations to boundary layer?	Yes	No
Frictional heating from turbulent dissipation?	No	Yes
Orogaphic drag scheme?	Yes	Yes
Land and sea surface scheme	JULES, nine tiles	JULES, nine tiles
Land-surface type and properties	Sandy soil	Varied soils
JULES land settings	As in R25-Africa	GL7
JULES sea settings	As in UKV	GL7
Hydrology scheme	PDM scheme	TOPMODEL
Vegetation cover data	CCI-LC	IGBP land cover
SST	Reynolds	Reynolds
Lake surface temp	ARC-Lake	GISST
Moisture conservation	New regional version	Global version
Simulation start-end dates	1 Jan 1997-1 March 2007	1 Sep 1988-1 Dec 2010

Adapted and modified from Stratton et al. (2018).

Table 3.1: The major differences in the physical parameterisation schemes and surface forcing between CP4A and G25

tential height are used). This dataset has a spatial resolution of 1^o x 1^o and a 6-hour temporal resolution at 2 pressure levels for 24^oS - 24^oN latitudinal belt, and includes equatorial waves with zonal wavenumbers k=2-40 and a period of 2-30 days. The equatorial wave dataset based on ERA-I is available from 1997 – 2018, however Chapter 4 uses the daily averaged data for the period 1998–2013 and Chapters 5 and 6 uses the same dataset but for the period 1998-2006. This thesis uses the method described above to generate an equatorial wave dataset based on a simulation from convection permitting regional climate model (CP4A). The method for generating this dataset is described below.

As noted above, the identification of Kelvin wave activity in both reanalysis and simulations follows a method developed in Yang et al. (2003). In the current chapter, the method for identifying equatorial waves is described in general but Chapters 4-6 use the equatorial wave dataset for Kelvin waves.

The identification of the different types of equatorial waves is done by projecting the dynamical fields onto various equatorial wave modes using their horizontal structures as described by parabolic cylinder functions in y and sinusoidal variations in x. Prior to projecting the dynamical field data onto the equatorial structure, the fields are filtered in a specified zonal wavenumber-frequency domain to separate into eastward and westward propagating components (Yang et al., 2003). One aspect that makes this dataset unique is that the data are projected onto each pressure level independently, allowing the data to reveal the vertical structure, rather than having to assume dispersion relations.

3.3.1.1 The basic equatorial wave theory

The solutions to the adiabatic, frictionless equations of motion on an equatorial beta plane linearised about a basic state and the separation of the vertical structure from that in the horizontal yields the equatorially trapped waves (Matsuno, 1966).The spatial (horizontal) and temporal variations in the zonal (u) and meridional (v) wind and the geopotential height (Z) satisfy the linearised shallow water equations with the gravity wave speed c, the separation constant from the vertical structure equation that can also satisfy the relevant surface and upper boundary conditions. This can only be achieved for a discrete values of the separation constant, c_e. The separation coefficient for an atmosphere with a constant buoyancy frequency N and a tropopause at height H with a rigid lid upper boundary conditions is, $c_e = \frac{NH}{m\pi}$, where m is the vertical mode number. The vertical modes are sinusoidal in z, with corrections for the density variation with height: $1/\rho_o \exp\left(\frac{z}{2H}\right)\exp(imz)$, where ρ_o is the density at the surface.

For the horizontal equations, the representation of u, v and Z fields are of the form:

$$\{u, v, Z\} = \{U(y), V(y), Z(y)\}\exp[i(kx - \omega t)] \tag{3.1}$$

where k is the zonal wavenumber and ω is the frequency. The equatorial wave solutions are most easily formulated in terms of new variables, q, r and v (Gill, 1980) where

$$q = u + \frac{gZ}{c_e},\ r = u - \frac{gZ}{c_e}. \tag{3.2}$$

A Kelvin wave solution can be obtained with $v = 0$ and $\omega = \frac{k}{c_e}$, and there are solutions for $v \neq 0$ with the dispersion relation:

$$\frac{\omega^2}{c_e\beta} - c_e\frac{k}{\omega} - \frac{c_e}{\beta}k^2 = 2n + 1,\ \text{for } n = 0, 1, 2, ... \tag{3.3}$$

In the above equation, $n =$ meridional mode number and $\beta = \frac{\partial f}{\partial y}$. For a Kelvin wave, equation 3.3 above is satisfied with $n = -1$ hence Kelvin waves are conventionally referred to as the $n = -1$ waves. The mixed Rossby Gravity waves (both eastward propagating (EMRG) and westward propagating (WMRG)) solutions are obtained when $n = 0$. The westward propagating equatorial Rossby waves and both westward propagating and eastward propagating gravity solutions are obtained when $n = 1$ or higher.

To describe the meridional (y) structures of equatorial waves, one considers the parabolic cylinder functions:

$$D_n\left(\frac{y}{y_0}\right) = \exp\left[-\frac{1}{4}\left(\frac{y}{y_0}\right)^2\right]P_n\left(\frac{y}{\sqrt{2}y_0}\right), \tag{3.4}$$

where

$$y_0 = \left(\frac{c_e}{2\beta}\right)^{1/2}, \tag{3.5}$$

is the meridional scale, P_n is proportional to a Hermite polynomial of order n, and the waves are confined within a few degrees from the equator on a scale $y_t = \sqrt{2}y_0$

Drawing from the equatorial wave theory, below is the description of the parabolic cylinder function expansions.

$$\begin{array}{rcccccc} q & = & q_0 D_0 & + & q_1 D_1 & + & \sum_{n=1}^{n=\infty} q_{n+1} D_{n+1} \\ v & = & 0 & + & v_0 D_0 & + & \sum_{n=1}^{n=\infty} v_n D_n \\ r & = & 0 & + & 0 & + & \sum_{n=1}^{n=\infty} r_{n-1} D_{n-1} \\ & & \uparrow & & \uparrow & & \uparrow \\ & & n=-1 & & n=0 & & n=1,2... \end{array} \tag{3.6}$$

Because these functions form a complete and orthogonal basis, and the projections in equation 3.6 above are general in that Kelvin waves are described by $q_0 D_0$, $q_1 D_1$ and $v_0 D_0$ describe $n = 0$ MRG waves, and $q_{n+1} D_{n+1}$ $v_n D_n$ and $r_{n-1} D_{n-1}$ yields the $n \geq 1$ equatorial Rossby waves or gravity waves.

The equatorial wave data for an entire latitudinal belt between of 24^oS-24^oN is obtained in four steps:

1. Formulation of the equatorial wave solutions in terms of v and two new variables:

$$q = u + \frac{gZ}{c_e},\ r = u - \frac{gZ}{c_e},$$

   where c_e is related to the trapping scale $y_0\left(\frac{c_e}{2\beta}\right)^{\frac{1}{2}}$ predetermined by the data fit.

2. This step involves filtering the data in the wavenumber-frequency domain. This step starts by removing the two dominant periodic cycles, the climatological annual and diurnal cycle from the raw fields to avoid aliasing in the filtering procedure. This is followed separating the variables v, q and r into eastward and westward-moving components using a space-time spectral analysis that transforms the data from the space-time domain into a wavenumber-frequency domain by performing a 2-Dimension Fast Fourier Transform in the zonal and time direction (Hayashi, 1982).

3. The output from step 2 above is then projected onto horizontal structures of equatorial waves. The coefficients of the FFT such as V(y) for each k and ω of the eastward or westward v, q and r are separately projected onto the meridional structures of the equatorial waves as described by the parabolic cylinder functions in equation 3.6 above to obtain the equatorial wave data at each isobaric surface. This comes with an advantage that the data itself shows the vertical structures and as such there is no need to assume a vertical structure, and obtaining the amplitudes for v, q and r one by one without assuming that the amplitude coefficients for these three variables are related via dispersion relations.

At this step, it is important to specify the meridional scale y_0 or trapping scale y_t thereby providing the value of c_e. Using equation in step 1 above, the values of q and r are obtained from u and Z. For the equatorial wave dataset used in this thesis, the value of $c_e = 20$ m s^{-1} (calculated using equation 3.5) and $y_0 = 6^o$ was used. The value of y_0 was determined from a best fit to the data, although it was found that the analysis is not sensitive to the particular value of chosen y_0. It is important to note that c_e is only used to calculate the new dependent variables q and r from u and Z and later to reverse the variable transform.

4. Finally, the Fourier coefficients for each wave mode from the projected q and r are then transformed back into physical space to obtain the equatorial wave dataset.

3.3.2 Modelled Equatorial Wave data

The isolation of equatorially trapped waves is best achieved using a zonally complete tropical domain, and so most studies have examined data from global observations or simulations. To detect Kelvin waves in CP4A, we start by regenerating a "new" global dataset that is comprised of both CP4A and G25. This is done by cutting out the African domain from G25 and replacing it with CP4A. Both simulations are coarse grained to a uniform grid before stitching them together. The sharp contrast at the longitudes ($\sim$24^{o}W and 56^{o}E) at which the joining is undertaken is smoothed by running a 5-point moving average along each latitude. The stitching is done for the sole purpose of creating an equatorial wave dataset and for all subsequent analysis, we use the CP4A's fields. The resulting equatorial wave data at say 850 hPa is the wind data for the different waves at spatial resolution of 1^{o}x 1^o on a daily time scale. Due to set up problems, CP4A's geopotential height and dynamical fields for the first 6 months of 1997 were not archived and so, year 1997 was excluded in the analysis. The methodology used here to identify Kelvin wave activity has been successfully applied in a wide range of studies to investigate CCKWs both in observations (Yang et al., 2007) and model evaluation (Yang et al., 2009), including the vertical propagation of equatorial waves in different phases of QBO (Yang et al., 2011, 2012), the influence of ENSO on equatorial waves and tropical convection (Yang and Hoskins, 2013, 2016), the connection between African easterly wave and equatorial waves (Yang et al., 2018), and the relationship between precipitation and equatorial waves in Southeast Asia (Ferrett et al., 2020).

3.3.3 Empirical Orthogonal Teleconnection (EOT)

The Empirical Orthogonal Teleconnection (EOT) is a multiple linear regression based technique that represents the patterns of variability over space or time. In the implementation of the EOT technique, one identifies a single point (base point), which, by multiple linear regression, accounts for the highest variance at all other points combined (Van den Dool et al., 2000). Each EOT is a spatial pattern of regression coefficients between the base point and all other points. It is important to note that the EOT technique is similar to the commonly used Empirical Orthogonal Function (EOF) technique; the differences are briefly discussed below.

Because it is not appropriate to treat WEA or EEA (shown in Figure 1.1) as a homogeneous region in

the context daily precipitation variability, they are further sub-divided into smaller sub-regions of similar daily precipitation characteristics using the EOT technique. Prior to performing the EOT on the daily precipitation dataset, the annual cycle was removed by subtracting a 30-day running mean of the daily 16-year rainfall climatology from each year used in the study. Since the interest here is to understand high frequency convection and precipitation variability, the influence of low frequency modes of variability such as ENSO was also removed by subtracting the 100-day moving average from the time series at every grid-point in the domain. The 100-day moving average was used because it is consistent with the 3 month running mean of sea surface temperature anomalies that is used to define the Oceanic Nino Index (ONI) at the National Oceanic Atmospheric Administration (NOAA) Climate Prediction Centre (CPC) (e.g., Huang et al., 2016). Finally, any long-term trend over the 16-year period was removed using linear regression. The remaining anomalies were then subjected to the EOT algorithm.

The purpose of the EOT technique is to objectively identify sub-regions exhibiting similar daily precipitation characteristics. This technique produces modes which are orthogonal in either space or time. In Van den Dool et al. (2000), the EOT technique entails first identifying a point (base point, a raw data time series) in space that accounts for the highest variance at all other points combined. Next, the first EOT pattern is obtained as a correlation coefficient pattern between the base point and the other points, and finally a residual of the "original" data set is calculated by removing the variance explained at each point by this EOT pattern using linear regression. This residual dataset is then used to obtain the next EOT pattern and the aforementioned process is repeated to isolate additional EOT patterns. Essentially, in Van den Dool et al. (2000), the EOT patterns are constrained by global variance, that is, the sum of squares of anomalies over the domain of interest (e.g., Smith, 2004). In the case of precipitation, the largest anomalies tend to be biased towards the regions with the highest precipitation totals and, when the global variance is used to describe the data, the aforementioned bias is amplified. Smith (2004) suggested that a less biased approach is to base the EOT technique on the global integral. In the suggested approach, the area averaged time series over the domain of interest is calculated, and then a base point accounting for the highest variance of the area averaged time series is identified. Here, we use the modified EOT approach as described in Smith (2004).

The modified EOT approach is implemented in a few steps. The first step is to search for a base point whose time series is best correlated to the area average time series of the domain. In the second step, the base point time series is then correlated with the time series of every grid-point in the entire domain. In the third step, the sub-region is obtained by finding the longitude-latitude box that encloses the meridional and zonal line segments intersecting the base point which include all contiguous grid points along those segments whose correlation coefficients between the grid point time series and the base point time series exceed 0.2 (this step is needed for the purposes of this study but not necessary for other EOT technique usage). Finally, the variance explained by the first base point is subtracted from every grid point in the domain, thus creating a new dataset (the residual). In each iteration, the four steps are repeated to identify a sub-region and thus the first iteration identifies sub-region 1, the second iteration identifies sub-region 2 etc until the desired number of sub-regions

is identified. It should be noted that the iteration at which a particular sub-region is identified is not indicative of its relative percentage of the total variance explained, and for this study, the main purpose of the EOT analysis is finding sub-regions of spatial co-variance rather than quantifying variances explained. Since the order in which the sub-regions are identified is not physically important, the identified sub-regions were renamed: for example, W1 represents sub-region 1 in WEA and E1 represents sub-region 1 in EEA (Section 4.3). Previous studies that successfully used the modified EOT approach in Smith (2004) and Stephan et al. (2018). The use of the EOT algorithm enabled an objective identification of sub-regions made up of points with relatively similar daily precipitation variability. The location and dimensions of the various sub-regions identified are the only outputs of the EOT analysis used in subsequent analysis in this thesis. For example, the sub-region's area average time series is computed by spatially averaging over the dimensions of the sub-region. The sub-regions identified are used to compute lead/lag correlation coefficients (§4.4 , spatio-temporal correlation (§4.5 and composite analysis (§4.7). The details of computations involved in correlation coefficient and composite analysis are presented in Section 4.2.2. Finally, it is important to note that the EOT technique is different for the commonly used Empirical Orthogonal Function (EOF) approach. One of the differences is in terms of the variance explained by each mode. In the EOF technique, the modes identified earlier in the iteration explain more variance than those identified later, whereas in the EOT approach, all the EOTs are equally important. Another difference relates to orthogonality in that, while the EOFs are orthogonal in both space and time, the EOTs are orthogonal in one direction, either space or time. By selecting a point in space as described above, the EOTs are orthogonal in time.

Chapter 4

The observed synoptic scale precipitation relationship between WEA and EEA

4.1 Purpose of the chapter

This chapter addresses the first two objectives of this thesis (§2.7): (a) To assess the precipitation linkage between WEA and EEA based on small sub-regions characterized by similar daily precipitation characteristics, and (b) To identify possible mechanisms driving variability associated with the precipitation connection between WEA and EEA. To address these objectives, this chapter examines daily observed precipitation (TRMM, described in Section 3.2.1, and GPCP-1DD, described in Section 3.2.2), and reanalysis dataset (ERA-I) described in Section 3.2.3.

Despite the critical importance of precipitation over Equatorial Africa (e.g., Chapter 1), the quality of short-to-medium-range precipitation forecasts in general still lags that in midlatitudes (Woodhams et al., 2018). One of the reasons for this is the inadequate understanding of the drivers that govern synoptic-timescale precipitation variability (e.g., Nicholson, 2018), and their representation in numerical weather prediction and climate models. Over tropical Africa, synoptic-timescale precipitation variability is mainly controlled by large-scale tropical disturbances like equatorial waves (e.g., Schlüter et al., 2017). As discussed in Chapter 2, several of studies have found that large-scale tropical disturbances such as equatorial waves tend to enhance precipitation over Equatorial Africa. For example, Sinclaire et al. (2015) noted that during March–June, eastward propagating CCKWs favour initiation of synoptic-scale convective systems and that annually, an average of six to seven CCKWs propagate through the Congo Basin in this period. Several studies that investigated Kelvin waves over Equatorial Africa (e.g., Nguyen and Duvel, 2008; Laing et al., 2011; Sandjon et al., 2012; Sinclaire et al., 2015; Mekonnen and Thorncroft, 2016; Jackson et al., 2019) applied spectral analysis of OLR or CBT to identify CCKWs. Here, a unique approach of identifying the CCKWs using a novel dynamics-based equatorial wave

dataset is used.

While the precipitation connection between WEA and EEA and the associated mechanisms are important, they have not been thoroughly investigated even though previous publications have suggested that WEA is meteorologically linked to EEA (e.g., Dezfuli et al., 2015; §2.1.3). What this means is that WEA and EEA are connected but the linkage between the two is not well understood. This chapter therefore, aims at advancing knowledge of the synoptic-scale interaction between WEA and EEA in the context of daily precipitation anomalies, which are more linked to convective processes and more relevant to human impacts than OLR.

It was discussed in Chapter 1 that Equatorial Africa is a large area (§1.1) with nonhomogeneous and complex precipitation climatology. The region is characterized by remarkable spatial variation at intraseasonal (e.g., Nguyen and Duvel, 2008), seasonal (e.g., Sandjon et al., 2014; Fotso-Kamga et al., 2020) and interannual (e.g., Janowiak, 1988) timescales. Because of the heterogeneity of precipitation over this region, previous studies delineated their areas of study into smaller sub-regions, using either monthly totals (e.g., Indeje et al., 2000; Dezfuli, 2011) or annual totals (e.g., Badr et al., 2016). In this thesis, we use high spatial resolution daily precipitation records to objectively identify small sub-regions that are characterized by similar daily precipitation variability over all of Equatorial Africa. The sub-regions identified are then used to study the precipitation relationship between WEA and EEA (§4.4 and §4.5), and identify the mechanism associated with the linkage between WEA and EEA.

The rest of this chapter is structured as follows. Section 4.2 presents a brief description of the methodology. In Section 4.3, the daily observed precipitation anomalies are used to identify the small sub-regions that are characterised by similar daily precipitation characteristics. Sections 4.4 and 4.5 discuss the correlation between WEA and EEA. Two indices, (a) precipitation-based index, and (b) Kelvin wave divergence-based index are developed in Section 4.6 and used to identify west-east propagating anomalous precipitation and Kelvin wave signal. Both the precipitation and Kelvin wave events identified are used to compute composites in Section 4.7. Finally, the discussion and the conclusions of this chapter are presented in Section 4.8.

4.2 Methodology

The detailed description of the methods used in this thesis is presented in Chapter 3. These are briefly summarised below for completeness.

4.2.1 Empirical Orthogonal Teleconnection (EOT) Analysis and calculation of anomalies

As noted above, precipitation over Equatorial Africa varies considerably over short distances. Since it would be inappropriate to average over large areas (WEA or EEA), a physically meaningful approach is to objectively subdivide the large area into smaller sub-regions of shared temporal variance. The observed daily precipitation anomalies were subjected to an Empirical Orthogonal Teleconnection (EOT) algorithm to identify

sub-regions of similar daily precipitation variability. The anomalies were calculated by subtracting a 30-day running mean of the daily 16 year precipitation climatology from each year to remove the annual cycle and this was followed by subtracting the 100-day running mean from the time series at every grid point. The subtraction of the 100-day moving average was undertaken to remove signals of low-frequency modes of climate variability. The details on how the EOT approach was used for obtaining sub-regions of similar daily precipitation variability is described in Chapter 3 (see §3.3.3).

4.2.2 Correlation and Composite Analysis

Correlation analysis is used for all pairs of sub-regions over various days of lead/lag in order to identify propagating signals. As presented in Figure 4.2, for any given pair of sub-regions, a positive value implies that EEA is lagging WEA. In all subsequent analysis, we use the word "lag" (with a positive value) to refer to days after the reference time (day 0) and likewise lag with a negative value for days before the reference time. The bootstrapping technique is used to test for the statistical significance of the correlation coefficient between the area averaged time series of a pair of sub-regions. For brevity, the time series for the sub-region in WEA is referred to as A and that of the sub-region in EEA as B here. The bootstrapping is done by holding A in its original order, and then, to preserve the original synoptic-timescale autocorrelation of B, it is divided into blocks of 100 days. A total of 1000 samples of B are constructed by randomly drawing the blocks with replacement and stitching the sampled blocks together so that each sample is the same size as B. Time-series A is then correlated with every sample and the 95^{th} percentile of the absolute value of these correlation coefficients is determined. If the absolute value of the correlation coefficient of the original time series is greater than this 95^{th} percentile, it is considered to be statistically significant at the 95% confidence level.

Composites are performed on events that were selected by considering a pair of sub-regions. So, for a given pair of sub-regions, a precipitation occurrence is defined as an "event" if two conditions are satisfied. First, precipitation occurs in excess of a threshold in a sub-region in WEA. Second, two days later, the precipitation in the corresponding sub-region in EEA exceeds that sub-region's threshold given that the previous day's precipitation was below the threshold. Our choice of 2 days in defining the event is informed by our early results in this study. It will be shown in Section 4.4 that the strength of the signal does peak on day 2 hence the use of 2 days in identifying events provides an opportunity to fully explore the greater spatial extent of the signal. The thresholds were determined by calculating the 66.7^{th} percentile for each particular sub-region. The 66.7^{th} percentile was chosen because it is an operational precipitation forecast threshold that categorises the heavy rainfall events that may be associated with organised convective systems. The area averaged time series of the anomalies of each sub-region were used to compute the threshold for each sub-region. All the days with zero area averaged raw precipitation amount were removed before computing the thresholds.

4.3 Identification of sub-regions

Daily TRMM anomalies for a 16-year period were subjected to EOT analysis and a total of 32 sub-regions were identified. The robustness (in terms of the identified sub-regions' location) of using TRMM daily anomalies was tested by subjecting 15 years of GPCP daily anomalies to the same EOT analysis. Figure 4.1 shows an example of the sub-regions identified using TRMM daily anomalies. Those identified using the GPCP dataset were generally in similar locations as those shown in Figure 4.1 (not shown). The 29^{o}E longitude was chosen to divide Equatorial Africa (defined above) into WEA and EEA for consistency with previous studies (e.g., see Sandjon et al., 2014; their Figure 1) and with an operational weather forecasting model over Lake Victoria in EEA (e.g., see Woodhams et al., 2018; their Figure 1). The sub-regions over ocean and those whose base-points were located on 29^{o}E were disregarded. A total of 17 sub-regions in WEA and 8 in EEA were considered for further analysis (see example in Figure 4.1). Re-running the algorithm without removing the trend, or removing it using Locally Estimated Scatterplot Smoothing (LOESS) instead of linear regression, did not influence the resulting sub-regions.

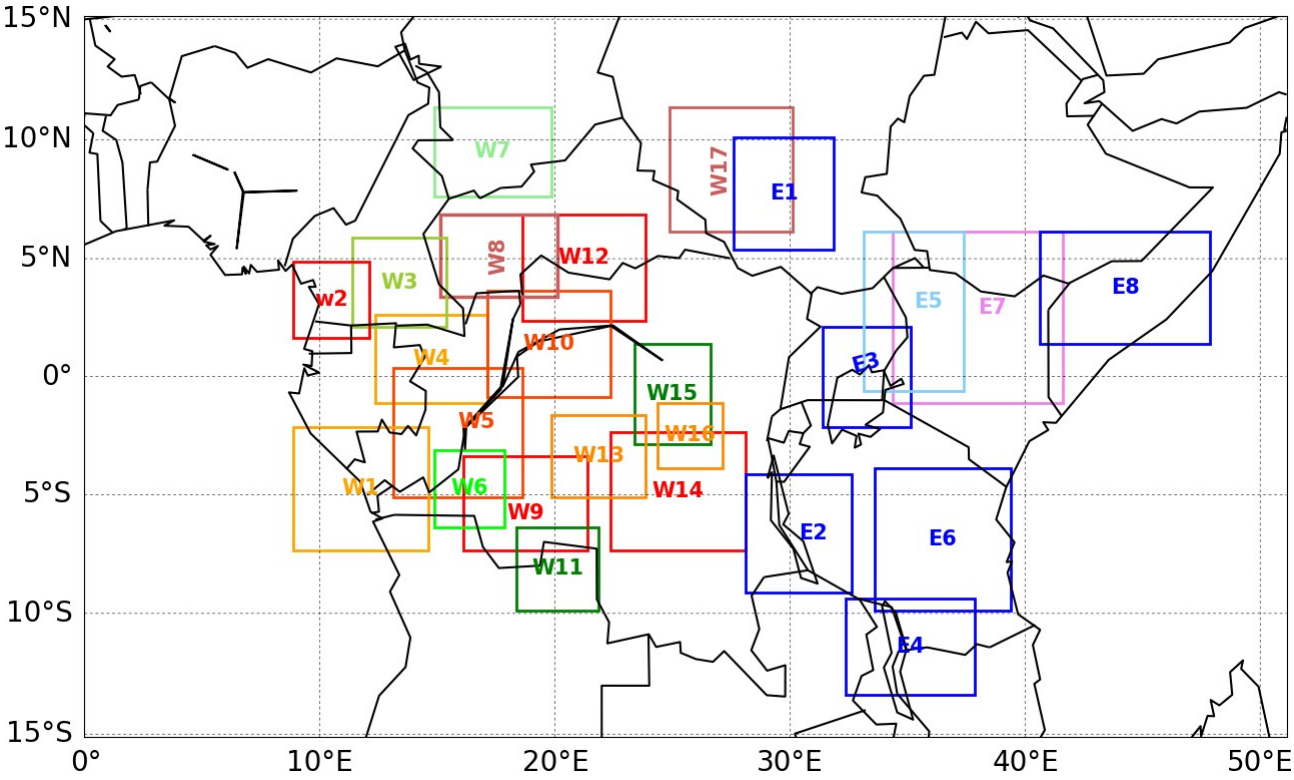

Figure 4.1: Example of sub-regions identified by subjecting 16-years of daily TRMM anomalies to an EOT. The letter "W" attached to the number in the red sub-regions indicates that the sub-region is located in Western Equatorial Africa and "E" likewise for EEA. Since the order in which these sub-regions were identified does not matter, they were renamed for clarity.

4.4 Lead/lag correlation coefficient analysis

Correlation coefficients between area-average time series of TRMM rainfall anomalies (§3.2.1) of each sub-region in EEA with every sub-region in WEA for lead/lag -5 to +5 days over the entire 16 years were calculated. Since there were 17 sub-regions identified in WEA and 8 sub-regions in EEA, there are a total of 136 different pairs. Sub-regions E1 and E3 have the strongest correlation when correlated with the various sub-regions in WEA (ignoring the strongly overlapping W17-E1 pair). We note that E3 is located over Lake Victoria, which strongly influences the climate over EEA (e.g., Song et al., 2004). Previous studies have found a strong influence of the eastward propagating signal of the MJO on precipitation over Lake Victoria (e.g., Hogan et al., 2015). The lead/lag correlation coefficient analysis for some sub-regions in WEA versus E1 and E3 in Figure 4.2 shows peak correlation coefficients at lag +1-2 days followed by a local minimum on lag +3-4 days. E3 (in Figure 4.2b) shows a peak correlation with W5, W9, W12, and W14 around lag +1-2. In comparison with Figure 4.2b, there are strong peak correlation coefficients on both sides of lag 0 (for W3 and W12) in Figure 4.2a, which could indicate an oscillation.

Tables 4.1 and 4.2 show example results of minimum and maximum correlations of area-average time series for E3 and E1 with every sub-region in WEA respectively. Values are all significant at the 95% level, though they are typically below magnitude 0.2 as expected for daily precipitation variability. In Table 4.1, the strongest positive correlation coefficients are seen on lag +1 (i.e. E3 versus W14), and the positive correlation coefficients on lag +2 (i.e. E3 versus W5, E3 versus W9) are generally weaker than those on lag +1. The strongest negative correlation coefficients for some regions seen on lag 0 in Tables 4.1 and 4.2 suggest a contrasting relationship between the different pairs of sub-regions. Note that from Table 4.1, it can be seen that the magnitude of the correlation coefficients is generally below 0.2.

Further analysis on peak correlation coefficients seen in Figure 4.2 is done by considering the correlation coefficients for each WEA sub-region versus every EEA sub-region and identifying the strongest correlation among all lags (0-5) for each pair. Then, for each WEA sub-region which is paired with each of the eight EEA sub-regions, the maximum of these correlations is retained for each lag and is plotted in the column for that WEA sub-region. This is shown in Figure 4.3. For example, the ninth column of Figure 4.3 shows that, of all pairs of sub-regions, E2 has the strongest correlation at lag +1 with W9. Similarly, for all such pairs with the strongest correlation at lag +2, E3 is the maximum. No pairs in the ninth column have the strongest correlation at any nonzero lag other than lag +1 or lag +2, so the colours for those lags do not appear in this column. We perform this analysis in order to show where the "peaks" of the lag-correlation distribution (like those shown in Figure 4.2) are largest for each WEA sub-region.

Figure 4.3 shows that 15 WEA sub-regions (all except W3 and W17) have at least one EEA pairing with its strongest correlation at lag +2, which is why all columns except 3 and 17 have a yellow cell. Lag +2 is therefore the most common lag measured in this way, followed by lag +1 with nine cells and lag +3 with eight

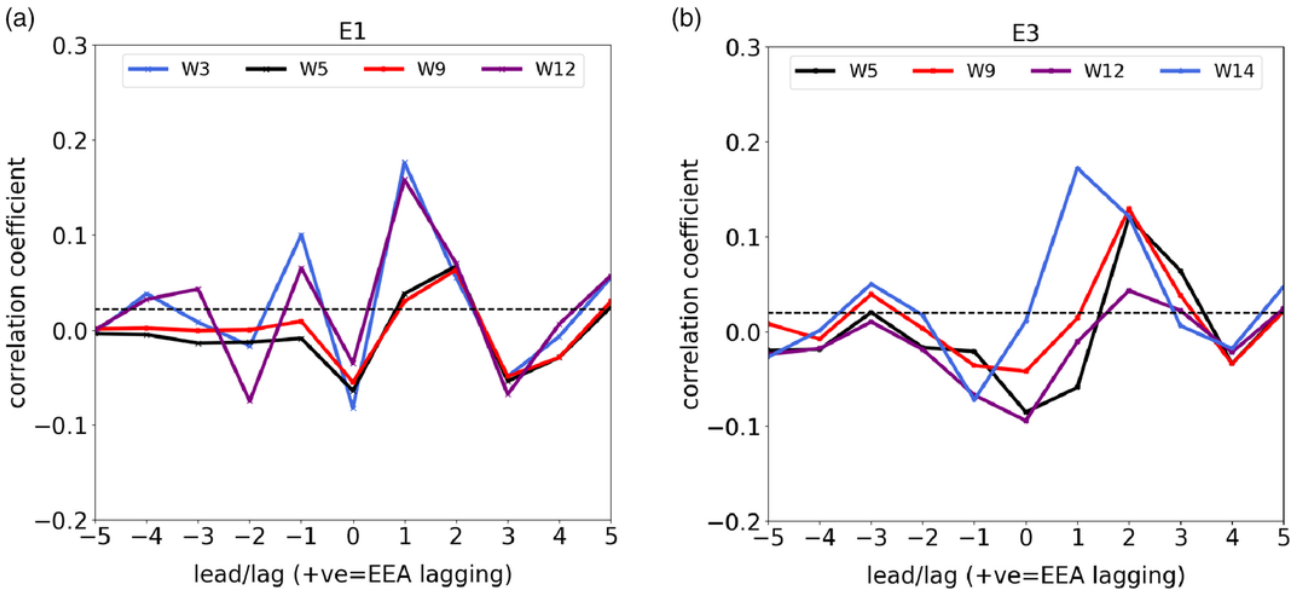

Figure 4.2: Lead/lag correlation coefficients of 16-year daily TRMM precipitation anomalies for (a) E1 versus W3, W5, W9 and W12 (b) E3 versus W5, W9, W12 and W14. The dashed line shows the largest minimum threshold for statistically significant positive correlation coefficients. For any given pair of sub-regions a positive value implies that EEA is lagging, and we use the word "lag" (with a positive value) to refer to days after the reference time (day 0) and likewise negative values for days before the reference time.

cells. Of those 15 WEA sub-regions with lag +2 values, eight (or 53%) have the maximum of these strongest correlations when paired with E3, which is why most yellow cells occur in the third row. This highlights a possible unique interaction between sub-regions in WEA and E3. Furthermore, of the pairings between all WEA sub-regions and E3 (row 3 in Figure 4.3), the strongest correlation coefficient is seen between E3 and W9 at lag +2. Also, the strongest correlation coefficients between the westernmost sub-regions (W1-3; see Figure 4.1 for the location of W1-2) and E3 occur at lag +3, which is why the first three cells in the third row are red. Subsequent work looks at E3 in more detail because it indicates the highest number of sub-regions in WEA with which it exhibits the strongest correlation coefficient at any lag; note that we focus on lag +2 in this chapter, for reasons discussed below. We acknowledge that the correlation between W11 and E2 (0.18) is stronger than that between W9 and E3 (0.13). Our choice to further analyse W9 and E3 is premised on the higher number of WEA sub-regions that exhibit the strongest correlation coefficient with E3 compared to E2. This suggests that overall, E3 is more likely to demonstrate WEA-EEA interaction. Also, we investigate the W11-E2 pairing, and E2 in general, to check sensitivity to sub-region choices. We also note that the W5-E3 pairing has only a slightly lower correlation (0.12) than the W9-E3 pairing, and that W5 is closer to the equatorial latitude range covered by E3, so we also investigate the W5-E3 pairing for sensitivity to choice of sub-region.

Over the continuum of lag 0 to +4, Figure 4.3 suggests that the strongest correlations are seen at lag +1 and +2. Figure 4.3 also shows that the correlations peak at lag +1 when the associated pair of sub-regions is closer to one another (e.g., W9 and E2, W14 and E3, W8 and E1) and similarly at lag +2 or +3 when they are further apart (e.g., W9 and E3, W5 and E3, W3 and E3). However, by lag +3, the correlation coefficients are

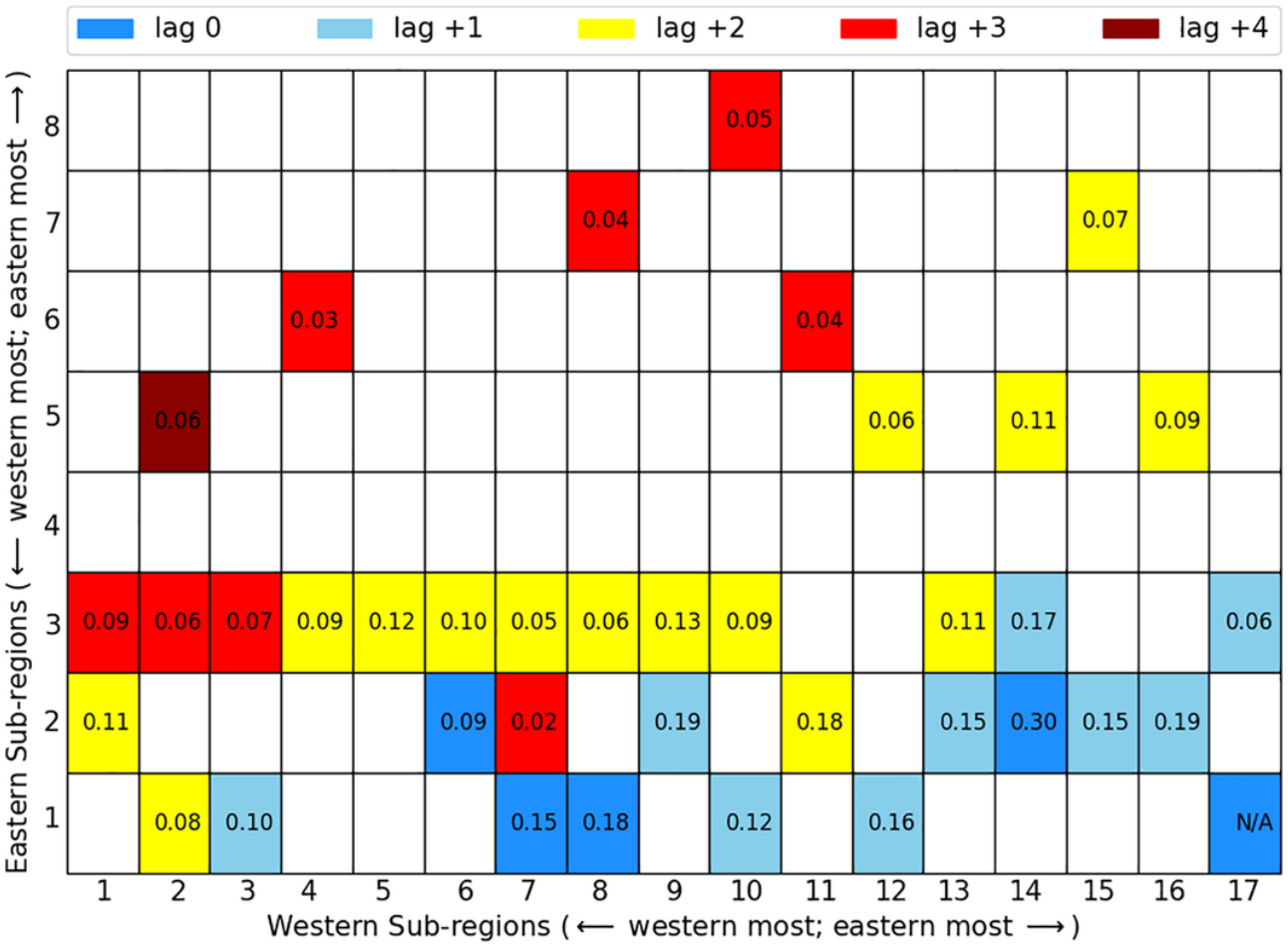

Figure 4.3: The maximum correlation coefficients between each WEA and EEA sub-region at various lag days. For each column (WEA sub-region), the dark blue, light blue, yellow, red and dark red cells indicate that the maximum correlation coefficient at lag 0, +1, +2, +3 and +4 respectively, out of all EEA sub-region pairings with the WEA sub-region, occurred with the corresponding row (EEA sub-region). Correlation coefficients are computed using the entire 16-years of TRMM daily precipitation anomalies and only correlation coefficients that are statistically significant at 95% confidence level are indicated in the figure. The correlation coefficient for column 17, row 1 was omitted because due to an extensive overlap between E1 and W17, it is expected that the correlation coefficient will be influenced by the overlapping grid points.

not as strong; thus, emphasis is placed on lag +2 as it provides an opportunity to understand the behavior of the signal across a wider west-east stretch of the domain under investigation, while still having relatively strong correlation coefficients.

The precipitation anomalies were also divided into four seasons consisting of MAM, June -August (JJA), SON and December-February (DJF), and lead/lag correlation coefficients over the various sub-regions were recalculated (not shown). The results showed that the strength of the correlation coefficients almost doubled in MAM and SON. This is likely due to more rainfall events occurring during those seasons. However, the peak of the correlation coefficients was seen at similar lead/lag days as those shown in Tables 4.1 and 4.2.

4.5 Spatio-temporal correlation coefficients

The spatio-temporal correlation pattern between W9's area-average time-series and every grid-point is shown in Figure 4.4. The strongest positive correlation coefficients occur on day +1 when the

E3 vs	Min corr	lag @ min corr	Max corr	lag @ max corr
W1	-0.084	0	0.093	3
W2	-0.094	1	0.055	3
W3	-0.085	1	0.068	3
W4	-0.063	1	0.088	2
W5	-0.025	0	0.120	2
W6	-0.044	0	0.101	2
W7	-0.042	0	0.050	2
W8	-0.111	0	0.061	2
W9	-0.029	0	0.129	2
W10	-0.094	0	0.091	2
W11	-0.063	-1	0.085	2
W12	-0.072	0	0.049	1
W13	-0.129	0	0.109	2
W14	-0.125	-1	0.172	1
W15	-0.084	-1	0.133	1

Table 4.1: Minimum and maximum correlation coefficients and corresponding lead/lags at which these occur, between sub-region E3 and various sub-regions in WEA. All correlation coefficients shown here are statistically significant at the 95% level

E1 vs	Min corr	lag @ min corr	Max corr	lag @ max corr
W1	-0.024	-1	0.029	2
W2	-0.028	0	0.077	2
W3	-0.061	0	0.098	1
W4	-0.068	0	0.079	2
W5	-0.064	0	0.067	2
W6	-0.041	0	0.044	2
W7	-0.056	0	0.154	1
W8	-0.082	0	0.176	1
W9	-0.055	0	0.063	2
W10	-0.107	0	0.123	1
W11	-0.024	3	0.046	2
W12	-0.074	-2	0.158	1
W13	-0.069	0	0.081	2
W14	-0.043	3	0.061	1
W15	-0.073	3	0.100	1

Table 4.2: Minimum and maximum correlation coefficients and corresponding lead/lags at which these occur, between sub-region E1 and various sub-regions in WEA. All correlation coefficients shown here are statistically significant at the 95% level

eastward/northeastward-propagating signal progresses from W9 and propagates to a region approximately centred on 5^{o}S, 25^{o}E (over W14), and then on day +2 the strongest positive correlation coefficients advance further east to a region approximately centred on 3^{o}N, 33^{o}E (over E3). By day +3 (and also day +4, not shown), the signal becomes much weaker. The pattern seen in Figure 4.4 suggests a coherent synoptic-scale eastward-propagating signal.

Figure 4.4 also shows little eastward propagation from day +2 to day +3, unlike previous days. This result is consistent, however, with the findings in Liebmann et al. (2009) (see their Figure 1), and several possible

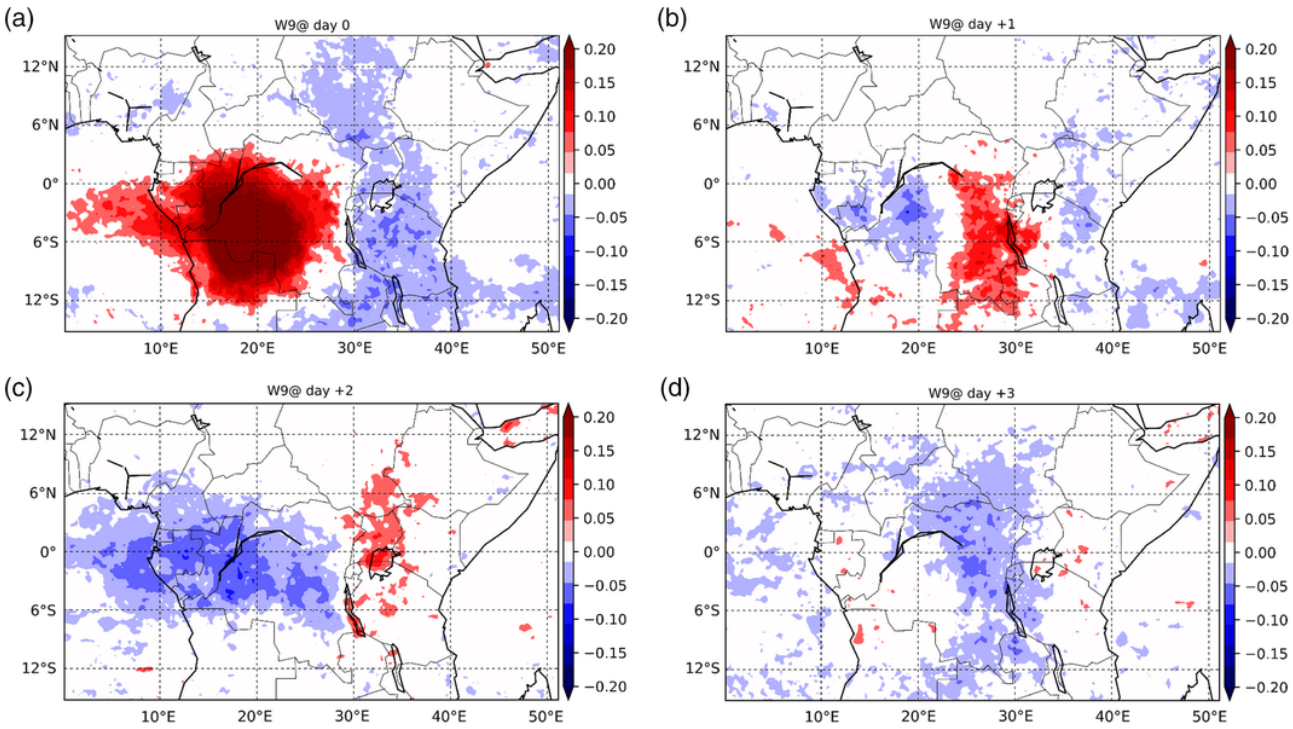

Figure 4.4: Correlation coefficients between area average time series based on 16-years of TRMM daily precipitation anomalies over W9 and every grid point in the domain for (a) day 0 (b) day +1, (c) day +2, (d) day +3. Only correlation coefficients that are statistically significant at 95% confidence level are shown.

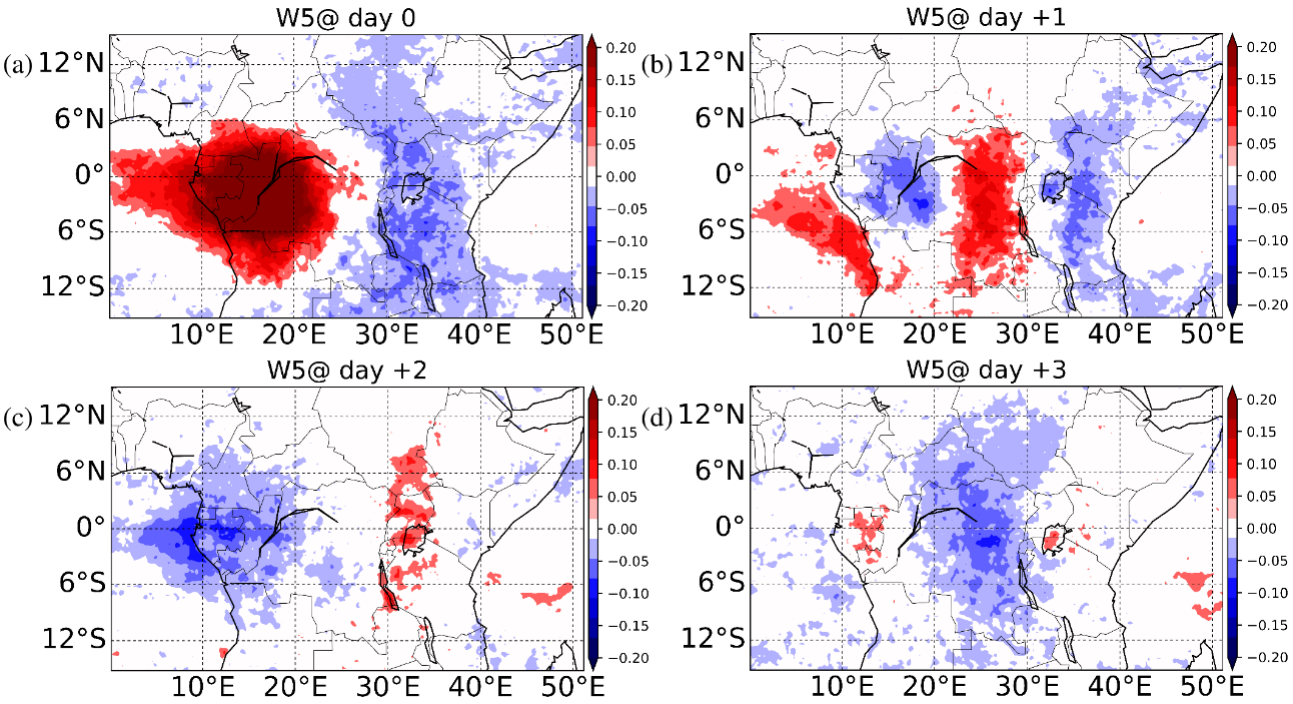

Figure 4.5: As in Figure 4.4 but for W5

reasons for this behaviour are discussed below. Note that we find a similar pattern to Figure 4.4 when we redo the same analysis but using either W5 or W11 in place of W9 (pattern for W5 is shown as Figure 4.5).

The area-average time series over all the sub-regions in EEA (e.g., E1-8) were correlated with every grid point in the domain at lag 0, -1, -2, and -3. Figure 4.6 shows the spatio-temporal distribution of the correlation coefficients for E1 (Figure 4.6a-d) and E3 (Figure 4.6e-h) for lag 0, -1, -2, and -3 (For E2, see Figure 4.5).

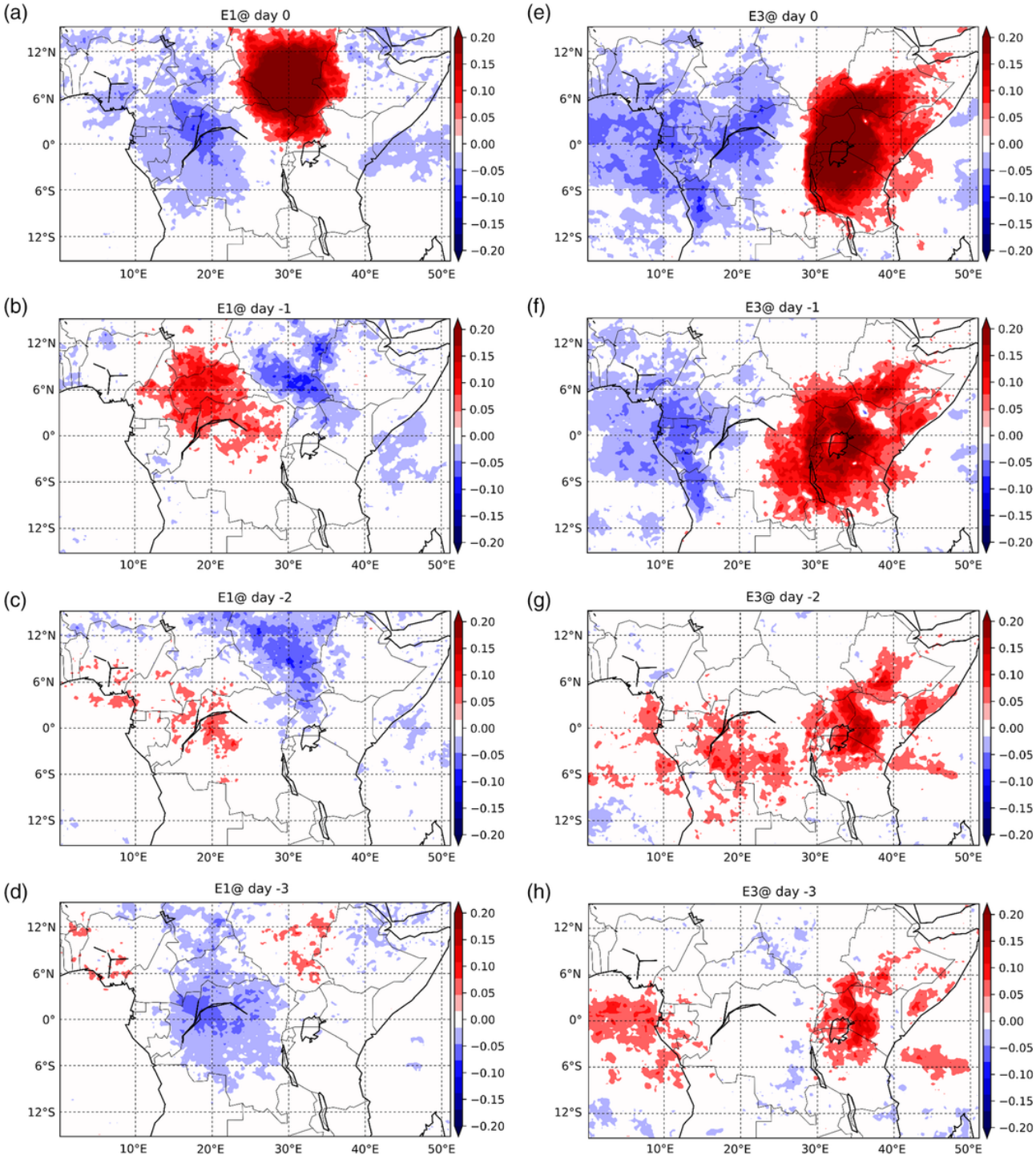

Figure 4.6: Correlation coefficients between area average time series based on 16-years of TRMM daily precipitation anomalies over E1 and every grid point in the domain for lag (a) 0, (b) -1, (c) -2, and (d) -3 and similarly over E3 for lag (e) 0, (f) -1, (g) -2, and (h) -3. Only correlation coefficients that are statistically significant at 95% confidence level are shown.

There is a clear difference in the structure of the correlation patterns over lag -1, -2, and -3. For E3, it is seen in Figure 4.6 that there is no switch in polarity of the local sub-region correlation signal over all lag days. However, E1 indicates a change in the polarity of the local signal over the four lag days. The correlation coefficient pattern seen in Figure 4.6a-d may be interpreted to mean that when wet anomalies dominate E1 (in South Sudan), dry anomalies occur in central WEA (e.g., over W3, W5, W8) and vice versa, suggesting a weak precipitation

dipole. Here, the word “dipole” is used to refer to behaviour leading to a two-pole (positive-negative) spatial structure of the signal on day 0 which is also similarly present on an earlier or later lag, and where a similar structure with reversed polarity is present between those two days. For E1 lag -3 (Figure 4.6d), the structure of the signal resembles that on day 0 (Figure 4.6a), though the signal is weak in Figure 4.6d. However, the correlation pattern seen in Figure 4.6h does not entirely resemble that in Figure 4.6e. The coefficient pattern seen in Figure 4.6a-d therefore suggests a precipitation dipole. This result is consistent with Mekonnen and Thorncroft (2016), who found a dipole in boreal summer OLR between the Congo Basin and Eastern Africa.

To test whether the unique behaviour of E1 was due to its off-equatorial location, a similar spatio-temporal correlation analysis over E2 was performed, since both E1 and E2 are located approximately along the same longitudinal band and distance from the equator. The structure of the correlation pattern over E2 (Figure 4.7) for lag 0, -1, -2, and -3 was similar to that of E3 (Figure 4.6e-h) and not that of E1 (Figure 4.6a-d). This suggests that the behaviour of E1 is not due simply to its distance from the equator.

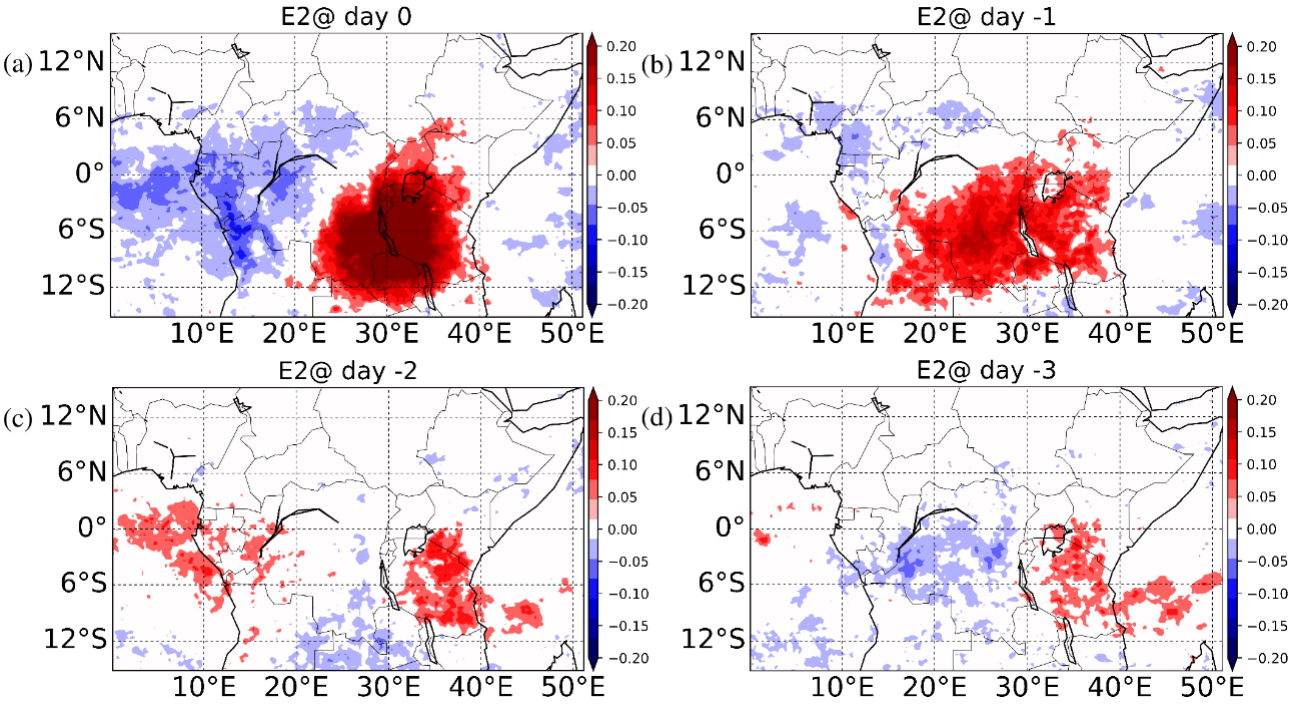

Figure 4.7: As in Figure 4.6 but for E2

Figure 4.6 shows a clear difference in the spatio-temporal correlation patterns of E3 and E1. Patterns for the other E sub-regions (e.g., E6, E8) were similar to that for E3, thus not shown. We speculate that for all sub-regions in EEA, except E1, a “local” influence within EEA persists for a longer timescale than the influence from WEA.

To further assess the relationship between precipitation in a sub-region and the driving circulation at every grid-point, area-averaged precipitation anomalies in W3, W5 and W9 were correlated with 850hPa zonal wind anomalies for the entire period, regardless of the season. Results indicate a coherent eastward/northeastward propagation signal similar to Figures 4.4 and 4.6, discussed further below.

Figures 4.4 and 4.6a-d highlight the approximately 12 m s-1 eastward/northeastward-propagating synoptic-timescale signal. Based on previous studies (Kiladis et al., 2009; Laing et al., 2011), the propagation speed of the signal seen in Figures 4.4 and 4.6a-d closely matches that of a CCKW.

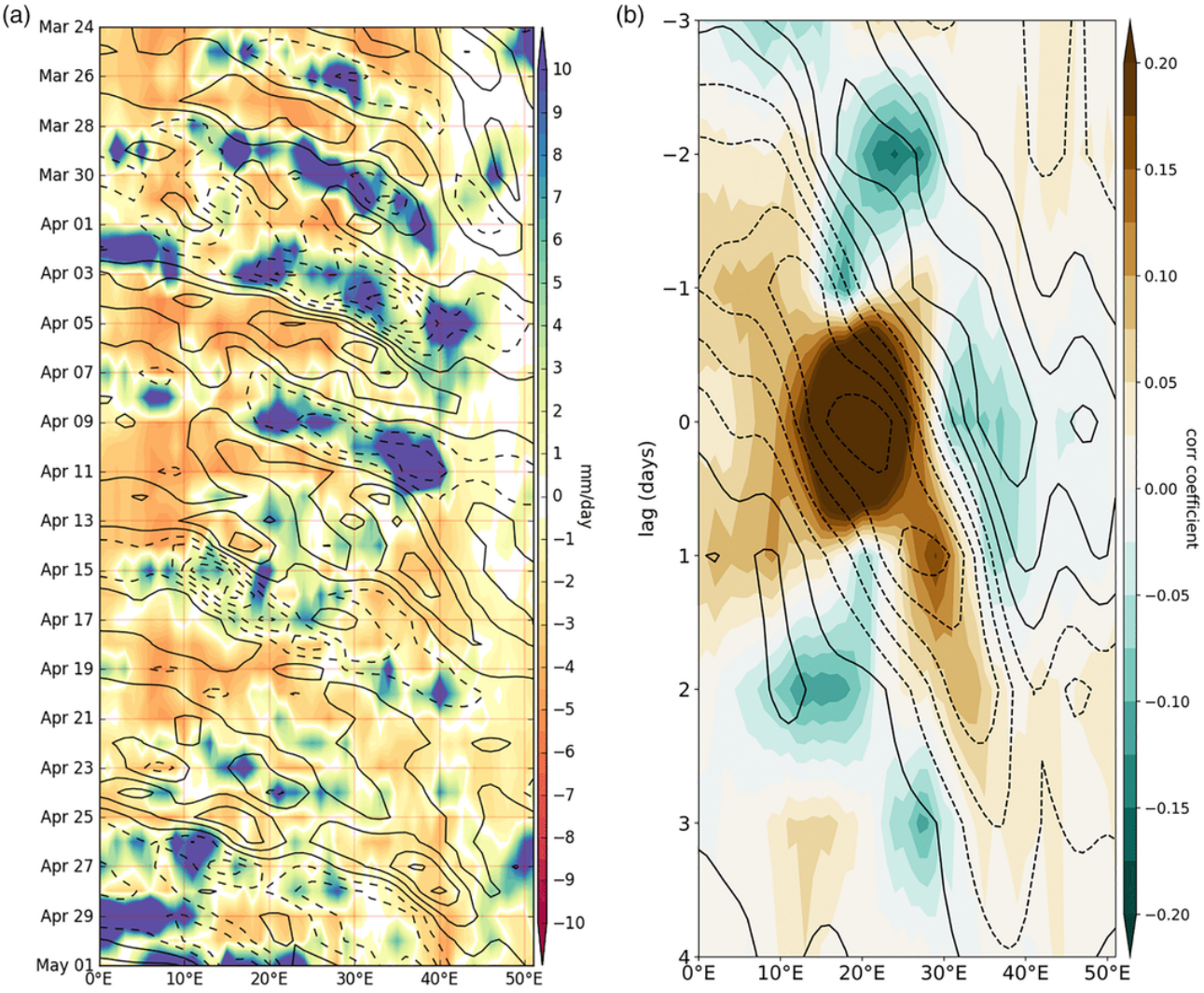

Figure 4.8: (a) Time-longitude section for daily precipitation anomalies for 24 March to 5 May 2004 (shaded) where the contour lines show Kelvin wave divergence (dashed lines negative) at 850 hPa and both divergence and precipitation are averaged between 7°S and 3°N. Contour line interval is $9.3 \times 10^{-7} S^{-1}$ (b) Contour lines show the lagged correlation coefficient between 16-years of daily precipitation anomalies over W9 and grid point 850 hPa Kelvin wave divergence (dashed lines negative) and shading shows the autolagged correlation of precipitation over W9 and grid point precipitation averaged over 7°S and 3°N.

Figure 4.8a shows a time-longitude plot of TRMM daily precipitation anomalies and the 850 hPa Kelvin wave divergence field for April 2004, as an example. The period shown here was selected because it includes several events (see §4.2.2 for definition, and §4.8 below for more discussion) that were indicated by several different pairs of near-equatorial sub-regions (e.g., W5-E3, W9-E3, and W4-E3, see Figure 4.1 for W4 location), suggesting that on these dates there was an eastward propagation of wet anomalies. For our primary pairing of W9-E3, there are three such events beginning March 25, April 17 and May 01. Note that in Figure 4.8, both precipitation and Kelvin wave divergence is averaged between 7°S and 3°N because W5 and E3 are also located within this latitudinal belt. Figure 4.8a shows that eastward-propagating wet anomalies coincide with

Kelvin wave low-level convergence, while dry anomalies coincide with Kelvin wave low-level divergence. The alignment of precipitation anomalies and Kelvin wave low-level divergence/convergence seen in Figure 4.8a suggests that CCKWs play a role in modulating the eastward propagating precipitation signal.

The relationship between precipitation in various sub-regions in WEA and the Kelvin wave divergence over lag -3 to lag +4 was also analysed. As an example, Figure 4.8b shows the lagged correlation coefficients between area-averaged precipitation anomalies in W9 and grid-point Kelvin wave divergence at 850 hPa over the 16-year period over lag -3 to lag +4. In agreement with Figure 4.8a, 4.8b reveals a signal of a Kelvin wave that progresses into WEA from the Atlantic Ocean and progresses into EEA with a phase speed of 10 m s-1. The pattern seen in Figure 4.8b is in agreement with Mekonnen et al. (2008), who suggested that CCKWs propagate into Africa from the Atlantic Ocean.

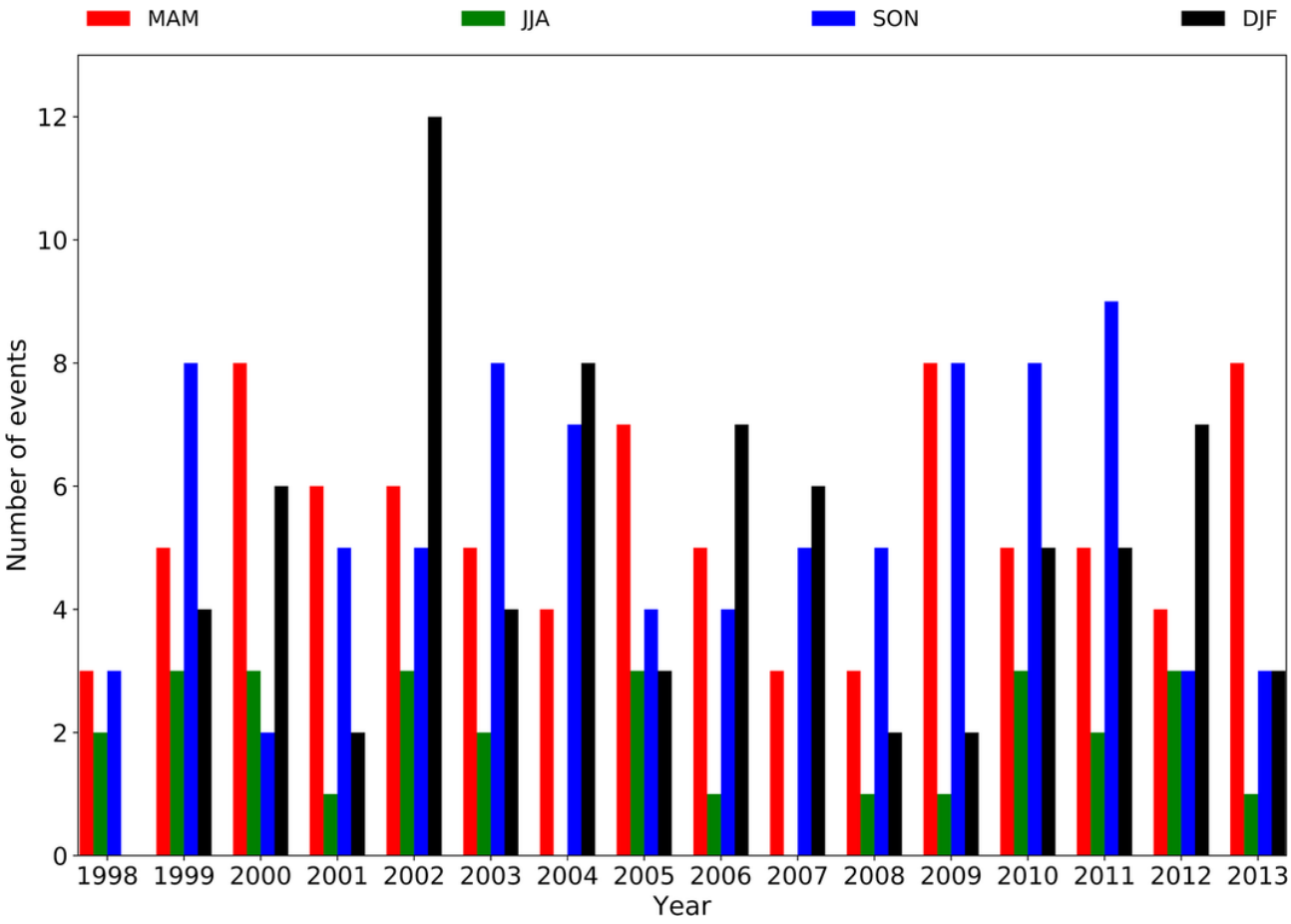

Figure 4.9: Season-to-season variability in the number of precipitation events for W9 – E3

4.6 Isolation of event time indices

A meaningful way of understanding the eastward/northeastward-propagating signal seen in Figures 4.4 and 4.6 is to count the "events" (see above definition) when precipitation exhibits eastward propagation. Figure 4.9 shows the number of events for W9-E3. Similarly, the number of events for other pairs of sub-regions was counted. For W9-E3, the approach identified 87 events during DJF, an average of about 5 events per season; for

W5-E3, a total number of 103 events during MAM were identified, an average of about 6 events per season.

In Figure 4.9, JJA shows the fewest events of any season. This could be because during these months, EEA is generally dry. DJF shows stronger interannual variability in the number of events. Results from calculating the standard deviation either including the outlier in DJF 2002 or replacing it with the mean of events across all DJF seasons indicate that the higher apparent variability in DJF in Figure 4.9 is due to the outlier in DJF 2002 and is otherwise not much higher than in MAM or SON (not shown). Figure 4.9 highlights that events are characterised by a large season-to-season variability. Note that similar figures, but for other pairs of sub-regions, also indicate a similar variability (not shown). Because seasonal precipitation over Equatorial Africa is strongly modulated by the ITCZ (Nicholson, 2018), we speculate that the synoptic-scale systems that modulate these events are likely associated with the ITCZ. For example, during DJF, the ITCZ is in the Southern Hemisphere in a location similar to that of W9, and this coincides with the period when W9-E3 has a higher number of events compared to JJA, when the ITCZ is in the Northern Hemisphere. Similarly, during JJA, when the ITCZ is in the Northern Hemisphere (in proximity with E1), W9-E1 shows a higher number of events (not shown).

4.7 Composite Analysis

Finally, the composite method (averaging over events) is used to investigate the average structure, characteristics and wind regime associated with the precipitation relationship between WEA and EEA. Because previous studies have indicated that the circulation patterns associated with precipitation variability in the different seasons varies markedly (Pohl and Camberlin, 2006a, 2006b), composites based on Equatorial Africa's known wet seasons are calculated. The events were first categorised by season and a composite was calculated only when the total number of events in a given season (MAM and SON, over the 16 year period) exceeded 60. In calculating a composite, day 0 corresponds to the day when wet anomalies exceeded the threshold in the sub-region in WEA, and negatively/positively lagged composites are computed to explore the propagation characteristics of the wet anomalies.

Figure 4.10 (for W9-E3) shows composites of precipitation anomalies and 850 hPa Kelvin wave divergence for MAM (Figure 4.10a-d) and SON (Figure 4.10e-h) over lag 0 to +3. Wet anomalies propagate eastward together with Kelvin wave convergence (dashed contours), while dry anomalies coincide with Kelvin wave divergence (solid contours). In addition, Figure 4.10 shows that Kelvin waves slowdown in EEA. The composites of events over various seasons for different sub-regions indicated a similar structure as that seen in Figure 4.10 (not shown). This Figure is consistent with Figures 4.9 and 4.4 and further highlights the role of CCKWs in modulating the 2-day precipitation connection between WEA and EEA.

Figure 4.11 shows a composite of SON daily precipitation anomalies and 850 hPa horizontal wind anomalies (a similar composite for MAM is shown in Figure 4.12). First, in all panels there is low-level convergence into the region of strong wet anomalies. Second, a wave-like signature is evident: dry anomalies (at $\sim 32^{o}$E) in

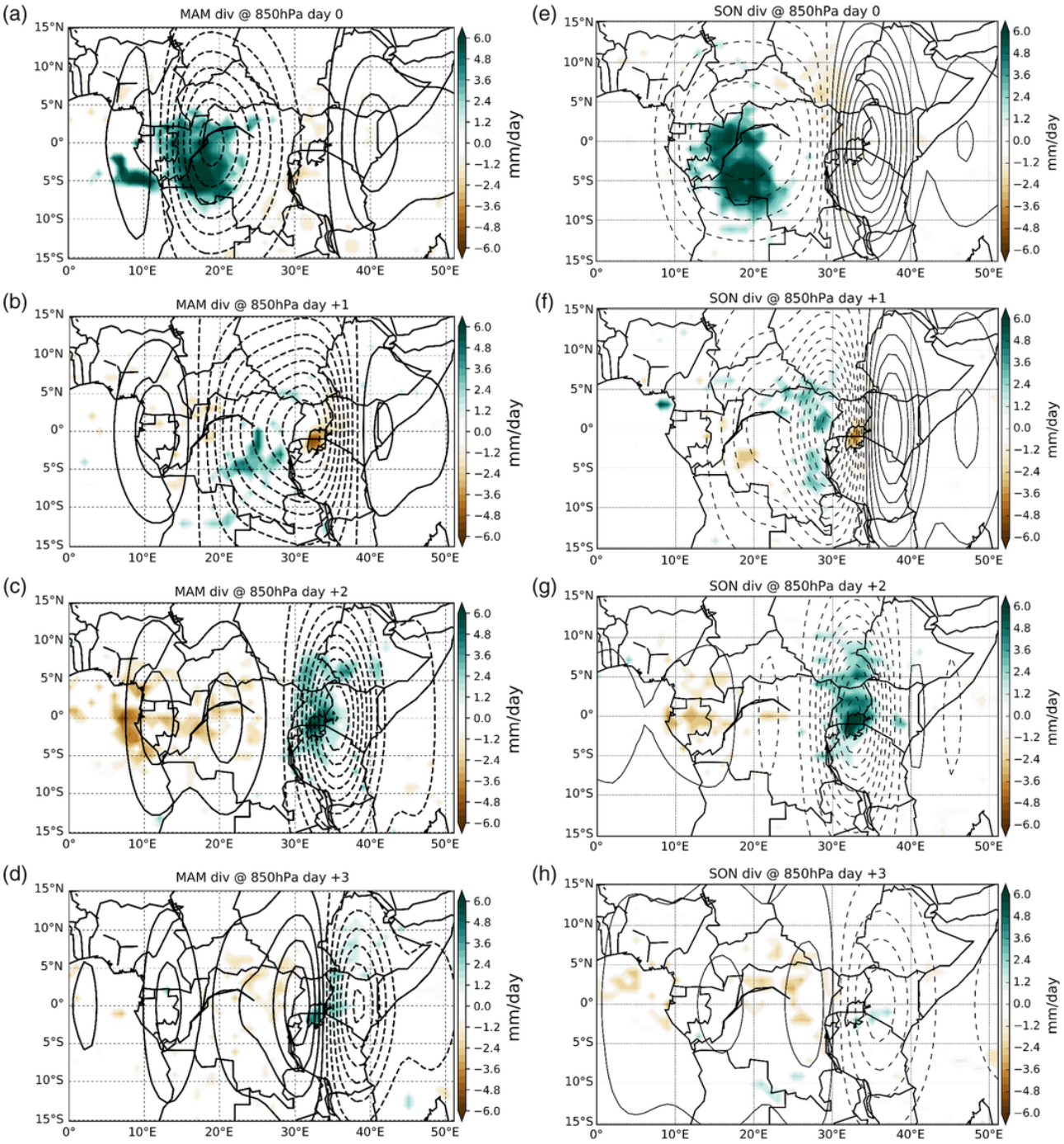

Figure 4.10: Lagged composite of W9-E3 events for (a, b, c, d) MAM and (e, f, g, h) SON for lag 0, +1, +2, and +3, respectively. Precipitation anomalies that are statistically significant at the 95% confidence level are shown. The contour lines show the 850 hPa Kelvin wave divergence (dashed lines negative). Contour line interval is $1.1 \times 10^{-7} S^{-1}$.

Figure 4.11b are just east of wet anomalies (∼25-30°E), and west of this dry anomalies are again seen (∼15-20°E), while further west (∼9°E) weak wet anomalies can be seen. This shows a "dry-wet-dry-wet" pattern, which further highlights the role of a convectively coupled wave in modulating the 1-2 day precipitation linkage between WEA and EEA. This figure also shows anomalous low-level westerly flow west of the positive rainfall anomaly. These anomalous westerlies move eastward on lag +1 and +2, but on lag +3 both the rainfall and wind signal are weak.

Composites of the mean sea level pressure (MSLP) in all seasons indicate that on day -2 and day -1, pos-

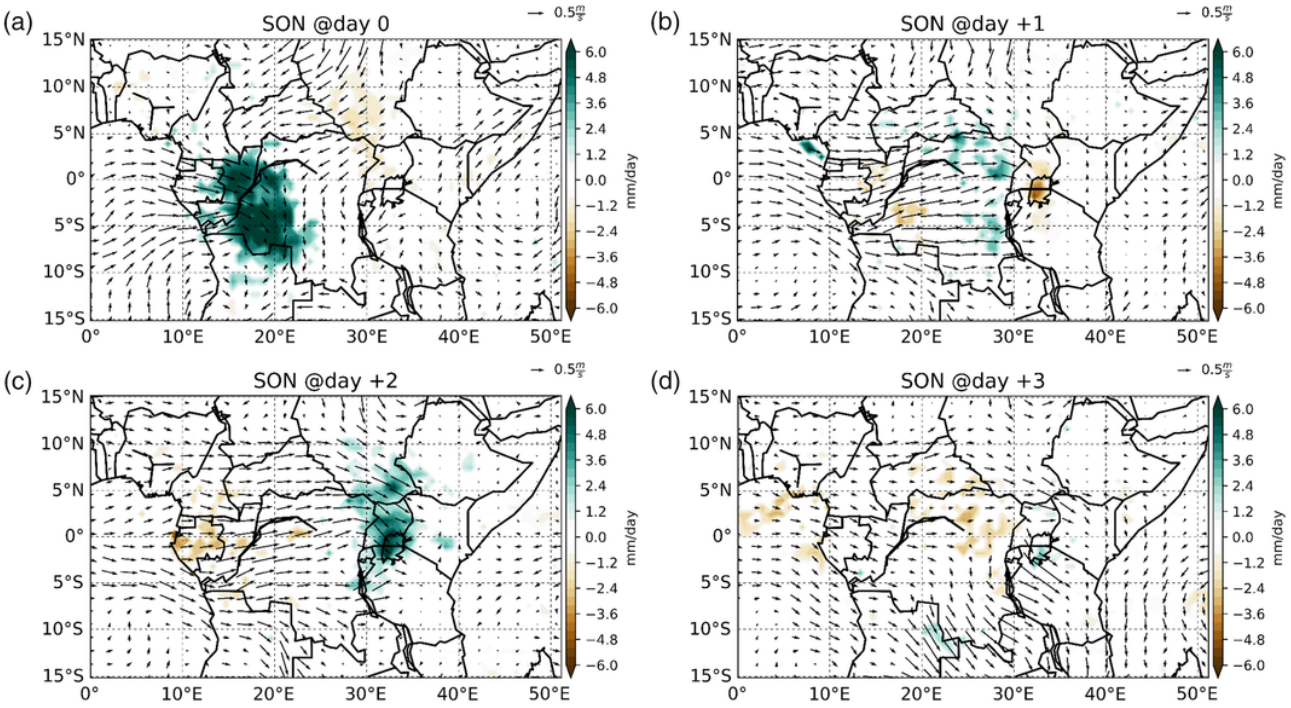

Figure 4.11: Composite of SON daily TRMM precipitation anomalies (shaded) and SON 850 hPa wind anomalies (vectors) on W9-E3 events at (a) day 0, (b) day +1, (c) day +2 and (d) day +3. Only precipitation anomalies that are statistically significant at the 95% confidence level are shown. The wind vectors are plotted regardless of statistical significance.

itive MSLP anomalies dominate the Atlantic Ocean while negative anomalies dominate the Indian Ocean (not shown). The positive MSLP anomalies shift eastward on day 0, +1, +2, +3 and +4. The orientation of the West-East pressure gradient is an indication of a travelling large-scale tropical disturbance. Examining geopotential height, Figure 4.13 shows a composite of MAM daily precipitation anomalies and 850 hPa geopotential height anomalies (SON is shown in Figure 4.14). Positive geopotential height anomalies advance eastward along with the wet anomalies from lag 0 to lag +3. Generally, the positive geopotential anomalies are in phase with the low-level westerly wind anomalies in Figure 4.12. Figure 4.13 provides further evidence of the role of Kelvin waves in modulating precipitation connection between WEA and EEA.

We also use the equatorial wave dataset and a percentile-based threshold to identify days (events) when a CCKW propagates through Equatorial Africa. The threshold is computed from the time series obtained from averaging the Kelvin wave low-level convergence along the central latitude but within the two longitudes of a sub-region (Kelvin wave events were defined only for WEA sub-regions). The Kelvin wave events are identified by selecting all the days on which the Kelvin wave induced low-level convergence is below the k^{th} percentile of the low-level divergence (i.e. above $(100 - k)^{th}$ percentile of convergence). For example, the 90^{th} percentile of Kelvin wave low-level convergence is defined by taking the 10^{th} percentile of low-level divergence (including negative and positive values). Using the 90^{th} percentile as a threshold over W9, for instance, we identified Kelvin wave events and then compared these to the events that were previously identified using the methodology described in section 3.2. The Kelvin wave events were matched to the "Day 0" of the precipitation events, when the precipitation was above the given threshold in the WEA sub-region. Events such as March

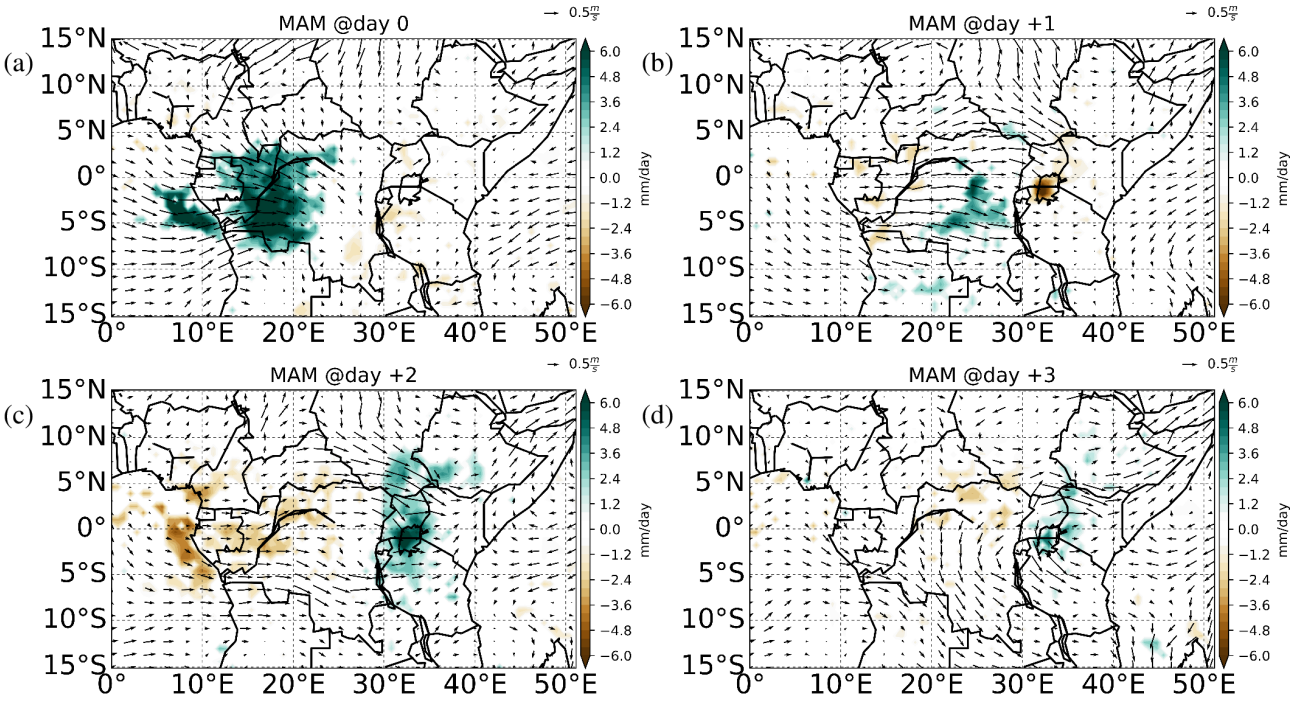

Figure 4.12: As in Figure 4.11 but for MAM

25, April 17 and May 01 (shown in Figure 4.8(a)) showed up as both Kelvin wave and precipitation events. We then calculated the percentage of precipitation events that were also Kelvin wave events and found a 25% and 60% overlap when the 90th and 60th percentile of Kelvin wave convergence is used as a threshold, respectively. This means, for instance, that 60% of the precipitation events identified over all seasons are associated with CCKW low-level convergence greater than the 60th percentile threshold (though this is a fairly weak Kelvin wave threshold, since values below the 50th percentile are divergent). Note that these percentages are higher than those expected purely by chance, which are simply the percentage of all days that are above the two Kelvin wave convergence thresholds (10% and 40% for the 90th and 60th percentile thresholds, respectively). On the other hand, a majority of Kelvin wave events (even defined at the high threshold) are not associated with precipitation events as previously defined, so Kelvin waves are not the only explanation for those events and most Kelvin waves do not cause such events; Chapter 6 looks into possible reasons for this, including event definitions and other possible drivers. Results similar to Figure 4.9, but based on W9's Kelvin wave events, showed that MAM indicated more Kelvin wave events than SON in 12 out of 16 years (not shown).

Figure 4.15 shows a composite of MAM 850 hPa Kelvin wave convergence and the corresponding daily precipitation anomalies for the W9 strong Kelvin wave events (above 90th percentile convergence). It can be seen in Figure 4.15 (similar to Figure 4.10(a-d)) that the Kelvin wave low-level convergence propagates eastward together with a wet signal, reaching EEA two days after its presence in WEA. As noted earlier, the wet signal persists over the Lake Victoria sub-region (E3) on day +3 (and on day +4, not shown). Again, both the Kelvin wave low-level convergence and the wet signal are not seen to coherently progress from central EEA into the Indian Ocean, which suggests a weakening of the CCKW signal as it propagates from WEA into EEA. A composite for SON, but based on CCKW events, was similar to Figure 4.10(e-h) (not shown).

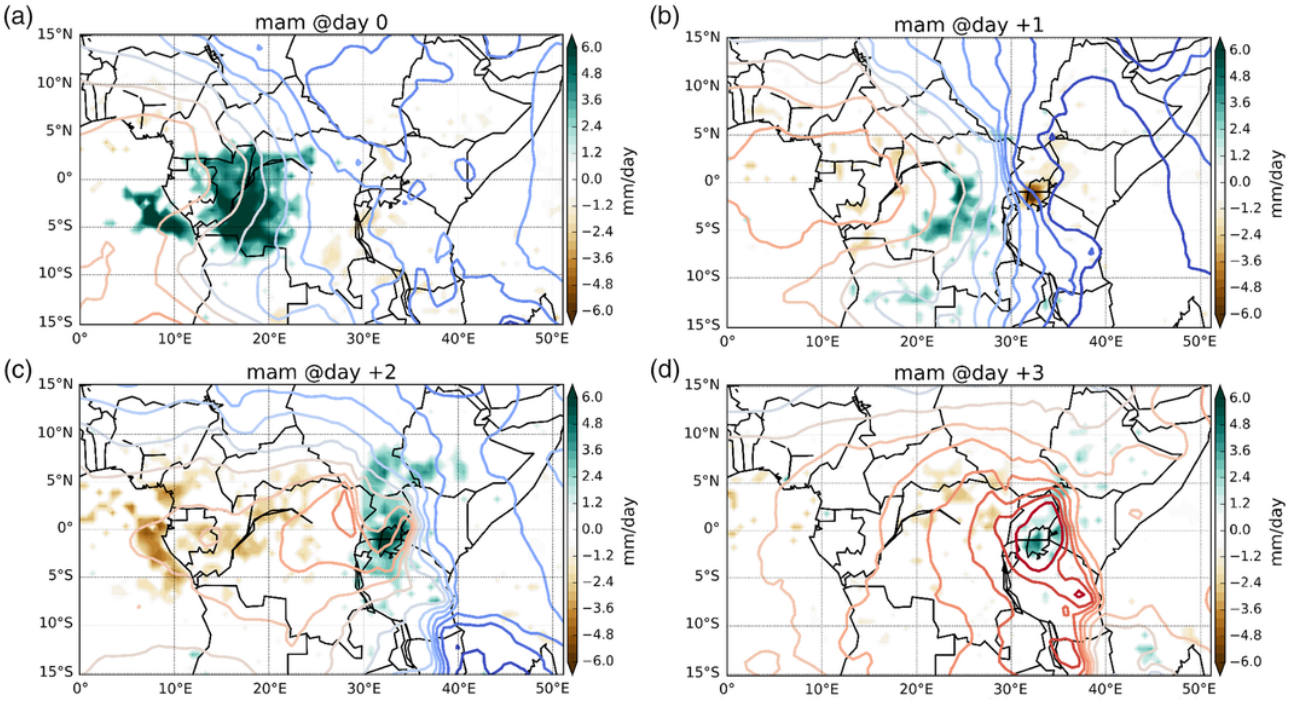

Figure 4.13: Composite of MAM daily TRMM precipitation anomalies (shaded) and MAM 850 hPa geopotential height anomalies (contour lines) for W9-E3 events on (a) day 0, (b) day +1, (c) day +2 and (d) day +3. Only precipitation anomalies that are statistically significant at the 95% confidence level are shown, and warm coloured contours indicate positive geopotential height anomalies while cool-coloured contours correspond to negative anomalies. Contour line interval is 5.0x10^1 geopotential metres (gpm).

It has been suggested that the MJO influences precipitation over sub-regions in EEA (e.g., Pohl and Camberlin, 2006a,b). We investigated whether the events identified in Section 4.6 occur in a preferred MJO phase using the Real-time Multivariate MJO Index RMM1 and RMM2 ((Wheeler and Hendon, 2004)). Our results indicate that the 2-day precipitation relationship may not be dependent on MJO activity, since no particular MJO phase is favourable for the occurrence of the events (not shown).

4.8 Discussion and Conclusions

A synoptic-scale relationship in precipitation between WEA and EEA has been detected and investigated. Lead/lag and spatio-temporal correlation analysis revealed that precipitation in EEA lags precipitation over WEA by 1-2 days. Some sub-regions in central WEA and South Sudan exhibit a synoptic-scale precipitation contrast, suggesting a weak precipitation dipole. Composite analysis shows that CCKWs play a role in facilitating the precipitation connection between WEA and EEA.

The lead/lag and spatio-temporal correlation analysis was performed on sub-regions identified using the EOT algorithm. Daily precipitation anomalies were used in this EOT analysis to objectively identify sub-regions of similar daily precipitation characteristics, rather than relying on a subjective identification. There are some differences between the locations of the various sub-regions identified in this study and those in previous publications, such as Indeje et al. (2000) and Badr et al. (2016). These discrepancies may be due to the method

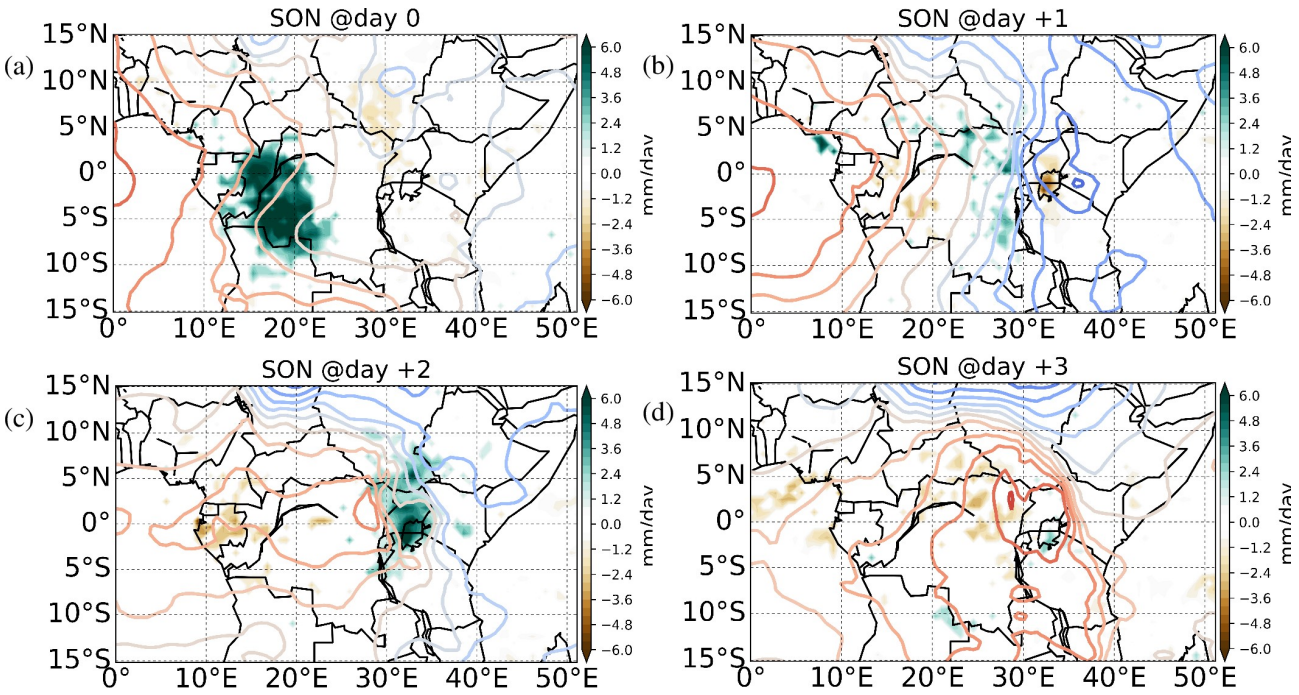

Figure 4.14: As in Figure 4.13 but for SON

and the temporal and spatial resolution of the dataset used (e.g., Nicholson, 2017). As pointed out by Nicholson (2017), the sub-regions that are frequently identified in the literature include Lake Victoria, the highlands and the coastal plains and our approach similarly identified sub-regions over Lake Victoria (E3), coastal areas (E6) and highlands (W17). These results highlight the previously documented spatial heterogeneity of daily precipitation, a result that is consistent with heterogeneity found in pentad (5 days) precipitation variability (e.g., Pohl and Camberlin, 2006a, 2006b).

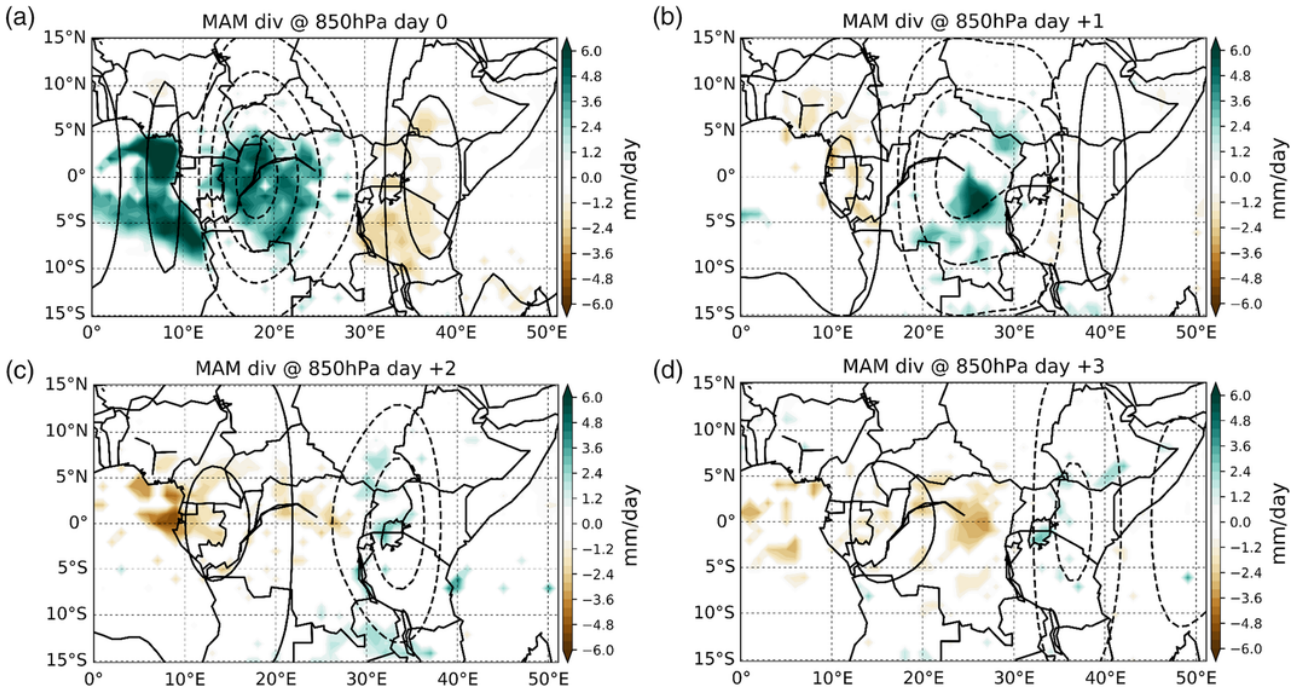

Figure 4.15: Same as Figure 4.10a – d but composite calculated using CCKW events defined for W9. Contour line interval is 6.0 x 10^{-7} s^{1}.

Results from the lead/lag correlation analysis of various pairs of sub-region area-averaged time series of precipitation anomalies indicate statistically significant peak correlation coefficients on day +1 or day +2, suggesting that precipitation over EEA lags that in WEA by 1–2days. It is also seen that the lag at which the correlation coefficient peaks is contingent upon the distance between the sub-regions. For sub-regions that are far apart (e.g., W5 and E3) the correlation coefficient peaks at lag +2, while for the sub-regions that are close to one another (e.g., W14 and E3) the correlation coefficient peaks on lag +1 (e.g., Figure 4.2b). This suggests a coherently propagating synoptic-scale system. We note, however, that the correlation coefficients are quite weak, and this may be explained by the "spotty" (i.e., scattered) nature of precipitation over much of Equatorial Africa. Sumner (1983) found similar weak correlation coefficients in their analysis of daily precipitation in Tanzania.

The propagation characteristics of the synoptic-scale signal highlighted above were investigated using spatio-temporal correlation analysis. The results revealed a coherent eastward/northeastward-propagating signal. The propagation structure of this signal (with an estimated phase speed of about 12 m/s) suggests a role of a large-scale disturbance in modulating the precipitation relationship between WEA and EEA. The speed of propagation closely matches that of CCKWs detected in Mekonnen et al. (2008) and Laing et al. (2011). Another aspect of our results is the weakening or complete decay of the coherent eastward/northeastward signal shown in Figure 4.4d and in composites (e.g., Figures 4.10 and 4.15). The coherent eastward/northeast signal is thus fairly short-lived, which may seem somewhat surprising. However, the propagation characteristics of this signal may be compared to the findings in Liebmann et al. (2009, Figure 1, see discontinuity at about 37^{o}E). Also, our results are in agreement with Mounier et al. (2007), who found that the CCKW footprint is characterized by a weak signature over East Africa. Our analysis also reveals a contrasting signal shown in the patterns between the sub-regions in South Sudan (E1) and central WEA, which can be interpreted as a weak precipitation dipole. This result lends support to Mekonnen and Thorncroft (2016), who proposed a dipole relationship in convective activity between East Africa and the Congo Basin.

The structure of the spatio-temporal correlation patterns for all sub-regions in EEA over lag 0, 1, 2 and 3 (with the exception of E1) was similar to that shown for E3 in Figure 4.6e–f. The persistence of positive correlation coefficients over EEA's sub-regions for lag 0 to 3 may suggest that rainfall over several sub-regions in EEA is particularly influenced by features that do not propagate from WEA but rather persist within EEA. We find this consistent with earlier studies that have suggested the local nature of precipitation over EEA (e.g., Sumner, 1983; Nicholson, 2011). Furthermore, the distinctive spatio-temporal correlation pattern for E1 over lag 0, 1, 2 and 3, while indicative of a weak dipole as mentioned above, does not mean that precipitation over this sub-region is solely driven by eastward/northeastward-propagating features either. Our results indicate that a comprehensive understanding of drivers of daily to synoptic-scale variability in precipitation requires that small sub-regions need to be considered separately.

The identification of events in each season allowed a further investigation into factors modulating the 1–2

days precipitation connection. There are an average of six events per year for W5–E3 in MAM and five events for W9–E3 in DJF. These numbers closely match the 6–7 CCKWs that propagate through the Congo basin during March–June according to previous studies (e.g., Sinclaire et al., 2015). Wheeler and Nguyen (2015, Figure 7) found an average of 5 CCKWs per boreal spring season, a result that is also consistent with our results.

The structure of the anomalous wind and the associated precipitation anomalies seen in Figure 4.11 resembles the observed Kelvin wave signature seen in Wheeler and Nguyen (2015, Figure 7). We used a novel equatorial wave dataset to find evidence of alignment of the eastward propagating precipitation anomalies and Kelvin wave convergence. The collocation of wet anomalies and Kelvin Wave convergence is evident in a time-longitude plot (Figure 4.8a) and composites (Figures 4.10, 4.11, 4.15). As shown in Wheeler and Nguyen (2015), it is also seen here that anomalous westerly flow and wet anomalies in Figure 4.11 are in phase with the positive geopotential height anomalies in Figure 4.13. The association between the anomalous westerly flow and the wet signal shown here (e.g., Figure 4.11c) is consistent with results from Finney et al. (2019). We also show that as the eastward propagating wet signal becomes weaker, so does the dynamical signature of the CCKWs. This confirms the role of CCKWs in facilitating the 1–2 days precipitation connection between WEA and EEA in most seasons, more particularly during MAM and SON.

Overall, composites on Kelvin wave convergence in Figure 4.15 confirms that CCKWs play a role in modulating precipitation linkage between WEA and EEA, although not all precipitation events are linked to Kelvin wave events, and most Kelvin wave events do not cause precipitation events; Chapters 5 and 6 undertakes further investigations on these definitions and mechanisms. Finally, over the 16-year period, Kelvin wave event numbers in MAM in each year were greater than those in SON of the same year in 75% of the period. This is consistent with the relatively stronger wet signal and the associated Kelvin wave induced convergence in Figures 4.10d and 4.15d, compared to the corresponding SON composite (Figure 4.10h). This result also appears to be consistent with the predominant occurrence of Kelvin waves found during boreal spring (e.g., Roundy and Frank, 2004).

Work in this chapter has shown that Kelvin waves play a role in the eastward propagation of precipitation. Chapter 5 uses a state-of-the-art high resolution simulation from a convection permitting regional climate model, a coarse global model, observed precipitation and reanalysis fields to investigate the physical mechanisms through which Kelvin waves influence the eastward propagation of precipitation.

Chapter 5

Linking Equatorial African precipitation to Kelvin wave processes in the CP4A

5.1 Purpose of the chapter

This chapter addresses the third thesis objective (§2.7): that is, to assess how well a state-of-the-art convection permitting model reproduces observational results in objectives (1) and (2), and to use this simulation as a "virtual laboratory" to further explore the physical mechanisms.

Work in chapter 4 found that Kelvin waves play a role in the synoptic-scale precipitation linkage between WEA and EEA. An extension of these results is, for example, (a) to investigate whether the eastward propagation of the precipitation signal is present in climate model simulations, (b) to probe the major structures of circulation anomalies associated with the interaction between CCKWs and the eastward propagating precipitation anomalies over Equatorial Africa, (c) to examine how the interaction between the eastward propagating CCKWs and the moisture field evolves in space and time across Equatorial Africa, and (d) to evaluate how well these interactions are captured in convection permitting regional climate and global models. To address these aspects, this chapter examines observations (3.2.1), reanalysis (3.2.3), a coarse global simulation (3.2.4.1), and a brand-new high resolution simulation from a convection permitting regional climate model (3.2.4.2).

Detailed examination of the observed and simulated dynamics involved in the coupling between CCKWs and precipitation over Equatorial Africa are uncommon. Nevertheless, there are some publications that have studied Kelvin waves (both wet and dry phase) over some regions in Africa (e.g., Nguyen and Duvel, 2008; Mekonnen et al., 2008; Mekonnen and Thorncroft, 2016; Schlueter et al., 2019) or Africa as a whole (e.g., Jackson et al., 2019). The conclusions from these studies are diverse but all echo the importance of CCKWs for synoptic-scale precipitation variability. For example, Jackson et al. (2019) attributed about 15% of variance in daily mean precipitation during April over some areas in EEA to CCKWs.

Wheeler and Nguyen (2015) pointed out that through monitoring African Kelvin waves, convective rainfall events can be predicted several days before occurrence. Recent work in Yang et al. (2021) suggested that recent numerical weather prediction models have some skill in predicting Kelvin waves. Despite the role of CCKWs in influencing Equatorial Africa's convection and precipitation (e.g., Nguyen and Duvel, 2008; Laing et al., 2011; Mekonnen and Thorncroft, 2016), the mechanisms through which CCKWs connect precipitation in WEA to that in EEA remain largely unclear. A thorough understanding of the physical mechanisms through which CCKWs influence the west-east propagation of precipitation across Equatorial Africa is an important step toward improving synoptic timescale forecasting.

The rest of this chapter is structured as follows. Section 5.2 highlights the methodology used in this chapter. In Section 5.3, the simulated precipitation anomalies are used to identify the small sub-regions that are characterised by similar daily precipitation characteristics. Section 5.4 displays the Kelvin wave activity obtained from the simulated equatorial wave dataset. An index based on Kelvin wave low-level divergence is developed, and used to analyse the eastward propagation of the simulated precipitation (§5.5), and the moisture field (§5.6). Section 5.7 focuses on the vertical structure of various fields associate with the propagation of CCKWs across Equatorial Africa and also includes a discussion on the interaction between the CCKW and the East African Highlands (§5.7.3) and the energetics associated with propagation of the CCKW across Equatorial Africa (§5.7.4). Finally, the discussion and the conclusions of this chapter are presented in section 5.8.

5.2 Methodology

The technique used to identify the small sub-regions based on simulated precipitation is similar to that described in chapters 3 and 4. The sub-regions identified are used as reference sub-regions for computing time lagged correlation coefficients and composites. The methodology used to generate a simulated equatorial wave dataset is given in chapter 3. In this chapter, all other analyses, anomalies on 1^{o} x 1^{o} are used for a period of 9 years (1998 - 2006).

5.3 Sub-region identification and the eastward propagating signal in observed and simulated precipitation

Results from subjecting the 9 year daily precipitation anomalies from TRMM and both simulations to an EOT algorithm show that while there are differences in the location of the sub-regions identified by TRMM and the simulated precipitation based sub-regions, there are several overlaps. For example, both CP4A and G25 identified a sub-region contained within 9^{o}S-3^{o}S, 16^{o}E-21^{o}E and also 4^{o}S-2^{o}N, 31^{o}E-36^{o}E (see Figure 5.1). These sub-regions are in correspondence with W9 and E3 in chapter 4 (Figure 4.1). As an example, a pair (green for WEA and brown for EEA) of sub-regions identified by an EOT algorithm is shown in top panels of Figure 5.1. Chapter 4 used 16 years of observed daily precipitation anomalies and identified 17 and 8 sub-

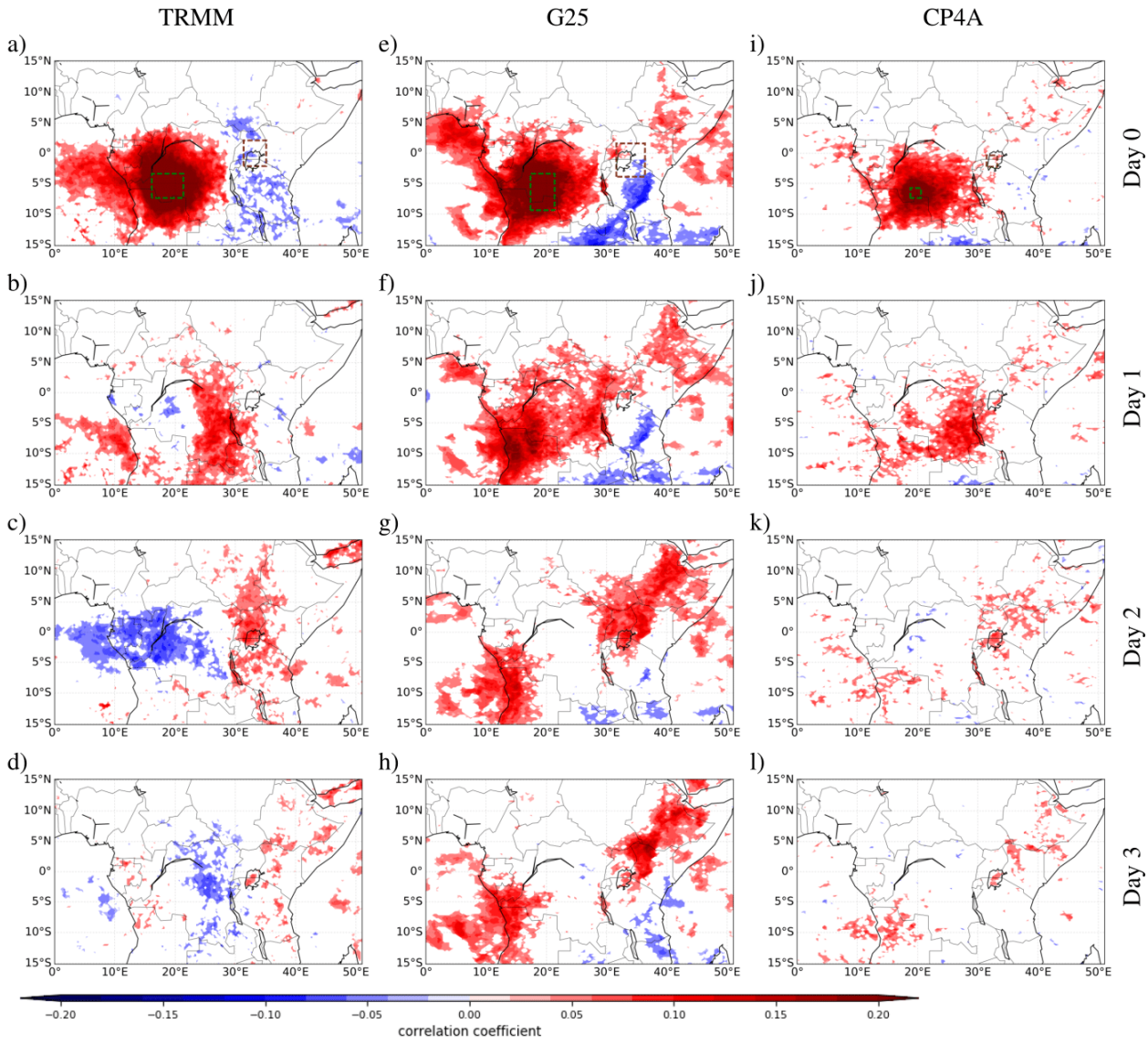

Figure 5.1: Lagged correlation coefficients between respective sub-region's (dashed green box in the top panels) area average time series and every grid point for (a)-(d) TRMM, (e)-(h) G25 and (i)-(l) CP4A based on 9 years of daily precipitation anomalies. The lags for which the correlation coefficients are calculated are shown on the right of each row. Correlation coefficients are calculated regardless of season and the shading shows the correlation coefficients that are statistically significant at 95% confidence level.

regions of similar daily precipitation characteristics in WEA and EEA respectively (see Figure 4.1). Recall that chapter 4 presented correlation coefficients for each sub-region in WEA with every sub-region in EEA and identified a sub-region in WEA (7°S-3°S, 16°-21°E) as a sub-region that indicated the strongest correlation coefficient with the highest number of sub-regions in EEA. It was shown that the pair of sub-regions (W9 and E3 in Figure 4.1) best demonstrated the 1-2 day relationship in precipitation between WEA and EEA. The pair of sub-regions used in this chapter (green and brown box in Figure 5.1) are in similar locations as W9 and E3 in Figure 4.1. So, a sub-region in WEA (green box) in each dataset is used as a sub-region of reference in the spatio-temporal correlation coefficient analysis and the subsequent composite analysis.

One way of assessing the characteristics of a propagating feature is to undertake spatio-temporal correlation coefficient analysis. Figure 5.1 shows the spatio-temporal correlation coefficient between area averaged

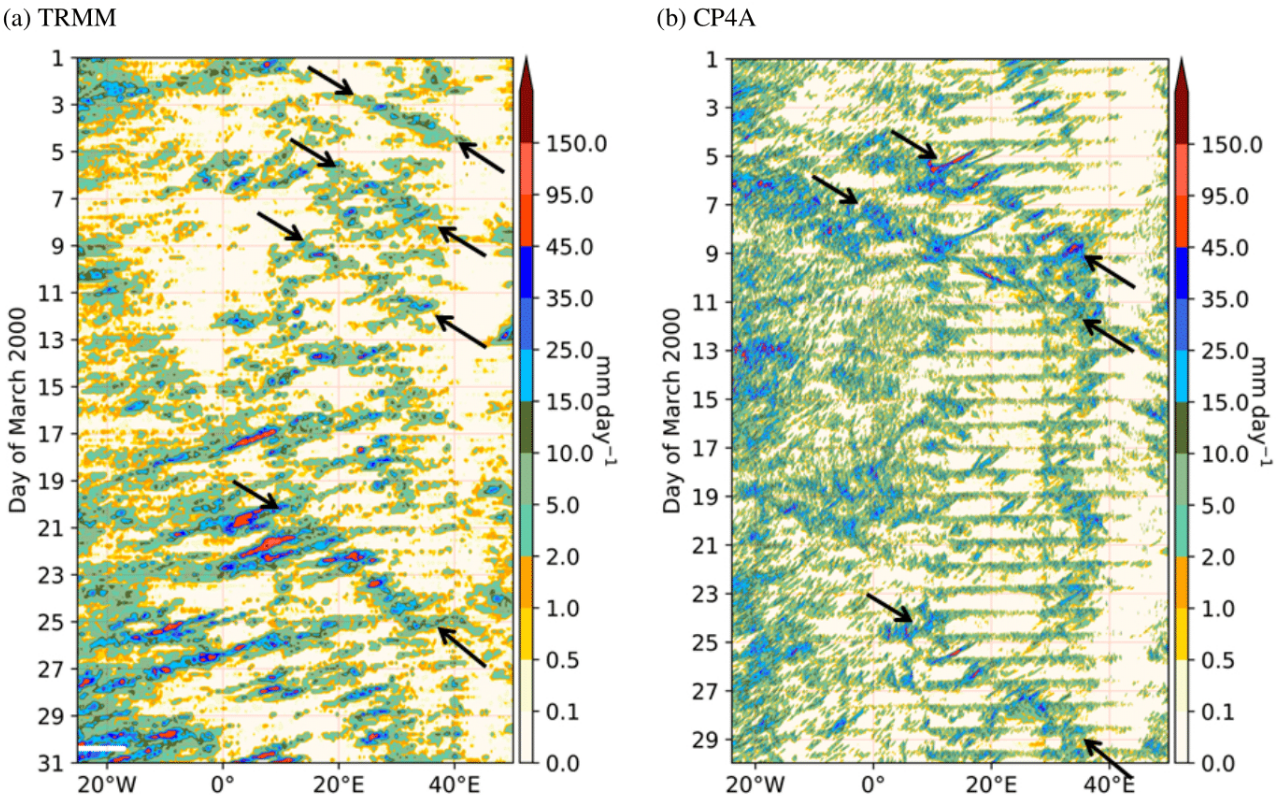

Figure 5.2: Time-longitude section for (a) TRMM 3-hourly precipitation rate (b) CP4 hourly precipitation rate. Both (a) and (b) are extracted from year 2000 and latitudinally averaged over 7°S-7°N. The black arrows highlight the eastward propagating precipitation.

time series over the sub-region in WEA (green dashed box) and every grid point in the domain. Day 0 for each data set is shown in the top row and the rest of the lagged sequence at which correlation coefficients are computed increase downwards for each column. In computing the correlation coefficients, the area average time series over the sub-region in WEA (green dashed box) is correlated with the time series of the daily precipitation anomalies at each grid-point, $P_{i,j}$ (i=latitude, j=longitude) and then, the time series of each grid-point is shifted so that the sub-region's time series lags the grid point time series by a day at a time. These correlation coefficients are calculated regardless of season and is not conditioned to any propagating tropical disturbance. One sees in Figure 5.1a-d a coherent eastward propagating signal that has a speed of approximately 7-8° per day (9 - 10 m s^{-1}). For day 1 (Figure 5.1b), the positive correlation signal has shifted east and is centered approximately halfway between where it was located on day 0 and EEA. By day 2 (Figure 5.1c), the positive correlation signal is seen over EEA while a negative correlation signal dominates WEA and by day 3 (Figure 5.1d), the positive correlation signal becomes weak and no clear coherent eastward progression is seen. This correlation coefficient pattern (Figure 5.1a-d) based on 9 years of daily precipitation anomalies is similar to that shown in Figure 4.1, based on 16 years of TRMM)

Looking at Figures 5.1e-h and i-l, an eastward propagating signal depicted in TRMM (Figure 5.1a-d) is generally present in the simulated precipitation anomalies. However, from day 0 to day 2 (i.e., Figure 5.1e-g) while an eastward shift of positive correlation coefficients can be seen, a reversal of the signal over WEA is

not seen. Further differences can also be seen in subsequent days. The propagation speed of the eastward propagating signal in the simulations is not remarkably different from that in the observations. Overall, the results in Figure 5.1 indicate that, generally, the eastward propagating signal is detectable in the simulated precipitation anomalies as seen in the observations. The sensitivity of the correlation coefficient pattern to the dimensions of the sub-region was tested by repeating the same analysis but using an identical sub-region from TRMM onto the simulated precipitation anomalies and the results were similar (not shown). The generally weak correlation coefficients seen in Figures 5.1 are not surprising because small spatial and temporal scales affect the strength of individual correlation coefficient. Because these correlation coefficients are statistically significant and spatially coherent signals provides confidence to our results.

To further investigate the eastward propagating signal in the simulated precipitation, Hovmöller plots of CP4A's total precipitation (Figure 5.2) showed eastward propagating wet episodes that are similar to those in TRMM (e.g., see Figure 4.8), a result that is consistent with the eastward propagation correlation coefficient signal shown in Figure 5.1i-l. Additionally, these plots also showed a strong diurnal cycle and multiple westward propagating episodes (presumably organised mesoscale convective systems) within envelopes of the eastward propagating wet signal. The time-longitude plots for precipitation over selected periods (Figure 5.2) were similar to that shown in Stratton et al.. (2018; their Fig.9a). The eastward propagating signal shown in Figure 5.1 may be compared to the eastward propagating convective signal shown in Dunkerton and Crum (1995) and the eastward propagating wet signal shown in Stratton et al. (2018).

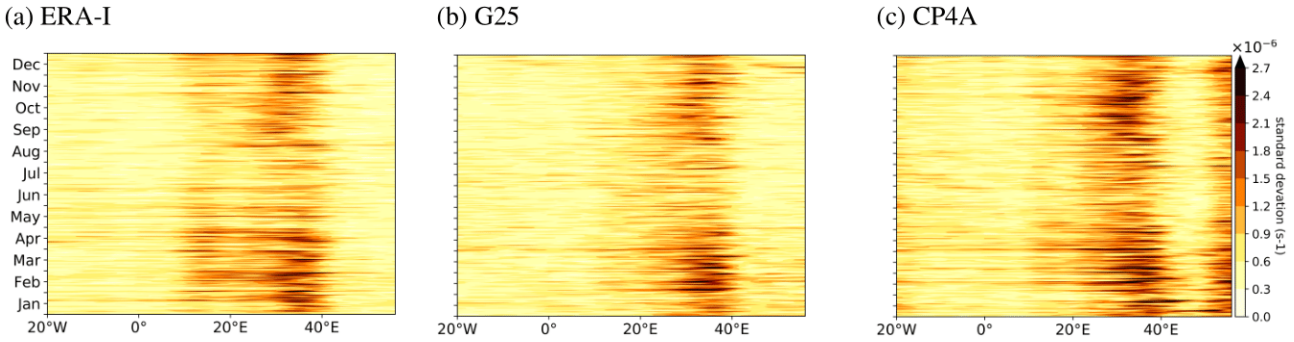

Figure 5.3: The seasonal cycle of Kelvin wave activity for (a) ERA-I (b) G25 and (c) CP4A as depicted by standard deviation of Kelvin wave 850 hPa divergence for 1998-2006. Kelvin wave divergence is latitudinally averaged over 7°S-7°N before calculating the standard deviation.

5.4 Kelvin wave activity

An overall picture of the Kelvin wave activity over equatorial Africa is shown in a climatological time-longitude plot of the standard deviation of Kelvin wave divergence in Figure 5.3. In this figure and other cross-sections, the field(s) are averaged in the latitudinal band 7°about the equator. This averaging range is informed by two aspects. First, Kiladis et al. (2009) showed that strongest signal of Kelvin waves is confined within a latitudinal belt of $\sim \pm 10^{o}$ about the equator (see their Figure 5a). Second, the previous chapter analysed the west-east precipitation linkage using sub-regions confined within $\sim \pm 7^{o}$ about the equator. In both ERA-I and

model simulations, the first peak of Kelvin wave activity is seen between January-May and the second between September-December. Weak Kelvin wave activity can be seen in relatively dry months (June-August) in both ERA-I and model simulations. In Figure 5.3, the simulated results are in agreement with those in ERA-I in the sense that there is a signal of Kelvin waves activity over equatorial Africa all year round. Both simulations reasonably capture the overall magnitude of the Kelvin wave activity in ERA-I (Figure 5.3a).

In terms of the spatial distribution, there are visible differences between ERA-I (Figure 5.3a) and the simulated Kelvin wave activity (Figure 5.3b and c). For example, Kelvin wave activity in ERA-I shows two longitudinal peaks, a weak peak between 10^{o}E - 20^{o}E and a strong peak between 30^{o}E - 40^{o}E. Both simulations capture the peak Kelvin wave activity between 30^{o}E - 40^{o}E but their peak activity between 10^{o}E - 20^{o}E is weaker than that in ERA-I. Unlike ERA-I and G25, CP4A (Figure 5.3c) shows a strong Kelvin wave activity east of about 50^{o}E. This might be due to the presence of the lateral boundary in this model. More generally, the reasons for an underactive Kelvin wave between 10^{o}E - 20^{o}E in both simulations and an overactive Kelvin wave over the Indian Ocean in CP4A remain unclear and beyond the scope of the current study. On comparing the Kelvin wave activity in stitched CP4A (Figure 5.3c) with that in the complete tropical belt in ERA-I (Figure 5.3a) and G25 (Figure 5.3b), it is likely that the stitching had a negligible impact on the coherent propagation of Kelvin wave signal. This is plausible because Kelvin waves are large-scale features and may not be significantly influenced by stitching of the data sets as described in section 2 above.

5.5 Eastward propagation of observed and simulated precipitation

Figure 5.4 shows a composite of precipitation anomalies on high amplitude Kelvin wave events of several fields. In both observations (Figure 5.4a-e) and simulations (Figure 5.4f-j,k-o), the eastward propagation of positive precipitation anomalies in association with anomalous low-level moisture flux convergence can be seen. Just like in observations, the simulated positive precipitation anomalies and anomalous low-level convergence propagate eastward in association with simulated Kelvin wave convergence (e.g., Figure 5.4f-j,k-o). As seen in previous observational studies, positive precipitation anomalies are in phase with anomalous low-level westerlies (e.g., Yang et al.. 2007; Yang et al.. 2009). Figure 5.4 provides evidence that the eastward propagation of precipitation is well represented in both simulations, and the connection between the simulated precipitation anomalies and Kelvin wave convergence is well captured. While the wind field in G25 is comparable to that in ERA-I, its precipitation signal is generally weak across the entire 5-day sequence, highlighting the likelihood of a weak interaction between the convection and large-scale circulation associated with Kelvin waves in G25 as seen in other studies of coarse global models (e.g., Yang et al., 2009). Although they did not focus on the role of Kelvin waves in modulating precipitation, Finney et al. (2020) also found that days with anomalous westerly flow experienced enhanced precipitation over EEA. In Figure 5.4a-e, the Kelvin wave divergence is well aligned with the negative precipitation anomalies however, the negative precipitation anomalies are generally missing in both simulations especially G25. It remains unclear why the suppressed convection is poorly

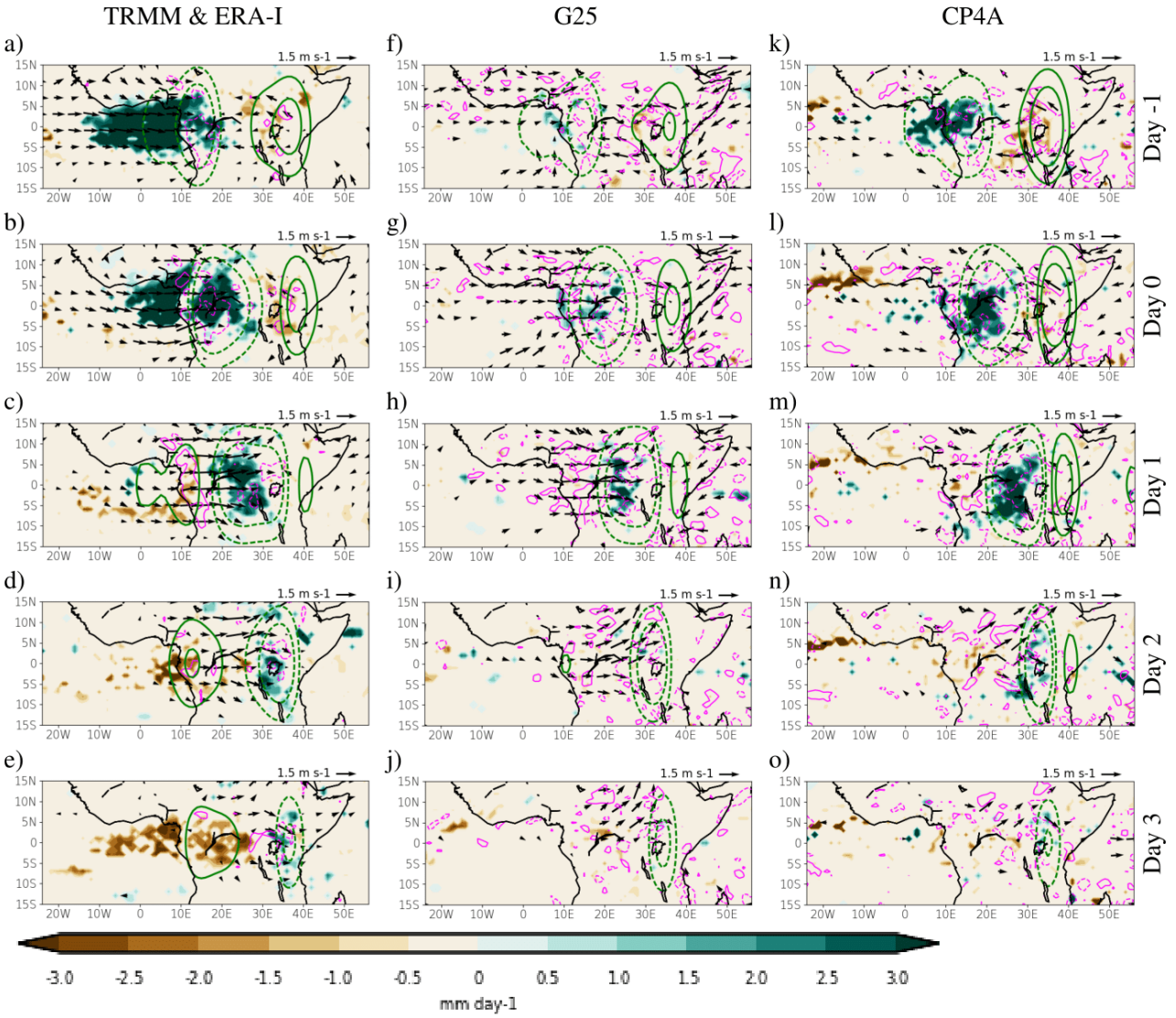

Figure 5.4: The lagged high-amplitude Kelvin wave event composite for (a-e) TRMM and ERA-I, (f-j) G25 and (k-o) CP4A, showing Kelvin wave low-level convergence (green dashed contours) and divergence (green solid contours), daily precipitation anomalies (shading), and 850 hPa wind anomalies (vectors). The lags for which a composite was computed are shown on the right of each row. Precipitation anomalies (shading) are plotted if statistically significant at 95% confidence level. Contour interval for divergence is 4 x 10^{-7} s^{-1} and wind vectors are plotted if zonal or meridional component is statistically significant at 95% confidence level. 850 hPa moisture flux divergence is shown with thin magenta contours (solid is divergence, dashed is convergence). Only the -2 x 10^{-8} and 2 x 10^{-8} kg kg^{-1} s^{-1} contours are shown.

simulated.

5.6 The horizontal moisture flux and propagation of Convectively Coupled Kelvin Waves (CCKWs) over Equatorial Africa

To gain insight into the sources of moisture associated with the anomalous precipitation signal in Figure 5.4, Figure 5.5 shows a lagged composite of anomalous horizontal moisture flux and evolution of CCKW activity at 850 hPa. Figure 5.5a and 5.5b, 5.5f and 5.5g, 5.5k and 5.5l show the horizontal wind structure that is broadly in agreement with the theoretically predicted structure for a Kelvin wave shown in Gill (1980).

ERA-I (Figure 5.5a-e) displays a coherent eastward propagating moisture flux with the propagation speed consistent with that shown in Figure 5.1. Recall that Figure 5.1 is based on precipitation without any conditioning to Kelvin wave events. In essence, Figure 5.1 and 5.5 are based on independent analysis methods but exhibit agreement. Also shown in Figure 5.5 is that the leading edge of the moisture flux is collocated with the Kelvin wave convergence. A day before day 0 (Figure 5.5a) anomalous moisture flux is seen over the Atlantic ocean and this is followed by low-level westerly anomalies appearing to strengthen between day -1 and day 1. This anomalous westerly flow is seen to advance eastward together with the Kelvin wave convergence and the positive anomalous zonal moisture flux. By days 2 and 3 (Figure 5.5d and e), an anomalous magnitude of moisture flux, the low-level anomalous westerly flow and the Kelvin wave convergence can be seen over EEA but all these fields have waned. This result (e.g., Figure 5.5a-e) suggests that CCKWs modulate low-level moisture flux through anomalous low-level westerly flow.

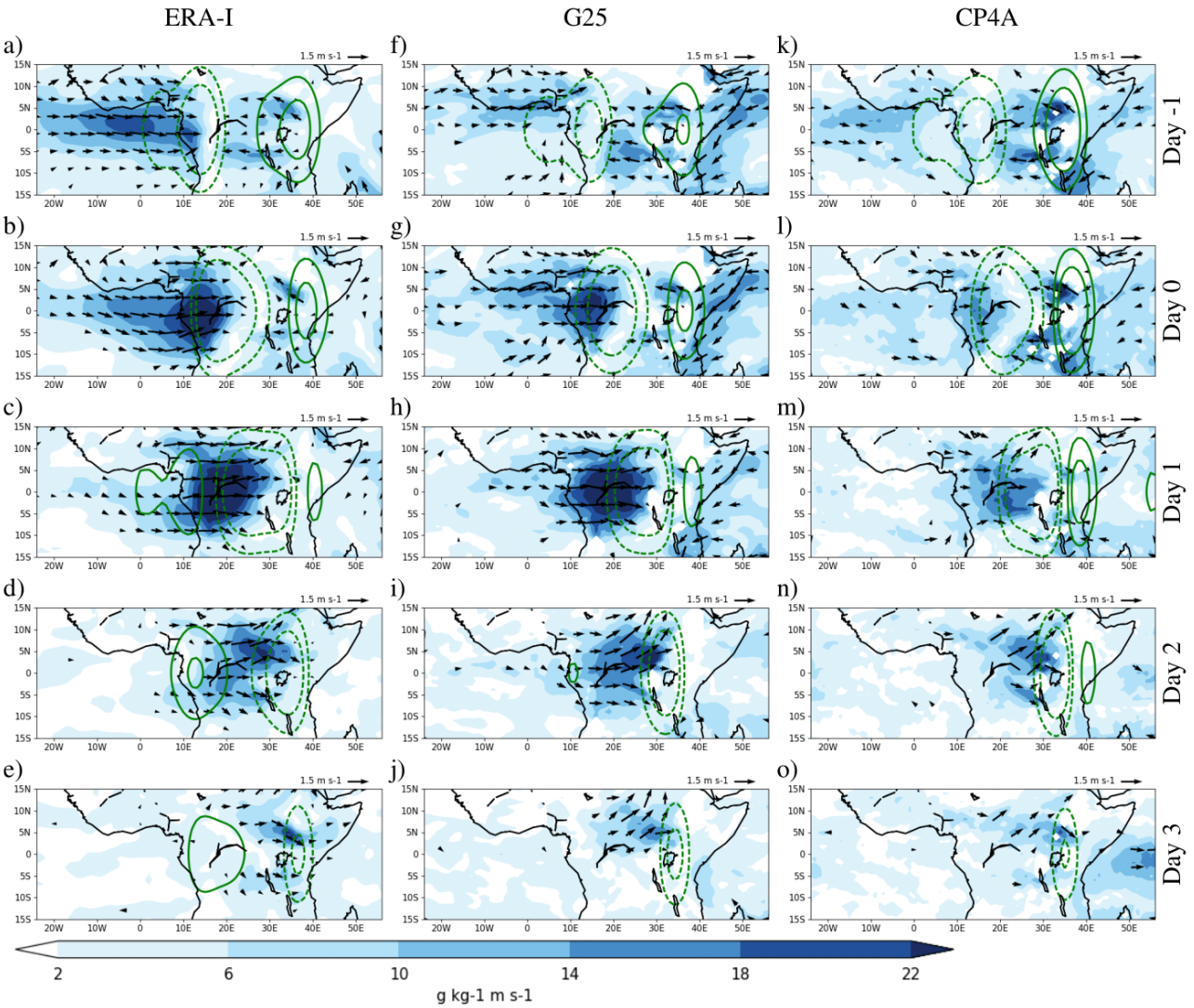

Figure 5.5: The 850 hPa lagged high-amplitude Kelvin wave event composite for (a-e) ERA-I, (f-j) G25 and (k-o) CP4A, Kelvin wave low-level convergence (green dashed contours) and divergence (green solid contours), magnitude of the anomalous 850 hPa horizontal moisture flux (shaded) and 850 hPa wind anomalies (vectors). The lags for which a composite was computed are shown on the right of each row. Contour interval for divergence is 4 x 10^{-7} s^{-1} and wind vectors are plotted if zonal or meridional component is statistically significant at 95% confidence level. Reference wind is shown at the top right of each panel.

Comparing the two simulations to ERA-I, one sees that the horizontal structure of the evolution of the Kelvin waves in G25 (Figure 5.5f-j) is in some aspects similar to that of ERA-I (Figure 5.5a-e). For example, from day -1 through to day 3, the Kelvin wave convergence is located on the leading edge of the low-level westerly anomalies (vectors) as seen in ERA-I. Also, for G25, the anomalous low-level westerly flow and Kelvin wave convergence appear to weaken on day 2 and 3, a similar evolution can be seen in ERA-I. One key difference between ERA-I and G25 can be seen in Figure 5.5a and f, in which the the magnitude of the moisture flux in G25 (Figure 5.5f) is considerably weaker than that in ERA-I (Figure 5.5a). The other difference that is easily noticeable is that G25 shows a relatively stronger low-level anomalous easterly moisture flux particularly from day -1 to day 1 that extends into the Indian Ocean. The easterly moisture flux anomalies seen in Figure 5.5f-j may be linked to the persistent positive correlation coefficients in simulated precipitation anomalies seen over EEA in Figure 5.1e-h. Although CP4A (Figure 5.5k-o) shows the eastward propagating zonal moisture anomalies that are collocated with eastward moving low-level Kelvin wave convergence, the magnitudes of all the fields are weaker and not as smooth as those in ERA-I and G25. However, CP4A shows anomalous easterly moisture flux that is quantitatively in better agreement to ERA-I than the G25. Figure 5.5 suggests that both simulations reasonably simulate the Kelvin wave low-level convergence and its eastward propagation phase speed. Easily noticeable is that CP4A shows weaker moisture flux in Figure 5.5 but stronger precipitation anomalies in Figure 5.4. One possible reason for this mismatch might be that the few storms formed in association with the weak moisture flux in CP4A are too intense compared to those in TRMM (Crook et al., 2019).

Percentiles (Kelvin conv threshold)	**TRMM (16 year period)**	**TRMM**	**G25**	**CP4A**
95	18.8	23.6	12.5	10.8
90	32.9	40.0	16.7	21.6
85	44.7	45.5	16.7	35.1
80	51.8	47.3	29.2	43.2
75	55.3	49.1	33.3	45.9
70	56.5	49.1	37.5	56.8
65	57.6	49.1	45.8	62.2
60	61.2	52.7	45.8	62.2

Table 5.1: Percentage of precipitation events that are also Kelvin wave events in MAM based on exceedance of a particular threshold of low-level Kelvin wave convergence for TRMM, G25 and CP4A. A 16 year period (1998-2013) was used for events in the second column while a 9 year period (1998-2006) was used for the three columns on the right.

Table 5.1 provides an insight on whether the precipitation events (as defined above) are linked to the corresponding Kelvin wave events. Results show that over a period of 9 years, about 53%, 46% and 62% of the precipitation events during MAM match Kelvin wave events with amplitude above the 60^{th} percentile of the Kelvin wave low-level convergence in ERA, G25 and CP4A respectively. Statistically, for the 60^{th} percentile threshold, the aforementioned percentages would be expected to be only 40% if the match between precipitation events and Kelvin wave events were purely due to random chance (ignoring any possible effects

of event clustering). This result suggests that the association between the precipitation events and the Kelvin waves is larger than random chance. In a similar vein, Table 5.1 suggests a significant number of precipitation events are not related to Kelvin wave events. These are not the focus of the rest of this study but would be a topic to explore in future work.

In comparison with TRMM and CP4A, except for the 95^{th} percentile, G25 (third column in Table 5.1) shows the lowest number of precipitation events that are also Kelvin wave events. This may be due to the weak interaction between the Kelvin wave dynamics and the precipitation in G25 (implied by the inconsistency between the wind field and the precipitation anomalies in Figure 5.4). It is possible that the explicit representation of convection in CP4A might have helped in the coupling between the Kelvin waves and the precipitation. To assess the robustness of the results, we looked at the number of precipitation events in TRMM that are also Kelvin wave events in the same season but over a 16 year period (see second column in Table 5.1). As shown in Table 5.1, the results over the 16 year period are generally consistent with those over the 9 year period.

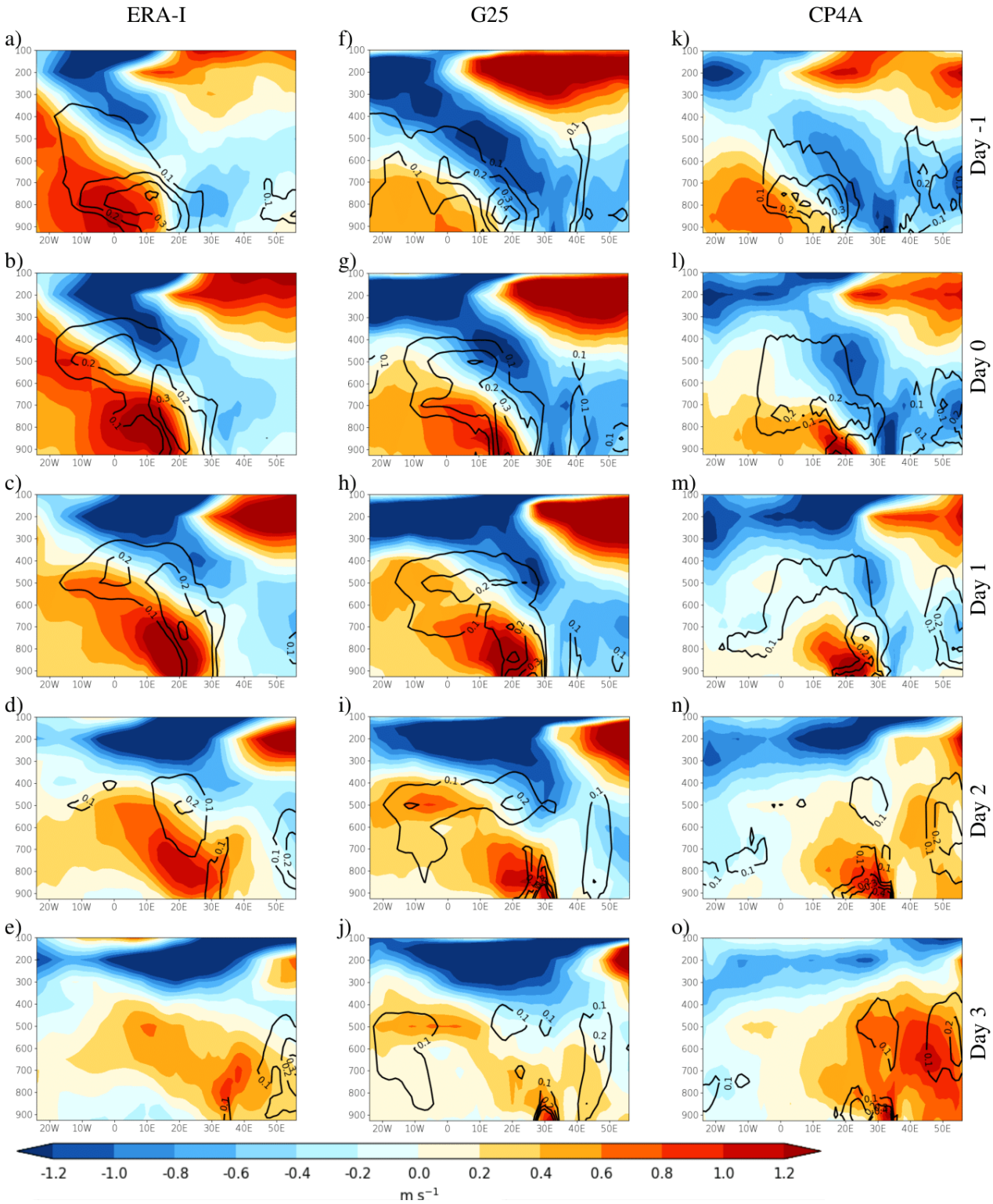

Figure 5.6: Lagged height-longitude high-amplitude Kelvin wave event composite for anomalous zonal wind (shaded) and specific humidity (black contours) for (a-e) TRMM and ERA-I, (f-j) G25 and (k-o) CP4A. The lags for which a composite was computed are shown on the right of each row. Both fields are latitudinally averaged over 7°S-7°N. Specific humidity contour interval is 1.0 x 10^{-4}kg kg^{-1}. Only the positive specific humidity contours are shown.

5.7 Composite of the vertical structure of high-amplitude CCKW events

5.7.1 Zonal wind and specific humidity

It is important to investigate the vertical structures of the zonal wind and the specific humidity that are associated with the propagation of CCKWs across Equatorial Africa. This is because vertical structures in the zonal wind play a role in the longevity of mesoscale convective systems (e.g., Schlueter et al., 2019) while moisture convergence is an important component in the convection-equatorial wave coupling (e.g., Wolding et al., 2020). The vertical section of the composite of anomalous zonal wind and specific humidity on high amplitude Kelvin wave events is shown in Figure 5.6. Figure 5.6 shows that in both ERA-I and the simulations, a day before day 0, a westward tilt with height in the anomalous zonal wind and specific humidity develops over the Atlantic Ocean. As the tilted structure propagates into Equatorial Africa, the anomalous westerly flow strengthens on day -1 through to day 1 before becoming weak near the surface on day 2 and 3 as seen in both reanalysis and simulations. The weak westerly anomalies may be linked to the weak positive precipitation anomalies on day 2 (Figure 5.4d,i,n) and 3 (Figure 5.4e,j,o).

Figure 5.6 also shows a leading edge of the anomalous westerly wind that is aligned with the anomalous specific humidity. This is consistent with results in Figure 5.5 and confirms the connection between the anomalous westerly flow and the transport of moisture from the Atlantic Ocean into the interior of equatorial Africa. On further scrutinising Figure 5.6, one sees that both ERA-I and the simulations show a drier lower-middle troposphere on day 2 and 3 in comparison to day -1, 0 and 1. We will return to this point in the next subsection. Another noticeable feature shown in both ERA-I and the simulations is that the zonal wind shows an eastward tilt with height above 200hPa, a result that is consistent with Wheeler et al. (2000). This signal may be interpreted to imply the transfer of momentum by anomalous easterly flow into the lower stratosphere (e.g., Yang et al.. 2007)

The vertical zonal wind and the specific humidity structures shown by the simulations show some differences from those in ERA-I. For example, while the depth of anomalous westerly flow in ERA-I starts from the surface to about 300hPa and the specific humidity anomaly appears to systematically and gradually weaken from day -1 into day 3, G25 shows a shallower and weaker anomalous westerlies particularly on day -1 and day 0 with an extensively moist midtroposphere on day 1 and 2. In comparison to ERA-I and G25, CP4A also shows shallower and weaker westerly anomalies particularly on day 1 and 2. Although CP4A's anomalous specific humidity is aligned with the leading edge of the weakly tilted zonal wind, its westward tilt with height is incoherent. This notwithstanding, the westward tilt with height and the eastward propagation in the zonal wind field are reasonably captured in both simulations but the magnitude of the anomalous zonal wind is generally weak. The weaker zonal wind anomaly in the simulations may be responsible for weaker moisture flux anomaly shown in Figure 5.5 for the simulations more especially in CP4A. The vertical structure of specific humidity field is generally poorly simulated in both models particularly CP4A. Because G25 is based on a convection

scheme, it is possible that the convection is not sufficiently responding to the large-scale circulation, which then results in errors in the large-scale vertical motion. In CP4A, the source of a poorly simulated vertical structure might be failure of the model to resolve small scale vertical motion or incorrect organisation of individual storms. Also, there are several potential reasons for the discrepancies between models and ERA-I. For example, the weak precipitation signal in G25 (e.g., Figure 5.4) might cause poor representation of the vertical structure of the zonal wind because the model lacks correct convectively-driven circulations. But also, the weak coupling between the parameterised convection and the moisture field may explain the difference between the vertical profile of the specific humidity in G25 and that in ERA-I. For CP4A, we speculate that the vertical structure of the specific humidity is a response to weaker zonal wind anomalies and/or difficulties in representing shallow convection in the model.

5.7.2 Anomalous potential temperature, horizontal mass divergence and zonal-vertical wind

Examining the vertical structure of the potential temperature and the zonal-vertical wind may be useful in understanding convection-wave interactions. The vertical structure composite on high amplitude Kelvin wave events for anomalous potential temperature, horizontal mass divergence and zonal-vertical wind is shown in Figure 5.7. ERA-I (Figure 5.7a-d) displays mid to upper level strong upward motion to the west of relatively weak low-level upward motion. The wind profile in which the low-level inflow is leading upper-level outflow by about 20^{o} (e.g., Figure 5.7a-c) suggests a westward tilt with height in the zonal-vertical wind structure. A similar tilted zonal-vertical wind structure was found by Wheeler et al. (2000) using NCEP-NCAR reanalysis and Straub and Kiladis (2003a) showed similar results using ECMWF's reanalysis. In Figure 5.7a, b, weak descending motion can be seen east of 30^{o}E. This subsidence is consistent with the negative precipitation anomalies over EEA in Figure 5.4a, b. The anomalous low-level horizontal mass convergence seen in Figure 5.7 might be associated with anomalous westerly flow (also see enhanced zonal winds in Figure 5.6). The tilted anomalous horizontal convergence in Figure 5.7 matches well with the tilted specific humidity anomalies in Figure 5.6, suggesting a possible gradual moistening of the troposphere.

As was seen in Figure 5.6, in Figure 5.7a-d, a strong and deep anomalous westerly flow is persistently apparent to the west of the location of positive TRMM precipitation anomalies (indicated by a bold purple "X") from day -1 to day 2. It can also be seen from day -1 to day 3 that the regions of upper-level divergence are generally to the west of the region of positive precipitation anomalies (Figure 5.7a-e), showing the link between precipitation and the convectively coupled circulation.

In Figures 5.7a-d, vigorous upward motion peaks between 400hPa and 300hPa and roughly coincides with regions of positive precipitation anomalies. By day 3 (Figure 5.7d) the anomalous westerly flow is weak, and the upward motion is also generally weak or nonexistent. This is consistent with the relatively drier EEA on day 3 in Figure 5.5e. In Figure 5.7a-c, the positive potential temperature anomalies between 400hPa-200hPa are nearly collocated with peak upward motion and generally in phase with positive precipitation anomalies.

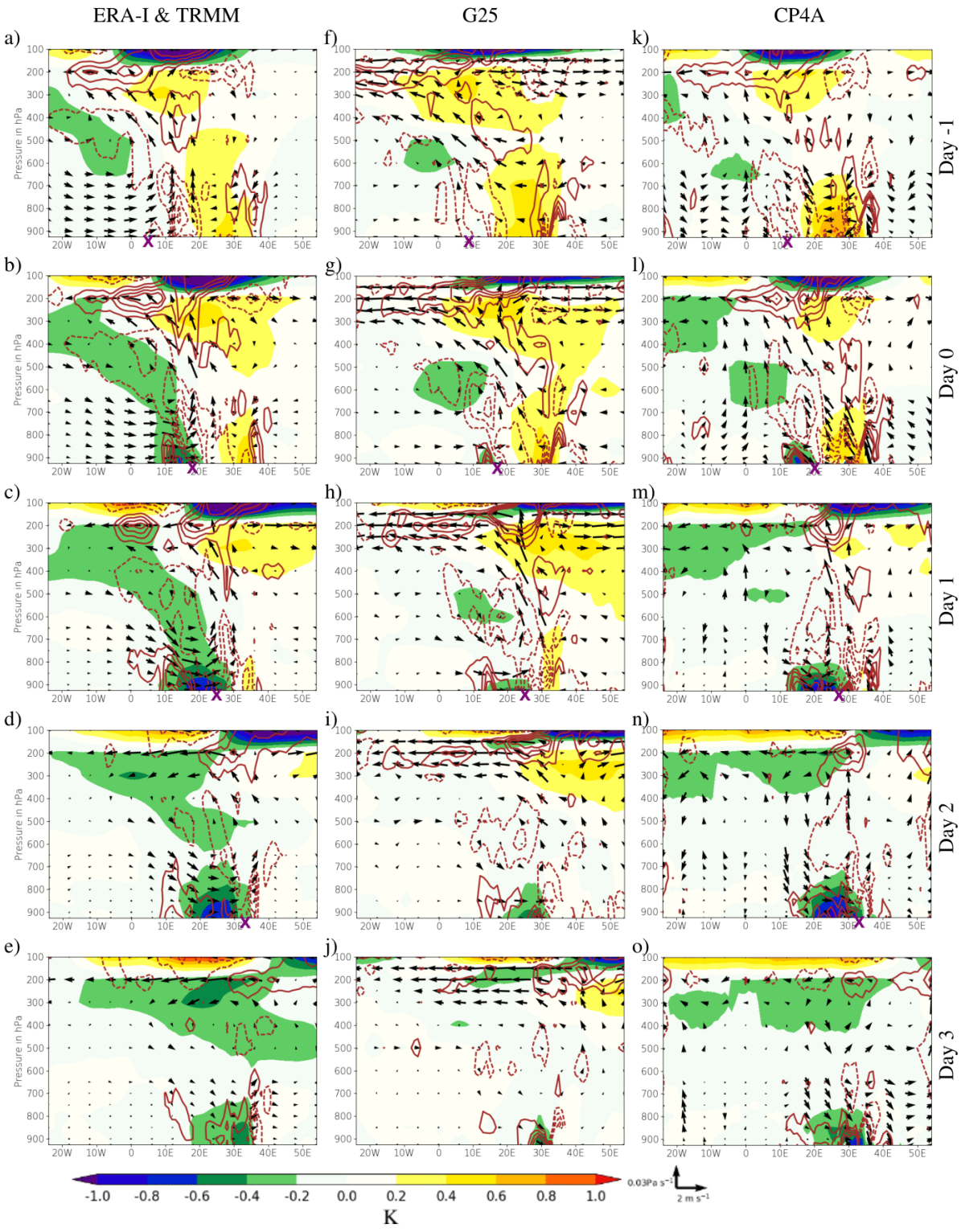

Figure 5.7: Lagged height-longitude plots for (a-e) TRMM and ERA-I, (f-j) G25 and (k-o) CP4A showing high-amplitude Kelvin wave event composite for anomalous horizontal mass convergence (brown contours), potential temperature anomalies (shading) and anomalous zonal-vertical wind (vectors). The lag for which a composite was computed is shown on the right of each row. All fields are latitudinally averaged over 7°S-7°N. Vertical structure of the horizontal mass divergence is contour interval is 5 x $10^{-7}$$s^{-1}$. The reference wind vector is shown at the bottom right. The bold purple "X" on the longitude axis indicates an estimated centre of the location of positive precipitation anomalies as seen in Figure 5.4. The bold purple "X" is excluded if the precipitation anomalies are generally weak or non-existent. The unit for potential temperature is K.

In Figure 5.7a-d, the surface negative potential temperature anomalies seen to the west of the regions of maximum ascent and positive precipitation anomalies are suggestive of a cold pool that might be associated with rain-evaporation-forced downdrafts. Although TRMM and ERA-I are obtained from different sources, their alignment shown in Figures 5.4 and 5.7a-e suggests our results are robust.

Results in G25 (Figure 5.7f-j) has some resemblance in some aspects with ERA-I/TRMM in features such as westward tilt with height in the wind field, potential temperature structure and mass divergence. As shown in ERA-I, the tilted horizontal mass convergence in Figure 5.7 f-i lines up with the tilted anomalous specific humidity in Figure 5.6f-i. The positive precipitation anomalies are generally collocated with regions of low-level horizontal convergence suggesting that Kelvin wave convergence is likely to be supportive in triggering precipitation as the wave propagates eastward. However, the westerly anomalies in G25 is generally weaker than that in ERA-I. In CP4A (Figure 5.7k-o), the westward tilt with height in horizontal mass convergence is similar to ERA-I and G25, particularly from day -1 to day 1. The regions of positive precipitation anomalies and negative potential temperature anomalies move together eastward as seen in ERA-I and G25. Also, it can be seen that the low-level negative potential temperature anomalies are generally more realistic in CP4A, although the reason for this remains unclear and may be a subject for future research.

There are some differences between the anomalous zonal-vertical wind structure in CP4A and that in ERA-I. For example, in Figure 5.7k-m, the circulation west of 10^{o}E appear to be weak and not as consistent as that in the corresponding panels in Figure 5.7a-c. And in comparison with G25 (Figure 5.7f-h), CP4A (Figure 5.7k-m) shows stronger upward motions than that in the corresponding panels of G25. In Figure 5.7m, vigorous upward motion can be seen between $\sim$ 10^{o}W and 0^{o}and also in proximity of 30^{o}E. Also, in Figure 5.7n, descending motion between 10^{o}E-20^{o}E is sandwiched by upward motion. The longitudinal distance between the two consecutive regions of upward motion sandwiching the downward motion is much shorter than what is expected of two consecutive phases of enhanced Kelvin wave-induced convection. This may suggest either the presence of waves of relatively shorter horizontal wavelength than the CCKW or perhaps just more small intense storm clusters as highlighted in Stratton et al. (2018).

5.7.3 Interaction of CCKWs with the East African highlands

Guo et al. (2014) suggested that weak amplitude Kelvin waves over South America and the tropical Atlantic region tend to be associated with a weak westward tilt with height. Here, we have shown in Figures 5.4 and 5.5 that Kelvin wave convergence tends to wane over EEA. In this subsection, we explore the clues about the interaction of CCKWs with the East African highlands. In the transition from day 1 (Figure 5.6c) into day 2 (Figure 5.6d), the coherent eastward propagating tilted structure of anomalous westerlies appears to get distorted at about 30^{o}E. Furthermore, one can also see in Figure 5.7c and 5.7d that the anomalous westerly flow appears not to coherently progress east of about 31^{o}E and the tilt in the vertical structure of the horizontal mass convergence seems weakened and distorted (Figure 5.7d and 5.7e) at about the same longitude. Finally,

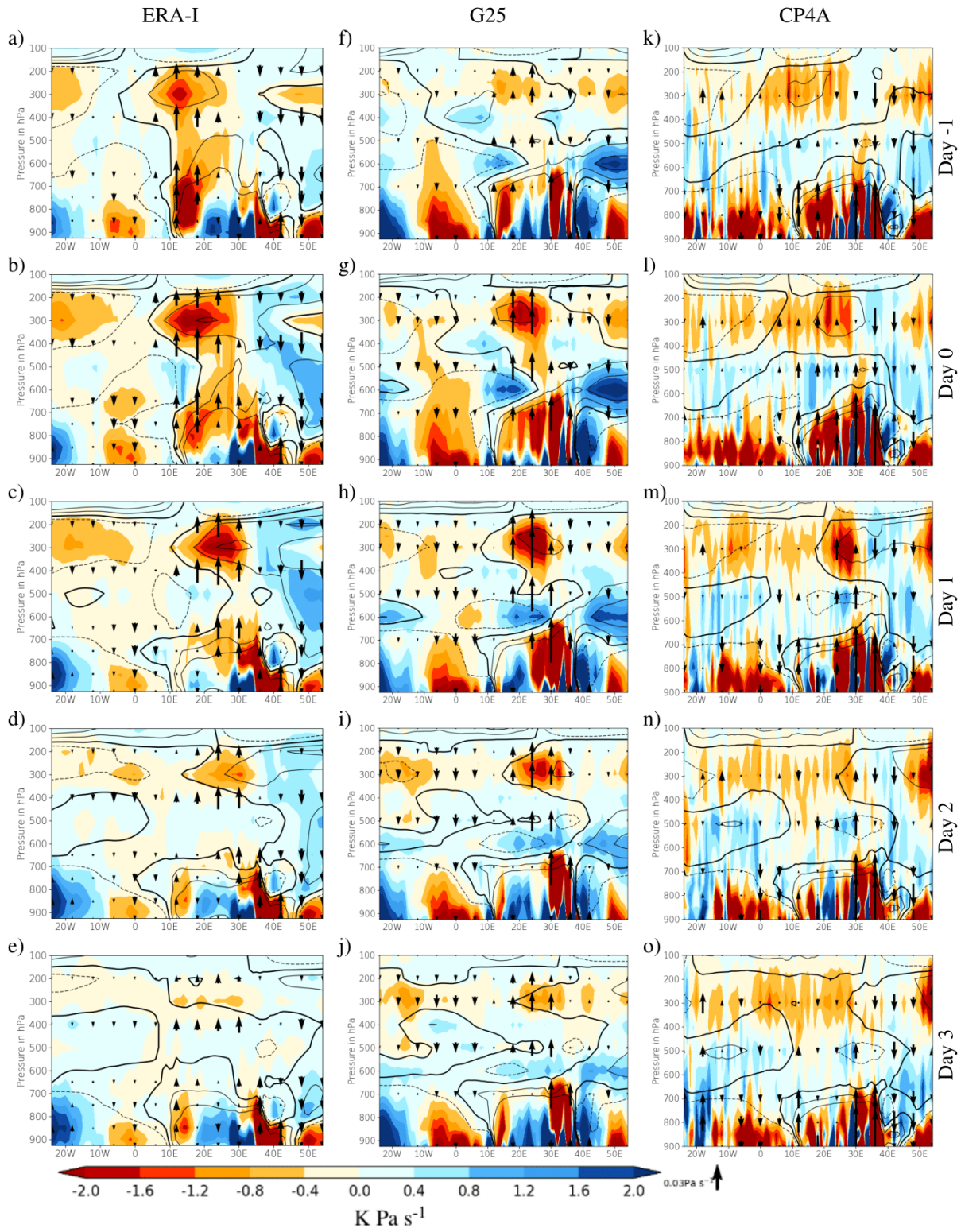

Figure 5.8: Longitude-pressure cross section for $T'\omega'$ (shading), ω' (vectors) and T' (contours, zero line is thicker and negative anomalies (computed as departure from the zonal mean) are dashed). Unit for T' is K, ω' in Pa s^{-1}. The lags for which a composite was computed are shown on the right. The contour interval is 2.0 x 10^{-1}K

Figure 5.6 may provide an additional clue about the interaction between topography and the eastward propagation of the CCKW. Considering a generally clear vertical structure of the anomalous specific humidity in Figure 5.6a-c, Figure 5.6d shows a fragmented vertical structure of the anomalous specific humidity at 30°E. It can also be seen that the anomalous westerly flow, specific humidity anomalies and Kelvin wave convergence

all weaken considerably from day 1 to day 2 (e.g., Figure 5.7). This is might be because moisture flow is interrupted by the highlands. The distortion of the specific humidity anomalies, mass convergence anomalies and the wind field seen in ERA-I are well captured in both simulations.

The interaction between the anomalous low-level westerlies and the highlands may suggest that the anomalous eastward moisture transport is reduced downstream. Following a suggestion advanced in Guo et al. (2014), we suggest that the obstruction of the tilted zonal-vertical wind structure may lead to the weakening of the Kelvin wave over EEA. Because the moisture is cut off and the Kelvin wave is weakened, the coupling between the convection and the Kelvin wave is weakened. This may partly explain the drier lower-to middle troposphere seen in Figure 5.6d,i,n,e,j,o and the weak precipitation anomalies in, for example, Figure 5.4d and e. The interaction between Kelvin waves and East Africa's highlands is also shown in Matthews (2000). Baranowski et al. (2016) also found a pronounced disintegration of Kelvin waves at about 30°E (e.g., their Figure 6a) and Yang et al. (2021) revealed the influence of East African highlands on the propagation of Kelvin waves in all seasons in both ERA-I and their model simulations.

5.7.4 Energetics of CCKWs over equatorial Africa

An idea on the energetics would be useful in understanding whether the models generate eddy potential energy and convert it into eddy kinetic eddy as seen in the observations. Following an approach used in Holloway et al. (2013), the energy terms over the domain are computed using anomalies from the zonal means over equatorial Africa (see definition in section 1) rather than at every longitude over the entire globe. For example, if $\overline{T}$ is the zonal mean temperature on a single day and pressure level and T is the temperature for a single longitude and pressure level, then that day's temperature anomaly at a single longitude and pressure level, T' = T - $\overline{T}$. The computations are done on fields that have been coarse-grained to 1°in both latitude and longitude. Figure 5.8 shows time-longitude composite plot for $T'\omega'$ (shading), T'(contours), and ω' (vectors) with all fields averaged between 7°S-7°N.

In Figure 5.8 a-d, one sees that the regions of strong upward motion in middle to upper troposphere are collocated with positive temperature anomalies (i.e., where $T'\omega' < 0$), indicating the conversion of Eddy Available Potential Energy (EAPE) into Eddy Kinetic Energy (EKE). However, previous publications such as Holloway et al. (2013) suggest that this is likely to be also associated with generation of EAPE since there is little storage of EAPE. Starting with day -1, (Figure 5.8a), the entire structure propagates eastward between day -1 and day 3 as was seen in zonal-vertical wind plot (Figure 5.7a-e) and in precipitation plot (Figure 5.4a-e). This signal of the energy generation and conversion is seen to become stronger from day -1 to day 1 and weakens on day 2 and 3, consistent with weakening of the wet signal over EEA. The energy conversion in G25 (Figure 5.8f-j) is qualitatively similar to that in ERA-I but ω' shows a weak signal. In comparison with ERA-I and G25, CP4A (Figure 5.8k-o) shows a mixed signal in the sense that the regions of conversion of available potential energy into eddy kinetic energy are erratic and generally qualitatively different from that in ERA-I

and G25. Also, like in G25, CP4A consistently shows weak values of ω'. Overall, both models show evidence of conversion of EAPE into EKE.

5.8 Discussion and Conclusions

In this chapter, the physical processes through which Convectively Coupled Kelvin Waves modulate the eastward propagation of precipitation across Equatorial Africa are investigated using a multi-year state-of-the-art Convection permitting simulation (CP4A), a relatively coarse resolution global simulation (G25), observations (TRMM) and reanalysis (ERA-I). The fidelity of CP4A and G25 in representing the dynamical structure of Kelvin wave events in the context of WEA-EEA convection and precipitation connection is evaluated.

It is found that the two important related processes through which CCKWs influence the propagation of convection and precipitation from west to east across Equatorial Africa are: 1) low-level westerly anomalies that lead to increased low-level convergence and, 2) westerly moisture flux anomalies that amplify the lower-to-mid-tropospheric specific humidity. These findings suggest that the important processes through which CCKWs modulate the eastward propagation of precipitation across Equatorial Africa are low-level moisture flux convergence and modification of lower-to-midtropospheric moisture.

Results from evaluation of CP4A and G25 in representing the dynamical structure of Kelvin wave events in the context of WEA-EEA convection and precipitation connection against TRMM and ERA-I show that both models capture the key features of propagation of CCKWs across equatorial Africa. However, G25 simulates a precipitation field that is weaker than that in TRMM while CP4A shows westerly anomalies that are too weak and shallow but the precipitation field is better simulated. In general, both models capture the eastward propagation of precipitation anomalies in association with Kelvin wave convergence. We believe that this is the first study over Equatorial Africa to use the precipitation field and Kelvin wave activity based on dynamical fields to: a) explore the connection between the Kelvin waves and the eastward propagating precipitation signal and the associated processes, and b) evaluate a multi-year state-of-the-art simulation from a convection permitting model.

Correlation coefficient analysis of daily precipitation anomalies for both observations (TRMM) and model simulations (CP4A and G25) shows an eastward propagating feature whose speed is about 9-10 m s^{-1} (e.g., Figure 5.1), suggesting a large-scale feature acting to organise precipitation. This result may be compared to an eastward propagating convective signal found in OLR in Mekonnen and Thorncroft (2016).

To explore the eastward propagation of precipitation across Equatorial Africa by gaining an insight into the number of days when precipitation is presumed to propagate eastward, we have used a percentile threshold to count the number of precipitation events based on a pair of sub-regions. We show in Table 5.1 the percentage of precipitation events that might be related to Kelvin wave events (see section 3 for the definition of the precipitation events and a Kelvin wave event). Results in Table 5.1 imply that, for example, over a period

of 9 years, about 53%, 46% and 62% of the precipitation events during MAM are related to Kelvin waves low-level convergence above the 60th percentile of the Kelvin wave low-level convergence in ERA, G25 and CP4A respectively. This means that, generally, the probability of a precipitation event being associated with a Kelvin wave event in both observations and simulations exceeds one that is expected by chance, and confirms that precipitation events in MAM are often related to Kelvin wave events (e.g., Huang and Huang, 2011; Laing et al., 2011). In Baranowski et al. (2020), Kelvin waves past Sumatra were found to be solely responsible for about 30% of anomalous precipitation events suggesting that not all precipitation events are linked to Kelvin wave events. Their result may be likened to our result that shows a significant number of Kelvin wave events that are not related to precipitation events.

The climatological variability of Kelvin wave activity across Equatorial Africa is shown in Figure 5.3. The Kelvin wave activity as depicted in ERA-I and both simulations, with a peak in MAM, is generally consistent with results in Roundy and Frank (2004) and Huang and Huang (2011, their Fig.5d) (e.g., Figure 5.3a). Notwithstanding the underactive Kelvin waves between $\sim$10^{o}E-20^{o}E, both simulations generally capture the spatial and temporal variability of Kelvin wave activity as shown in ERA-I. This result is in agreement with results in Jackson et al. (2019) who found that the G25 simulated CCKWs with amplitude close to observations. The two peaks of Kelvin wave activity shown in Figure 5.3 coincide with Africa's two equatorial rainfall seasons that follow the north-south migration of the ITCZ, highlighting a likely connection between Kelvin wave activity and the ITCZ (e.g., Dias and Pauluis, 2011).

While our results show evidence of anomalous westerly moisture flux, this might be enhancing the locally available moisture (e.g., Pokam et al., 2012). By compositing the wind and specific humidity field on high amplitude Kelvin waves, we show that 1 day before day 0, the anomalous zonal flow over the Atlantic Ocean is strengthened (e.g., Figure. 5.5a,b and Figure 5.6a,b). This leads to low-level convergence as shown in the entire sequence (e.g., Figure 5.5a-e, f-j and k-o). At the eastern edge of the westerly anomalies there is enhanced anomalous convergence. This low-level convergence is important because it provides an environment favourable for convection. Figures 5.5, 5.6, and 5.7 reveal that the anomalous low-level westerly flow transports moisture into a region of Kelvin wave low-level convergence and positive precipitation anomalies (e.g., Straub and Kiladis, 2003a), suggesting that the Kelvin wave-precipitation coupling is supported by an enhanced supply of moisture (e.g., Wolding et al., 2020).

From the co-location of the simulated Kelvin wave low-level convergence and the simulated precipitation anomalies (e.g., Figure 5.4) we show that the simulations examined in this study reasonably represent an eastward propagating convective and precipitation signal that is associated with CCKWs previously only found in observational studies. We will return to this result later. In comparison to G25, CP4A indicated a better representation of precipitation (e.g., Figure 5.4) which demonstrates the value of explicit representation of convection. The better representation of daily precipitation in CP4A in comparison to simulations in which convection was parameterised has been shown in previous other studies such as Stratton et al. (2018), Finney

et al. (2019) and Berthou et al. (2019).

The eastward propagation of convection and precipitation require successive formation of new convective cells to the east of deep convective systems (e.g., Nakazawa, 1988). The anomalous zonal-vertical wind structure in ERA-I (Figure 5.7) reveals weak upward motion that develops into strong mid-to upper tropospheric upward motion. This is indicative of shallow convection at the leading edge of deep convection. Despite the weak zonal-vertical circulation in G25, both simulations generally reproduce the zonal-vertical wind structure that is qualitatively similar to that in ERA-I.

It is also shown that Kelvin wave convergence tends to weaken over EEA (e.g., Figures 5.4 and 5.5) (e.g., Mounier et al., 2007; Nguyen and Duvel, 2008). Also, anomalous low-level westerly flow appears not to coherently progress east of about 30^{o}E (e.g., Figures 5.6 and 5.7). The highlands on the western branch of the East African rift valley appear to distort the coherent eastward propagation of the tilted structure of both the anomalous westerly flow and specific humidity thereby impacting the supply of moisture as the CCKW approaches EEA (e.g., Dunkerton and Crum, 1995; Matthews, 2000). Once large-scale low-level horizontal convergence is distorted and at the same time the supply of moisture is possibly diminished, the precipitation signal over EEA weakens. We suggest that a weak CCKW over EEA may be partly associated with a weakened westward tilt with height in dynamical fields and anomalous specific humidity (e.g., Guo et al., 2014).

The co-location of simulated positive precipitation anomalies and the corresponding Kelvin wave low-level convergence (e.g., Figure 5.4f-j, 5.4k-o) is consistent with results in observational studies that found an association between convective activity and Kelvin waves over Equatorial Africa (e.g., Nguyen and Duvel, 2008; Laing et al., 2011; Mekonnen and Thorncroft, 2016). However, the anomalous precipitation signal in G25 is much weaker than the observed. The weak precipitation signal in G25 is not surprising because previous studies such as Stephens et al. (2010) reported that rainfall in GCMs tends to be frequent and weak. As earlier discussed, although the Kevin wave activity in G25 matches that in ERA-I, the composite of precipitation anomalies on high-amplitude Kelvin wave events displays a precipitation signal in G25 (e.g., Figure 5.4f-j) that is weaker than that in TRMM (e.g., Figure 5.4a-e). This likely indicates too-weak coupling between the precipitation and Kelvin waves in G25 (e.g., Yang et al., 2009; Straub et al., 2010). This is supported by the results in Table 5.1 (fourth column) that show a smaller percentage of precipitation events that are also Kelvin wave events in G25. The anomalous precipitation signal in CP4A nearly matches that in ERA-I especially on day 2 (e.g., Figure 5.4c and m). Generally, both CP4A and G25 capture the eastward propagation of precipitation as shown in TRMM (e.g., Figure 5.1 and 5.4) and the role of CCKWs in modulating the West-East propagation of precipitation is well simulated.

In agreement with Zebaze et al. (2017), our results in both observations and simulations show that CCKWs influence zonal flow and in turn modulate the advection of moisture into regions of convective activity and precipitation (e.g., Figures 5.4-6). Much of the anomalous moisture that is supporting the eastward propagation of precipitation appears to be transported from the Atlantic Ocean as compared to the Indian Ocean (e.g.,

Figure 5.5). Berhane et al. (2015) and Finney et al. (2020) have also documented enhanced rainy days over EEA that are associated with low-level westerly wind anomalies. The implication is that low-level circulation plays a key role in precipitation variability over Equatorial Africa.

Both CP4A and G25 portray a westward tilt with height in the anomalous zonal wind and specific humidity (e.g., Figures 5.6 and 5.7), which provides evidence of the presence of a Kelvin wave signal in the model simulations that is broadly comparable to that in ERA-I (e.g., Wheeler et al., 2000; Straub and Kiladis, 2002; Frierson, 2007; Tulich and Mapes, 2008). Both models reasonably simulate key features of CCKWs in the sense that they both reveal low-level anomalous westerly flow that is in phase with positive precipitation anomalies (e.g., Figures 5.4 and 5.7) (e.g., Yang et al., 2009).

The negative potential temperature anomalies (e.g., Figure 5.7) shown to the west of the positive precipitation anomalies may be interpreted to be a result of descending cold and dry air resulting from evaporative cooling of stratiform precipitation, suggesting an involvement of diabatic processes as documented in Kiladis et al. (2005). In comparison to G25, the low-level negative potential temperature anomalies appear to be more realistic in CP4A, probably because of more realistically complete convective features (e.g., day 1-3 in Figure 5.7). Unlike CP4A, G25 fails to simulate the negative potential temperature anomalies (e.g., Figure 5.7f-j). This might be due to its deficiency in realistically simulating convection in G25 (e.g., Thayer-Calder and Randall, 2012). Results of energetics show that both models have a signal of generation of available potential energy and conversion of that energy into eddy kinetic energy with magnitudes that are closely similar to that in ERA-I. It has been shown that the precipitation signal in G25 is generally weak. Since the eastward propagation of precipitation is the major focus of this study, this implies that G25 has a major limitation in the context of revealing the role of Kelvin waves in modulating the eastward propagation of precipitation across Equatorial Africa. In general, modelling results in this chapter provide support to observational studies such as Mekonnen and Thorncroft (2016) in that the interaction they found in cloud brightness temperature is also present in simulated precipitation.

Finally, this chapter reveals that some precipitation events are not related to Kelvin wave events (e.g., Table 5.1). A similar result was shown in Chapter 4 (§4.7). This result warrants further scrutiny. So, in Chapter 6, high-amplitude Kelvin wave events are isolated and their linkage with precipitation over Equatorial Africa is investigated. Further, Chapter 6 examines case studies with a lens on eastward propagating extreme precipitation episodes and high-amplitude Kelvin waves.

Chapter 6

Extreme precipitation and its relationship with CCKWs over Equatorial Africa

6.1 Purpose of this Chapter

The work in this chapter is intended to achieve the fourth thesis objective: that is, to evaluate the role of CCKWs in influencing extreme precipitation episodes over Equatorial Africa. Focus is placed on precipitation variability within MAM because this season accounts for more than 40% of the annual precipitation over several sub-regions over EEA (Pohl and Camberlin, 2006b), and there is a relatively high frequency of Kelvin waves during this season (e.g., Roundy and Frank, 2004). Work in this chapter is presented in two parts. The first part investigates the statistical link between high-amplitude Kelvin wave events and extreme precipitation over Equatorial Africa. This part aims at providing a description of the extent to which the occurrence of extreme precipitation is influenced by the presence of high-amplitude CCKWs over this region. Following Ferrett et al. (2020), a metric that quantifies the change in the likelihood of occurrence of extreme precipitation is used to examine the role of high-amplitude Kelvin waves in influencing extreme precipitation during boreal spring. In the second part, the linkage between specific eastward propagating extreme precipitation episodes (case studies) and CCKWs is investigated. This part attempts to shed light on how the large-scale atmospheric fields and the precipitation distribution are impacted by high-amplitude CCKWs (or their absence) on a case-by-case basis.

Chapters 4 and 5 demonstrated that there is a connection between CCKWs and the eastward propagating precipitation in observed and simulated precipitation over Equatorial Africa. The results in the aforementioned chapters provide a general picture of the influence of CCKWs on the eastward propagation of precipitation. The current chapter provides greater details concerning the typical patterns of the eastward propagating precipitation in the presence of a CCKW. This chapter goes beyond the influence of CCKWs as a large-scale driver of synoptic scale precipitation variability, and looks at the small-scale precipitation characteristics. As it will be

demonstrated in the subsequent sections, work in this chapter is important because it comprehensively addresses the fine detail regarding the response of precipitation to the propagation of a CCKW across Equatorial Africa. Previous studies have not addressed this subject using both observations and model simulations.

Extreme precipitation episodes tend to be accompanied by flash floods that cause displacement of communities, disruption of essential services, damage to infrastructure, submersion of farmland, death of livestock, and loss of human life (e.g., Jonkman, 2005). It has been reported that over Africa, an average of 42 people are killed per flood (Jonkman, 2005). In March 2020, nearly 1.3 million people in EEA were displaced by flooding following extreme precipitation episodes (OCHA, 2020). Extreme precipitation may be caused by both large-scale disturbances such as the MJO and CCKWs, and localised atmospheric processes (e.g., Kilavi et al., 2018). Understanding the primary drivers of extreme precipitation episodes is important in aiding operational weather forecasting.

The results in Chapters 4 and 5 showed that the eastward propagating wet signal is often (but not always) linked to CCKWs. Both Nguyen and Duvel (2008) and Laing et al. (2011) found evidence of larger and longer-lived MCSs modulated by CCKWs. Following the findings in aforementioned publications, it is plausible that Kelvin waves modulate the eastward propagating extreme precipitation episodes. However, not much can be found in the literature on extreme precipitation events in this region (e.g., Willenbockel, 2012), and there are even fewer studies on the role of CCKWs in influencing extreme precipitation over Equatorial Africa. The purpose of this chapter, therefore, is to: (a) characterise extreme precipitation, and its relationship to CCKWs in observations; (b) explore how well CP4A and G25 capture the distribution of extreme precipitation in comparison to observations; (c) assess the statistical linkage between high-amplitude Kelvin waves and the observed and simulated daily extreme precipitation; and (d) explore the processes through which high-amplitude CCKWs influence extreme precipitation episodes using a case study approach.

The rest of the chapter is organised as follows. Section 6.2 presents the methodology, and Section 6.3 focuses on the linkage between high-amplitude Kelvin waves and extreme precipitation. In Section 6.4, the impact of high-amplitude Kelvin waves on observed extreme eastward propagating precipitation episodes is provided. This is followed by the impact of simulated high-amplitude Kelvin wave events on simulated extreme precipitation episodes in Section 6.5. Finally, Section 6.6 presents the discussion and conclusions of this chapter.

6.2 Methodology

6.2.1 Definition of an extreme precipitation episode and a high-amplitude Kelvin wave event

The definition of a precipitation event described in Chapter 4 (§4.2.2) is slightly modified in the current chapter to identify extreme precipitation episodes that potentially propagated from WEA into EEA. That is, for a pair of sub-regions, a precipitation occurrence is defined as an "extreme precipitation episode" if two condi-

tions are satisfied. First, precipitation occurs in excess of the 95th percentile (as opposed to 66.7th percentile in Chapter 4) of 1998-2006 precipitation anomalies over the sub-region in WEA (i.e., 7^{o}S-3^{o}S, 16^{o}E-21^{o}E, hereafter W). Second, two days later, the precipitation in the corresponding sub-region in EEA (i.e., 2^{o}S-2^{o}N, 31^{o}E-36^{o}E, hereafter E) exceeds that sub-region's 95th percentile (again as opposed to 66.7th percentile in Chapter 4) of 1998-2006 precipitation anomalies given that the previous day's precipitation amount was below the 95th percentile. Note that the two sub-regions (W and E) correspond to W9 and E3 in Figures 4.1 and 5.1a (green and brown boxes). For the simulations, the same definition is used except that the pair of sub-regions used to isolate simulated eastward propagating extreme precipitation episodes are shown in Figure 5.1e and Figure 5.1i for G25 and CP4A respectively.

The equatorial wave dataset described in Chapter 3 (§3.3.1) is used here to isolate high-amplitude Kelvin wave events by identifying all the days on which the Kelvin wave convergence at 850 hPa exceeded the 90th percentile of 1998-2006 Kelvin wave convergence over the sub-region in WEA (W). Note that for a high-amplitude Kelvin wave event, only the sub-region in WEA is used. The purpose here is to investigate the precipitation patterns associated with the passage of high-amplitude Kelvin waves across Equatorial Africa.

6.3 The linkage between high-amplitude CCKWs and precipitation

6.3.1 Extreme precipitation thresholds

Extreme precipitation rate at each grid point is defined as the precipitation rate found at the high end of the probability distribution function regardless of whether or not they were associated with loss of life, property and infrastructure damages. At each grid point, a daily precipitation rate is regarded as extreme when it exceeds the 95th percentile threshold value computed over the 1998-2006 MAM period. The percentile approach is used here because it allows for a direct comparison of the spatial and temporal distribution of extreme precipitation episodes in different datasets (e.g., Klein Tank et al., 2009). The percentile approach has been used in previous studies such as Salack et al. (2018), Subudhi and Landu (2019) and Ferrett et al. (2020).

Figure 6.1 shows the spatial distribution of the 95th percentile precipitation rate at each grid point during boreal spring as depicted in TRMM, G25 and CP4A (row-wise, top to bottom). The percentile precipitation rates are calculated in one of the two ways (without, left column, or with, middle column, values below 0.1 mm day^{-1}) and the difference between these is shown in the right column. It can be seen that there is a remarkable spatial heterogeneity in the distribution of the 95th percentile precipitation rates. This heterogeneity might be explained by the various drivers of daily precipitation as well as interactions between large-scale and localised drivers of the climate (e.g., Nicholson, 2002; Dezfuli, 2017).

Also easily noticeable in Figure 6.1d is that G25 displays lower threshold rates (excluding light values) than TRMM (Figure 6.1a), but the threshold rates (including all values) in G25 (Figure 6.1e) are broadly quantitatively similar to that in TRMM (Figure 6.1b). This is suggestive of frequent light rainfall in G25. This result

is consistent with the conclusion in Stephens et al. (2010), who reported that global models tend to produce frequent but light precipitation, and Brown et al. (2010), who examined daily precipitation from the Australian Community Climate and Earth-System Simulator (ACCESS) global climate model and arrived at similar results as Stephens et al. (2010). Brown et al. (2010) attributed the too light and too frequent precipitation in their global model to the physical parameterisation rather than the large-scale dynamics.

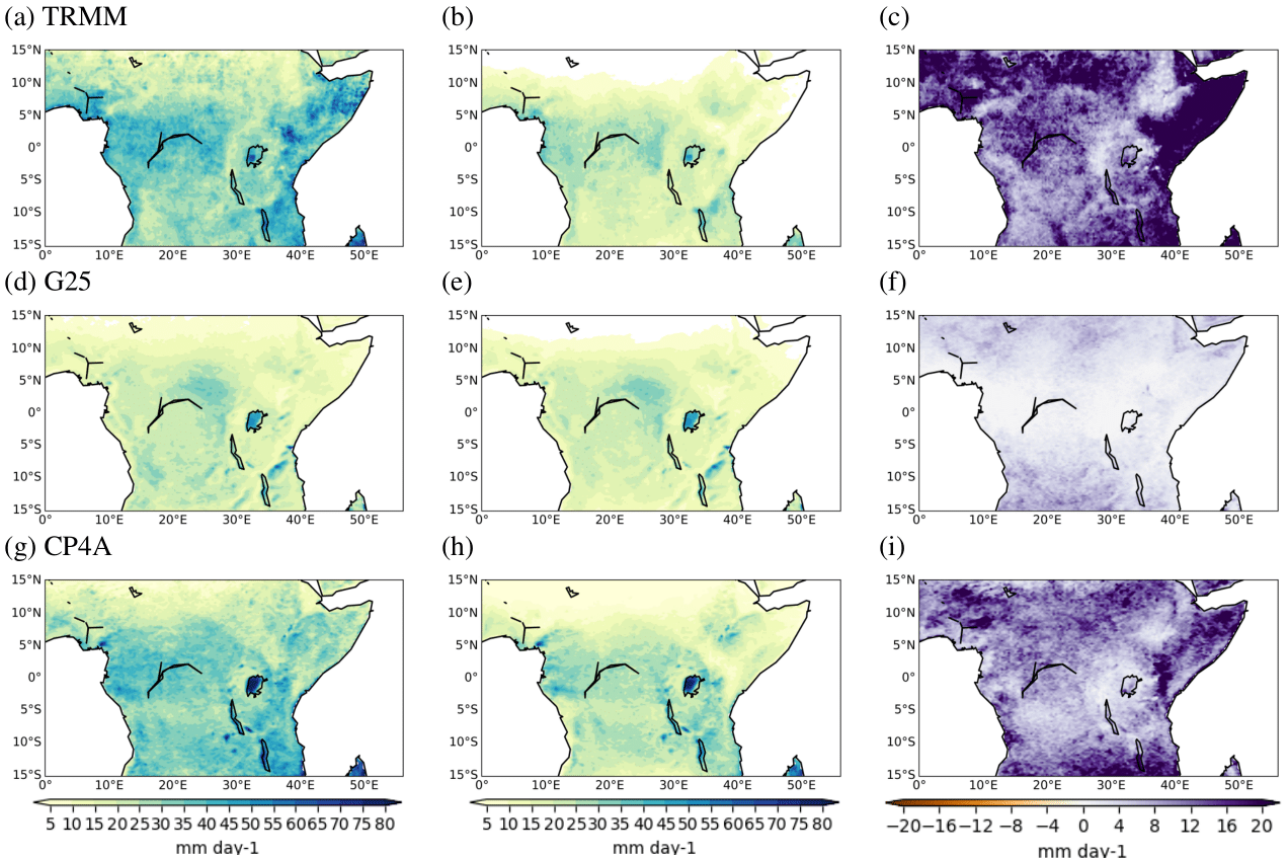

Figure 6.1: The threshold in March-April-May for 1998-2006 (a) 95th percentile of TRMM daily precipitation excluding precipitation rates less that 0.1 mm day^{-1} (b) same as (a) but for all days (i.e., including zeros), (c) difference between (a) and (b). (d-f) same as (a-c) but for G25. (g-i) same as (a-c) but for CP4A.

On the other hand, CP4A (Figure 6.1g, h) shows a remarkable resemblance to TRMM (Figure 6.1a, b). One reason for the more realistic simulation of thresholds by CP4A might be that the model has a better simulation of several processes that are responsible for extreme precipitation events (e.g., Crook et al., 2019). For example, because CP4A explicitly represents deep convection, it is expected that it captures heavy precipitation associated with MCSs (e.g., Stratton et al., 2018; Pal et al., 2019). Also, considering that CP4A has higher resolution orography than G25 and given that both Nguyen and Duvel (2008) and Jackson et al. (2009) found strong MCSs linked to orographic effects, this could also be a factor allowing CP4A to capture extreme precipitation more realistically. Results for CP4A in Figure 6.1 are consistent with findings in Prein et al. (2015) that convection permitting simulations tend to produce a precipitation distribution that agrees with the observations. Both Stratton et al. (2018) and Kendon et al. (2019) found that CP4A, simulated a precipitation distribution that is comparable to that in observations.

Figure 6.1 (right column) shows the differences between the thresholds calculated including all precipi-

tation rates and those based on non-zero (rates greater than 0.1 mm day^{-1}) precipitation. As discussed above, these differences are smaller in G25 (Figure 6.1f) than in CP4A (Figure 6.1i) and TRMM (Figure 6.1c). The highest differences in threshold rates in TRMM and CP4A can be seen over the Horn of Africa. For regions such as the Horn of Africa that have either a high number of days with zero or low precipitation rates (e.g., Berhane and Zaitchik, 2014; their Figure 1), the precipitation rates on days isolated as extreme precipitation episodes may not be exceptionally different from those on other rainy days. For a large part of the domain under investigation, the difference between the thresholds including zero precipitation rate and those excluding low (less than 0.1 mm day^{-1}) precipitation rates are small. Ferrett et al. (2020) used thresholds computed over all days (including days with zero precipitation) and found robust linkages between equatorial waves and extreme precipitation in Southeast Asia. Taking the above points into consideration, the subsequent analysis uses the thresholds based on all days in the season (middle column in Figure 6.1).

6.3.2 High-amplitude Kelvin waves and extreme precipitation statistics

This section first assesses the likelihood of extreme precipitation associated with high-amplitude Kelvin wave events. Figure 6.2 shows the likelihood of precipitation exceeding a grid-point's threshold (that is, 95th percentile of all MAM days in the period 1998-2006) during days with a high-amplitude CCKW over WEA (left) and EEA (right). This figure provides evidence of an increase in the probability of occurrence of an extreme precipitation episode on days when a high-amplitude Kelvin wave is located over WEA or EEA. Since exceedance of the 95th percentile threshold implies a 5% chance of occurrence of extreme precipitation for all days in MAM, the grid points in Figure 6.2 that indicate a likelihood of 10% are twice as likely as climatology to experience extreme precipitation and those with 15% are three times as likely to record extreme precipitation compared to climatology. Both the observations and the simulations show that an extreme precipitation episode is up to twice as likely compared to climatology to occur over Equatorial Africa when a high-amplitude CCKW is located over the region. The regions with low thresholds (Figure 6.1), such as the Horn of Africa, indicate low probabilities of precipitation exceeding the threshold in both observed and simulated precipitation. Figure 6.2 is consistent with the discussion just above regarding the precipitation rates to use in the computation of the grid point threshold rates. Despite the agreement in terms of the likelihood of occurrence of an extreme precipitation event in the presence of a CCKW, there are differences in the patterns of the probabilities shown in the observations and the simulations.

Comparing G25 (Figure 6.2c) with TRMM (Figure 6.2a) and CP4A TRMM (Figure 6.2e), it can be seen that G25 shows a fragmented pattern of increased probabilities of extreme precipitation when a high-amplitude Kelvin wave is located over W (WEA). Also, it fails to capture the signal over the Atlantic Ocean (although this is not an area of interest in this thesis). Similarly, for a CCKW over sub-region E (EEA), again G25 (Figure 6.2d) shows fragmented pattern of increased probabilities of extreme precipitation compared to TRMM (Figure 6.2b) and CP4A (Figure 6.2e). Further, unlike TRMM (Figure 6.2b) and CP4 (Figure 6.2f), G25

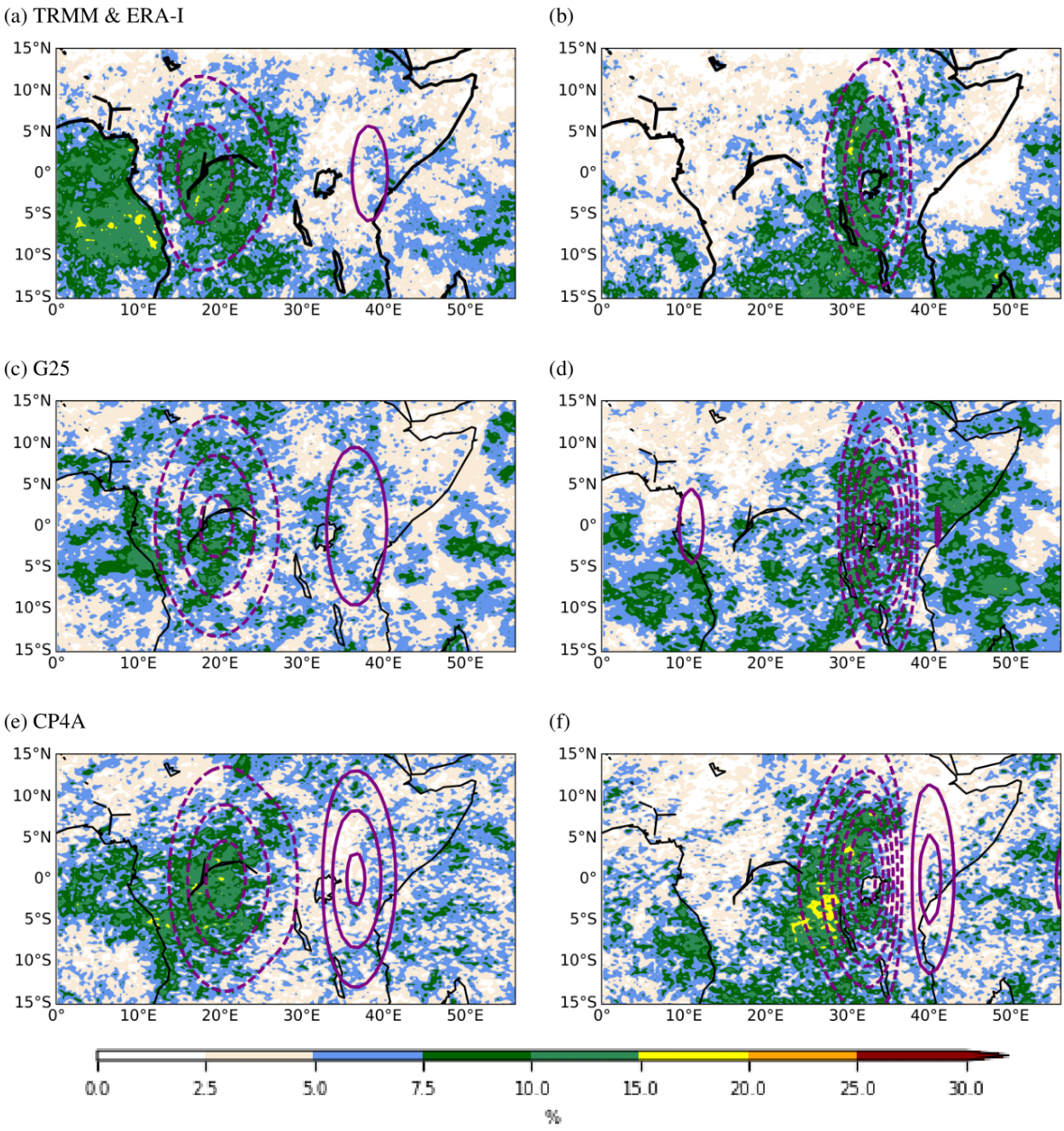

Figure 6.2: The likelihood of extreme precipitation exceeding the 95th percentile at each grid-point during the days with high-amplitude Kelvin waves in March-April-May (MAM) for (a), (b) TRMM (c), (d) G25 and (e), (f) CP4A. Kelvin wave composite is based on high amplitude Kelvin wave days over WEA (W, left column) and EEA (right column). Contours show the 850 hPa Kelvin wave convergence composite on high amplitude waves. contour interval is 5.0 x 10^{-7} s^{-1}. Dashed contours indicate convergence and the solid ones show divergence.

(Figure 6.2d) shows a large area in Somalia where the likelihood of extreme precipitation is increased on days with a high-amplitude Kelvin wave over EEA. Recall that this is a climatologically drier sub-region in comparison to Equatorial Africa's other sub-regions (e.g., Figure 2.1). CP4A (Figure 6.2e) has a probability distribution that is similar to that in TRMM (Figure 6.2a) except over the Atlantic Ocean when the Kelvin wave is located over WEA. Similarly, when the CCKW is located over E, CP4A (Figure 6.2f) shows grid point probabilities of extreme precipitation that are similar to those in TRMM (Figure 6.2b) except over a few grid cells in southwestern Lake Victoria that show up to 15% likelihood of occurrence of extreme precipitation when

a CCKW is located over EEA. Another feature to note is that CP4A (Figure 6.2f) shows lower probabilities over Kenya and Ethiopia compared to TRMM (Figure 6.2b). This might be due to the stronger divergence in CP4A compared to ERA-I (see strong divergence at about 40°E in CP4A (Figure 6.2f). As discussed above, CP4A has an edge over G25 in simulating extreme precipitation patterns.

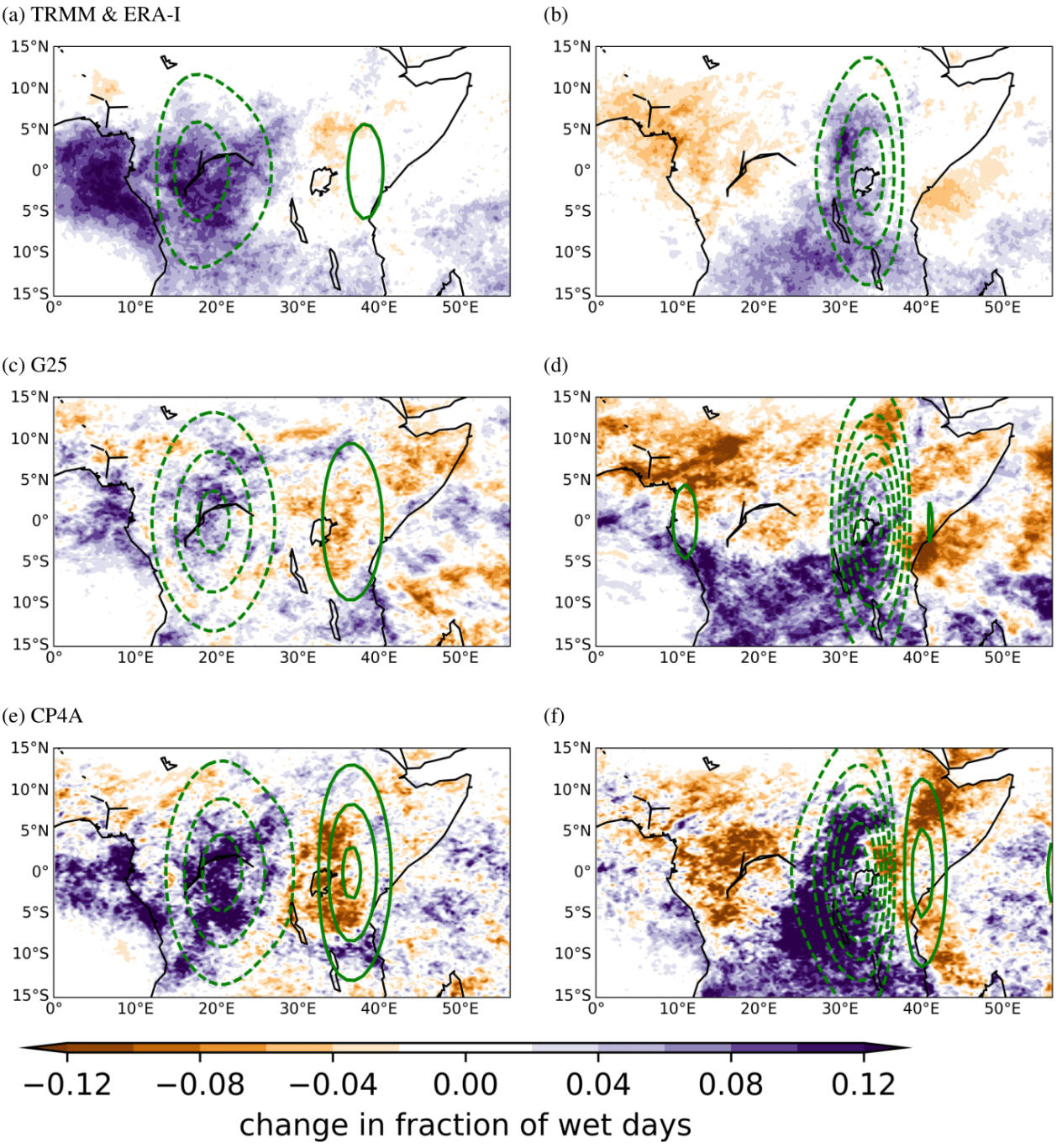

Figure 6.3: The difference in fraction of the days with precipitation greater than 1 mm day^{-1} between the average for high-amplitude Kelvin wave days and the seasonal mean in MAM over WEA (sub-region W) (left) and EEA (sub-region E) (right) for (a), (b) TRMM (c), (d) G25 and (e), (f) CP4A. Contours show the ERA-I based 850 hPa Kelvin wave convergence composite on high-amplitude waves. contour interval is 5.0 x 10^{-7} s^{-1}. Dashed contours indicate convergence and the solid ones show divergence.

Focus is now placed on the likelihood of occurrence of a wet day when a high-amplitude Kelvin wave propagates over Equatorial Africa. Here, a wet day is defined as one on which the day's precipitation exceeds

1 mm day^{-1}. A similar definition of a wet day has been used in several studies (e.g., Philippon et al., 2015; Ongoma et al., 2018; Ferrett et al., 2020; Jiang et al., 2021). This analysis is useful in revealing whether an increase in precipitation during the passage of CCKWs is due to an increase in the frequency of wet days or an increase in precipitation intensity. Jackson et al. (2019) investigated the impact of CCKWs on dry-day frequency and wet day intensity over Africa using TRMM and CP4A, and found that both metrics explained suppressed precipitation in Kelvin wave phase 5-7 and enhanced precipitation in Kelvin wave phases 1-3 (Kelvin wave phases are defined in their study). It is noted that Jackson et al. (2019) focused on April only and their metric for Kelvin wave activity is based on wavenumber-frequency filtering of OLR. Here, a Kelvin wave dataset based on dynamical fields (see §3.3.1) for boreal spring is used.

Figure 6.3 shows the spatial distribution of the difference in fraction of the days with precipitation greater than 1 mm day^{-1} between high-amplitude Kelvin wave and MAM climatology. In this figure, the grid points with a positive change in fraction indicate an increase in the frequency of occurrence of wet days. Figure 6.3 shows that, there is an increase in the frequency of wet days when high-amplitude Kelvin waves are located over a sub-region in Equatorial Africa. Both simulations are in agreement with TRMM in terms of having an overall increase in the fraction of wet days in the same general region. However, G25 (Figure 6.3c) shows a lower fractional increase of wet days compared to TRMM (Figure 6.3a) and CP4A (Figure 6.3e). Also visible is a stronger suppression of occurrence of wet days over EEA in G25 (Figure 6.3c) than TRMM (Figure 6.3a) when the Kelvin wave is located over WEA. When the Kelvin wave convergence is located over EEA, G25 (Figure 6.3d) shows a somewhat higher frequency of wet days compared to TRMM (Figure 6.3b) but nearly comparable to CP4A (Figure 6.3f). CP4A (Figure 6.3e) shows an increased frequency of wet days when a high-amplitude Kelvin wave is located over WEA that is comparable to TRMM (Figure 6.3a) but higher that G25 (Figure 6.3c). One noticeable difference between TRMM (Figure 6.3a, b) and CP4A (Figure 6.3e, f) is that CP4A shows a stronger suppression of the frequency of wet days over EEA. As discussed above, this might be due to the stronger Kelvin wave divergence in CP4A compared to that in ERA-I (see strong divergence over EEA in CP4A in Figure 6.3e compared to that in ERA-I in Figure 6.3a, and also Kelvin wave divergence at about 40^{o}E in Figure 6.3f that is absent in ERA-I, Figure 6.3b). Jackson et al. (2019) found a better response of CP4A to dry days associated with Kelvin waves. Another feature in Figure 6.3 to note is that the regions with the lowest 95th percentile thresholds (Figure 6.1) show the least frequency of wet days, for example, over the Horn of Africa.

Results in Figure 6.4 show enhanced precipitation intensities on wet days associated with high-amplitude Kelvin waves compared to the seasonal mean. For example, precipitation increases by up to 4 mm day^{-1} on wet days when a CCKW is located over Equatorial Africa. In agreement with TRMM, both simulations (Figure 6.4c-f) generally indicate an increase in precipitation intensities on wet days with a Kelvin wave. However, Figure 6.4 shows quantitative differences between TRMM and the simulated wet day precipitation. For example, G25 (Figure 6.4c) shows weaker precipitation intensities than TRMM (Figure 6.4a) and CP4A (Figure 6.4e) over both WEA and EEA. Similarly, when the Kelvin wave convergence is positioned over EEA (Figure 6.4d),

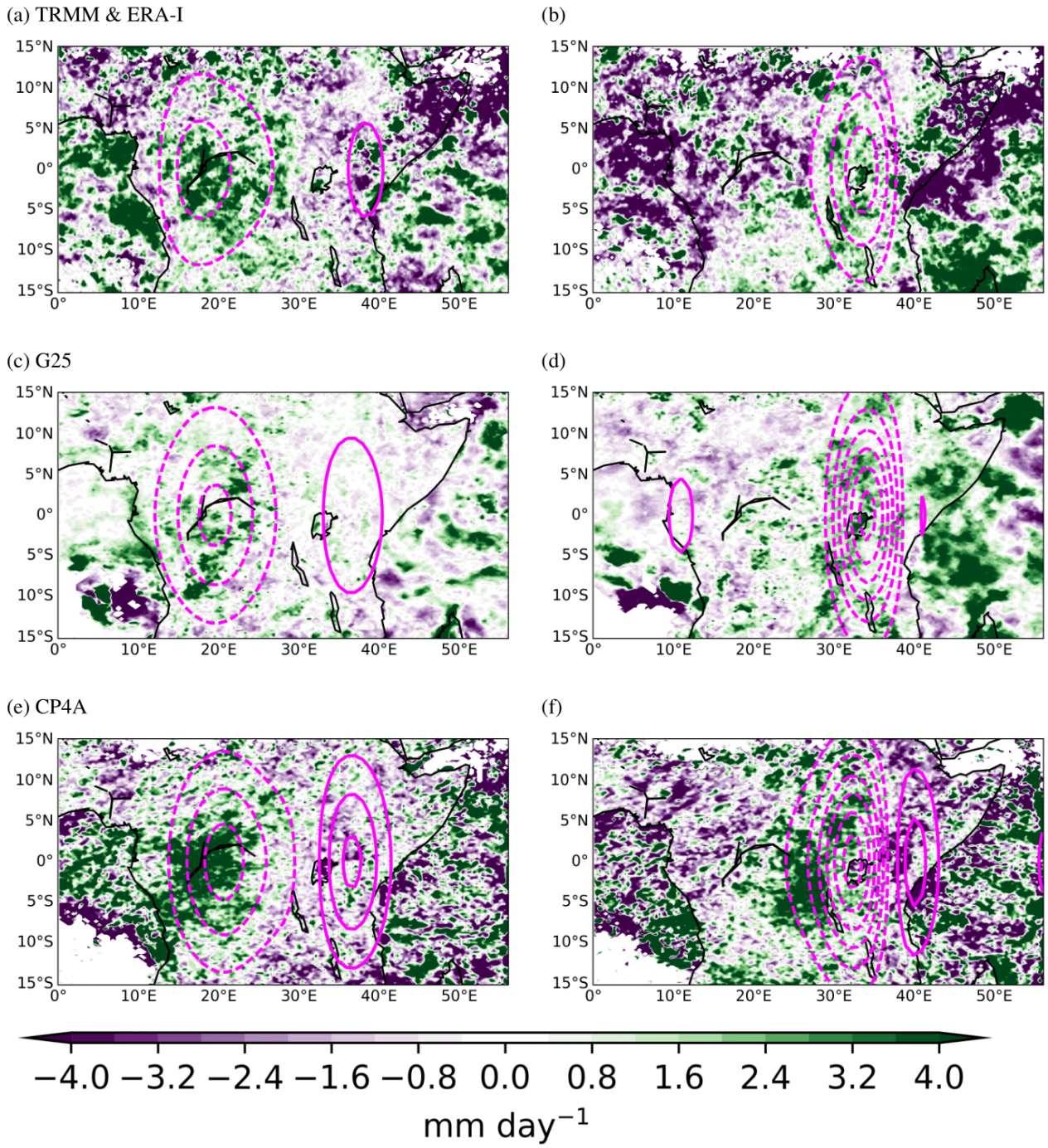

Figure 6.4: As in Figure 6.3 but for the difference in mean precipitation on days with precipitation greater than 1 mm day^{-1} in MAM for (a) and (b) TRMM, (c) and (d) G25, and (e) and (f) CP4A

the precipitation intensities in G25 are weaker but the pattern is similar to that in TRMM (Figure 6.4b) and CP4A (Figure 6.4f). With the Kelvin wave convergence located over EEA, increased precipitation intensities in G25 (Figure 6.4d) extend to the Horn of Africa while TRMM (Figure 6.4b) and CP4A (Figure 6.4c) show suppressed precipitation intensities over the Horn of Africa. The precipitation intensities in CP4A (Figure 6.4e) are similar to those in TRMM (Figure 6.4a). However, the signal stretches westward at about 30^{o}E, 5^{o}S in CP4A (Figure 6.4f) compared to TRMM (Figure 6.4b) and G25 (Figure 6.4d). It remains unclear why CP4A produces such a pattern but it might be due to the strong divergence at about 40^{o}E.

6.4 Impact of high-amplitude CCKWs on particular observed extreme precipitation events: A case study approach

Although taking an average over many events provides a general picture of a phenomenon, how a single event of a phenomenon evolves in space and time can be quite different. Undertaking a case-by-case approach reveals more details since the focus is placed on individual events, which is why the current chapter looks at case studies. This section focuses on case studies to further explore the role of high-amplitude CCKWs in influencing the eastward propagation of extreme precipitation episodes. First, the eastward propagating extreme precipitation episodes are identified using the definition described in Section 6.2. The eastward propagating extreme precipitation days identified are shown in the first column in Table 6.1. Each date shown in column 1 of Table 6.1 is the date when extreme precipitation is first detected in WEA (over W). To build a case study, two days preceding that date and three days following that date are used. For example, if extreme precipitation was detected in W on 23-03-1998 then the case study period starts 21-03-1998 and ends 26-03-1998. Case studies in Table 6.1 are based on observations (TRMM). These case studies are "extraordinary" extreme precipitation episodes because they are based on dates when precipitation is in the top in top 5% over a pair of sub-regions' 10 year climatology.

Date	Collocated with Kelv Conv	Case study period		Case study number
23-03-1998	Yes	21-03-1998	26-03-1998	8
12-01-1999	Yes	10-01-1999	15-01-1999	7
14-11-2000	Yes	12-11-2000	17-11-2000	6
05-04-2001	**No**	**03-04-2001**	**08-04-2001**	**4**
10-04-2002	**Yes**	**08-04-2002**	**13-04-2002**	**1**
17-04-2002	**Yes**	**15-04-2002**	**20-04-2002**	**2**
28-04-2002	**Yes**	**26-04-2002**	**01-05-2002**	**3**
21-12-2002	Yes	19-12-2002	24-12-2002	9
28-12-2002	Yes	26-12-2002	31-12-2002	10
17-03-2006	**No**	**15-03-2006**	**20-03-2006**	**5**

Table 6.1: Extreme precipitation days in TRMM as identified using a pair of sub-regions shown in Figure 5.1a. The dates in the first column (days when extreme precipitation is first observed in a sub-region in WEA (W)) are used as centres for case studies. In second column, "Collocated with Kelv Conv" means that the extreme precipitation over W coincides with a high-amplitude Kelvin wave event. These case studies are numbered for purposes of presentation of analysis and results with a focus on those case studies in bold.

From Table 6.1, it can be seen that 40% of the case studies identified are in April, which corresponds to a month with high precipitation rate as shown in Figure 2.1. Jackson et al. (2019) analysed Kelvin wave activity in April because it is a month characterised by maximum precipitation over Equatorial Africa (also see Figure 2.1), and their results showed that April has the greatest variance in OLR caused by Kelvin waves. The case studies 1-3 (in rows 5, 6, 7, and in bold) are considered for further analysis because: firstly, these occurred in the same month and year, and so this analysis may not be affected by the differences in large-scale background state. Ridout and Flatau (2011) analysed two consecutive Kelvin wave case studies that propagated

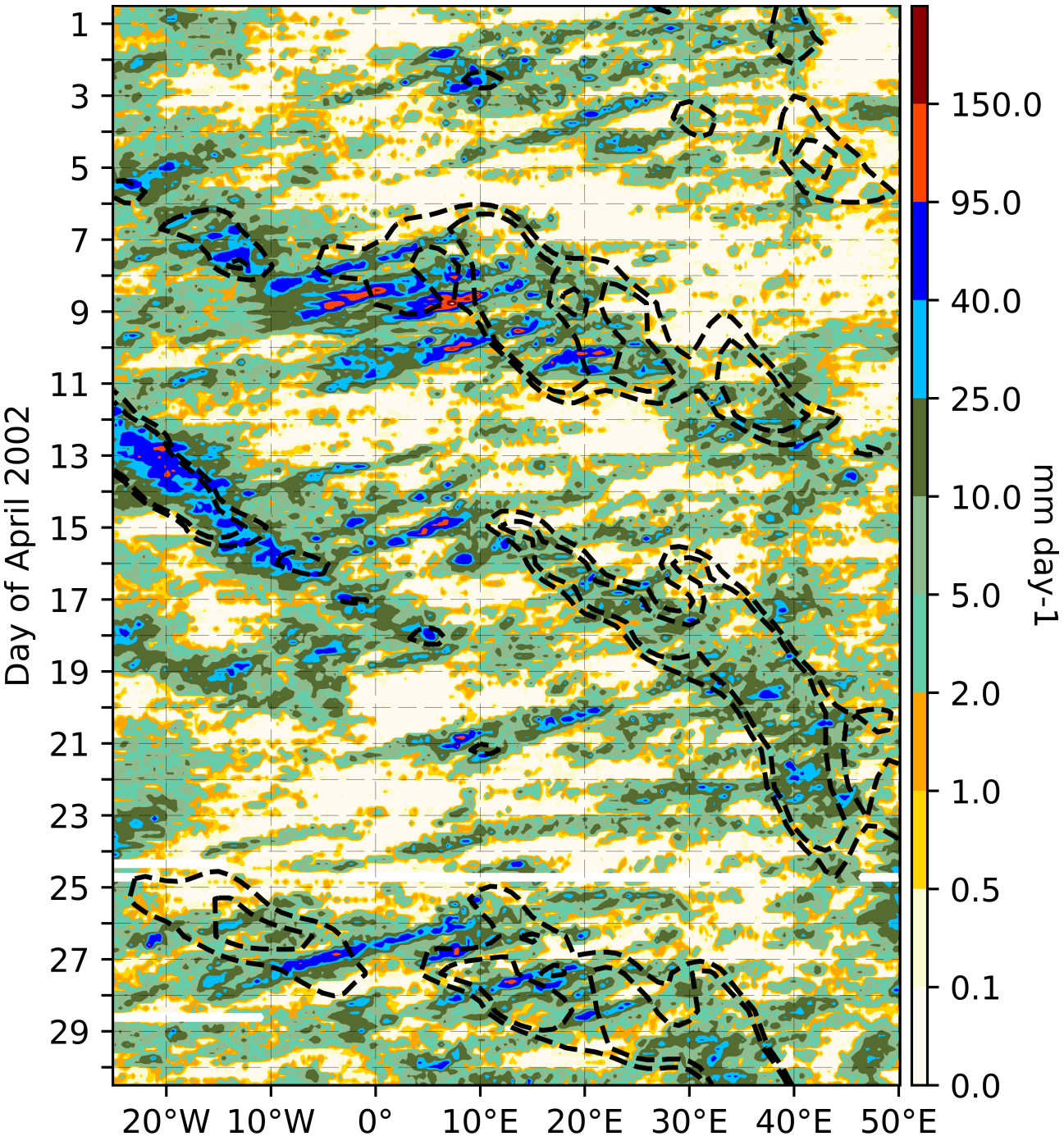

Figure 6.5: The Hovmöller based on total 3-hourly TRMM precipitation (shading) and Kelvin wave convergence for the same period (only Kelvin wave convergence amplitude of 1.5 x 10^{-8} s^{-1} and 1.1 x 10^{-8} s^{-1}). These two values are determined as described in Section 6.2.1. Both fields are latitudinally averaged over 7°S-7°N.

past Sumatra in June 2006, and Zhu and Li (2017) analysed two Kelvin wave case studies that occurred in the Indian Ocean in November 2011. Secondly, using case studies in April makes it easier to compare the results with those in Jackson et al. (2019), who studied the response of precipitation to Kelvin waves over Africa during April. And thirdly, this chapter focuses on Kelvin waves and precipitation in MAM. The other two case studies (case studies 4 and 5 in rows 4 and 10) are considered to be "unrelated" to high-amplitude Kelvin wave events (based on the definition of an high-amplitude Kelvin wave event as described in Section 6.2). These case studies are important to this study because they help us to answer the question relating to other possible forms

of precipitation variability besides high-amplitude Kelvin waves that might cause the eastward propagation of extreme precipitation across Equatorial Africa.

In order to gain a more detailed understanding of how each of the case studies might be associated with CCKWs, a Hovmöller plot showing Kelvin wave convergence overlaid on total precipitation is plotted for all the ten case studies in third column in Table 6.1. Then, by eye, checking is done to determine whether or not the Kelvin wave convergence (dashed contours e.g., see Figure 6.5) is collocated with the precipitation over the longitudinal extent of W. Since it is expected that extreme precipitation episodes are associated with strong Kelvin wave events, only Kelvin wave convergence above the 90^{th} percentile that is calculated over the sub-region W in WEA is plotted. Hovmöller diagrams are useful in understanding the dynamics of propagating atmospheric features (e.g., Persson, 2017), and they have been used in previous studies such as Nakazawa (1988) in exploring the eastward propagation of cloud clusters and in Glatt et al. (2011) in diagnosing Rossby wave trains. The term "Kelvin wave convergence" is used here to refer to convergence of the Kelvin wave wind field in the equatorial wave dataset described in Chapter 3 (§3.3.1).

Three eastward propagating extreme precipitation episodes shown in Table 6.1 are visible in Figure 6.5 for the latitudinal band 7^{o}S-7^{o}N. These constitute case studies, 8-13 April, 15-20 April, 26 April-1 May (hereafter referred to as case study 1, 2 and 3 respectively). Recall that a case study is defined as a sequence of six days [2 days preceding the day when precipitation occurs over a sub-region in WEA (shown in column 1 of Table 6.1) and 3 days after]. Figure 6.5 also shows high-amplitude Kelvin wave convergence that is collocated with high precipitation totals. An interesting feature in Figure 6.5 is that each eastward propagating band of precipitation is preceded by a dry signal suggesting suppressed convection. This confirms that a wave-like disturbance played a role in modulating extreme precipitation in each of the case studies. It was discussed in Chapter 4 that over the period March-June, 5-7 CCKWs propagate across Equatorial Africa on average (e.g., Wheeler and Nguyen, 2015; Sinclaire et al., 2015). This suggests that April 2002 is an interesting period to study because Figure 6.5 shows that three (about 50% of an average season's events) high-amplitude Kelvin wave events propagated across Equatorial Africa within a span of about 30 days.

It is also evident in Figure 6.5 that within each eastward propagating wet episode, coherent multiple westward propagating wet events with speed of between $15\text{-}20^{o}$ per day (approx. 19-25 m s^{-1}) can be seen. These could plausibly be westward propagating MCSs organised by an eastward propagating high-amplitude Kelvin wave (e.g., Mounier et al., 2007; Laing et al., 2011). This example is comparable to the eastward moving supercluster found in Nakazawa (1988). These westward propagating rain-producing systems that are modulated by CCKWs have been previously studied (e.g., Mounier et al., 2007; Jackson et al., 2009; Laing et al., 2011). Results in these studies showed that MCSs tend to grow larger and live longer in the presence of CCKWs. These westward propagating rain bands are beyond the scope of this thesis but would be interesting to explore. Since the MJO interacts with CCKWs (e.g., Haertel et al., 2015; Sobel and Kim, 2012), the Real-time Multivariate MJO series 1 (RMM1) and RMM2 (MJO Phase diagram on `www.bom.gov.au/climate/`

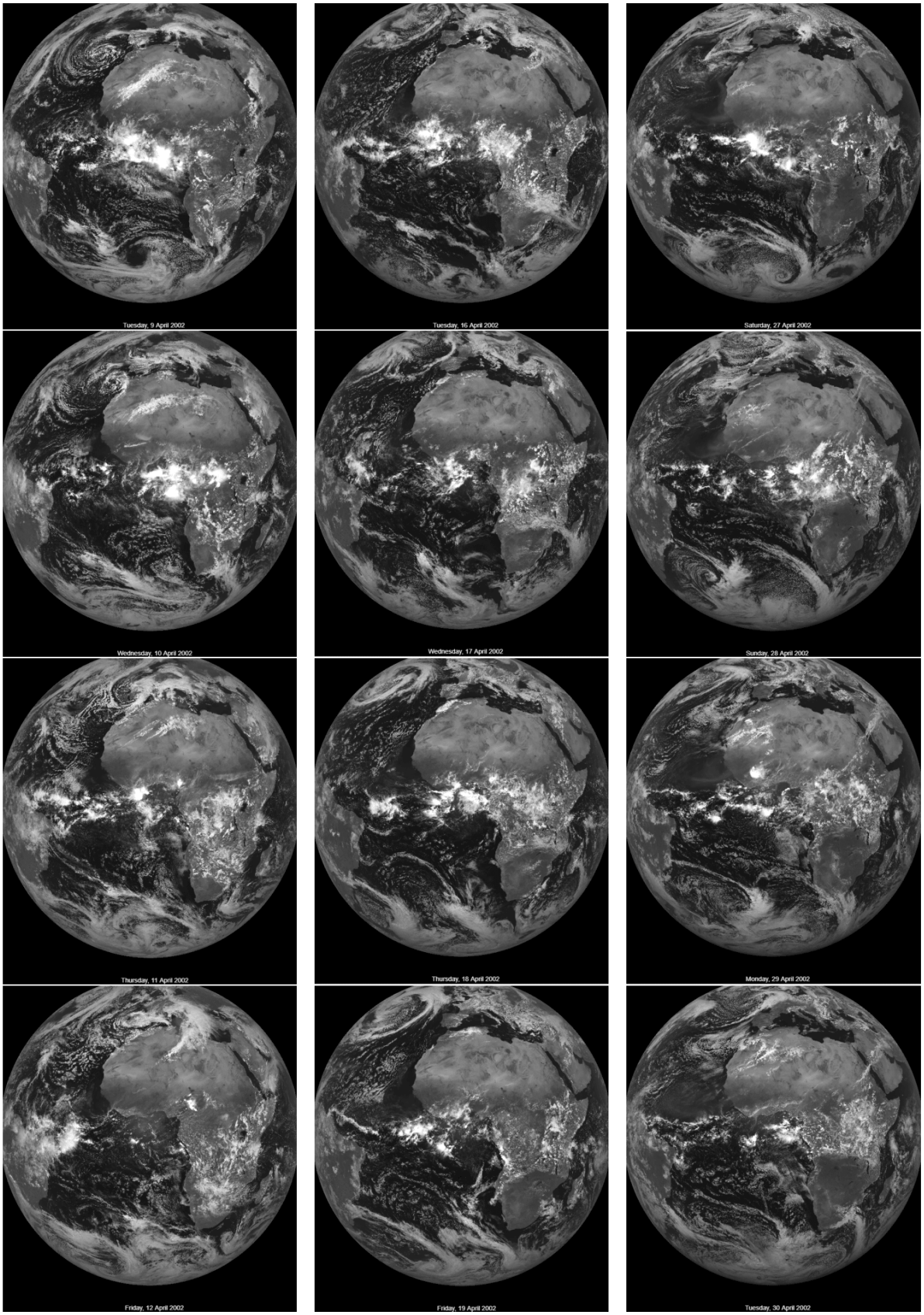

Figure 6.6: Satellite images from the visible channel for 1200UTC on each day showing convective clouds over some days in the case studies, 9-12 April (left), 16-19 April (middle column) and 27-30 April (Right column). The date for each image is shown at the bottom centre of each image. Images taken from EUMETSAT (`https://pics.eumetsat.int/viewer/index.html`).

mjo) were used to check whether the case studies shown in Table 6.1 have a preferred phase of the MJO. It is found that 10%, 10%, 30% and 50% occurred when the MJO was in phase 8, 4, 2, and weak MJO respectively (see Figure 1.2 for the location of active MJO convection). Case studies 1, 2, 4 and 5 occurred when the MJO amplitude was weak while case study 3 coincide with phase 2. Although the number of case studies is small, it is likely that the MJO is not a major factor in these case studies since the highest percentage occurred when the amplitude of the MJO was weak.

First, this section examines case studies 1-3, which are related to high-amplitude CCKWs. Two of the case studies shown in Table 6.1 are not associated with high-amplitude Kelvin waves. What, then, might be causing the eastward propagation of the wet signal in these case studies? To address this issue, Section 6.4.6 focuses on those two case studies, which are labelled case study 4 and 5. Below, the description of the synoptic situation associated with case studies 1-3 is given. An analysis of the dynamical and thermodynamical fields associated with extreme precipitation episodes and high-amplitude Kelvin waves that propagated across Equatorial Africa in April 2002 is presented.

6.4.1 Satellite imagery for case studies 1-3

Nakazawa (1988) used the Geostationary Meteorological Satellite (GMS) Infrared (IR) images to study eastward propagating cloud clusters (e.g., their Figure 3), and later, Straub and Kiladis (2002) used satellite images from NOAA's Geostationary Operational Environmental Satellite Program (GOES-9) in a case study of a CCKW in the eastern Pacific Ocean (e.g., their Figure 4). Several other scientists have used OLR to isolate Kelvin wave activity (e.g., Wheeler et al., 2000; Sinclaire et al., 2015; Mekonnen and Thorncroft, 2016; Jackson et al., 2019). This motivates an interest in examining the degree of convection organisation (by eye) in the cloudiness field over some days in case studies 1-3. For each case study, four satellite images are shown, spanning the period from one day before precipitation is observed over W until two days after. Unlike the studies above, visible satellite images are shown to provide greater resolution and detail.

In Figure 6.6, one sees that 1 day before precipitation is detected in WEA (i.e., on 9, 16, and 27 April, "organised" deep convective clouds can be seen over the Atlantic Ocean while much of Equatorial Africa is dominated by isolated and less bright cloudiness. The large white patches of cloudiness are seen to propagate eastward and by 10, 17 and 28 April, organised deep convective clouds can be seen mainly over WEA, while over EEA the clouds are isolated and less organised. These convective clouds are aligned with TRMM precipitation on 10, 17 and 28 April shown in Figure 6.7. More interesting cloudiness patterns can be seen on the 16 and 17 April, in which to the west of less organised clouds (over EEA), one sees a signal of well organised deep convection over WEA and further west, a cloudless region can be seen. The convective cloud pattern shown on 16 and 17 April fits a description of alternating regions of enhanced and suppressed convection associated with a Kelvin wave (e.g., Jackson et al., 2019). And 2-3 days after the precipitation was detected over WEA, the Kelvin wave has propagated across much of Equatorial Africa. This explains why the convective cloudiness on

12, 19 and 30 April is more present and organised over EEA compared with WEA. Figure 6.6 demonstrates the role of high-amplitude Kelvin waves in organising convection and the associated precipitation. This figure gives us confidence in the case studies identified in that as would be expected, the precipitation in the case studies is associated with the regional cloud pattern. It is worth noting that Figure 6.6 indicates multiscale convective features suggesting that disentangling these features to identify the role of CCKWs in organising convection and precipitation over these case studies may not be straightforward.

6.4.2 The structure and characteristics of daily total precipitation and horizontal wind

The pattern of daily total precipitation and 850 hPa horizontal wind for case studies 1-3 are now analysed. Figure 6.7 shows the patterns of the daily total precipitation for each day (over each case study) and 850 hPa horizontal wind. The precipitation over the Atlantic Ocean on 9 and 10 April in Figure 6.7 matches with the cloudiness in Figure 6.6 (note that Figure 6.6 spans 9-12, 16-19 and 27-30 April for left, middle and right column respectively, while Figure 6.7 spans 8-13, 15-20 April, 26 April-1 May for left, middle and right column respectively). Also, on 12 April in Figure 6.6 (column 1, bottom panel) much of the cloudiness is seen over EEA, extending from southwest to northeast EEA. This is clearly aligned with the precipitation pattern on 12 April in Figure 6.7. Similar matching cloudiness in Figure 6.6 with the precipitation patterns in Figure 6.7 can be seen in case studies 2 and 3.

The eastward propagating wet signal that is broadly associated with the Kelvin wave convergence can be seen in each of the case studies 1-3. The precipitation episodes displayed in these case studies show that the rains over the coast of WEA (e.g., west of about 11^{o}E) seem to persist for a day or two before it is detected over WEA. The spatial precipitation rate variations shown in Figure 6.7 may be suggesting that there are several factors influencing the precipitation variability over this region. 8 and 12 April (in case study 1: left column) display a pattern similar to the composite (e.g., Figure 5.4) in which when precipitation is enhanced over WEA, it is suppressed over EEA and vice versa (e.g., Mekonnen and Thorncroft, 2016).

When the strong precipitation signal dominates the west coast of Equatorial Africa, the low-level wind is generally easterly over the whole of Equatorial Africa and generally weak over the Atlantic (e.g., on 8, 9, 15 and 26 April) but as the precipitation penetrates inland, the winds strengthen and become westerly near the equator (e.g., on 10, 11, 17, 18, 28, and 29 April in Figure 6.7). The climatological mean of 850 hPa horizontal wind during April is generally easterly (e.g., Sinclaire et al., 2015; their Figure 3), showing that these Kelvin waves are likely causing a reversal of the climatological zonal wind direction, and this westerly flow is important in transporting moisture from Atlantic into the interior of Equatorial Africa (e.g., Pokam et al., 2012) as discussed below. On 10, 17, 18 and 29 April, the strong precipitation signal appears to be located on the leading edge of the total westerly winds (Figure 6.7). As the precipitation signal progresses further east (located over EEA, i.e. 2-3 days after it was detected in WEA), the westerly flow appears to become weaker, and then changes to easterly (e.g., 13, 14 and 21 April) as the CCKWs exit EEA. Such a structure of the wind field is similar to

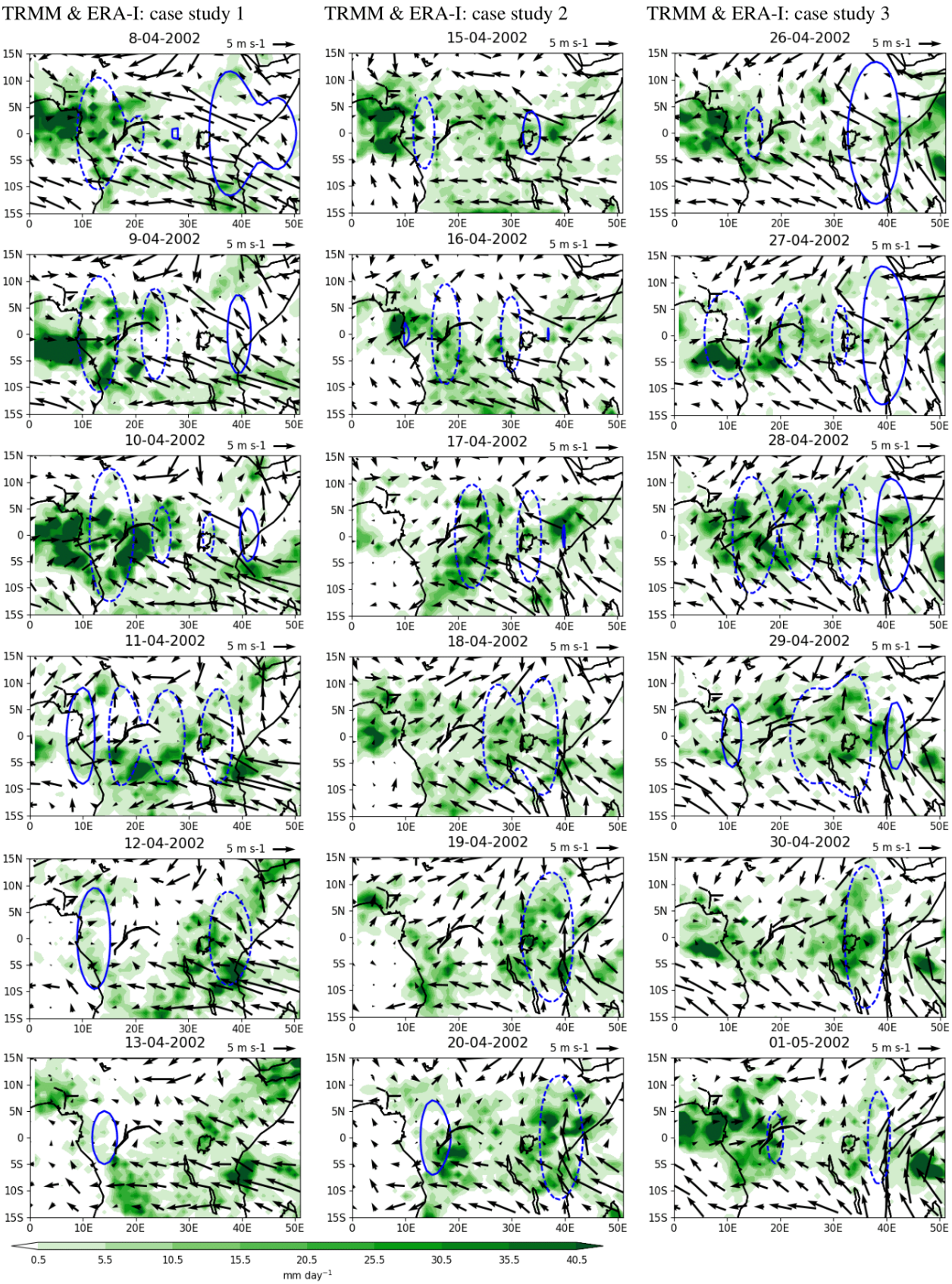

Figure 6.7: The characteristics of daily total TRMM precipitation (shading), Kelvin wave divergence for each day (blue contours: solid is divergence, dashed is convergence) and ERA-I 850 hPa total horizontal wind (vectors) for case study 1 (8-13 April) (left), case study 2 (15-20 April) (middle column) and case study 3 (26 April-1 May) (Right column). contour interval is 1.5 x 10^{-6} s^{-1}, and zero contour is not shown. Reference wind is shown at the top right of each panel.

that shown in Gill (1980), observational studies (e.g., Straub and Kiladis, 2002), and model experiments (e.g., Tulich and Mapes, 2008). The structure of the wind field in Figure 6.7 confirms the role of low-level westerly flow in the eastward propagation of convection and precipitation.

6.4.3 Low-level (850 hPa) anomalous moisture flux divergence and horizontal wind anomalies

Moisture flux convergence/divergence is analysed here because it is an important component in the coupling of convection and precipitation. Figure 6.8 shows the anomalous low-level moisture flux divergence, Kelvin wave convergence and 850 hPa horizontal wind anomalies for case studies 1-3. Broadly, the patterns in the anomalous moisture flux convergence are consistent with the precipitation patterns in Figure 6.7. This is physically consistent because moisture flux convergence is the main moisture source for strong tropical precipitation. Notably, although the moisture flux convergence appears to be noisy, there is a signature of eastward propagation that is aligned with the Kelvin wave convergence particularly in case study 2 (15-20 April). Also, the westerly wind anomalies can be seen to converge into regions of enhanced moisture flux convergence suggesting that the anomalous westerly flow is helping to transport moisture.

6.4.4 Specific humidity profiles

The vertical profile of specific humidity in ERA-I associated with case studies 1-5 is also examined. The area average of the anomalous specific humidity over the sub-regions shows that low-to-midtropospheric specific humidity tends to increase in the vicinity of a CCKW. The vertical structure of the anomalous specific humidity shows a westward tilt with height (figure not shown). A similar plot but based on CP4A simulated anomalous specific humidity is shown in Section 6.5.3. The structure of the specific humidity in ERA-I for case studies 1-3 is broadly similar to that shown for the CP4A case study on 18-23 April 1998 in Figure 6.13, which is discussed more in Section 6.5.3.

6.4.5 vertical profile of vertical velocity

Finally, the structure of upward motion over case studies 1-3 is examined because vertical motion is important for transporting moisture into the lower-to-midtroposphere. Figure 6.9 shows the total vertical velocity over case studies 1-3. The large-scale ascent seen on 8-9, 15-16, and 26-27 April in Figure 6.9 matches the precipitation signal seen west of 20^{o}E on the same dates in Figure 6.7. On 10, 17 and 28 April, the upward motion has shifted eastward together with the precipitation (see Figure 6.7). As the CCKW propagates into EEA, the upward motion is generally weaker (e.g., on 12, 19, 30 April). Also noticeable is that on 12, 19 and 30 April, upward motion from the mid-to-upper troposphere and descending motion from the mid-troposphere to the surface is suggestive of stratiform precipitation. Figure 6.7 (e.g., 12-13, 19, 20 and 30 April-1 May) shows widespread precipitation over much of EEA, consistent with the structure of upward motion in Figure 6.9. Besides the large-scale ascent seen in Figure 6.9, small-scale convective features extending from the surface into

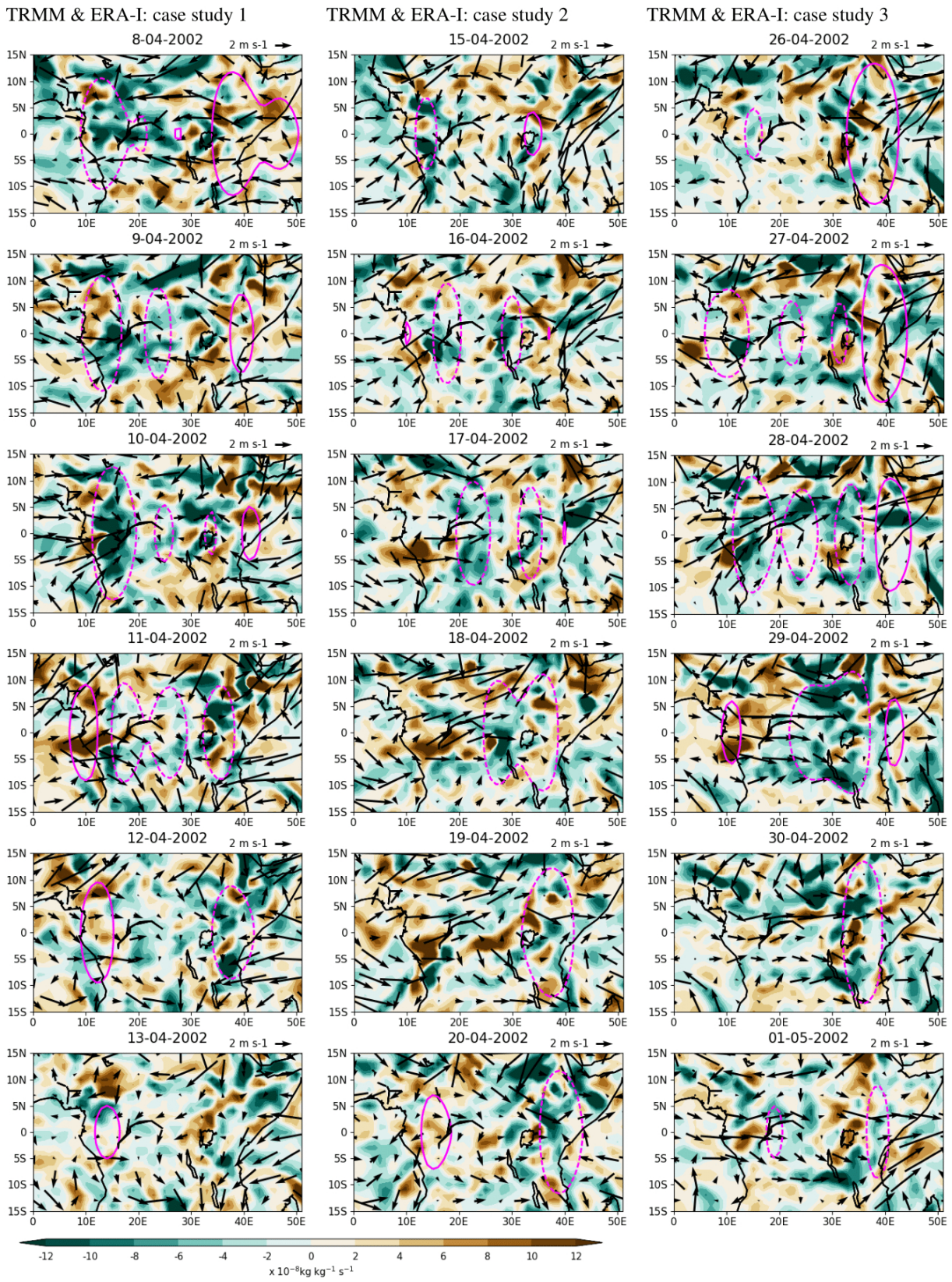

Figure 6.8: The evolution of 850 hPa moisture flux divergence anomalies (shading), Kelvin wave divergence for each day (magenta contours: solid is divergence, dashed is convergence) and ERA-I 850 hPa horizontal wind anomalies (vectors) for case study 1 (8-13 April) (left), case study 2 (15-20 April) (middle column) and case study 3 (26 April-1 May) (Right column). contour interval is 1.5 x 10^{-6} s^{-1}, and zero contour is not shown. Reference wind is shown at the top right of each panel.

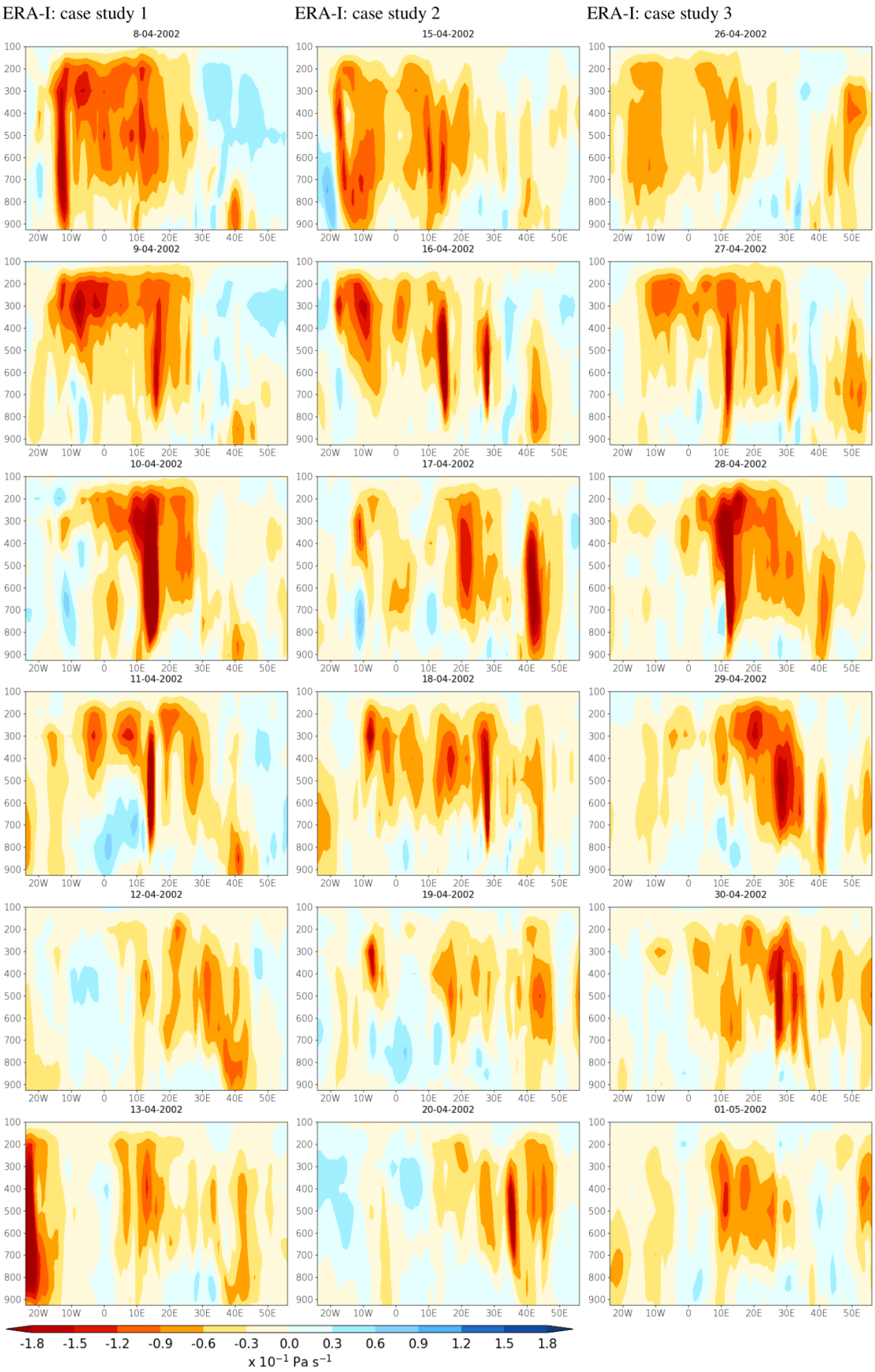

Figure 6.9: The height-longitude plot of vertical pressure velocity for case study 1 (8-13 April) (left), case study 2 (15-20 April) (middle column) and case study 3 (26 April-1 May) (Right column). The negative values (red shading) represent ascent, and likewise positive values (blue shading) for descent. Vertical velocity is averaged between 7°S-7°N.

the upper troposphere can be seen. These are further discussed in Section 6.4.7. The westward tilt of upward motion on, for example, 9, 10, 11, 12, 16, 17, 20, 28 and 30 April suggest gradual transport of moisture into the mid-to-upper troposphere. However, spiky upward motion can be seen as part of the large-scale upward motion (e.g., on 11 April between 10-20°E, and at 41°E), these may be interpreted to be small-scale disturbances embedded in the large-scale upward motion associated with Kelvin waves. A similar plot but for case studies 4 and 5 shows similar spikes of upward motion aligned with patches of grid points with high precipitation rates (not shown).

6.4.6 Precipitation events "unrelated" to a Kelvin wave event

Chapters 4 and 5 showed that a significant fraction of eastward propagating precipitation events are unrelated to a Kelvin wave event. Table 6.1 shows two case studies (case study 4: 3-8 April 2001 and case study 5: 15-20 March 2006) that are not associated with high-amplitude Kelvin wave events. Figure 6.10 shows the total precipitation, the 850 hPa Kelvin wave convergence and the 850 hPa total horizontal wind. The patterns of the fields in Figures 6.7 (case studies 1, 2 and 3) and 6.10 (case studies 4-5) are somewhat different, for example, the Kelvin wave convergence is generally weaker in case studies 4 and 5. Generally, the precipitation signal in case studies 4-5 is weaker than that in case studies 1-3. This might be due to weaker Kelvin wave convergence in case studies 4-5. In comparison to Figure 6.7, the eastward propagation of precipitation across the entire 6 day sequence in case studies 4 and 5 is not easily noticeable particularly in case study 5. For instance, in case study 4, after 5 April (centre of the case study), a strong precipitation signal is expected to propagate eastward but instead it is seen to persist over WEA (see 6 April 2001), and in case study 5, the precipitation across Equatorial Africa is weak on 15 and 16 March, and only becomes strong on 17 March and appears to propagate eastward.

Looking at the low-level horizontal wind patterns, case study 4 (left column of Figure 6.10) is in several aspects different from case study 5 (right column). For example, on 3 and 4 April (1-2 days before precipitation is detected in the sub-region in WEA), relatively strong westerly flow can be seen to the west of the location of the precipitation and easterly flow to the east of it, but this is not the case in case study 5 (on 15 and 16). In case study 5, the winds are mainly easterly and weak over central WEA. The lack of the westerlies in case study 5 might explain the weak precipitation signal on 15 and 16 (Figure 6.10). On 20 March, weak easterlies can be seen as the precipitation signal weakens. The coherent eastward shift of the leading edge of the easterly flow in case study 5 still suggests the presence of an eastward propagating disturbance (similar to Figure 6.7).

In case studies 4-5, there is evidence of a Kelvin wave propagating eastward which is linked to the weakly perturbed wind field, particularly in case study 5. An important feature to note in Case study 4 is that a weak Kelvin convergence can be seen east of a strong precipitation signal on 3 April. This Kelvin wave convergence is seen to coherently propagate eastward, but it is plausible that deep convection associated with the strong precipitation signal at about 19° initialised this weak Kelvin wave to the east. The Kelvin wave in case study 5

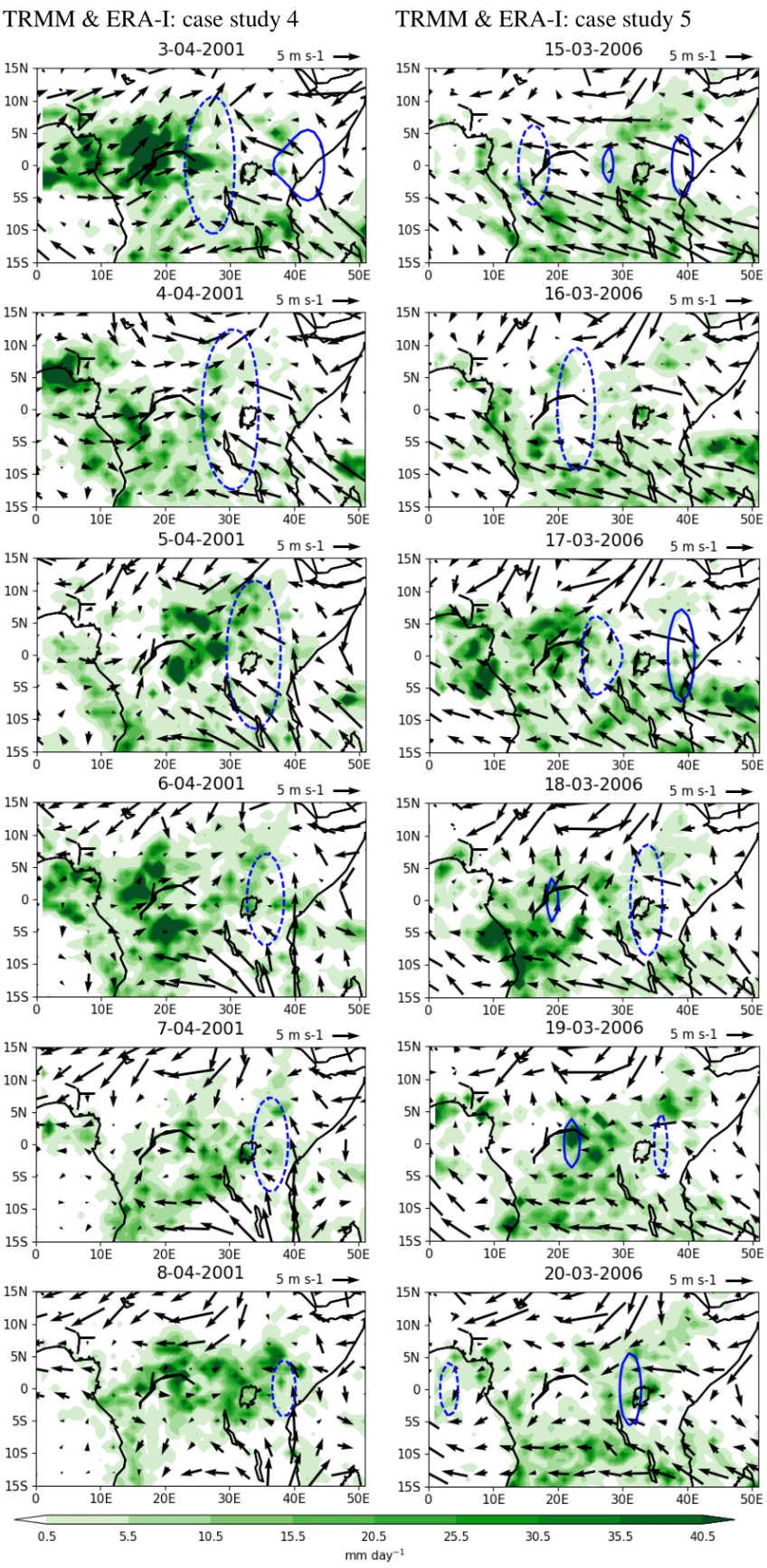

Figure 6.10: As in Figure 6.7 but for precipitation events that are unrelated to high-amplitude Kelvin waves. Case study 4 (3-8 April 2001) (left) and case study 5 (15-20 March 2006) (Right). The case studies are centred on 5 April and 17 March respectively.

might have propagated into the region as a weak Kelvin wave. The other possibility is that a weak Kelvin wave event was initiated in association with the preexisting deep convection over WEA as seems to be the case in case study 4 (e.g., Lindzen, 2003).

6.4.7 Small-scale convective and precipitation variability in the cases studies

In this section, the small-scale patterns of precipitation in the case studies discussed above are examined. These small-scale convective features are important processes of precipitation variability especially over EEA (Finney et al., 2020). Small-scale precipitation variability is generally associated with short-lived atmospheric processes (e.g., Laing et al., 2011), while the large-scale drivers of precipitation variability remain active for more than a day. Based on this, it is possible to speculate whether or not the precipitation in a particular grid cell is associated with a small-scale or large-scale mechanism. A closer examination of panels in Figure 6.6 shows multiscale convective features in the different case studies. For example, isolated patches of cloudiness can be seen over EEA on 11, 18, and 29 April in Figure 6.6. On visually inspecting the spatial patterns of precipitation in Figures 6.7 and 6.10, it is likely that precipitation in these case studies is influenced by both the small-scale and large-scale mechanisms. For example, precipitation west of about 20^{o}E appears to last for 2-3 days (e.g., 8-11, 15-17, 26-28 April in case studies 1, 2 and 3 respectively). While the CCKW is located over west of about 20^{o}E (e.g., on 8-9, 15-16 and 26-27 April), patches of strong precipitation rates can also be seen over EEA. On 18 April when the Kelvin wave convergence is located over EEA, one would expect precipitation over WEA to be suppressed but instead several small-scale precipitation features with a strong wet signal can be seen. To further illustrate this aspect, typical examples can be seen over the period 17-18 April (middle column) and 28-29 April (right column). On 17 April, the CCKW is located over WEA and can be seen to be associated with an extensive area of high precipitation rates at about 20^{o}E. On the same day, a smaller patch of precipitation above 35 mm day^{-1} covering an area of about 1-2^{o} in both longitude and latitude can be seen at about 40^{o}E. This rainy patch is linked to small-scale ascent on the same date in Figure 6.9. It would be expected that as the CCKW approaches EEA, this particular storm would grow larger and become more intense (e.g., Nguyen and Duvel, 2008; Laing et al., 2011). The presence of the Kelvin wave convergence on 19 April (2 days after the precipitation patch was seen) does not appear to enhance the size and the life cycle of this particular precipitation episode. In another typical example, on 28 April (right column), an area less than about 500 km^{2} with a high precipitation rate of more than 25 mm day^{-1} can be seen at about 40^{o}E. This rainy patch is aligned with upward motion (on 28 April in Figure 6.9) and Kelvin wave divergence, suggesting that the precipitation is most likely being driven by a small-scale feature. Two days later (30 April), although the Kelvin wave convergence can be seen over EEA, this rainy patch has waned. These short-lived rainy patches appear to be common to eastern and northeastern Lake Victoria including days when the Kelvin wave convergence is located over EEA. Other examples of small-scale precipitation features can be seen in several other panels in Figures 6.7 and 6.10, for instance both east and west of Lake Victoria on 15 April. Similar rainy patches that

may not be caused by CCKWs can also be seen over WEA (e.g., around 19^{o}E on 20 April 2002 in Figure 6.7 and 6 April 2001 in Figure 6.10). Overall, Figures 6.7 and 6.10 show several patches with high precipitation rates that may not be associated with the CCKWs.

6.5 Impact of simulated high-amplitude Kelvin waves on extreme precipitation: Case studies in G25 and CP4A

6.5.1 Case studies identified in the simulations

Having identified and examined case studies based on observations (TRMM) and ERA-I (§6.4), attention is shifted to case studies based on simulations. The methodology for identification of the case studies is as described in Section 6.2. Tables 6.2 and 6.3 show extreme precipitation episodes and the associated case studies in G25 and CP4A respectively. In both G25 and CP4A, the highest number of case studies are identified in April with 28% and 27% of the total number of case studies respectively. The dates for the case studies in the simulations (Tables 6.2 and 6.3) are not identical to those in TRMM (Table 6.1), and in any case, they are not expected to be identical since both simulations are free running. It is expected that the large scale forcing related to SST patterns would be similar to that in observations.

Date	Collocated with Kelv Conv	Case study period		Case study number
19-03-1998	Yes	17-03-1998	22-03-1998	A6
10-04-1999	**Yes**	**08-04-1999**	**13-04-1999**	**A1**
21-04-2000	**Yes**	**19-04-2000**	**24-04-2000**	**A2**
01-01-2001	Yes	29-12-2000	04-01-2001	A7
08-04-2001	**No**	**06-04-2001**	**11-04-2001**	**A4**
12-04-2001	**Yes**	**10-04-2001**	**15-04-2001**	**A3**
28-03-2003	**No**	**26-03-2003**	**01-04-2003**	**A5**
04-02-2004	No	02-02-2004	07-02-2004	A8
09-12-2004	No	07-12-2004	12-12-2004	A9
29-02-2005	No	27-02-2005	02-03-2005	A10
04-03-2005	Yes	02-03-2005	07-03-2005	A11
29-03-2005	No	27-03-2005	02-04-2005	A12
26-03-2006	Yes	24-03-2006	29-03-2006	A13
29-10-2006	No	27-10-2006	02-11-2006	A14

Table 6.2: Extreme precipitation days in G25 as identified using a pair of sub-regions shown in Figure 5.1e. The dates in column 1 (days when extreme precipitation is first observed in a sub-region is WEA; green box in Figure 5.1e) are used as centres for case studies. These case studies are numbered for purposes of presentation of results and analysis for those in bold is shown. The letter "A" attached to the case study number in column 4 is only meant to make these case studies unique.

Date	Collocated with Kelv Conv	Case study period		Case study number
20-01-1998	No	18-01-1998	23-01-1998	B5
11-03-1998	Yes	09-03-1998	14-01-1998	B6
20-04-1998	**Yes**	**18-04-1998**	**23-04-1998**	**B1**
15-05-1998	Yes	13-50-1998	18-05-1998	B7
19-05-1998	Yes	17-05-1998	22-05-1998	B8
25-03-2002	**No**	**23-03-2002**	**28-03-2002**	**B4**
07-12-2003	No	05-12-2003	10-12-2003	B9
13-11-2004	Yes	11-11-2004	16-11-2004	B10
25-11-2004	No	23-11-2004	28-11-2004	B11
13-04-2005	**Yes**	**11-04-2005**	**16-04-2005**	**B2**
29-04-2005	**Yes**	**27-04-2005**	**02-04-2005**	**B3**

Table 6.3: Same as Table 6.2 but for CP4A as identified using a pair of sub-regions shown in Figure 5.1i. The dates in column 1 (days when extreme precipitation is first observed in a sub-region is WEA; green box in Figure 5.1i) are used as centres for case studies. The letter "B" attached to the case study number in column 4 is only meant to make these case studies unique.

6.5.2 The structure and evolution characteristics of simulated daily total precipitation and horizontal wind

Figure 6.11 shows daily total precipitation and 850 hPa horizontal wind based on G25. It is important to note that the three case studies shown in Figure 6.11 are all in April but in different years. It is assumed that these should still be similar to each other in several respects due to their occurrence at the same time of year. In all the three case studies shown in Figure 6.11, the eastward propagation of precipitation can be seen (e.g., from 21-April 2000, 12-April 2001 and 10-April 1999 to the end of each case study). Also, it can be seen that the eastward propagation of precipitation in case study A1 is most evident between 10-13 April and is well aligned with Kelvin wave convergence. In all the case studies A1-A3, the precipitation appears to be generally over the equator as would be expected during April. The horizontal wind in case study A1 shows westerly flow accompanying the precipitation and the Kelvin wave convergence from 9-13 April 1999. Also, case study A1 shows the convergence of westerly flow and easterly flow, and the sub-region of low-level convergence is seen to propagate eastward together with Kelvin wave convergence. This low-level convergence is an important component for convection. The winds in case study A2 (middle column) are not consistent (mainly southeasterly for the first two days, that is, 19-04-2000 and 20-04-2000), becoming weak on 21-04-2000 (when precipitation is first observed in WEA) and then becoming westerly on 22-04-2000. The pattern of the wind field in the last two days of case study A2 (23-04-2000 and 24-04-2000) are broadly similar to that in the first two days of the case study (described above). Case study A3 (left column; 10-15 April 2001) has a similar pattern to that in case study A1 (right column, 8-13 April), albeit rather weaker. Returning to the precipitation patterns in case studies A1-A3, it can be seen that the precipitation rates in case study A1 (left column) are generally greater than those in case study A3 (right column). This might be because the westerly flow in case study A1 is stronger than that in case study A3. The nearly absent westerly flow and low-level convergence in case study A2 might partially account for the weak precipitation signal in this case study. This

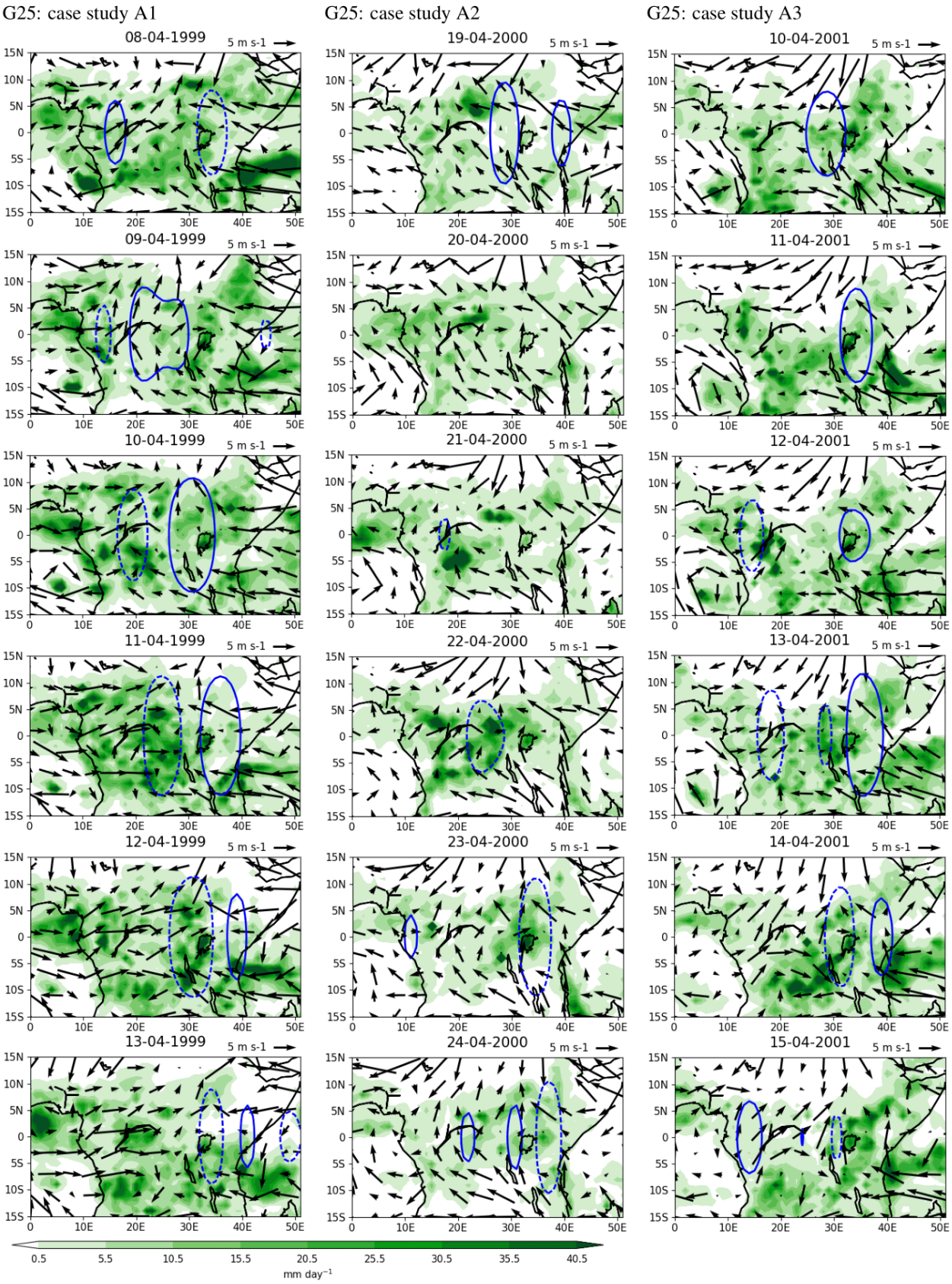

Figure 6.11: Same as in Figure 6.7 but for G25 for case study A1 (8-13 April 1999) (left), case study A2 (19-24 April 2000) (middle column) and case study A3 (10-15 April 2001) (Right column). Reference wind is shown at the top right of each panel.

result is consistent with results in the observations (e.g., §6.4.3).

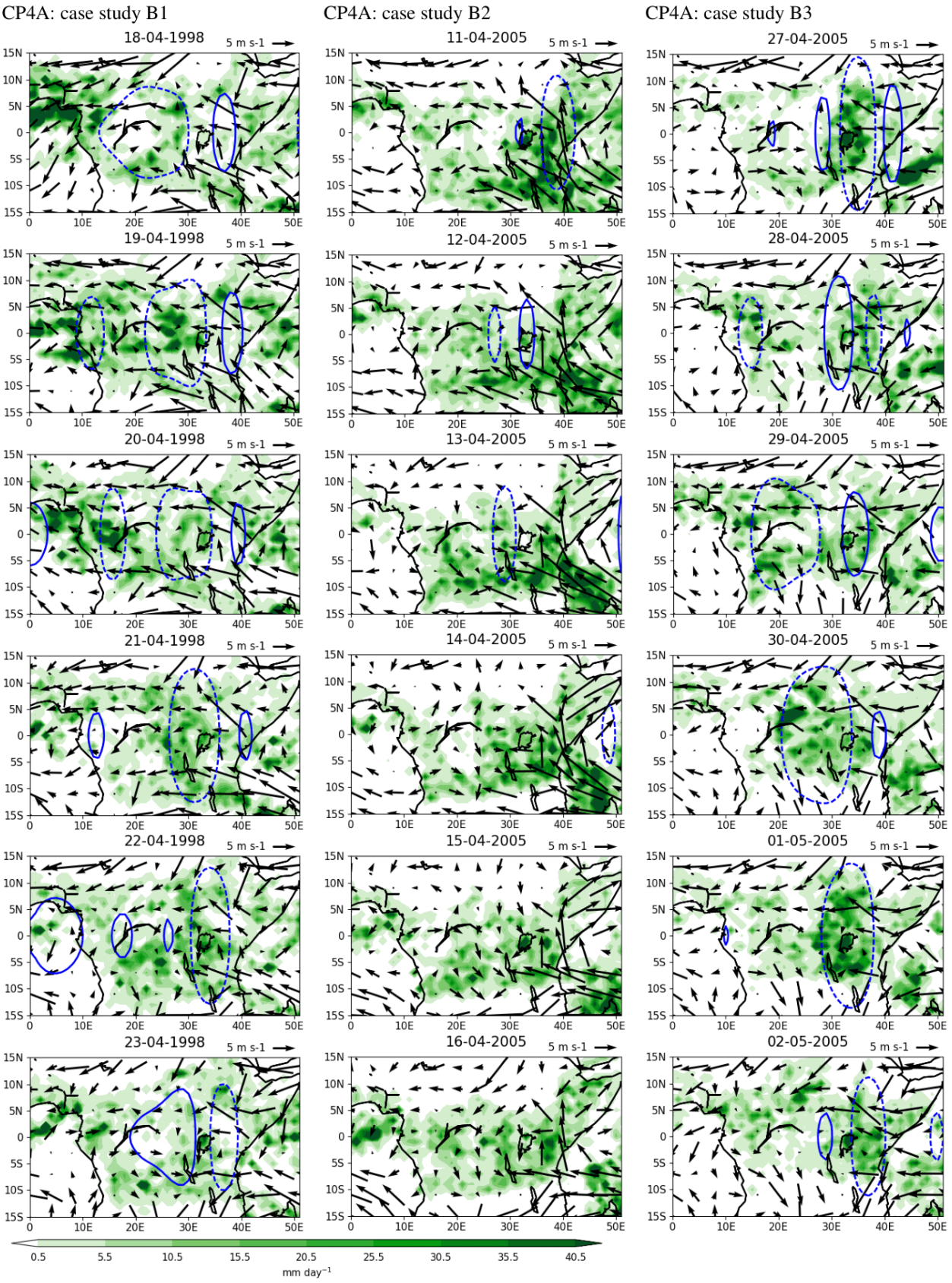

Figure 6.12: Same as in Figure 6.7 but for CP4A for case study B1 (18-23 April 1998) (left), case study B2 (11-16 April 2005) (middle column) and case study B3 (27 April-2 May 2005) (Right column). Reference wind is shown at the top right of each panel.

Comparing the precipitation and the wind field in case studies A1-A3 of Figure 6.11 to that in observed precipitation and ERA-I in Figure 6.7, (recall that these are not the same dates), the precipitation in Figure 6.11 is widespread and lighter compared to that in Figure 6.7 which appears more organised. However, the wind field is generally in agreement, particularly in case studies A1 and A3. Regarding the small-scale precipitation variability, G25 shows several patches of high precipitation rates. For example, between 10-13 April 2001, the Lake Victoria sub-region shows high precipitation rates that are aligned with Kelvin divergence, suggesting that Kelvin waves may not be modulating these small-scale features.

Focus is now placed on the case studies based on CP4A. Figure 6.12 shows three case studies identified as described in Section 6.2. It is important to note that these case studies are in April (similar to observations in Table 6.1) but different dates (in terms day and year). These case studies are examined because of the need to use CP4A as a scientific tool to further understand the role of high-amplitude Kelvin wave events in modulating extreme precipitation. The eastward propagation of extreme precipitation together with Kelvin wave convergence can be seen in all the three cases studies but it is clearer in case study B1 (left column, 18-23 April 1998) and case study B3 (right column, 27-April to 2-May 2005). For instance, weak easterly flow seen between 18-22 April 1998 becomes weak and westerly, at least near the equator on 23-April 1998. Several panels in Case studies B2 and B3 can be seen with weak westerlies converging with relatively stronger low-level easterlies (e.g., 13-15, 27-29 April 2005). The Kelvin wave convergence is generally smaller than the observed, at least in case study B2. Overall, the structure of the wind pattern in case studies B1-B3 (Figure 6.12) shows a weak similarity to that in Figures 6.11, 6.7, and that shown in case studies in previous publications such as Ridout and Flatau (2011), and Zhu and Li (2017).

Similar to observations, CP4A shows the variable spatial patterns of precipitation from case study to case study. The precipitation pattern in CP4A is generally similar to that in TRMM (Figure 6.7). For example, the high precipitation rates on the coast of WEA on 18-20 April 1998 have a similar structure to that in Figure 6.7 8-10 April 2002 and 26-28 April 2002. Figure 6.12 shows large areas of high precipitation rates, but small patches of high precipitation rates can also be seen. CP4A also shows sub-regions with high precipitation rates that seem unrelated to Kelvin wave convergence (e.g., on 29 April 2005). Also, analysis was done on CP4A's case study B4 which is unrated to an high-amplitude Kelvin wave. The patterns of precipitation were similar to that shown in Figure 6.12 but the Kelvin wave convergence was weaker across the 6 day period (figure not shown).

6.5.3 The structure of anomalous specific humidity in CP4A

Figure 6.13 shows the vertical profile of anomalous specific humidity for CP4A's case studies B1 (left column), case study B2 (middle column), and case study B3 (right column). A westward tilt with height in anomalous specific humidity can be seen in nearly all days of case study B1, but this is absent in case studies B2 and B3. The regions of anomalous moisture in Figure 6.13 are aligned with the precipitation signal in

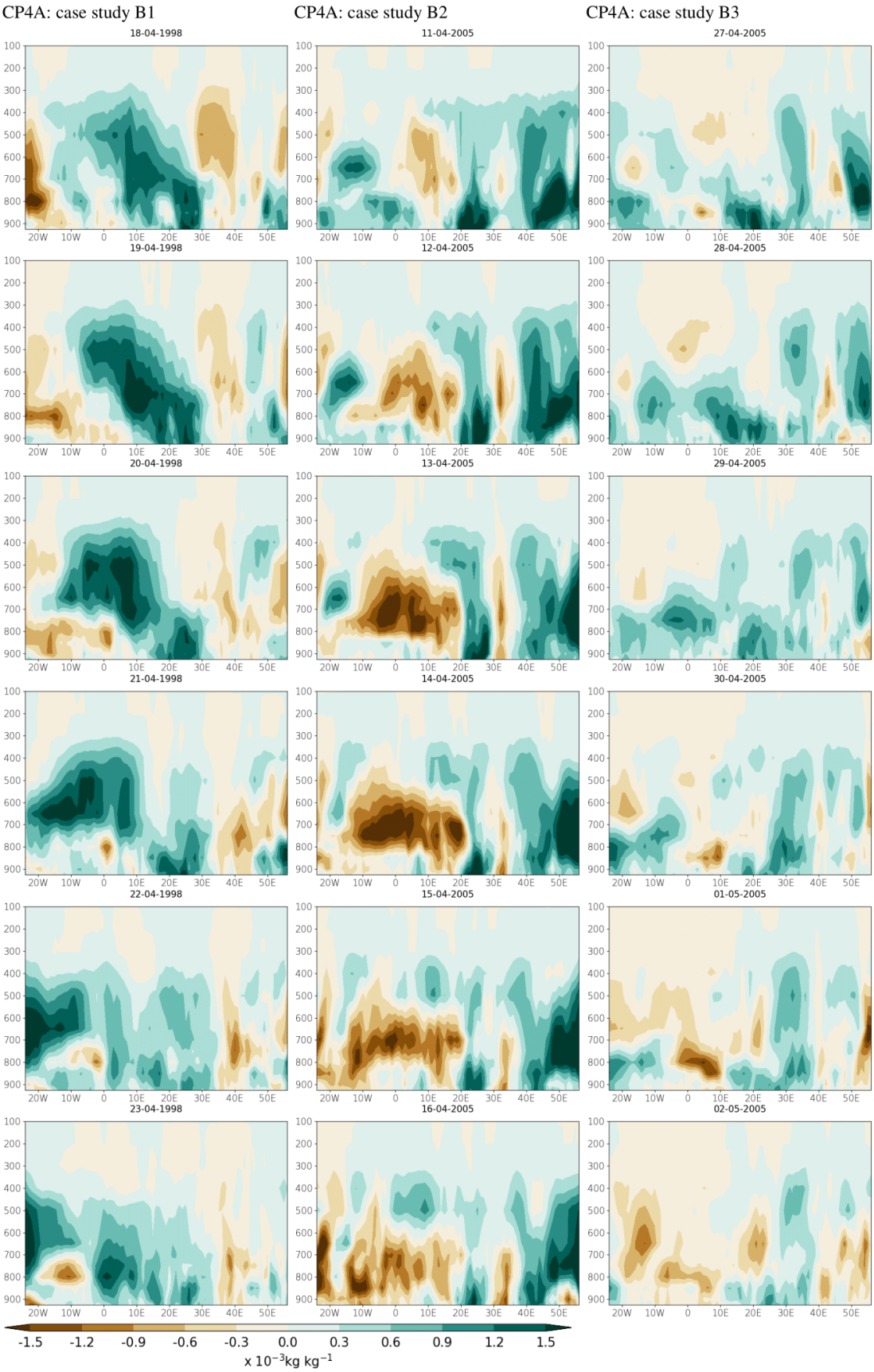

Figure 6.13: The height-longitude plot of anomalous specific humidity based on CP4A for case study B1 (18-23 April 1998) (left), case study B2 (11-16 April 2005) (middle column) and case study B3 (27 April- 2 May 2005) (Right column). Specific humidity is averaged between 7°S-7°N.

Figure 6.12. It can be seen that as the CCKW propagates to the east (e.g., 22-23 April 1998), the anomalous specific humidity weakens. In case study B2 (middle column), extensive areas that are anomalously dry can be seen, especially over WEA. This is consistent with the weak precipitation rates over much of WEA in Figure 6.12 (middle column). Also, small-scale moisture deficient sub-regions can be over EEA especially in case studies B1 and B2 (e.g., between 30-40^{o}E).

6.6 Discussion and conclusions

Chapter 4 of this thesis showed that Kelvin waves play a role in the eastward propagation of precipitation across Equatorial Africa, and chapter 5 explored the physical mechanisms through which Kelvin waves influence this propagation. In the first part of the current chapter, the statistical relationship between high-amplitude CCKWs and extreme precipitation over Equatorial Africa is investigated. It is found that extreme precipitation is up to twice as likely to occur compared to climatology over a sub-region in Equatorial Africa in the presence of a high-amplitude CCKW. It is also shown that there is an increased frequency of wet days, and the intensity of precipitation on wet days is enhanced by up to $\sim$4 mm day^{-1} when a high-amplitude CCKW is located over Equatorial Africa. Further, results based on case studies in which extreme precipitation is related or unrelated to high-amplitude Kelvin waves show that high-amplitude Kelvin wave events have significant, but somewhat varied, influence on the patterns of extreme precipitation. Small-scale non-propagating precipitation features that appear to be unmodulated by Kelvin waves are also found.

Regarding the 95th percentile thresholds for identifying extreme precipitation, CP4A shows grid point precipitation threshold rates that are comparable to TRMM (Figure 6.1). The precipitation threshold rates for G25 are generally weaker, highlighting the inability of the global model to simulate realistic extreme precipitation episodes, (e.g., Vogel et al., 2020). This might be due to both resolution and the physics in G25 (e.g., Brown et al., 2010). Based on the thresholds in Figure 6.1, the statistical relationship between high amplitude CCKWs and extreme precipitation over Equatorial Africa shows an increased likelihood of occurrence of an extreme precipitation episode with sub-regions showing up to 10% chance of occurrence of extreme precipitation (Figure 6.2) when a high-amplitude Kelvin wave convergence is located over a sub-region in Equatorial Africa. Subudhi and Landu (2019) found a 26% chance of occurrence of extreme precipitation due to a Kelvin wave located over India, and Ferrett et al. (2020) found a probability of occurrence of extreme rainfall of up to 15% when a Kelvin wave is positioned over east Malaysia and Indonesia. The difference between the result in the current study and the results in Subudhi and Landu (2019) and Ferrett et al. (2020) might be due to a weak Kelvin wave signal over Africa compared to that over the Maritime continent and India (e.g., Guo et al., 2014; Figure 2.4)

The linkage between the eastward propagating extreme precipitation episodes and the high-amplitude Kelvin waves is suggested by the overlap between the extreme precipitation and the Kelvin wave convergence in Figure 6.5. This figure is suggestive of the importance of high-amplitude Kelvin waves in providing a

favourable environment for the development of small scale convective systems into organised large scale convective features that are associated with extreme precipitation (e.g., Nguyen and Duvel, 2008; Ventrice and Thorncroft, 2013).

The results based on total wind field in this chapter suggest that a CCKW modulates the low-level wind flow in a manner that favours westerly flow and in turn westerly moisture transport from Atlantic Ocean into the interior of Equatorial Africa (e.g., Figures 6.7 and 6.8). It is shown that CCKWs perturb a low-level horizontal wind by weakening the easterly flow over WEA and establishing and maintaining westerly flow at least in the days shown in Figures 6.7 and 6.8. In most of the panels in Figure 6.7, the low-level westerlies are seen to converge with the easterlies and the region of convergence is seen to coherently shift eastward. These regions of low-level wind convergence generally coincide with the regions of moisture flux convergence (Figure 6.8) and precipitation shown in Figure 6.7. This indicates that Kelvin wave convergence is important for the eastward propagation of extreme precipitation in these case studies. In two CCKW case studies, Ridout and Flatau (2011) also showed westerlies associated with the precipitation as CCKWs propagate past Sumatra (see their Figures 14 and 18). In a CCKW case study in the eastern Pacific ITCZ, Straub and Kiladis (2002) showed that low-level anomalous winds associated with the passage of a CCKW changed from easterly to westerly in coincidence with deep convective activity. In agreement with Straub and Kiladis (2002), Figure 6.8 shows westerly anomalies aligned with the precipitation (Figure 6.7).

Although the eastward propagation of daily precipitation is evident in all case studies shown in Figure 6.7 and partly in Figure 6.10, the precipitation is spatially variable (e.g., Mekonnen et al., 2008). What this suggests is that CCKWs may not be the only factor influencing the convection and precipitation over these case studies. Some extreme precipitation events may not be related to high-amplitude Kelvin wave events (e.g., Table 6.1). Results from analysis of low-level horizontal wind for precipitation case studies that are unrelated to high-amplitude Kelvin wave events (e.g., Figure 6.10) shows structures that are broadly similar to that shown in case studies that are related to high-amplitude Kelvin wave events (e.g., Figure 6.7). The interpretation here is that these extreme precipitation case studies might be partly linked to lower-amplitude Kelvin wave events that were not captured by the definition of an high-amplitude Kelvin wave event. The Kelvin waves in the case studies (at least case study 4) in Figure 6.10 were likely initialised in response to deep convection over WEA (e.g., Lindzen, 2003; Baranowski et al., 2016).

The structure of the horizontal wind field, and the westward tilt with height of anomalous specific humidity associated with high-amplitude Kelvin waves shown in CP4A (e.g., Figures 6.12 and 6.13), appear to suggest that the simulated Kelvin waves weakly modulate both the wind and the moisture field. Both the wind field and the moisture are important for coupling between the Kelvin wave and the convection (e.g., Tulich et al., 2011). It is likely that in these case studies, CP4A inadequately simulated the shallow convection (Stratton et al., 2018) such that the bulk of the precipitation in Figure 6.12 comes from deep convection. If deep convection is the dominant precipitation-producing process in these case studies, then it is plausible that the westward tilt with

height similar to that shown in Figure 2.6 will be either weak or absent in the model (e.g., case studies B2-B3 in Figure 6.13). In the CP4A's case studies presented in this chapter, CP4A does not show consistent patterns of horizontal wind field and the vertical structure of anomalous specific humidity, and the patterns do not closely resemble the observed structure. As noted above, the westward tilt with height in anomalous specific humidity seen in ERA-I (e.g., Figure 5.6a-e and Zhu and Li, 2017; Figure 5) is absent in case studies B2-B3. However, ERA-I relies on a convection parametrisation scheme and a fairly coarse model. This means that ERA-I may struggle to trigger convection in the correct places and yet, the vertical structure of the specific humidity is strongly tied to the convection. Also, since there are few observations (radiosonde) over Africa that go into the data assimilation in production of ERA-I, and considering that satellite data has a low vertical resolution, it is likely that the vertical structure of anomalous specific humidity may not be very well determined by the input data (observations and satellite date). Due to the limitations in ERA-I, Figure 6.13 may be suggesting that the vertical structure of anomalous specific humidity for each case study might be quite different in the real atmosphere. This is an important result since it opens room for further inquiry. On the other hand, it is also possible that despite the convection being explicitly represented, a weakness in the coupling between the Kelvin waves and the convection might have caused the differences seen in Figure 6.13. For future work, examining several model fields (e.g., temperature profile and the associated cold pools) in many more individual case studies similar to those examined in this chapter may help to reach a robust conclusion.

The case studies analysed here have shown small-scale precipitation features that appear to independently develop and decay regardless of the phase of the Kelvin wave (e.g., Figures 6.7, 6.11, 6.12). Kelvin wave divergence would be expected to induce subsidence and suppress convection, and therefore cause dryness, but the small-scale precipitation patches composed of grid points of high precipitation rates appear to develop in regions of Kelvin wave divergence or decay even in the presence of Kelvin wave convergence. The interpretation is that these small-scale features are not modulated by CCKWs. This result appears to contradict results in Nguyen and Duvel (2008) and Laing et al. (2011) who found that CCKWs provide a favourable environment for MCSs to become larger and long-lived. It remains unclear how CCKWs interact with these small-scale features. It is also possible that the eastward propagating precipitation that is unrelated to Kelvin wave events discussed in Chapters 4 and 5 might be linked to a series of these seemingly non-propagating small-scale precipitation features (Kim et al., 2014). One way to further understand the characteristics of these small-scale convective and precipitation features would be to use radar data to identify and track these features using an approach described in Johnson et al. (1998) on days with and without an high-amplitude Kelvin wave event.

The extreme precipitation episodes studied in this chapter (defined as precipitation exceeding the 95th percentile of a sub-region's precipitation climatology) are rare precipitation events. However, when they occur, they can cause major distress to communities at the very least. In view of global warming, the Intergovernmental Panel on Climate Change (IPCC) Assessment Report 6 (AR6) (IPCC, 2021) confirmed what was reported in AR5 (IPCC, 2014) about an increase in the intensification of extreme precipitation episodes in various regions over the globe (Stocker, 2014; Seneviratne et al., 2021), and as such, studying extreme precipitation episodes

is important. This chapter has explored the characteristics of the eastward propagating extreme precipitation episodes, and the associated physical processes. These results provide a benchmark for studies that will focus on how these extreme precipitation episodes and the physical mechanisms will respond to global warming.

The key finding of this chapter is that both the observations and the simulations show that when a high-amplitude Kelvin wave is located over Equatorial Africa, extreme precipitation is up to twice as likely to occur compared to climatology. It is also found that high-amplitude Kelvin waves are likely to cause an increase of precipitation intensity of up to 4 mm day^{-1}. The extreme precipitation associated with high-amplitude Kelvin wave events is characterised by spatial and temporal variations. Furthermore, regardless of the phase of the Kelvin wave, small-scale convective systems develop and decay over the region. These small-scale features are, perhaps, controlled by localised drivers and not high-amplitude Kelvin wave events as might be expected. Further, the findings in this chapter confirm results presented in Chapters 4 and 5 that as a CCKW propagates into Equatorial Africa, precipitation over the region tends to be accompanied by low-level westerlies. The Kelvin waves modify the low-level horizontal wind from easterly to westerly flow, at least in the case studies examined here. The low-level westerlies then act to transport moisture from Atlantic Ocean into the interior of Equatorial Africa. The moisture transported into the region is an important component in the eastward propagation of the CCKW-precipitation coupled structure. The results in this chapter confirm the role of CCKWs in influencing extreme precipitation over Equatorial Africa. CP4A performs better than G25 in representing the precipitation characteristics associated with high-amplitude Kelvin wave events, albeit it does not show the westward tilt with height in the moisture field shown in ERA-I (e.g., Figure 5.6a-e). G25 on the other hand simulates the dynamical and thermodynamical fields that are similar to those in ERA-I. Considering that a limited number of simulated case studies have been examined, it is difficult to draw a robust conclusion regarding the capability of both models in simulating the individual Kelvin wave-precipitation linkage case studies. The association between eastward propagating extreme precipitation episodes and CCKWs suggests the potential source of predictability of extreme precipitation that may be obtained from Kelvin waves. It is therefore important that the interaction between Kelvin waves and large-scale circulation is satisfactorily represented in both numerical weather prediction and climate models.

Chapter 7

Conclusions

7.1 Purpose of this chapter

This chapter mainly discusses the key findings of this thesis and highlights how the objectives of the thesis outlined in Chapter 2 (§2.7) have been addressed. Section 7.2 summarises the key findings of this thesis, as detailed in Chapters 4-6, and discusses how these link to the objectives provided in Section 2.7. In Section 7.3, the known limitations of this work are indicated, and possible lines of future research are discussed. Finally, Section 7.4 highlights the implications of the findings of this thesis, and presents the scientific advances from this thesis.

7.2 Key findings

7.2.1 The observed precipitation relationship between Western Equatorial Africa and Eastern Equatorial Africa

The first two objectives of this thesis are to "assess the precipitation linkage between WEA and EEA based on small sub-regions characterized by similar daily precipitation characteristics" and "identify the possible mechanisms driving variability associated with the precipitation connection between WEA and EEA" (§2.7). Mekonnen and Thorncroft (2016) suggested a convective activity connection between the Congo Basin and East Africa during boreal summer using 22 years of cloud brightness temperature (e.g. see §2.1.3). However, these authors did not evaluate whether the connection between the Congo Basin and East Africa is present in precipitation and whether this connection is detectable in other rainy seasons.

To address the first objective, Chapter 4 examines daily TRMM precipitation estimates (§3.2.1), GPCP-1DD precipitation (§3.2.2, ERA-Interim atmospheric fields (§3.2.3) and a dynamics-based equatorial wave dataset (§3.3.1). Using the EOT technique (§3.3.3), this thesis has, for the first time, objectively subdivided most of Equatorial Africa into small sub-regions of similar daily precipitation characteristics (Chapter 4, Section 4.3). Using lead-lag correlation coefficient analysis between various pairs of WEA-EEA sub-regions and spatio-temporal correlation coefficient analysis over the domain under investigation, a synoptic-scale relationship in precipitation between WEA and EEA in which precipitation over EEA lags precipitation over WEA by 1–2 days is found (Sections 4.4 and 4.5). This relationship in precipitation depends on the particular pair of sub-regions under consideration. For instance, it is found that when precipitation over central WEA is enhanced, precipitation over sub-regions in South Sudan is suppressed and vice-versa (§4.5). So, a weak precipitation dipole between central WEA and South Sudan is suggested.

To address the second objective, two indices are developed, one based on daily precipitation (§4.6) and the other based on the equatorial wave dataset (§4.7). One key advantage of using this dynamics-based equatorial wave dataset over other methods used in several previous publications is that it does not use OLR to identify the equatorial wave modes, and uses no information that is directly related to precipitation or clouds. This means that the relationship between the equatorial wave dataset and precipitation is independent of the method used to produce the wave dataset. The indices are used to construct composites on precipitation anomalies and equatorial wave convergence (§4.7). Based on the composites, an apparent connection between eastward/northeastward propagating anomalous precipitation and Kelvin wave induced low-level convergence is shown (§4.7). It is also shown that both the Kelvin wave low-level convergence and the anomalous precipitation signal tend to weaken as they propagate over EEA. It is therefore postulated that Convectively Coupled Kelvin Waves (CCKWs) play a role in the 1-2 day connection in precipitation between WEA and EEA (Chapter 4).

7.2.2 Linking Equatorial African precipitation to Kelvin wave processes in the CP4-Africa convection-permitting regional climate simulation (CP4A) and a Global model (G25)

The third objective of this thesis is "to assess how well a state-of-the-art convection permitting model reproduces observational findings in the above two objectives, and to explore the associated physical mechanisms" (§2.7). To address this objective, Chapter 5 examines the first multi-year state-of-the-art Africa-wide convection permitting simulation (CP4A) (§3.2.4.2) and a coarse global simulation (G25) (§3.2.4.1), and evaluates both against observations (§3.2.1) and reanalysis (3.2.3), with a focus on precipitation and Kelvin wave activity. In essence, the synoptic-scale precipitation relationship between WEA and EEA is studied using both simulations. An equatorial wave dataset is developed for each of the simulations (§3.3.2) to explore the processes through which CCKWs influence the eastward propagation of precipitation across Equatorial Africa.

It is found that both simulations capture the eastward propagation of anomalous precipitation associated with simulated CCKWs (Chapter 5, Section 5.3). However, in comparison to TRMM, the precipitation anomalies are weaker in G25 (e.g., Stephens et al., 2010) while those in CP4A are realistic (e.g., Finney et al., 2019) (e.g., Sections 5.5 and 5.6). CCKWs modulate the eastward propagation of convection and precipitation across Equatorial Africa through two related physical processes. These are: 1) modulation of the low-level anomalous westerly flow that causes an increase in the low-level convergence, and 2) westerly moisture flux anomalies that amplify the lower-to-mid-tropospheric specific humidity. In short, these results suggest that what is important in the eastward propagation of precipitation across Equatorial Africa is the low-level moisture flux convergence and modification of lower-to-midtropospheric moisture (e.g., Section 5.7). Regarding the representation of CCKWs, both CP4A and G25 generally simulate the key horizontal structure of CCKWs, with anomalous low-level westerlies in phase with positive precipitation anomalies. However, the zonal-vertical wind field is generally weak in G25 while that in CP4A is incoherent (e.g., Section 5.7).

7.2.3 The impact of high-amplitude Kelvin waves on extreme precipitation over Equatorial Africa

The fourth objective of this thesis is "to evaluate the role of high-amplitude Kelvin waves in influencing extreme precipitation episodes over Equatorial Africa" (§2.7). To address this objective, the first part of Chapter 6 identifies grid-point based extreme precipitation (§6.3) and presents a statistical analysis of the role of high-amplitude Kelvin waves in modulating extreme precipitation across Equatorial Africa. It is found that the passage of high-amplitude Kelvin waves over Equatorial Africa increases the precipitation by up to 4 mm day^{-1} above the seasonal mean precipitation amount. It is also shown that extreme precipitation is up to twice as likely to occur compared to climatology in a sub-region over which a CCKW is located. Enhanced precipitation intensities on wet days and increased frequency of wet days associated with high-amplitude Kelvin waves have also been found. A similar result was reported in Jackson et al. (2019), but the results here extend their findings in that we have looked at a whole season rather than April only. This thesis used a dynamics-based equatorial wave dataset as discussed above, which lends further credibility to these results.

Besides the eastward propagating precipitation episodes that are associated with CCKWs, this thesis found a significant number of eastward propagating precipitation events that are not related to Kelvin waves in both observations and simulations (Sections 4.7 and 5.6). In the second part of Chapter 6 which addresses the fourth thesis objective, eastward propagating extreme precipitation events are isolated using a definition of a precipitation event (Section 4.2.2) and case studies are built around the identified dates associated with extreme precipitation (e.g., Tables 6.1, 6.2 and 6.3). Results from analysis of case studies associated with high-amplitude Kelvin waves show precipitation patterns that vary from case study to case study, highlighting the variability of the impact of high-amplitude Kelvin waves in influencing extreme precipitation over Equatorial Africa (e.g., Mekonnen et al., 2008) (Chapter 6, Section 6.4). Findings from analysis of case studies "unrelated" to high-

amplitude Kelvin waves (as defined in this thesis) also show variations in the precipitation patterns between the individual case studies, but the low-level horizontal wind structure is similar to that shown in case studies related to high-amplitude Kelvin waves. For case studies unrelated to high-amplitude Kelvin waves, it is plausible that a Kelvin wave initiated by preexisting convection (e.g., Baranowski et al., 2016) modulated the low-level horizontal winds thereby impacting the precipitation (Section 6.4.6). Results from these case studies are consistent with our earlier results in that, high-amplitude CCKWs influence extreme precipitation episodes through modification of the low-level horizontal winds to favour westerly winds that help to transport moisture from the Atlantic Ocean into the eastward propagating CCKW-precipitation coupled feature. It is also found that the low-level convergence of the westerlies and the easterlies acts as a source of convective instability for the eastward propagation of convection and precipitation, at least in the case studies examined in this thesis. The findings from case studies in particular are supported by several previous studies such as Levin et al. (2009), Williams and Funk (2011) and Finney et al. (2020) that found a connection between westerlies and precipitation over East Africa. It is likely that the days with westerly flow found in Finney et al. (2020) are days with Kelvin waves propagating across Equatorial Africa. In both observed and simulated case studies, small-scale convection and precipitation features that are not related to Kelvin waves have been found. These small-scale precipitation features develop and decay irrespective of the phase of the Kelvin waves. It is likely that the eastward propagating events that are unrelated to Kelvin waves may partly be associated with these small-scale features (Section 6.4.7).

7.3 Limitations and Future work

It was noted in chapter 3 that the major difference between CP4A and G25 is that G25 employs a deep convection scheme that is different from the default Gregory and Rowntree (1990) convection scheme implemented in the Met Office's UM. It is hypothesised that implementing a different convection scheme and model physics in G25 would cause a difference in the results in Chapters 5 and 6. For example, changing the model parameterisation schemes and improving the representation of the sub-grid scale processes might reduce the precipitation bias in G25 (e.g., Brown et al., 2010). Another limitation worth noting is the relatively low resolution of G25. It has been suggested that increasing the model resolution leads to improved coupling between the large-scale circulation and the precipitation (Vellinga et al., 2016). However, increasing the resolution alone without changing the physics may not guarantee a better realisation of the precipitation field and its coupling with Kelvin waves, which is why this thesis analysed the higher resolution convection permitting CP4A.

Climate models are important tools for understanding the processes that govern the climate system. It is therefore important that models are evaluated against observations to gain an insight in their capability to simulate the real atmosphere (e.g., Woodhams et al., 2018; Jackson et al., 2019). This thesis evaluates CP4A and G25 in reproducing the observed eastward propagation of precipitation found in TRMM. It further explores the structure and activity of CCKWs in both simulations, and relies on ERA-I (§3.2.3) as a proxy to observations (Chapter 5). ERA-I is a low resolution dataset compared to the recent reanalysis products such as ERA5. It

is likely that using contemporary high spatial and temporal resolution datasets such as Global Precipitation Measurement-Integrated Multi-satellitE Retrievals (GPM-IMERG) and ERA5 could alter the results in Chapters 5 and 6. However, it is important to bear in mind that even ERA5 relies on a convection parameterisation scheme for fields related to convective activity and precipitation, and data assimilation relies on fairly sparse observations over Africa. So, it is worth taking caution while using any reanalysis as the "truth".

In comparison to the G25, CP4A was run at a very high resolution because of the desire for explicit representation of convection. However, convection is important for a wide range of spatial scales. At a resolution of 4.5km, small-scale convective features less than 4.5km are not adequately resolved. What this means is that the performance of the model in representing small cumulus clouds might have been unsatisfactory, and the representation of development of cumulus into deep convective clouds was most likely sub-optimal. This might have affected our results regarding extreme precipitation and the small-scale convection and precipitation distribution.

The expected state of the future climate is an area of active research. Future work needs to investigate how the convective interaction between WEA and EEA will evolve in light of a changing climate. For example, a projected increase in moisture transport from the Congo Basin into EEA (e.g., Giannini et al., 2018) will have an implication for the relationship between WEA and EEA. One obvious area of future work is to redo analysis done in this thesis using the CP4A's sibling 10 year future climate of Africa run and compare the results with future runs from global models such as the new CMIP6 models. The CP4A run for the future climate is also an atmosphere-only simulation for the period 2097-2106 for IPCC Representative Concentration Pathway 8.5 (RCP8.5).

Chapter 5 presented clues that suggest an interaction between the Kelvin wave-convection coupled structure and the East African Highlands. This interaction might explain the weak precipitation and CCKW signal highlighted in Chapter 4. Although Wheeler et al. (2000) proposed that the East African Highlands block the coherent eastward propagation of CCKWs, their results are based on observations. Model experiments with a focus on the sensitivity of the eastward propagating Kelvin waves to orographic effects of the East African Highlands may be useful in exploring the extent to which these highlands interact with CCKWs. For example, the sensitivity experiments analogous to idealised GCM experiments in Slingo et al. (2005) or Sommerfeld et al. (2016) might be useful. Also, Chapters 4 and 5 found a weak signal for both the anomalous precipitation and CCKW over EEA. If the interaction between the highlands and CCKW-precipitation coupled system is not the cause of the weak precipitation and Kelvin wave convergence over EEA, then future work could test the hypothesis that the large-scale subsidence over East Africa (e.g., Vellinga and Milton, 2018) and moisture deficiency over EEA (e.g., Munday et al., 2021) provide unfavourable conditions for the coupling between CCKWs and the precipitation.

Targeted high spatial and temporal resolution (e.g., 3 hourly) ground-based observations including radiosonde data is needed to further understand the interaction between high-amplitude Kelvin waves and lo-

calised convective features, particularly over Lake Victoria. For example, data from the newly installed radar at the shores of Lake Victoria (I. Mugume, personal communication) and radiosonde data would be useful in exploring the detailed vertical structure of the Kelvin wave and its interaction with the localised convective systems.

The case studies presented in Chapter 6 exhibit varying precipitation patterns. These case studies provide an important step toward drawing general conclusions about all the day-to-day impact of high-amplitude Kelvin waves on extreme precipitation episodes. One way of increasing on the sample size of case studies is to apply a lower threshold in the definition of a precipitation event described in Section 6.2.1. Several case studies based on CP4A may help to further explore the differences in structures of the various fields. In light of the findings in Kendon et al. (2019), who found a future increase of extreme 3-hourly precipitation in future-climate CP4A, such case studies would provide an opportunity to not only examine eastward propagating precipitation events that are not even related to weak Kelvin wave events (e.g., Section 4.7) but also further explore the processes that are associated with the small-scale convective features seen in the case studies, and how high-amplitude Kelvin waves interact with these processes. Findings on the dynamics and thermodynamics associated with the influence of high-amplitude Kelvin waves on extreme precipitation episodes from such future work will be important for the wider scientific community, especially the current COordinated Regional Climate Downscaling EXperiment (CORDEX) Flagship Pilot Study (FPS) ELVIC (climate Extremes in the Lake VICtoria basin).

Due to computational resource constraints, several National Meteorological and Hydrological Services (NMHSs) depend on model output from global operational forecast models as a forecasting tool. Future work needs to investigate the representation of CCKWs-precipitation coupling in NWP models such as the Met Office operational convection permitting model over tropical Africa and the global operational forecast model. The low skill in the global operational forecast model in comparison to the convection permitting model over East Africa (e.g., Woodhams et al., 2018) might be due to unsatisfactory representation of the eastward propagating CCKW-precipitation coupled structures. This thesis has identified some of the key physical processes that have to be satisfactorily represented in NWP and climate models to simulate the coupling between waves and precipitation, that is, the modulation of large-scale horizontal wind and low-level convergence and the interaction of convection with these fields. Improving these processes in NWP models may lead to an improvement in the daily to synoptic timescale forecasts.

Results from this thesis imply that there is a need to study the above physical processes because they might change with a changing climate considering that some studies such as Stocker (2014) show that extreme precipitation is likely to change with climate change. Failure of normal GCM climate projections to correctly capture the key processes is a major concern because then we will not have a full picture of what climate change will look like over Equatorial Africa using GCMs alone.

7.4 Implications and Scientific advances

This thesis makes several new contributions to the study of the meteorology of Equatorial Africa. Firstly, for the first time, Equatorial Africa is subdivided into small sub-regions of similar daily precipitation variability. These sub-regions have shared temporal variance, and therefore they may be used in future studies since they are objectively identified. Studying such objectively identified sub-regions have advantages over using arbitrary boxes like several past studies. Secondly, a 1-2 days relationship in precipitation between WEA and EEA is found. This relationship and the associated physical processes will benefit the operational forecasting community because it is part of the knowledge needed to develop or improve the forecasting systems for synoptic-timescale precipitation over Eastern Equatorial Africa. Thirdly, examination of the literature indicates that several publications that focused on the influence of Kelvin waves in influencing convection and precipitation in Equatorial Africa (e.g., Nguyen and Duvel, 2008; Laing et al., 2011; Sandjon et al., 2012; Sinclaire et al., 2015; Mekonnen and Thorncroft, 2016; Jackson et al., 2019) applied the space-time spectral analysis of OLR or CBT to isolate Kelvin wave activity. What this means is that until now, knowledge on Kelvin wave activity over Equatorial Africa was mainly limited to the use of cloud-based wave indices. It is worth noting that Kelvin wave activity identified from an OLR signal cannot easily be used independently to relate the precipitation signal to the wave structure.

This thesis has demonstrated the importance of CCKWs in the eastward propagation of convection and precipitation across Equatorial Africa. The findings suggest that synoptic-scale weather forecasters over EEA need to monitor the propagation of CCKWs into and through the region in real time. Results in Yang et al. (2021) present a new approach for identifying Kelvin waves in forecasts. However, forecasters need to be mindful that the speed of CCKWs may vary depending on how strongly the wave is coupled to convection, and not all CCKWs will necessarily lead to eastward propagating synoptic-scale precipitation events. In addition, findings in this thesis can be useful in developing statistical methods (e.g., Schlüter et al.. 2017) for synoptic-timescale precipitation forecasting over EEA. Finally, these results highlight the potential value that could be gained from a realistic representation of CCKWs and their interaction with localized convective systems in high-resolution operational forecasting systems such as the new Met Office operational convection-permitting model for tropical Africa.

References

Aguilar, E., Aziz Barry, A., Brunet, M., Ekang, L., Fernandes, A., Massoukina, M., Mbah, J., Mhanda, A., Do Nascimento, D., Peterson, T., et al. (2009). Changes in temperature and precipitation extremes in western central Africa, Guinea Conakry, and Zimbabwe, 1955–2006. *Journal of Geophysical Research: Atmospheres*, 114(D2).

Alsdorf, D., Beighley, E., Laraque, A., Lee, H., Tshimanga, R., O'Loughlin, F., Mahé, G., Dinga, B., Moukandi, G., and Spencer, R. G. (2016). Opportunities for hydrologic research in the Congo Basin. *Reviews of Geophysics*, 54(2):378–409.

Arakawa, A. (1977). Computational design of the basic dynamical processes of the UCLA general circulation model. Methods in Computational Physics. *Advances in Research and Application, Vol. 17: General circulation models of the atmosphere*, 337.

Arkin, P. A. (1979). The relationship between fractional coverage of high cloud and rainfall accumulations during GATE over the B-scale array. *Monthly Weather Review*, 107(10):1382–1387.

Ayesiga, G., Holloway, C. E., Williams, C. J., Yang, G.-Y., and Ferrett, S. (2021). The observed synoptic scale precipitation relationship between Western Equatorial Africa and Eastern Equatorial Africa. *International Journal of Climatology*, 41:E582–E601.

Ayesiga, G., Holloway, C. E., Williams, C. J., Yang, G.-Y., Stratton, R., and Roberts, M. (2022). Linking equatorial african precipitation to kelvin wave processes in the cp4-africa convection-permitting regional climate simulation. *Journal of the Atmospheric Sciences*, 79(5):1271–1289.

Badr, H. S., Dezfuli, A. K., Zaitchik, B. F., and Peters-Lidard, C. D. (2016). Regionalizing Africa: patterns of precipitation variability in observations and global climate models. *Journal of Climate*, 29(24):9027–9043.

Balas, N., Nicholson, S., and Klotter, D. (2007). The relationship of rainfall variability in West Central Africa to sea-surface temperature fluctuations. *International Journal of Climatology*, 27(10):1335–1349.

Baranowski, D. B., Flatau, M. K., Flatau, P. J., Karnawati, D., Barabasz, K., Labuz, M., Latos, B., Schmidt, J. M., Paski, J. A., et al. (2020). Social-media and newspaper reports reveal large-scale meteorological drivers of floods on Sumatra. *Nature communications*, 11(1):1–10.

Baranowski, D. B., Flatau, M. K., Flatau, P. J., and Matthews, A. J. (2016). Impact of atmospheric convectively

coupled equatorial Kelvin waves on upper ocean variability. *Journal of Geophysical Research: Atmospheres*, 121(5):2045–2059.

Barlow, M., Wheeler, M., Lyon, B., and Cullen, H. (2005). Modulation of daily precipitation over southwest Asia by the Madden–Julian Oscillation. *Monthly weather review*, 133(12):3579–3594.

Basalirwa, C. (1995). Delineation of Uganda into climatological rainfall zones using the method of principal component analysis. *International Journal of climatology*, 15(10):1161–1177.

Behrend, H. (1987). Teleconnections of rainfall anomalies and of the Southern Oscillation over the entire tropics and their seasonal dependence. *Tellus A*, 39(2):138–151.

Belay, A., Demissie, T., Recha, J. W., Oludhe, C., Osano, P. M., Olaka, L. A., Solomon, D., and Berhane, Z. (2021). Analysis of Climate Variability and Trends in southern Ethiopia. *Climate*, 9(6):96.

Beltrando, G. (1990). Space–time variability of rainfall in April and October–November over East Africa during the period 1932–1983. *International Journal of Climatology*, 10(7):691–702.

Beltrando, G. and Cadet, D. (1990). Interannual variability of the short rain season in East Africa: Relationships with general atmospheric circulation. *Veille Climatique Satellitaire*, 33:19–36.

Berhane, F. and Zaitchik, B. (2014). Modulation of daily precipitation over East Africa by the Madden–Julian Oscillation. *Journal of climate*, 27(15):6016–6034.

Berhane, F., Zaitchik, B., and Badr, H. S. (2015). The Madden–Julian Oscillation's influence on spring rainy season precipitation over equatorial West Africa. *Journal of Climate*, 28(22):8653–8672.

Berthou, S., Kendon, E., Rowell, D., Roberts, M., Tucker, S., and Stratton, R. (2019). Larger Future Intensification of Rainfall in the West African Sahel in a Convection-Permitting Model. *Geophysical Research Letters*, 46(22):13299–13307.

Black, E. (2005). The relationship between Indian Ocean sea–surface temperature and East African rainfall. *Philosophical Transactions of the Royal Society A: Mathematical, Physical and Engineering Sciences*, 363(1826):43–47.

Black, E., Slingo, J., and Sperber, K. R. (2003). An observational study of the relationship between excessively strong short rains in coastal East Africa and Indian Ocean SST. *Monthly Weather Review*, 131(1):74–94.

Black, E., Tarnavsky, E., Maidment, R., Greatrex, H., Mookerjee, A., Quaife, T., and Brown, M. (2016). The use of remotely sensed rainfall for managing drought risk: A case study of weather index insurance in Zambia. *Remote Sensing*, 8(4):342.

Brown, A., Beare, R., Edwards, J., Lock, A., Keogh, S., Milton, S., and Walters, D. (2008). Upgrades to the boundary-layer scheme in the met office numerical weather prediction model. *Boundary-layer meteorology*, 128(1):117–132.

Brown, J. R., Jakob, C., and Haynes, J. M. (2010). An evaluation of rainfall frequency and intensity over the Australian region in a global climate model. *Journal of Climate*, 23(24):6504–6525.

Camberlin, P., Kpanou, M., and Roucou, P. (2020). Classification of Intense Rainfall Days in Southern West Africa and Associated Atmospheric Circulation. *Atmosphere*, 11(2):188.

Camberlin, P. and Philippon, N. (2002). The East African March–May rainy season: Associated atmospheric dynamics and predictability over the 1968–97 period. *Journal of Climate*, 15(9):1002–1019.

Camberlin, P. and Planchon, O. (1997). Coastal precipitation regimes in Kenya. *Geografiska Annaler: Series A, Physical Geography*, 79(1-2):109–119.

Chan, R., Vuille, M., Hardy, D., and Bradley, R. (2008). Intraseasonal precipitation variability on Kilimanjaro and the East African region and its relationship to the large-scale circulation. *Theoretical and Applied Climatology*, 93(3-4):149–165.

Charney, J. G. and Phillips, N. (1953). Numerical integration of the quasi-geostrophic equations for barotropic and simple baroclinic flows. *Journal of Atmospheric Sciences*, 10(2):71–99.

Corfidi, S. (2017). Forecasting severe convective storms. In *Oxford Research Encyclopedia of Climate Science*. Oxford University Press.

Crétat, J., Vizy, E. K., and Cook, K. H. (2014). How well are daily intense rainfall events captured by current climate models over Africa? *Climate dynamics*, 42(9-10):2691–2711.

Crook, J., Klein, C., Folwell, S., Taylor, C. M., Parker, D. J., Stratton, R., and Stein, T. (2019). Assessment of the representation of West African storm lifecycles in convection-permitting simulations. *Earth and Space Science*, 6(5):818–835.

Davies, T., Cullen, M. J., Malcolm, A. J., Mawson, M., Staniforth, A., White, A., and Wood, N. (2005). A new dynamical core for the met office's global and regional modelling of the atmosphere. *Quarterly Journal of the Royal Meteorological Society*, 131(608):1759–1782.

Dee, D. P., Uppala, S. M., Simmons, A., Berrisford, P., Poli, P., Kobayashi, S., Andrae, U., Balmaseda, M., Balsamo, G., Bauer, d. P., et al. (2011). The ERA-Interim reanalysis: Configuration and performance of the data assimilation system. *Quarterly Journal of the royal meteorological society*, 137(656):553–597.

Dezfuli, A. (2017). Climate of western and central equatorial africa. In *Oxford Research Encyclopedia of Climate Science*.

Dezfuli, A. K. (2011). Spatio-temporal variability of seasonal rainfall in western equatorial Africa. *Theoretical and applied climatology*, 104(1-2):57–69.

Dezfuli, A. K., Zaitchik, B. F., and Gnanadesikan, A. (2015). Regional atmospheric circulation and rainfall variability in south equatorial Africa. *Journal of Climate*, 28(2):809–818.

Dias, J. and Pauluis, O. (2011). Modulations of the phase speed of convectively coupled Kelvin waves by the ITCZ. *Journal of the atmospheric sciences*, 68(7):1446–1459.

Dinku, T., Ceccato, P., Grover-Kopec, E., Lemma, M., Connor, S., and Ropelewski, C. (2007). Validation of satellite rainfall products over East Africa's complex topography. *International Journal of Remote Sensing*, 28(7):1503–1526.

Donald, A., Meinke, H., Power, B., Wheeler, M., and Ribbe, J. (2004). Forecasting with the Madden–Julian Oscillation and the applications for risk management. In *Proceedings of the 4th International Crop Science Congress (ICSC 2004)*.

Duchon, C. E. (1979). Lanczos filtering in one and two dimensions. *Journal of Applied Meteorology and Climatology*, 18(8):1016–1022.

Dunkerton, T. J. and Crum, F. X. (1995). Eastward propagating 2-to 15-day equatorial convection and its relation to the tropical intraseasonal oscillation. *Journal of Geophysical Research: Atmospheres*, 100(D12):25781–25790.

Dunning, C. M., Black, E. C., and Allan, R. P. (2016). The onset and cessation of seasonal rainfall over Africa. *Journal of Geophysical Research: Atmospheres*, 121(19):11–405.

Dyer, E. L., Jones, D. B., Nusbaumer, J., Li, H., Collins, O., Vettoretti, G., and Noone, D. (2017). Congo Basin precipitation: Assessing seasonality, regional interactions, and sources of moisture. *Journal of Geophysical Research: Atmospheres*, 122(13):6882–6898.

Edwards, J. and Slingo, A. (1996). Studies with a flexible new radiation code. i: Choosing a configuration for a large-scale model. *Quarterly Journal of the Royal Meteorological Society*, 122(531):689–719.

Eltahir, E. A. (1996). Role of vegetation in sustaining large-scale atmospheric circulations in the tropics. *Journal of Geophysical Research: Atmospheres*, 101(D2):4255–4268.

FAO, I. (2016). Wfp. the state of Food Insecurity in the World: Meeting the 2015 international hunger targets: taking stock of uneven progress. 2015.

Farnsworth, A., White, E., Williams, C. J., Black, E., and Kniveton, D. R. (2011). Understanding the large scale driving mechanisms of rainfall variability over Central Africa. In *African climate and climate change*, pages 101–122. Springer.

Ferrett, S., Yang, G.-Y., Woolnough, S. J., Methven, J., Hodges, K., and Holloway, C. E. (2020). Linking extreme precipitation in Southeast Asia to equatorial waves. *Quarterly Journal of the Royal Meteorological Society*, 146(727):665–684.

Finney, D. L., Marsham, J. H., Jackson, L. S., Kendon, E. J., Rowell, D. P., Boorman, P. M., Keane, R. J., Stratton, R. A., and Senior, C. A. (2019). Implications of improved representation of convection for the East Africa water budget using a convection-permitting model. *Journal of Climate*, 32(7):2109–2129.

Finney, D. L., Marsham, J. H., Walker, D. P., Birch, C. E., Woodhams, B. J., Jackson, L. S., and Hardy, S. (2020). The effect of westerlies on East African rainfall and the associated role of tropical cyclones and the Madden–Julian Oscillation. *Quarterly Journal of the Royal Meteorological Society*, 146(727):647–664.

Fotso-Kamga, G., Fotso-Nguemo, T. C., Diallo, I., Yepdo, Z. D., Pokam, W. M., Vondou, D. A., and Lenouo, A. (2020). An evaluation of COSMO-CLM regional climate model in simulating precipitation over Central Africa. *International Journal of Climatology*, 40(5):2891–2912.

Frierson, D. M. (2007). Convectively coupled Kelvin waves in an idealized moist general circulation model. *Journal of the atmospheric sciences*, 64(6):2076–2090.

Frierson, D. M., Kim, D., Kang, I.-S., Lee, M.-I., and Lin, J. (2011). Structure of AGCM-simulated convectively coupled kelvin waves and sensitivity to convective parameterization. *Journal of the atmospheric sciences*, 68(1):26–45.

Fritsch, J. and Chappell, C. (1980). Numerical prediction of convectively driven mesoscale pressure systems. part i: Convective parameterization. *Journal of Atmospheric Sciences*, 37(8):1722–1733.

Fujiwara, M., Wright, J. S., Manney, G. L., Gray, L. J., Anstey, J., Birner, T., Davis, S., Gerber, E. P., Harvey, V. L., Hegglin, M. I., et al. (2017). Introduction to the SPARC Reanalysis Intercomparison Project (S-RIP) and overview of the reanalysis systems. *Atmospheric Chemistry and Physics*, 17(2):1417–1452.

Gebremicael, T. G., Mohamed, Y. A., Zaag, P. v. d., Gebremedhin, A., Gebremeskel, G., Yazew, E., and Kifle, M. (2019). Evaluation of multiple satellite rainfall products over the rugged topography of the Tekeze-Atbara basin in Ethiopia. *International Journal of Remote Sensing*, 40(11):4326–4345.

Giannini, A., Lyon, B., Seager, R., and Vigaud, N. (2018). Dynamical and thermodynamic elements of modeled climate change at the East African margin of convection. *Geophysical Research Letters*, 45(2):992–1000.

Gill, A. E. (1980). Some simple solutions for heat-induced tropical circulation. *Quarterly Journal of the Royal Meteorological Society*, 106(449):447–462.

Gissila, T., Black, E., Grimes, D., and Slingo, J. (2004). Seasonal forecasting of the Ethiopian summer rains. *International Journal of Climatology*, 24(11):1345–1358.

Gitau, W., Camberlin, P., Ogallo, L., and Okoola, R. (2015). Oceanic and atmospheric linkages with short rainfall season intraseasonal statistics over Equatorial Eastern Africa and their predictive potential. *International Journal of Climatology*, 35(9):2382–2399.

Glatt, I., Dornbrack, A., Jones, S., Keller, J., Martius, O., Muller, A., Peters, D. H., and Wirth, V. (2011). Utility of Hovmöller diagrams to diagnose rossby wave trains. *Tellus A: Dynamic Meteorology and Oceanography*, 63(5):991–1006.

Glover, J., Robinson, P., and Henderson, J. (1954). Provisional maps of the reliability of annual rainfall in East Africa. *Quarterly Journal of the Royal Meteorological Society*, 80(346):602–609.

Gong, D.-Y., Guo, D., Mao, R., Yang, J., Gao, Y., and Kim, S.-J. (2016). Interannual modulation of East African early short rains by the winter Arctic Oscillation. *Journal of Geophysical Research: Atmospheres*, 121(16):9441–9457.

Graham, R., Visman, E., Wade, S., Amato, R., Bain, C., Janes, T., Leathes, B., Lumbroso, D., Cornforth, R., Boyd, E., et al. (2015). Scoping, options analysis and design of a 'climate information and services programme' for Africa (CIASA): literature review. *literature review*.

Grant, A. (2001). Cloud-base fluxes in the cumulus-capped boundary layer. *Quarterly Journal of the Royal Meteorological Society*, 127(572):407–421.

Gregory, D. and Rowntree, P. (1990). A mass flux convection scheme with representation of cloud ensemble characteristics and stability-dependent closure. *Monthly Weather Review*, 118(7):1483–1506.

Guo, Y., Jiang, X., and Waliser, D. E. (2014). Modulation of the convectively coupled Kelvin waves over South America and the tropical Atlantic Ocean in association with the madden–julian oscillation. *Journal of the Atmospheric Sciences*, 71(4):1371–1388.

Haertel, P., Straub, K., and Budsock, A. (2015). Transforming circumnavigating Kelvin waves that initi-

ate and dissipate the Madden–Julian Oscillation. *Quarterly Journal of the Royal Meteorological Society*, 141(690):1586–1602.

Harrison, L., Funk, C., and Peterson, P. (2019). Identifying changing precipitation extremes in Sub-Saharan Africa with gauge and satellite products. *Environmental Research Letters*, 14(8):085007.

Hartman, A. T. (2021). Tracking mesoscale convective systems in central equatorial Africa. *International Journal of Climatology*, 41(1):469–482.

Hastenrath, S. (2000). Zonal circulations over the equatorial Indian Ocean. *Journal of Climate*, 13(15):2746–2756.

Hayashi, Y. (1982). Space-time spectral analysis and its applications to atmospheric waves. *Journal of the Meteorological Society of Japan. Ser. II*, 60(1):156–171.

Hendon, H. H. and Liebmann, B. (1991). The structure and annual variation of antisymmetric fluctuations of tropical convection and their association with Rossby–gravity waves. *Journal of Atmospheric Sciences*, 48(19):2127–2140.

Hills, R. C. (1979). The structure of the inter-tropical convergence zone in equatorial Africa and its relationship to East African rainfall. *Transactions of the Institute of British Geographers*, pages 329–352.

Hogan, E., Shelly, A., and Xavier, P. (2015). The observed and modelled influence of the Madden–Julian Oscillation on East African rainfall. *Meteorological Applications*, 22(3):459–469.

Holloway, C. E., Woolnough, S. J., and Lister, G. M. (2013). The effects of explicit versus parameterized convection on the MJO in a large-domain high-resolution tropical case study. part i: Characterization of large-scale organization and propagation. *Journal of the Atmospheric Sciences*, 70(5):1342–1369.

Howard, E. and Washington, R. (2019). Drylines in southern Africa: Rediscovering the Congo air boundary. *Journal of Climate*, 32(23):8223–8242.

Huang, B., L'Heureux, M., Hu, Z.-Z., and Zhang, H.-M. (2016). Ranking the strongest ENSO events while incorporating SST uncertainty. *Geophysical Research Letters*, 43(17):9165–9172.

Huang, P., Chou, C., and Huang, R. (2013). The activity of convectively coupled equatorial waves in CMIP3 global climate models. *Theoretical and applied climatology*, 112(3-4):697–711.

Huang, P. and Huang, R. (2011). Climatology and interannual variability of convectively coupled equatorial waves activity. *Journal of climate*, 24(16):4451–4465.

Huffman, G. J., Adler, R. F., Morrissey, M. M., Bolvin, D. T., Curtis, S., Joyce, R., McGavock, B., and Susskind, J. (2001). Global precipitation at one-degree daily resolution from multisatellite observations. *Journal of hydrometeorology*, 2(1):36–50.

Huffman, G. J., Bolvin, D. T., Nelkin, E. J., Wolff, D. B., Adler, R. F., Gu, G., Hong, Y., Bowman, K. P., and Stocker, E. F. (2007). The TRMM multisatellite precipitation analysis (TMPA): Quasi-global, multiyear, combined-sensor precipitation estimates at fine scales. *Journal of hydrometeorology*, 8(1):38–55.

Indeje, M., Semazzi, F. H., and Ogallo, L. J. (2000). Enso signals in east african rainfall seasons. *International Journal of Climatology*, 20(1):19–46.

Indeje, M., Semazzi, F. H., Xie, L., and Ogallo, L. J. (2001). Mechanistic model simulations of the East African climate using NCAR regional climate model: influence of large-scale orography on the Turkana low-level jet. *Journal of Climate*, 14(12):2710–2724.

IPCC (2014). Synthesis Report. Contribution of Working Groups I, II and III to the Fifth Assessment Report of the Intergovernmental Panel on Climate Change [Core Writing Team, R.K. Pachauri and L.A. Meyer (eds.)].

IPCC (2021). Climate Change 2021: The Physical Science Basis. Contribution of Working Group I to the Sixth Assessment Report of the Intergovernmental Panel on Climate Change [Masson-Delmotte, V., P. Zhai, A. Pirani, S. L. Connors, C. Péan, S. Berger, N. Caud, Y. Chen, L. Goldfarb, M. I. Gomis, M. Huang, K. Leitzell, E. Lonnoy, J. B. R. Matthews, T. K. Maycock, T. Waterfield, O. Yelekçi, R. Yu and B. Zhou (eds.).

Jackson, B., Nicholson, S. E., and Klotter, D. (2009). Mesoscale convective systems over western equatorial Africa and their relationship to large-scale circulation. *Monthly Weather Review*, 137(4):1272–1294.

Jackson, L. S., Keane, R. J., Finney, D. L., Marsham, J. H., Parker, D. J., Senior, C. A., and Stratton, R. A. (2019). Regional differences in the response of rainfall to convectively coupled Kelvin waves over tropical Africa. *Journal of Climate*, 32(23):8143–8165.

James, R., Washington, R., Abiodun, B., Kay, G., Mutemi, J., Pokam, W., Hart, N., Artan, G., and Senior, C. (2018). Evaluating climate models with an African lens. *Bulletin of the American Meteorological Society*, 99(2):313–336.

Janowiak, J. E. (1988). An investigation of interannual rainfall variability in africa. *Journal of Climate*, 1(3):240–255.

Jiang, Y., Zhou, L., Roundy, P. E., Hua, W., and Raghavendra, A. (2021). Increasing Influence of Indian Ocean Dipole on Precipitation over Central Equatorial Africa. *Geophysical Research Letters*, 48(8):e2020GL092370.

Johnson, J., MacKeen, P. L., Witt, A., Mitchell, E. D. W., Stumpf, G. J., Eilts, M. D., and Thomas, K. W. (1998). The storm cell identification and tracking algorithm: An enhanced WSR-88D algorithm. *Weather and forecasting*, 13(2):263–276.

Jonkman, S. N. (2005). Global perspectives on loss of human life caused by floods. *Natural hazards*, 34(2):151–175.

Kamsu-Tamo, P., Janicot, S., Monkam, D., and Lenouo, A. (2014). Convection activity over the Guinean coast and Central Africa during northern spring from synoptic to intra-seasonal timescales. *Climate dynamics*, 43(12):3377–3401.

Kendon, E. J., Stratton, R. A., Tucker, S., Marsham, J. H., Berthou, S., Rowell, D. P., and Senior, C. A. (2019). Enhanced future changes in wet and dry extremes over Africa at convection-permitting scale. *Nature communications*, 10(1):1–14.

Kiladis, G. N., Straub, K. H., and Haertel, P. T. (2005). Zonal and vertical structure of the Madden–Julian oscillation. *Journal of the atmospheric sciences*, 62(8):2790–2809.

Kiladis, G. N. and Wheeler, M. (1995). Horizontal and vertical structure of observed tropospheric equatorial

Rossby waves. *Journal of Geophysical Research: Atmospheres*, 100(D11):22981–22997.

Kiladis, G. N., Wheeler, M. C., Haertel, P. T., Straub, K. H., and Roundy, P. E. (2009). Convectively coupled equatorial waves. *Reviews of Geophysics*, 47(2).

Kilavi, M., MacLeod, D., Ambani, M., Robbins, J., Dankers, R., Graham, R., Titley, H., Salih, A. A., and Todd, M. C. (2018). Extreme rainfall and flooding over central Kenya including Nairobi city during the long-rains season 2018: causes, predictability, and potential for early warning and actions. *Atmosphere*, 9(12):472.

Kim, D., Kug, J.-S., and Sobel, A. H. (2014). Propagating versus nonpropagating Madden–Julian oscillation events. *Journal of Climate*, 27(1):111–125.

Kinuthia, J. and Asnani, G. (1982). A newly found jet in North Kenya (Turkana Channel). *Monthly Weather Review*, 110(11):1722–1728.

Kirkby, M. and Beven, K. (1979). A physically based, variable contributing area model of basin hydrology. *Hydrological Sciences Journal*, 24(1):43–69.

Klein Tank, A., Zwiers, F., and Zhang, X. (2009). Climate data and monitoring WCDMP-705 NO. 72.

Laing, A. G., Carbone, R. E., and Levizzani, V. (2011). Cycles and propagation of deep convection over equatorial Africa. *Monthly Weather Review*, 139(9):2832–2853.

Levin, N. E., Zipser, E. J., and Cerling, T. E. (2009). Isotopic composition of waters from Ethiopia and Kenya: Insights into moisture sources for eastern Africa. *Journal of Geophysical Research: Atmospheres*, 114(D23).

Liebmann, B., Kiladis, G. N., Carvalho, L. M., Jones, C., Vera, C. S., Bladé, I., and Allured, D. (2009). Origin of convectively coupled Kelvin waves over South America. *Journal of climate*, 22(2):300–315.

Lin, J.-L., Kiladis, G. N., Mapes, B. E., Weickmann, K. M., Sperber, K. R., Lin, W., Wheeler, M. C., Schubert, S. D., Del Genio, A., Donner, L. J., et al. (2006). Tropical intraseasonal variability in 14 IPCC AR4 climate models. Part I: Convective signals. *Journal of climate*, 19(12):2665–2690.

Lindzen, R. S. (2003). The interaction of waves and convection in the tropics. *Journal of the atmospheric sciences*, 60(24):3009–3020.

Liu, W. (2020). *Understanding precipitation variability over Africa: observational analysis and regional climate model simulations*. PhD thesis.

Lock, A. (2001). The numerical representation of entrainment in parameterizations of boundary layer turbulent mixing. *Monthly Weather Review*, 129(5):1148–1163.

Lock, A., Brown, A., Bush, M., Martin, G., and Smith, R. (2000). A new boundary layer mixing scheme. Part I: Scheme description and single-column model tests. *Monthly weather review*, 128(9):3187–3199.

Longandjo, G.-N. T. and Rouault, M. (2020). On the structure of the regional-scale circulation over central Africa: seasonal evolution, variability, and mechanisms. *Journal of Climate*, 33(1):145–162.

Madden, R. A. and Julian, P. R. (1971). Detection of a 40–50 day oscillation in the zonal wind in the tropical Pacific. *Journal of Atmospheric Sciences*, 28(5):702–708.

Madden, R. A. and Julian, P. R. (1972). Description of global-scale circulation cells in the tropics with a 40–50 day period. *Journal of Atmospheric Sciences*, 29(6):1109–1123.

Madden, R. A. and Julian, P. R. (1994). Observations of the 40–50-day tropical oscillation? A review. *Monthly weather review*, 122(5):814–837.

Matari, E. E. (2002). *Impacts of Congo convection on tropical Africa's circulation, rainfall and resources*. PhD thesis.

Matsuno, T. (1966). Quasi-geostrophic motions in the equatorial area. *Journal of the Meteorological Society of Japan. Ser. II*, 44(1):25–43.

Matthews, A. J. (2000). Propagation mechanisms for the Madden–Julian oscillation. *Quarterly Journal of the Royal Meteorological Society*, 126(569):2637–2651.

McCollum, J. R., Gruber, A., and Ba, M. B. (2000). Discrepancy between gauges and satellite estimates of rainfall in equatorial Africa. *Journal of Applied Meteorology*, 39(5):666–679.

Mekonnen, A. and Thorncroft, C. D. (2016). On mechanisms that determine synoptic time scale convection over East Africa. *International Journal of Climatology*, 36(12):4045–4057.

Mekonnen, A., Thorncroft, C. D., Aiyyer, A. R., and Kiladis, G. N. (2008). Convectively coupled Kelvin waves over tropical Africa during the boreal summer: Structure and variability. *Journal of Climate*, 21(24):6649–6667.

Moore, S. M., Azman, A. S., Zaitchik, B. F., Mintz, E. D., Brunkard, J., Legros, D., Hill, A., McKay, H., Luquero, F. J., Olson, D., et al. (2017). El Niño and the shifting geography of cholera in Africa. *Proceedings of the National Academy of Sciences*, 114(17):4436–4441.

Mounier, F., Kiladis, G. N., and Janicot, S. (2007). Analysis of the dominant mode of convectively coupled Kelvin waves in the West African monsoon. *Journal of climate*, 20(8):1487–1503.

Mpeta, E. J. and Jury, M. R. (2001). Intra-seasonal convective structure and evolution over tropical East Africa. *Climate Research*, 17(1):83–92.

Munday, C., Washington, R., and Hart, N. (2021). African Low-Level Jets and Their importance for Water Vapor Transport and Rainfall. *Geophysical Research Letters*, 48(1):e2020GL090999.

Mutai, C., Ward, M., and Colman, A. (1998). Towards the prediction of the East Africa short rains based on sea-surface temperature–atmosphere coupling. *International Journal of Climatology*, 18(9):975–997.

Mutai, C. C. and Ward, M. N. (2000). East African rainfall and the tropical circulation/convection on intraseasonal to interannual timescales. *Journal of Climate*, 13(22):3915–3939.

Nakazawa, T. (1988). Tropical super clusters within intraseasonal variations over the western Pacific. *Journal of the Meteorological Society of Japan. Ser. II*, 66(6):823–839.

Nguyen, H. and Duvel, J.-P. (2008). Synoptic wave perturbations and convective systems over equatorial Africa. *Journal of Climate*, 21(23):6372–6388.

Nicholson, S. (2002). A review of climate dynamics and climate variability in Eastern Africa.

Nicholson, S. (2016). The Turkana low-level jet: mean climatology and association with regional aridity. *International Journal of Climatology*, 36(6):2598–2614.

Nicholson, S. E. (2017). Climate and climatic variability of rainfall over eastern Africa. *Reviews of Geophysics*,

55(3):590–635.

Nicholson, S. E. (2018). The ITCZ and the seasonal cycle over equatorial Africa. *Bulletin of the American Meteorological Society*, 99(2):337–348.

Nicholson, S. E. and Dezfuli, A. K. (2013). The relationship of rainfall variability in western equatorial Africa to the tropical oceans and atmospheric circulation. part i: The boreal spring. *Journal of climate*, 26(1):45–65.

Nicholson, S. E. and Grist, J. P. (2003). The seasonal evolution of the atmospheric circulation over West Africa and equatorial Africa. *Journal of climate*, 16(7):1013–1030.

Nieuwolt, S. (1978). Rainfall Variability and Drought Frequencies in East Africa (niederschlagsschwankungen und häufigkeit von dürren in ostafrika). *Erdkunde*, pages 81–88.

OCHA (2020). Eastern Africa Region: Floods and Locust outbreak snapshot (May 2020). `https://reliefweb.int/report/ethiopia/eastern-africa-region-floods-and-locust-outbreak-snapshot-may-2020`. Accessed: 2021-08-23.

OECD/FAO (2016). Agriculture in Sub-Saharan Africa: Prospects and challenges for the next decade. *OECD-FAO Agricultural Outlook 2016-2025*.

Ogallo, L. (1988). Relationships between seasonal rainfall in East Africa and the Southern Oscillation. *Journal of Climatology*, 8(1):31–43.

Ogwang, B. A., Chen, H., Li, X., and Gao, C. (2014). The influence of topography on East African October to December climate: sensitivity experiments with RegCM4. *Advances in Meteorology*, 2014.

Omondi, P. A., Awange, J. L., Forootan, E., Ogallo, L. A., Barakiza, R., Girmaw, G. B., Fesseha, I., Kululetera, V., Kilembe, C., Mbati, M. M., et al. (2014). Changes in temperature and precipitation extremes over the Greater Horn of Africa region from 1961 to 2010. *International Journal of Climatology*, 34(4):1262–1277.

Ongoma, V., Chen, H., and Omony, G. W. (2018). Variability of extreme weather events over the equatorial East Africa, a case study of rainfall in Kenya and Uganda. *Theoretical and applied climatology*, 131(1-2):295–308.

Pal, S., Chang, H.-I., Castro, C. L., and Dominguez, F. (2019). Credibility of convection-permitting modeling to improve seasonal precipitation forecasting in the southwestern United States. *Frontiers in Earth Science*, 7:11.

Parker, D. J. and Diop-Kane, M. (2017). *Meteorology of tropical West Africa: The forecasters' handbook*. John Wiley & Sons.

Persson, A. (2017). The story of the Hovmöller diagram: An (almost) eyewitness account. *Bulletin of the American Meteorological Society*, 98(5):949–957.

Philip, S., Kew, S. F., Jan van Oldenborgh, G., Otto, F., O'Keefe, S., Haustein, K., King, A., Zegeye, A., Eshetu, Z., Hailemariam, K., et al. (2018). Attribution analysis of the Ethiopian drought of 2015. *Journal of Climate*, 31(6):2465–2486.

Philippon, N., Camberlin, P., and Fauchereau, N. (2002). Empirical predictability study of October–December

East African rainfall. *Quarterly Journal of the Royal Meteorological Society*, 128(585):2239–2256.

Philippon, N., Camberlin, P., Moron, V., and Boyard-Micheau, J. (2015). Anomalously wet and dry rainy seasons in Equatorial East Africa and associated differences in intra-seasonal characteristics. *Climate Dynamics*, 45(7):2101–2121.

Pohl, B. and Camberlin, P. (2006). Influence of the Madden–Julian oscillation on East African rainfall. I: Intraseasonal variability and regional dependency. *Quarterly Journal of the Royal Meteorological Society: A journal of the atmospheric sciences, applied meteorology and physical oceanography*, 132(621):2521–2539.

Pokam, W. M., Bain, C. L., Chadwick, R. S., Graham, R., Sonwa, D. J., and Kamga, F. M. (2014). Identification of processes driving low-level westerlies in west equatorial Africa. *Journal of Climate*, 27(11):4245–4262.

Pokam, W. M., Djiotang, L. A. T., and Mkankam, F. K. (2012). Atmospheric water vapor transport and recycling in Equatorial Central Africa through NCEP/NCAR reanalysis data. *Climate Dynamics*, 38(9):1715–1729.

Prein, A. F., Langhans, W., Fosser, G., Ferrone, A., Ban, N., Goergen, K., Keller, M., Tölle, M., Gutjahr, O., Feser, F., et al. (2015). A review on regional convection-permitting climate modeling: Demonstrations, prospects, and challenges. *Reviews of geophysics*, 53(2):323–361.

Ray, D. K., Gerber, J. S., MacDonald, G. K., and West, P. C. (2015). Climate variation explains a third of global crop yield variability. *Nature communications*, 6(1):1–9.

Reed, R. J., Norquist, D. C., and Recker, E. E. (1977). The structure and properties of African wave disturbances as observed during phase III of GATE. *Monthly Weather Review*, 105(3):317–333.

Respati, M. R. and Lubis, S. W. (2021). Impacts of convectively coupled equatorial waves on rainfall extremes in Java, Indonesia. Technical report, Copernicus Meetings.

Ridout, J. A. and Flatau, M. K. (2011). Convectively coupled Kelvin wave propagation past Sumatra: A June case and corresponding composite analysis. *Journal of Geophysical Research: Atmospheres*, 116(D7).

Ropelewski, C. F. and Halpert, M. S. (1987). Global and regional scale precipitation patterns associated with the El niño/Southern Oscillation. *Monthly weather review*, 115(8):1606–1626.

Roundy, P. E. (2008). Analysis of convectively coupled Kelvin waves in the Indian Ocean MJO. *Journal of the Atmospheric Sciences*, 65(4):1342–1359.

Roundy, P. E. and Frank, W. M. (2004). A climatology of waves in the equatorial region. *Journal of the atmospheric sciences*, 61(17):2105–2132.

Salack, S., Saley, I. A., and Bliefernicht, J. (2018). Observed data of extreme rainfall events over the West African Sahel. *Data in brief*, 20:1274–1278.

Salerno, J., Diem, J. E., Konecky, B. L., and Hartter, J. (2019). Recent intensification of the seasonal rainfall cycle in equatorial Africa revealed by farmer perceptions, satellite-based estimates, and ground-based station measurements. *Climatic Change*, 153(1-2):123–139.

Sandjon, A. T., Nzeukou, A., and Tchawoua, C. (2012). Intraseasonal atmospheric variability and its interan-

nual modulation in central Africa. *Meteorology and Atmospheric Physics*, 117(3):167–179.

Sandjon, A. T., Nzeukou, A., Tchawoua, C., and Siddi, T. (2014). On the differences in the intraseasonal rainfall variability between western and eastern central Africa: Case of 10–25-day oscillations. *Journal of Climatology*, 2014.

Schlueter, A. (2020). Synoptic to Intraseasonal Variability of African Rainfall. In *Oxford Research Encyclopedia of Climate Science*. Oxford University Press.

Schlueter, A., Fink, A. H., and Knippertz, P. (2019). A systematic comparison of tropical waves over northern Africa. part ii: Dynamics and thermodynamics. *Journal of Climate*, 32(9):2605–2625.

Schlüter, A., Klar, M., Vogel, P., Gneiting, T., Fink, A. H., and Knippertz, P. (2017). Statistical forecasting of tropical rainfall using equatorial waves. In *EGU General Assembly Conference Abstracts*, page 16045.

Schneider, U., Fuchs, T., Meyer-Christoffer, A., and Rudolf, B. (2008). Global precipitation analysis products of the GPCC. *Global Precipitation Climatology Centre (GPCC), DWD, Internet Publikation*, 112.

Seneviratne, Z. M., Adnan, B., Dereczynski, D. L., Ghosh, I., Kossin, L., Otto, P., Satoh, V.-S., Wehner, Z., et al. (2021). Weather and Climate Extreme Events in a Changing Climate. In: Climate Change 2021: The Physical Science Basis. Contribution of Working Group I to the Sixth Assessment Report of the Intergovernmental Panel on Climate Change [Masson-Delmotte, V., P. Zhai, A. Pirani, S. L. Connors, C. Péan, S. Berger, N. Caud, Y. Chen, L. Goldfarb, M. I. Gomis, M. Huang, K. Leitzell, E. Lonnoy, J. B. R. Matthews, T. K. Maycock, T. Waterfield, O. Yelekçi, R. Yu and B. Zhou (eds.)].

Senior, C., Finney, D., Owiti, Z., Rowell, D., Marsham, J., Jackson, L., Berthou, S., Kendon, E., and Misiani, H. (2020). *Technical guidelines for using CP4-Africa simulation data*.

Shongwe, M. E., van Oldenborgh, G. J., van den Hurk, B., and van Aalst, M. (2011). Projected changes in mean and extreme precipitation in Africa under global warming. part ii: East Africa. *Journal of climate*, 24(14):3718–3733.

Sinclaire, Z., Lenouo, A., Tchawoua, C., and Janicot, S. (2015). Synoptic Kelvin type perturbation waves over Congo basin over the period 1979–2010. *Journal of Atmospheric and Solar-Terrestrial Physics*, 130:43–56.

Slingo, J., Spencer, H., Hoskins, B., Berrisford, P., and Black, E. (2005). The meteorology of the Western Indian Ocean, and the influence of the East African Highlands. *Philosophical Transactions of the Royal Society A: Mathematical, Physical and Engineering Sciences*, 363(1826):25–42.

Smith, I. (2004). An assessment of recent trends in Australian rainfall. *Australian Meteorological Magazine*, 53(3):163–173.

Smith, R. (1990). A scheme for predicting layer clouds and their water content in a general circulation model. *Quarterly Journal of the Royal Meteorological Society*, 116(492):435–460.

So, D. and Shin, D.-B. (2018). Classification of precipitating clouds using satellite infrared observations and its implications for rainfall estimation. *Quarterly Journal of the Royal Meteorological Society*, 144:133–144.

Sobel, A. and Kim, D. (2012). The MJO-Kelvin wave transition. *Geophysical research letters*, 39(20).

Sommerfeld, A., Prömmel, K., and Cubasch, U. (2016). The East African Rift System and the impact of oro-

graphic changes on regional climate and the resulting aridification. *International Journal of Earth Sciences*, 105(6):1779–1794.

Song, Y., Semazzi, F. H., Xie, L., and Ogallo, L. J. (2004). A coupled regional climate model for the Lake Victoria basin of East Africa. *International Journal of Climatology*, 24(1):57–75.

Stechmann, S. N., Majda, A. J., and Skjorshammer, D. (2013). Convectively coupled wave–environment interactions. *Theoretical and Computational Fluid Dynamics*, 27(3):513–532.

Stein, T. H., Parker, D. J., Hogan, R. J., Birch, C. E., Holloway, C. E., Lister, G. M., Marsham, J. H., and Woolnough, S. J. (2015). The representation of the West African monsoon vertical cloud structure in the Met Office Unified Model: an evaluation with Cloudsat. *Quarterly Journal of the Royal Meteorological Society*, 141(693):3312–3324.

Stephan, C. C., Klingaman, N. P., Vidale, P. L., Turner, A. G., Demory, M.-E., and Guo, L. (2018). A comprehensive analysis of coherent rainfall patterns in China and potential drivers. Part I: Interannual variability. *Climate Dynamics*, 50(11-12):4405–4424.

Stephens, G. L., L'Ecuyer, T., Forbes, R., Gettelmen, A., Golaz, J.-C., Bodas-Salcedo, A., Suzuki, K., Gabriel, P., and Haynes, J. (2010). Dreary state of precipitation in global models. *Journal of Geophysical Research: Atmospheres*, 115(D24).

Stocker, T. (2014). *Climate change 2013: the physical science basis: Working Group I contribution to the Fifth assessment report of the Intergovernmental Panel on Climate Change*. Cambridge university press.

Stratton, R. A., Senior, C. A., Vosper, S. B., Folwell, S. S., Boutle, I. A., Earnshaw, P. D., Kendon, E., Lock, A. P., Malcolm, A., Manners, J., et al. (2018). A Pan-African convection-permitting regional climate simulation with the met office unified model: CP4-Africa. *Journal of Climate*, 31(9):3485–3508.

Straub, K. H., Haertel, P. T., and Kiladis, G. N. (2010). An analysis of convectively coupled Kelvin waves in 20 WCRP CMIP3 global coupled climate models. *Journal of climate*, 23(11):3031–3056.

Straub, K. H. and Kiladis, G. N. (2002). Observations of a convectively coupled Kelvin wave in the eastern Pacific ITCZ. *Journal of the atmospheric sciences*, 59(1):30–53.

Straub, K. H. and Kiladis, G. N. (2003a). Extratropical forcing of convectively coupled Kelvin waves during austral winter. *Journal of the atmospheric sciences*, 60(3):526–543.

Straub, K. H. and Kiladis, G. N. (2003b). The observed structure of convectively coupled Kelvin waves: Comparison with simple models of coupled wave instability. *Journal of the atmospheric sciences*, 60(14):1655–1668.

Subudhi, A. K. and Landu, K. (2019). Influence of convectively coupled equatorial waves and intra-seasonal oscillations on rainfall extremes over India. *International Journal of Climatology*, 39(5):2786–2792.

Sumner, G. (1983). Daily rainfall variability in coastal Tanzania. *Geografiska Annaler: Series A, Physical Geography*, 65(1-2):53–66.

Sun, X., Xie, L., Semazzi, F., and Liu, B. (2015). Effect of lake surface temperature on the spatial distribution and intensity of the precipitation over the Lake Victoria basin. *Monthly Weather Review*, 143(4):1179–1192.

Tall, A., Jay, A., and Hansen, J. (2013). Scaling up climate services for farmers in Africa and South asia: workshop report.

Taylor, C. M., Gounou, A., Guichard, F., Harris, P. P., Ellis, R. J., Couvreux, F., and De Kauwe, M. (2011). Frequency of sahelian storm initiation enhanced over mesoscale soil-moisture patterns. *Nature Geoscience*, 4(7):430–433.

Taylor, R. G., Favreau, G., Scanlon, B. R., and Villholth, K. G. (2019). Topical collection: Determining groundwater sustainability from long-term piezometry in Sub-Saharan Africa. *Hydrogeology Journal*, 27(2):443–446.

Tchatchou, B., Sonwa, D. J., Ifo, S., and Tiani, A. M. (2015). Deforestation and forest degradation in the Congo Basin: State of knowledge, current causes and perspectives.

Thayer-Calder, K. and Randall, D. (2012). A convective downdraft parameterization guided by high-resolution cloud modeling. In *AGU Fall Meeting Abstracts*, volume 2012, pages A53F–0189.

Todd, M. C. and Washington, R. (2004). Climate variability in central equatorial Africa: Influence from the Atlantic sector. *Geophysical Research Letters*, 31(23).

Tomšík, K., Smutka, L., Lubanda, J.-P., and Rohn, H. (2015). Position of agriculture in Sub-Saharan GDP structure and economic performance. *Agris on-line Papers in Economics and Informatics*, 7(665-2016-45047):69–80.

Tulich, S. N., Kiladis, G. N., and Suzuki-Parker, A. (2011). Convectively coupled Kelvin and easterly waves in a regional climate simulation of the tropics. *Climate dynamics*, 36(1-2):185–203.

Tulich, S. N. and Mapes, B. E. (2008). Multiscale convective wave disturbances in the tropics: Insights from a two-dimensional cloud-resolving model. *Journal of the atmospheric sciences*, 65(1):140–155.

Usman, M. T. and Reason, C. (2004). Dry spell frequencies and their variability over southern Africa. *Climate research*, 26(3):199–211.

Van den Dool, H., Saha, S., and Johansson, Å. (2000). Empirical orthogonal teleconnections. *Journal of Climate*, 13(8):1421–1435.

Van der Ent, R. J., Savenije, H. H., Schaefli, B., and Steele-Dunne, S. C. (2010). Origin and fate of atmospheric moisture over continents. *Water Resources Research*, 46(9).

Van Genuchten, M. T. (1980). A closed-form equation for predicting the hydraulic conductivity of unsaturated soils. *Soil science society of America journal*, 44(5):892–898.

Vellinga, M. and Milton, S. F. (2018). Drivers of interannual variability of the East African Long Rains. *Quarterly Journal of the Royal Meteorological Society*, 144(712):861–876.

Vellinga, M., Roberts, M., Vidale, P. L., Mizielinski, M. S., Demory, M.-E., Schiemann, R., Strachan, J., and Bain, C. (2016). Sahel decadal rainfall variability and the role of model horizontal resolution. *Geophysical Research Letters*, 43(1):326–333.

Ventrice, M. J. and Thorncroft, C. D. (2013). The role of convectively coupled atmospheric Kelvin waves on African easterly wave activity. *Monthly weather review*, 141(6):1910–1924.

Vizy, E. K. and Cook, K. H. (2019). Observed relationship between the Turkana low-level jet and boreal summer convection. *Climate Dynamics*, 53(7):4037–4058.

Vogel, P., Knippertz, P., Fink, A. H., Schlueter, A., and Gneiting, T. (2020). Skill of global raw and Postprocessed Ensemble Predictions of Rainfall in the Tropics. *Weather and Forecasting*, 35(6):2367–2385.

Walters, D., Baran, A. J., Boutle, I., Brooks, M., Earnshaw, P., Edwards, J., Furtado, K., Hill, P., Lock, A., Manners, J., et al. (2019). The Met Office Unified Model global atmosphere 7.0/7.1 and JULES global land 7.0 configurations. *Geoscientific Model Development*, 12(5):1909–1963.

Wang, B. (1988). Dynamics of tropical low-frequency waves: An analysis of the moist Kelvin wave. *Journal of Atmospheric Sciences*, 45(14):2051–2065.

Wang, H. and Fu, R. (2007). The influence of Amazon rainfall on the atlantic ITCZ through convectively coupled Kelvin waves. *Journal of climate*, 20(7):1188–1201.

Wang, L. and Li, T. (2017). Convectively coupled Kelvin waves in CMIP5 coupled climate models. *Climate Dynamics*, 48(3-4):767–781.

Wani, S. P., Sreedevi, T., Rockström, J., Ramakrishna, Y., et al. (2009). Rainfed agriculture–past trends and future prospects. *Rainfed agriculture: Unlocking the potential*, pages 1–35.

Washington, R., James, R., Pearce, H., Pokam, W. M., and Moufouma-Okia, W. (2013). Congo Basin rainfall climatology: can we believe the climate models? *Philosophical Transactions of the Royal Society B: Biological Sciences*, 368(1625):20120296.

Weber, N. J., Kim, D., and Mass, C. F. (2021). Convection–Kelvin Wave Coupling in a Global Convection-Permitting Model. *Journal of the Atmospheric Sciences*, 78(4):1039–1055.

Weickmann, K. M., Lussky, G. R., and Kutzbach, J. E. (1985). Intraseasonal (30–60 day) fluctuations of outgoing longwave radiation and 250 mb streamfunction during northern winter. *Monthly Weather Review*, 113(6):941–961.

Wenhaji Ndomeni, C., Cattani, E., Merino, A., and Levizzani, V. (2018). An observational study of the variability of East African rainfall with respect to sea surface temperature and soil moisture. *Quarterly Journal of the Royal Meteorological Society*, 144:384–404.

Wheeler, M. and Kiladis, G. N. (1999). Convectively coupled equatorial waves: Analysis of clouds and temperature in the wavenumber–frequency domain. *Journal of the Atmospheric Sciences*, 56(3):374–399.

Wheeler, M., Kiladis, G. N., and Webster, P. J. (2000). Large-scale dynamical fields associated with convectively coupled equatorial waves. *Journal of the Atmospheric Sciences*, 57(5):613–640.

Wheeler, M. and Nguyen, H. (2015). Tropical meteorology and climate— equatorial waves. *Encylopedia of Atmospheric Sciences 2nd Edition, volume 6*.

Wheeler, M. and Weickmann, K. M. (2001). Real-time monitoring and prediction of modes of coherent synoptic to intraseasonal tropical variability. *Monthly Weather Review*, 129(11):2677–2694.

Wheeler, M. C. and Hendon, H. H. (2004). An all-season real-time multivariate MJO index: Development of an index for monitoring and prediction. *Monthly weather review*, 132(8):1917–1932.

Willenbockel, D. (2012). *Extreme weather events and crop price spikes in a changing climate: Illustrative global simulation scenarios*. Oxfam International.

Williams, A. P. and Funk, C. (2011). A westward extension of the warm pool leads to a westward extension of the Walker circulation, drying eastern africa. *Climate Dynamics*, 37(11-12):2417–2435.

Wilson, D. R. and Ballard, S. P. (1999). A microphysically based precipitation scheme for the UK Meteorological Office Unified Model. *Quarterly Journal of the Royal Meteorological Society*, 125(557):1607–1636.

Wilson, D. R., Bushell, A. C., Kerr-Munslow, A. M., Price, J. D., and Morcrette, C. J. (2008). Pc2: A prognostic cloud fraction and condensation scheme. I: Scheme description. *Quarterly Journal of the Royal Meteorological Society*, 134(637):2093–2107.

Wolding, B., Dias, J., Kiladis, G., Maloney, E., and Branson, M. (2020). Interactions between moisture and tropical convection. part ii: The convective coupling of equatorial waves. *Journal of the Atmospheric Sciences*, 77(5):1801–1819.

Wood, N., Staniforth, A., White, A., Allen, T., Diamantakis, M., Gross, M., Melvin, T., Smith, C., Vosper, S., Zerroukat, M., et al. (2014). An inherently mass-conserving semi-implicit semi-lagrangian discretization of the deep-atmosphere global non-hydrostatic equations. *Quarterly Journal of the Royal Meteorological Society*, 140(682):1505–1520.

Woodhams, B. J., Birch, C. E., Marsham, J. H., Bain, C. L., Roberts, N. M., and Boyd, D. F. (2018). What is the added value of a convection-permitting model for forecasting extreme rainfall over tropical East Africa? *Monthly Weather Review*, 146(9):2757–2780.

Yang, G.-Y., Ferrett, S., Woolnough, S., Methven, J., and Holloway, C. (2021). Real-time identification of equatorial waves and evaluation of waves in global forecasts. *Weather and Forecasting*, 36(1):171–193.

Yang, G.-Y. and Hoskins, B. (2013). ENSO impact on Kelvin waves and associated tropical convection. *Journal of the atmospheric sciences*, 70(11):3513–3532.

Yang, G.-Y., Hoskins, B., and Gray, L. (2012). The influence of the QBO on the propagation of equatorial waves into the stratosphere. *Journal of the atmospheric sciences*, 69(10):2959–2982.

Yang, G.-Y., Hoskins, B., and Slingo, J. (2003). Convectively coupled equatorial waves: A new methodology for identifying wave structures in observational data. *Journal of the atmospheric sciences*, 60(14):1637–1654.

Yang, G.-Y., Hoskins, B., and Slingo, J. (2007). Convectively coupled equatorial waves. Part I: Horizontal and vertical structures. *Journal of the atmospheric sciences*, 64(10):3406–3423.

Yang, G.-Y. and Hoskins, B. J. (2016). ENSO-related variation of equatorial MRG and Rossby waves and forcing from higher latitudes. *Quarterly Journal of the Royal Meteorological Society*, 142(699):2488–2504.

Yang, G.-Y., Hoskins, B. J., and Slingo, J. M. (2011). Equatorial waves in opposite QBO phases. *Journal of the Atmospheric Sciences*, 68(4):839–862.

Yang, G.-Y., Methven, J., Woolnough, S., Hodges, K., and Hoskins, B. (2018). Linking African easterly wave activity with equatorial waves and the influence of Rossby waves from the Southern Hemisphere. *Journal of*

the Atmospheric Sciences, 75(6):1783–1809.

Yang, G.-Y., Slingo, J., and Hoskins, B. (2009). Convectively coupled equatorial waves in high-resolution Hadley Centre climate models. *Journal of climate*, 22(8):1897–1919.

Yang, W., Seager, R., Cane, M. A., and Lyon, B. (2015). The annual cycle of East African precipitation. *Journal of Climate*, 28(6):2385–2404.

Zaitchik, B. F., Berhane, F., and Gnanadesikan, A. (2015). An MJO-Mediated mechanism to explain ENSO and IOD impacts on East African Short Rains. In *AGU Fall Meeting Abstracts*, volume 2015, pages A22E–04.

Zebaze, S., Lenouo, A., Tchawoua, C., Gaye, A. T., and Kamga, F. M. (2017). Interaction between moisture transport and Kelvin waves events over Equatorial Africa through ERA-interim. *Atmospheric Science Letters*, 18(7):300–306.

Zhang, C. (2005). Madden-Julian Oscillation. *Reviews of Geophysics*, 43(2).

Zhu, L. and Li, T. (2017). A special MJO event with a double Kelvin wave structure. *Journal of Meteorological Research*, 31(2):295–308.

Zipser, E. J., Cecil, D. J., Liu, C., Nesbitt, S. W., and Yorty, D. P. (2006). Where are the most intense thunderstorms on Earth? *Bulletin of the American Meteorological Society*, 87(8):1057–1072.